


Politecnico di Torino

ScuDo
Scuola di Dottorato ~ Doctoral School
WHAT YOU ARE, TAKES YOU FAR

Doctoral Dissertation
Doctoral Program in Mechanical Engineering (*XXXVII* cycle)

# Development of Methodologies, Mechatronic Solutions and Controls for Upper Body Rehabilitative Robotics

By

**Giulia Bodo**

******

**Supervisors:**
Prof. A. Tonoli, Supervisor, Politecnico di Torino
PhD. F. Tessari, Co-Supervisor, Massachusetts Institute of Technology
PhD. M. Laffranchi, Co-Supervisor, Italian Institute of Technology

**Doctoral Examination Committee:**
Prof. R. Riener , Referee, Eidgenössische Technische Hochschule, Zürich
Prof. W.T. Ang, Referee, Nanyang Technological University, Singapore

Politecnico di Torino
$14^{th}$ April, 2025

# Declaration

I hereby declare that, the contents and organization of this dissertation constitute my own original work and does not compromise in any way the rights of third parties, including those relating to the security of personal data.

Giulia Bodo
$14^{th}$ April, 2025

* This dissertation is presented in partial fulfillment of the requirements for **Ph.D. degree** in the Graduate School of Politecnico di Torino (ScuDo).

# Acknowledgements

I would like to express my sincere gratitude to the Rehab Technologies-INAIL Laboratory for providing the financial support that made this doctoral project possible.

My heartfelt thanks go to my supervisors, Dr. Stefano Buccelli and Dr. Federico Tessari, for their invaluable guidance and unwavering support throughout my research journey. I owe to them the passion I have developed for this work, as well as the resilience and confidence they instilled in me. Their mentorship taught me to view challenges as opportunities rather than obstacles, a transformative perspective.

I am deeply grateful to Eng. Luca De Guglielmo for his mentorship, which significantly enriched my mechanical expertise. His support, along with that of Eng. Gianluca Capitta was instrumental in turning my ideas and projects into reality. Thank you both for creating a welcoming and inspiring environment in our laboratory.

I extend my appreciation to Professor Andrea Tonoli for his valuable guidance and insightful advice throughout this journey.

A special note of gratitude goes to my supervisor, Dr. Matteo Laffranchi, for his trust in my abilities and for providing numerous opportunities for both personal and professional growth. His advice and collaboration have been pivotal during this important phase of my life.

# Summary

Statistical data reveals that approximately one-sixth of the global population lives with some form of disability affecting motor abilities. In this context, robot-mediated rehabilitation can serve as a powerful tool supporting clinicians in delivering effective rehabilitative therapy.

This doctoral thesis investigates design guidelines for developing robotic rehabilitative systems that can effectively couple with physiological movement, with a particular focus on enhancing the rehabilitative potential of the Float exoskeleton.

The research addresses several aspects, beginning with exploring how different kinematic solutions can expand the device's workspace and improve its manipulability. By optimizing the exoskeleton's range of motion, the aim is to enable more effective and adaptable rehabilitation exercises.

The thesis provides a comprehensive review of the state-of-the-art in upper body rehabilitation (Chapter 2), focusing on the biomechanics of the upper limb, the effects of neurological and orthopedic impairments on the scapulohumeral complex, and the impact of neurological injuries on trunk proprioception and control. It explores current robotic rehabilitation solutions for the shoulder and trunk and evaluates control strategies used in robotic devices.

The literature analysis reveals the need for methodologies to evaluate the performance of different mechatronic designs, providing a framework of quantitative metrics to assess the potential and limitations of various solutions.

Additionally, it identifies insufficient documentation on defining actuation mechanical requirements for rehabilitative robotic systems that interface with the human body, and highlights the importance of trunk recovery during early rehabilitation stages.

In response to these identified needs, this doctoral thesis investigates whether clear metrics and methodologies can be defined to evaluate the effectiveness of different upper limb rehabilitative exoskeleton topologies in replicating human motion. It defines a subset of kinematic analysis, modelling, and simulation techniques to assess upper limb exoskeletons' ability to replicate physiological motion, which can also inform control algorithm development (Chapter 3).

Additionally, the thesis evaluates Series Elastic Actuators capable of detecting Human-Robot Interactions (HRI), offering a systematic characterization and analysis of the compliant element of the actuation mechanism. This includes mechanical evaluations through finite element analysis, frequency response, and hysteresis testing (Chapter 4).

Understanding HRI is crucial for enhancing the exoskeleton's responsiveness and safety during rehabilitation. This research examines various control paradigms to identify the most suitable strategies for achieving smooth, intuitive, and adaptive assistance that aligns with the user's physiological needs. A framework for human-in-the-loop control is proposed to enable various rehabilitation modes such as assistive, resistive, and gravity-compensated (Chapter 5).

Another key focus is exploring how the Float exoskeleton can be modified to extend its functionality beyond arm rehabilitation to support trunk movement. By addressing this broader scope, a novel prototype for trunk movement assistance is presented, extending the capabilities of the current Float passive multi-jointed arm by implementing structural redesigns and adding powered components. The goal is to transform the Float device into a comprehensive tool for upper-body rehabilitation, increasing its therapeutic versatility and ability to assist patients in recovering a wider range of motor functions (Chapter 6).

To summarize, this research contributes to robotic rehabilitation by providing (I) a methodology for assessing robotic systems' ability to mimic physiological motion, (II) a procedure to evaluate and characterize SEA sensing components, (III) control algorithms for treating impaired populations, (IV) a new approach to trunk rehabilitation. These tools establish a strong foundation for designing effective rehabilitation systems and assisting clinicians in delivering precise, high-intensity care.

# Contents

**Summary** iv

**List of Figures** x

**List of Tables** xx

**1 Introduction** 1

1.1 Background . . . . . 1

1.2 Challenges and needs in the development of rehabilitation technology . . . . . 2

1.3 Thesis structure overview . . . . . 3

**2 State-of-the-Art** 5

2.1 Upper limb biomechanics . . . . . 6

2.2 Upper body complex impairment . . . . . 9

2.2.1 Orthopaedic . . . . . 9

2.2.2 Neurological . . . . . 9

2.2.3 Trunk control impairment . . . . . 10

2.3 Upper-limb exoskeletons . . . . . 11

2.3.1 Understanding exoskeleton capability to mimic physiological patterns . . 11

2.3.2 Kinematic analysis for shoulder synergy monitoring . . . . . 12

2.3.3 Commercial exoskeleton . . . . . 13

2.3.4 Float and FloatEVO . . . . . 15

2.4 Trunk commercial rehabilitation devices . . . . . 16

2.5 Actuation system for exoskeletons . . . 18
2.5.1 Electric, pneumatic and hydraulic actuations . . . 18
2.5.2 Series Elastic Actuators . . . 19
2.6 Control . . . 20
2.6.1 Inverse kinematics approaches for rehabilitative robotics . . . 21
2.6.2 Assistive modes . . . 24
2.6.3 Corrective modes . . . 26
2.6.4 Resistive modes . . . 27
2.7 Rapid Control Prototyping . . . 27
2.8 Rationale behind the research project . . . 28

**3 Kinematic Analysis 30**
3.1 Kinematic analysis of upper limb exoskeleton design . . . 30
3.1.1 Float . . . 31
3.1.2 Spherical Float . . . 32
3.1.3 FloatEVO . . . 32
3.2 Assessment methodology for evaluating the capability of a mechatronic system to mimic physiological shoulder movements . . . 35
3.2.1 Size of glenohumeral reachable workspace, from Eulerian to RPY Wrist kinematic design . . . 35
3.2.2 Manipulability evaluation . . . 37
3.2.3 Internal-external rotation performances . . . 38
3.3 Preliminary analysis of scapular synergies . . . 40
3.4 Comparative analysis of inverse kinematics methods for upper limb exoskeleton . 43

**4 Actuation System: SEA for a compliant human-machine interaction 46**
4.1 SEA design . . . 46
4.1.1 SEA components . . . 47
4.2 Compliant elements analysis . . . 49
4.2.1 Design under evaluation . . . 49

4.2.2 FEM analysis . . . . . 50
4.2.3 Joint test at the bench: experimental set-up . . . . . 52
4.2.4 Stiffness evaluation . . . . . 53
4.2.5 Frequency analysis . . . . . 55
4.2.6 Hysteresis evaluation . . . . . 57

**5 Upper Limb Exoskeleton Control 60**
5.1 SEA non-linearity compensation for improved torque sensing . . . . . 60
5.1.1 Methodology . . . . . 61
5.1.2 Error compensation for improved torque and pHRI estimation . . . . . 62
5.1.3 Test on the exoskeleton . . . . . 67
5.2 Preliminary control architecture implementation: RCP approach . . . . . 67
5.2.1 Hardware platform for RCP-HIL test: Spherical Float setup . . . . . 68
5.2.2 Central control unit: Real-Time target machine for RCP development . . 69
5.2.3 Control design methodology . . . . . 69
5.3 FloatEVO embedded control . . . . . 80
5.3.1 Control layer architecture . . . . . 80
5.3.2 Control modes . . . . . 81

**6 Design of an Upper Body Robotic Mobilizer for Neurological Disorders 97**
6.1 Device design . . . . . 97
6.1.1 Kinematics . . . . . 98
6.1.2 Actuation . . . . . 100
6.1.3 System sizing . . . . . 100
6.1.4 Electronic setup . . . . . 102
6.1.5 Human-Robotic Device interface . . . . . 102
6.2 Control design . . . . . 103
6.2.1 SEA torque estimation . . . . . 104
6.2.2 Control modes . . . . . 104

**7 Discussion** **109**

7.1 Insights from kinematic analysis: key outcomes . . . . . 109

7.2 Series Elastic Actuators: sensing challenges and design considerations . . . . . 110

7.3 Reflections on control architecture design and implementation . . . . . 112

7.4 FloatEVO's next frontier: advancing trunk rehabilitation . . . . . 113

7.5 Future perspectives . . . . . 114

**Appendix A PhD Secondary Activities** **115**

**Appendix B Publications** **130**

**References** **133**

# List of Figures


2.1 Scheme of the physiological reference planes: specifically, (A) Sagittal plane: this plane runs in an anteroposterior direction, vertically dividing the body into two symmetrical halves, left and right, known as antimeres; (B) Frontal plane: this plane is perpendicular to the sagittal plane and divides the body into anterior and posterior portions; (C) Horizontal plane: this plane divides the body into an upper and a lower portion. . . . . 6

2.2 Fundamental movements of the shoulder and elbow: For the shoulder, the following movements are represented: (I) Extension-Flexion, (II) Adduction, (III) Abduction, (IVb-c) Horizontal Adduction-Abduction, and (V) External Rotation. (VI) depicts Elbow Flexion-Extension. . . . . 7

2.3 The representation and labelling of upper body muscles highlight those involved in elementary motions, such as shoulder flexion, extension, internal and external rotation, and abduction. Images from. . . . . 8

2.4 Exoskeleton devices for upper limb rehabilitation: a) Alex, b) ArmeoPower, c) Anyexo, d) Harmony, and e) Aramis. . . . . 14

2.5 Float (a) and FloatEVO (b) exoskeletons for upper limb rehabilitation. The devices are equipped with a movable base on which the multi-jointed arm is mounted, allowing the subject to explore a wide range of motion while performing activities of daily living (ADL) movements. The Graphic User Interfaces (GUIs) used by clinicians to control the devices are also shown. . . . . 15

2.6 Commercial devices for trunk rehabilitation: (a) Hunova, (b) Trunk Control Robot 3DBT-33, (c) T-Chair and (d) SpaceBalance 3D . . . . . 16

3.1 Design of IIT-Rtech Laboratory upper limb exoskeletons. (a) Float: 5-Dof device, (b) Spherical Float: 6-Dof prototype, (c) FloatEVO: optimized 7-Dof design. . . 31

3.2 The figure (a) depicts the relationship between the achieved angles of abduction and flexion in the Eulerian and RPY design (both for Spherical Float and FloatEVO). The plots illustrate which angle of abduction is attainable at a certain angle of flexion. Figure (b) shows some reference configurations identified by flexion-abduction angles: at 0 deg flexion - 0 deg abduction, the arm is considered relaxed along the body. Negative values of $\theta$ represent shoulder extension (meaning exploring the space behind the back), and negative abduction represents the arm closing towards the counter-side shoulder. . . . . 37

3.3 Manipulability study and representation. Comparison between the three different kinematics: all the combinations of joint values inside the joint's working range (resulting in RPY-considered combinations) were used to compute the manipulability associated with that pose. . . . . 38

3.4 Comparison between the internal-external rotation achievable with the 3-DOF Eulerian (Float) and RPY wrist solutions (Spherical Float and FloatEVO) within the analyzed range. The intra-extra rotation is quantified by the blue semi-circles, representing the range between maximum and minimum roll angles computed in that configuration, identified by yaw (GH Horizontal Rotation) and pitch (GH Elevation Rotation) coordinates on the planetary. This visualization method is recommended by A. H. Stienen and A. Q. Keemink. . . . . 39

3.5 2DoF mechanism for the alignment of the physiological shoulder joint center (yellow), with the robotic spherical wrist center (red), namely the intersection point between the three rotational axes of the joint dedicated to the shoulder complex of FloatEVO. The red arrow indicates the direction of the alignment movement on the sagittal and frontal planes. . . . . 40

3.6 Rigid body tree at the starting position for shoulder flexion and horizontal abduction. The orange line shows the computed shoulder center trajectory via direct kinematics, while the yellow area represents the scapular activation range during these movements. 42

3.7 Overall comparison of the trajectory and joint angles trends in Spherical Float. . . 45

4.1 Components view of a custom-made joint. The main components include: (1) the Maxon BLDC motor, (2) the harmonic drive, (3) encoders, and (4) the compliant element (torsional spring with spiral geometry). . . . . 47

4.2 Designed by the IIT-Rehab Technologies Laboratory, these compliant elements feature various geometries to optimize performance. The SPT2P and SPTF1P are titanium spiral springs, while the SPS1P is a steel spiral spring. The STS is a steel star spring, showcasing a diverse range of materials and designs tailored for specific applications. . . . . 50

4.3 Von Mises stresses under the maximum torsional load applicable by design, results from FEM analysis. . . . . 51

4.4 Von Mises tensions under the maximum torsional load applicable by project, results from FEM analysis. . . . . 51

4.5 Experimental hardware set-up adopted to test the joint under different load-frequency solicitations. . . . . 53

4.6 Schematic representation of the signal applied to and recorded from the SEA joint during the testing procedure, utilized for stiffness evaluation (linear characteristic analysis), hysteresis analysis, and frequency response assessment. . . . . 53

4.7 These graphs illustrate the relationship between the torque measured by the torsiometer and the torsional spring deformation angle measured by the encoders. The slope of the linear model corresponds to the spring stiffness. The experimental spring characteristic is shown in blue, while the linear approximation is represented in red. . . . . 54

4.8 Identified dynamics response of the different SEAs. The four plots report the magnitude Bode plots of the actuating units with the four different springs: SPT2P (top-left), SPTF1P (top-right), SPS1P (bottom-left), and STS (bottom-right). The frequency responses presented are the results of the analysis conducted using the MATLAB System Identification Toolbox, which is used for creating models of linear and nonlinear dynamic systems from input and output data. For this analysis, the input data was the motor's measured current, and the output data was the torque recorded by the SEA sensor when the joint was constrained in rotation. . . . . 56

4.9 Hysteresis behaviour around the origin of the torque-angle diagram, the picture is a zoom in of Figure 4.7. The x-axis represents the torsional spring deformation angle measured by the encoders, while the y-axis displays the torque measured by the industrial torsiometer at the joint output shaft under constrained rotation conditions. 57

5.1 SEAs springs experimental characterization: by expressing the relation between the dynamic model ($\tau_{dynM}$) computed torque and the spring deformation ($\Delta\theta$) it is possible to determine the linear behaviour of the compliant element, thus its stiffness and torque offset (residual torsional torque on the spring due to assembly procedure). The experimental data (blue line) are then interpolated by exploiting a linear fitting regression model (red line). The results are shown for two different SEAs with reduction ratios of 1:80 and 1:50 in (a) and (b) respectively. . . . . 63

5.2 Analysis of the torque error affecting the SEA measurement at no load condition. The results are shown for the two analyzed SEAs with reduction ratios of 1:80 and 1:50 in (a) and (b) respectively. The torque error, computed as the difference between the dynamic model torque and the SEA one, is expressed in the function of the encoder at the motor side (Aksim2). This error is successfully approximated by a 5th-order Fourier Series. The recomputed errors, after the corrections, are shown. The corrected measure results centred around the origin, reduced in amplitude, and linearised in shape. . . . . 63

5.3 In the figures are reported the torque errors, expressed in function of the motor side Aksim2 encoder, computed for SEAs with reduction ratio 1:80 and 1:50 in (a) and (b) respectively. The errors computed at the different load conditions are shown highlighting the load-dependent non-linear behavior of the SEA systems. This effect resulted in being amplified for a higher reduction ratio. . . . . 64

5.4 The load-condition errors shown in figure 5.3 are corrected with the no-load 5th order Fourier Series (green line), obtaining the signals here reported in yellow, orange, and blue lines. Then the second correction, 8th order Fourier Series (red line), is applied to the signals providing the final corrected SEAs torque measurements for the joints with reduction ratio 1:80 and 1:50 in (a) and (b) respectively. . . . . 64

5.5 Experimental test, on FloatEVO exoskeleton, for evaluating the pHRI, the following scenarios are depicted: (a) and (b) show a non-interaction scenario wherein the SEA joint, controlled in position control, adheres to the predefined trajectory. Subsequently, in (c), a user interacts with the exoskeleton by exerting resistance to the movement, which is subsequently recorded by the SEA sensor. . . . . 67

5.6 The joint with a reduction ratio of 1:80 was tested once assembled on the exoskeleton. The following tests were performed: flexion-extension without HRI (flexion-extension with external disturbance given by the HRI (right) to mimic the possible resistance of a user in performing the movement. The joint was controlled in position to follow a predefined trajectory. The graph shows the estimated torque of the SEA joint calculated with and without Fourier correction and the gravity torque calculated using the dynamic model. . . . . 68

5.7 Hardware setup: EPOS motor controller and SEA sensors are connected via CAN to Speedgoat Baseline real-time target machine. Speedgoat can communicate via ethernet with the host computer (Control Panel) receiving inputs from the GUI and providing feedback data about the running simulation. . . . . 68

5.8 Top Layer of the Simulink control model. The model is built and then deployed on Speedgoat's real-time target machine. In this layer it is possible to identify four main blocks: CAN communication setup, readings of sensor data, processing of all the received data (this unit establishes the exoskeleton behaviour), and the output block that sends over the CAN line the command signals. . . . . 70

5.9 Graphical User Interface Welcome Panel: within this tab of the GUI, crafted using the App Designer MATLAB Tool, users can establish the preferred working mode of the exoskeleton. This includes initiating straightforward exercises under passive or compliant control (with selectable levels of assistance) and configuring the number of repetitions, timing, and target positions for the exercises. Users can command the robot to return to the Home position or activate transparency mode. Additionally, functionalities such as learning and replaying are accessible. The GUI provides comprehensive information about the current phase of the exercise, the direction of the movement to be followed, the status of the machine (sleep, operative, fault), also, information about the joint's position and the end-effector orientation angles are available. . . . . 71

5.10 (**a**) Rigid Body tree representing the kinematic chain of the 6−degree−of−freedom prototype. The Modified Denavit−Hartenberg (mDH) convention was followed for describing the kinematics. Each reference frame, representing a rotational degree of freedom, is associated with the dynamic properties of the body, including mass, the centre of mass coordinates, and the inertia tensor. (**b**) Graphical comparison between the torques estimated by the model and the ones measured by SEAs sensors. During the test, the exoskeleton was moved in position control without a user or a load. In the plot are reported, for each joint, the torques estimated by the SEAs and the ones real−time computed from the model through the robotic toolbox. 72

5.11 Workflow to develop the gravity torque estimation model: the dynamic model characterization for real-time gravity torque computation involves the utilization of various tools. In the CAD model of the prototype, the set of reference frames is re-defined following the modified Denavit-Hartenberg (mDH) convention. Properties such as mass, the centre of mass, and inertia tensor for the different components of the device are then computed concerning these reference frames. Using these dynamically derived properties, a rigid body tree model is constructed in MATLAB, adhering to the aforementioned mDH convention. This characterized model can be imported into the Gravity Torque function, which, in real-time, provides the joint torques necessary to maintain the robot at a specific configuration. . . . . 72

5.12 The impedance control scheme employs the presented algorithm individually for each joint to compute the control signal. The reference target, representing the desired position, has to be reached by ensuring a certain compliance between the user and the device. The difference between the target and actual positions represents the delta displacement of a virtual spring, that multiplied by a virtual stiffness coefficient ($k_v$) provides the spring torsional torque. The actual joint speed introduces a viscous behavior, determined by the viscous coefficient ($\beta_v$). The interaction torque, calculated as the difference between the estimated SEA torque and the gravity torque, serves as the feed-forward term. This ensures that the user can displace the exoskeleton in a compliant manner. . . . . 74

5.13 Experimental results of impedance-based assistive control: three levels of assistance were tested by varying the stiffness−viscosity parameters of the impedance control (stiffness−viscosity couples are reported in Table 5.3). In the figure, the black line indicates the joint reference target, while the blue, orange, and yellow lines represent the results of three tests at different assistance levels. The displayed oscillations are the consequences of human interaction with the robot. It is noticeable that lower assistance (high compliance, low stiffness) allows for greater interaction with the robot, enabling the user to deviate significantly from the target trajectory. Higher assistance (low compliance, high stiffness) leads to better adherence to the target trajectory, albeit restricting interaction with the device to some extent. . . . . 75

5.14 Simulink blocks for the implementation of admittance filter, the same control is implemented to control each joint of the exoskeleton prototype. . . . . 78

5.15 Overview of the FloatEVO control layer architecture. . . . . 80

5.16 The Trinamic control architecture integrates PI motor control for current, velocity, and position, providing precise and efficient motor regulation across all control levels. 81

5.17 The transparency control block schema includes a PI torque controller that compares the torque measurements from the SEAs with those provided by the dynamic model, while also managing the End of Travel (EOT) conditions. The resulting control signal is then processed by the inner current PI loop, which translates it into a motor current control signal. This process also incorporates a feedforward term for friction compensation, ensuring precise and responsive control. From the SEA are received the position (q), velocity (w) and torque (t) measurements. . . . . 82

5.18 The schema of the Learn and Replay mode operates as follows: the exoskeleton functions in transparency mode (torque control), allowing for natural user-driven movement. When the learn function is activated, joint signals are recorded, filtered, and saved to a file. Subsequently, the recorded movement can be reproduced in position control mode by reading and executing the saved data. . . . . 83

5.19 The block representation of the exoskeleton kinematic mode operates as follows: From the GUI, the user can select the desired exercise, range of motion (ROM), number of repetitions, and timing. These inputs are used to compute the corresponding trajectory (for each joint). If the Assistance-As-Needed (AAN) mode is activated, the impedance filter is triggered, and the exercise is executed by the exoskeleton in torque control. Alternatively, if the passive mode is selected, the exoskeleton rigidly mobilizes the arm using position control. . . . . 85

5.20 Cartesian trajectory of the end-effector (positioned at wrist level) during elbow flexion performed at the maximum allowable range of motion (ROM). Joint J7 is the only active joint during this movement. . . . . 86

5.21 Cartesian trajectory of the end-effector (positioned at wrist level) during shoulder abduction performed at the maximum range of motion (ROM). The movement is primarily guided by Joint J6, with Joint J2 contributing to scapular elevation as needed. . . . . 86

5.22 Cartesian trajectory of the end-effector (positioned at wrist level) during shoulder horizontal abduction at the maximum range of motion (ROM). The movement occurs on the horizontal plane and is primarily guided by Joint J6, with J1 and J3 contributing to scapular protraction as needed. . . . . 87

5.23 Cartesian trajectory showing the position of the end-effector (positioned at wrist level) at the maximum internal and external rotation configurations. The movement is guided by Joint J5, with J4 and J6 coupled to it. . . . . 87

5.24 Cartesian trajectory of the end-effector (positioned at wrist level) during the performance of a flexion-extension at the maximum range of motion (ROM). To ensure subject comfort in the starting position, the trajectory begins in an abducted configuration before transitioning to the sagittal plane for the exercise. The movement involves Joint J6, with J4 and J5 coupled to it, and Joint J2, which facilitates scapular elevation coupling. . . . . 88

5.25 Shoulder flexion paths are defined in the sagittal plane within Cartesian space, with varying link sizes (S, M, L) to accommodate different user anthropometries. Joint J1 aligns with the fixed base and focuses on scapular motion, while J4, J5, and J6 represent the glenohumeral joints, enabling diverse shoulder movements. The end-effector (EE) is positioned at elbow level to accurately replicate the desired motion. . . . . 89

5.26 Reference end-effector trajectories (obtained with ellipse parametrization) for FloatEVO, specifically: (a) FloatEVO tunnel section (green) on the YZ plane of the flexion path (red). (b) Tunnel section at maximum diameter for assistance (case of 180 *deg* of flexion), with the reference trajectory point (*t2*) in light blue. The violet marker denotes the current end-effector position (*a2*). Assistance is provided only inside the tunnel based on the Euclidean norm between the coordinates. . . . 91

5.27 Control algorithm for implementing time-independent assist-as-needed mode in the task space: parameters such as joint position, velocity, and estimated torque contribute to gravity, friction, and assistance compensations. Forward kinematics calculates the end-effector pose, which is mapped onto the reference trajectory to determine assistance (force in task space, translated to joint torque via the transposed Jacobian). Joint-level impedance can be implemented to provide additional guidance. The contributions are summed up following the superposition principle, yielding the reference control torque. . . . . 91

5.28 Results from the experimental test on the upper limb exoskeleton are presented. Blue and yellow data are collected In Test1, a flexion was executed while staying inside the tunnel, depicting the reference (blue) and actual (yellow) paths. Assist-as-needed (AAN) forces are applied at the end effector, aiding in the movement performance in both directions (flexion-extension). Test 2 demonstrates that AAN is exclusively applied inside the tunnel. . . . . 93

5.29 The assistance was designed to provide a torque contribution of approximately ±2 Nm at the joint level. The figure shows at the left the x, y, and z components of the force that need to be applied at the end-effector to deliver the intended assistance. On the right, the computed joint torques necessary to achieve this force are displayed. 94

5.30 The resistive control leverages the presence of a Series Elastic Actuator (SEA) and is implemented using a closed-loop torque control approach. Once the target trajectory for the desired exercise is computed, a low-impedance filter is applied to ensure compliance with the user's voluntary motion. The resistive contribution, which acts as a resistance to the motion, is calculated based on the actual position of the joint leading the movement. This contribution is derived using a Gaussian function to model the resistance profile. The resistive torque is subtracted from the control signal, effectively opposing voluntary motion while maintaining smooth interaction. Friction is compensated using a feedforward term, which is calculated with an observer proposed by Le Tien et al. . . . . 95

5.31 (a) A Cartesian representation of the end-effector trajectory and the resistance applied is presented, as it is directly correlated to the motion of Joint 6 ($J_6$), which is responsible for horizontal abduction. All other joints remain stationary once the starting position is reached and are not involved in the motion. The colour map illustrates the variations in resistive contribution, varying from the initial state shown to the maximum range of motion achieved. The starting configuration shown in (a) corresponds to the joint angle $\theta_{J_6} = 2.56$ rad, as depicted in (b). The Gaussian profile was designed for a low resistance level, modulated with a factor of 0.5 relative to the maximum achievable torque of 7.5 Nm, which is reached at the highest selectable resistance level. . . . . 96

6.1 The mechanical design of the trunk device features a planar system composed of J1, J2, and J3, which enables the exploration of a wide working area. When combined with the rotations of J4 and J5, the system facilitates rotational and flexion movements. 98

6.2 Graphical representation of the Denavit-Hartenberg convention parameters, as defined in Table 6.1. The parameters $a$ and $d$ correspond to translations along the x- and z-axes of the current frame, respectively. The depicted configuration represents the zero-rotation reference for each joint. Consequently, the range of motion (ROM) values in Table 6.2 should be considered relative to this reference. 99

6.3 Configurations adopted for the load static analysis. . . . . 101

6.4 The prototype is shown during a preliminary usability test with two subjects. It is possible to notice the corset used to interface the upper body with the device's end effector, which facilitates trunk mobilisation for performing the desired exercises. 102

6.5 The proposed torque control scheme operates as follows: the internal loop generates the target torque signal, which is compared with the SEA torque through a closed-loop sensor measurement (green). The control signal is converted to a current signal and managed by the PID controller (orange) of the EPOS driver boards. Gravity and friction compensation (in black) remain active in all modes. A state machine governs control modes and algorithms, with input from the GUI (in violet). The GUI facilitates trajectory generation for assistive mode, setting reference values for impedance and resistive reference values control. In constant resistance mode, a predefined joint-level resistance opposes motion. In "keep posture" mode, the impedance target aligns with the homing position, while in "against interaction" mode, each joint applies counterforces proportional to human-robot interaction forces. . . . . 104

6.6 Rigid body tree of the trunk device with the end effector trajectory (yellow) shown for the maximum range of movement in the sagittal plane (from $-10$ *deg* to 30 *deg* for extension-flexion). . . . . 105

6.7 A rigid body tree of the trunk device is shown, with the end effector trajectory (orange) for the maximum range of movement in the frontal plane (from $-20$ *deg* to 20 *deg* for lateral flexion). . . . . 105

6.8 Trunk device kinematic configurations at the frontal flexion maximum range of motion: (a, b) 30 deg flexion and (c, d) -10 deg extension . . . . . 106

6.9 Trunk device kinematic configurations at the lateral flexion maximum range of motion: (a, b) 20 deg lateral flexion and (c, d) -20 deg lateral flexion. . . . . 106

6.10 Experimental Testing of the Keep Posture Mode: during experimental testing, the robotic device operates in torque control mode. (a) The target position is fixed at the homing configuration. (b) Perturbations are simulated by an operator manually moving the device from the outside, mimicking a patient's deviation from the correct posture. (c) In response, the device applies a recall force at all joints generated by the impedance parameters. (d) This recall force continues to act until the device returns to the target position. . . . . 107

# List of Tables


2.1 Physiological Joint Ranges of Motion . . . . . 9

2.2 Technical features comparison of devices used for trunk rehabilitation. . . . . 17

3.1 Modified Denavit-Hartenberg parameters for the Float Exoskeleton . . . . . 31

3.2 Parameters of modified Denavit-Hartenberg for the Spherical Float Exoskeleton . 32

3.3 FloatEVO joints ranges of motion. . . . . 35

3.4 Gimbal locks configurations for the analyzed devices. . . . . 36

3.5 Spherical Float - RMSE on the 3 axes of motion between the reference and effective Cartesian trajectories computed with the three different IK methods: differential inverse kinematics, gradient projection method, and ANFIS networks. . . . . 44

3.6 Comparison of RMSE between reference and predicted Cartesian trajectories with two different ANFIS networks: one trained considering robot redundancy, one trained in a non-redundant task configuration. . . . . 44

4.1 Materials properties and geometrical design characteristics of the proposed springs, including diameter, thickness, mass, and theoretical stiffness computed through FEM analysis. . . . . 51

4.2 The table presents data related to different spring geometries, including maximum tolerable torsional load, experimental spring stiffness, Aksim encoder bit resolution, and sensor sensitivity on the torque measurements. The sensor sensitivity depends on the Aksim bit resolution and the spring stiffness. . . . . 52

4.3 Experimental spring characteristic evaluation: considering the linear approximation, stiffness (angular coefficient), intercept, regression coefficient, and the relative error concerning the FEM theoretical stiffness are computed. . . . . 55

4.4 Dynamic and frequency characteristics obtained from system identification of the SEAs springs, it is reported the level of confidence of the fitting. . . . . 56

4.5 Comparison of spring types, including their advantages and limitations. . . . . 58

5.1 Fourier Series correction Error Analysis: the minimum (m) and maximum (M) absolute errors in Nm are reported for the different load condition tests. The errors are computed in three different cases: (I) no correction is applied, (II) the no-load (NL) Fourier Series correction is applied, (III) both the no-load (NL) and the load (L) Fourier compensations are applied to the measurements. . . . . 66

5.2 Residual Error Analysis for Gaussian and Sum of Sines approximations: Minimum (m) and maximum (M) absolute errors (in Nm) are reported for a 15 kg load, with and without load (NL and L) compensations. Gaussian approximations use the 6th order for NL and the 8th order for L, while Sum of Sines uses the 5th order for NL and the 8th order for L, matching the Fourier series. . . . . 66

5.3 Pairs of stiffness and viscosity parameters ($k_v$ and $\beta_v$) utilized in the impedance dynamic model to implement three different levels of assistance: decreasing $k_v$ corresponds to lower support and higher compliance. . . . . 74

5.4 Root Mean Square Error (RMSE) and maximum error values for different joints. The maximum errors and RMSE ($\varepsilon_{\max}$) are computed by comparing the experimental measurements of SEA sensors with the output from the built-in gravity torque calculation function in the MATLAB Robotic Toolbox. The experiment was conducted with the exoskeleton covering various zones within the workspace while operating in position control to validate the consistency of the SEA sensor readings with the MATLAB model. . . . . 77

5.5 Ellipse Parameters for FloatEVO flexion path. . . . . 90

6.1 Trunk device Denavit-Hartenberg kinematic parameters. . . . . 99

6.2 Ranges of motion for each joint limited by its mechanical end of travel. . . . . 99

6.3 Value of the spring stiffness $k$, and linear intercept $\Delta_{\tau_{lm}}$ of the linear model of the spring inside the joints. . . . . 100

6.4 Torque values, simulated in CREO PTC Mechanism analysis, for maximum lateral and frontal flexion across joints. . . . . 101

# Chapter 1

# Introduction

## 1.1 Background

The glenohumeral shoulder complex is one of the most intricate structures of the human body, presenting significant challenges for the development of robotic systems capable of effectively interfacing with this complex joint. Designing a robotic device that can mimic the physiological spatiotemporal rhythm of the shoulder requires both an accurate kinematic analysis and the implementation of advanced control strategies to ensure safe and compliant human-exoskeleton interaction.

Statistical data reveal that approximately one-sixth of the global population lives with some form of disability, significantly impacting motor abilities [1]. Furthermore, it is estimated that just under 1% of the world's population suffers from severe disabilities that prevent autonomous movement. Regardless of the severity of the condition, a decline in quality of life is consistently observed, particularly in terms of reduced autonomy in performing even simple daily activities [2, 3].

The upper limb complex is frequently affected by orthopedic and neurological conditions, which compromise the ability to independently perform functional tasks essential to daily life, such as dressing, grooming, or feeding. Even if improving workplace safety is a potential strategy to reduce the incidence of trauma-related disabilities, occupational injuries represent only one of the many causes of temporary or permanent motor impairments. Consequently, it is crucial to have access to effective rehabilitation protocols to preserve and enhance residual abilities in patients with permanent injuries, as well as to accelerate and optimize recovery for those with temporary impairments.

In orthopaedic contexts, exaggerated joint stiffness is a common consequence of post-surgical immobilization [4]. Joint mobilization is typically performed by physiotherapists using manual

techniques [5]. However, these methods are inherently limited by their dependency on the therapist's direct intervention, constraining both the duration and intensity of the therapy. The scenario becomes even more complex when disabilities arise from neurological disorders. For example, stroke survivors may experience spastic behaviour and abnormal muscle tone, consisting of uncontrolled muscle co-activation that tends to over-stiffen the joints. In such cases, additional challenges, such as spasticity, synkinesias, and cognitive or sensory deficits, exacerbate the limitations of traditional rehabilitation approaches, making treatment even more critical [6].

Rehabilitation in neurological cases is most effective and sustainable when patients are actively involved in the process. Voluntary movement is essential for stimulating the relearning of motion paths related to functional tasks [6–9]. Not only is the shoulder complex affected in such conditions, but the trunk is also frequently impacted, particularly in neurological disorders. The trunk plays a vital role in stabilizing the upper body, and impairments in its function can lead to difficulties in maintaining balance and performing routine tasks. For example, stroke patients typically exhibit weaker isometric and isokinetic trunk muscle contractions compared to healthy individuals. Studies have shown strong correlations between trunk impairment, functional performance, and muscle activity in stroke patients. Similarly, individuals with spinal cord injuries (SCI) who experience trunk muscle paralysis [10] often struggle with diminished trunk control and maintaining stable posture [11].

## 1.2 Challenges and needs in the development of rehabilitation technology

The demand for technologies supporting neuromotor and functional rehabilitation of the upper body is steadily increasing, particularly for conditions such as traumatic shoulder injuries, spinal cord injuries, cerebral lesions, and strokes [6, 7, 9, 12–15]. Developing innovative technological solutions with significant healthcare applications is therefore a priority in the field of rehabilitative robotics.

Robotic devices present a promising opportunity in this context. Multi-degree-of-freedom robots enable distributed interaction along the entire limb being rehabilitated, replicating the quality of movements facilitated by a therapist. These systems can adapt the number of repetitions and the intensity of therapy to individual patients' specific needs, making them ideal tools to complement therapists' work. Robotic therapy has shown great promise in enhancing motor training [6, 9, 16, 17], both in neurological [18–22] and orthopaedic [23, 24] rehabilitation contexts.

Despite growing interest in robotic-mediated rehabilitation, the literature lacks specific methodologies and validated frameworks for assessing its effectiveness.

This thesis investigates design guidelines for developing systems that replicate physiological movement, with a particular focus on enhancing the rehabilitative potential of the Float exoskeleton.

The literature review reveals a lack of metrics and methodologies for evaluating and comparing kinematic solutions that work in close contact with human physiology. The definition of such methods could guide novel approaches for rehabilitation robot development, enabling performance assessment of different devices. For these reasons, Chapter 3 proposes a methodology for evaluating the topology design of upper limb (UL) rehabilitative robots.

Additionally, particularly for actuation systems suitable for rehabilitative robotics, there is insufficient documentation on defining and addressing the mechanical requirements of systems that interface with the human body. Chapter 4 provides a systematic, detailed characterization and analysis of compliant actuation mechanisms that satisfy design goals.

Furthermore, to offer clinicians various control strategies that meet different patient needs, Chapter 5 presents a human-in-the-loop control framework supporting multiple rehabilitation modes (assistive, resistive, gravity-compensated, etc.).

Literature analysis and discussions with clinicians revealed the crucial importance of including trunk mobilization in rehabilitative protocols, especially during early-stage rehabilitation when trunk control is absent. Utilizing the actuation study methodology proposed in Chapter 4 and the rapid control prototyping approach from Chapter 5, Chapter 6 introduces a novel paradigm for trunk rehabilitation that advances beyond existing robotic methods to address this critical need.

## 1.3 Thesis structure overview

This dissertation consists of seven chapters, beginning with a brief introduction that justifies the need for research in upper body rehabilitation. The second chapter provides a comprehensive review of the state-of-the-art in upper body rehabilitation, addressing upper limb biomechanics, the impact of neurological and orthopaedic impairments on the scapulohumeral complex, and the effects of neurological injuries on trunk proprioception and control. It also discusses existing shoulder and trunk rehabilitation solutions and evaluates control strategies previously explored in robotic rehabilitation devices.

The third chapter focuses on developing kinematic analyses, modelling, and simulation approaches to assess upper limb exoskeletons' ability to replicate physiological motion. These kinematic models were instrumental in informing control algorithm design. This chapter provides a mechatronic analysis of various kinematic solutions for the shoulder complex, followed by an in-depth examination of the actuation system, particularly the Series Elastic Actuator (SEA). It details the mechanical evaluation of the SEA compliant element through finite element analysis

(FEM), frequency response, and hysteresis testing to determine the optimal spring design for integration.

The dissertation continues by detailing the development of control platforms and algorithms specifically tailored for rehabilitative applications. This includes low-level SEA control addressing non-idealities, a preliminary rapid control prototyping (RCP) framework for modelling the full control architecture, and the implementation of embedded control strategies in the final exoskeleton prototype. Designed for clinical trials with orthopaedic and neurological patients, this prototype emphasizes SEA torque estimation to implement compliant and assistive control strategies, ensuring effective human-machine interaction.

To further enhance rehabilitative training and promote the adoption of robotic-mediated rehabilitation during the early stages following adverse events, when trunk control has not yet been regained, this dissertation presents the development of a novel SEA-actuated robotic mobilizer specifically designed for trunk rehabilitation. The proposed solution involves modifying the passive, multi-jointed Float support arm to create a more dynamic system capable of addressing trunk movement.

The long-term objective is to integrate this new trunk mobilizer with an improved version of the Float exoskeleton, resulting in a comprehensive robotic device capable of supporting full upper-body rehabilitation. By combining these two systems, the design aims to facilitate coordinated and effective training for both trunk and upper-limb recovery, targeting a wider range of motor impairments.

The trunk device's kinematic and mechanical designs are presented, along with a preliminary control architecture developed using the RCP methodology applied to the upper limb exoskeleton prototype.

This approach to trunk rehabilitation aspires to push beyond the limitations of existing robotic rehabilitation methods by addressing a critical gap in the field. By enabling early-stage intervention and offering a complete rehabilitation experience, the proposed system could have the potential to significantly improve patient outcomes and advance the current state of robotic-assisted therapy.

The conclusion chapter summarizes the findings and contributions of the work presented in the previous sections.

# Chapter 2

# State-of-the-Art

This chapter provides a comprehensive review of upper limb robotic-mediated rehabilitation. Given the thesis focus on developing and implementing mechatronic solutions and control strategies for effective rehabilitation through optimal human-robot interaction, the review examines four key areas: upper limb injuries, robotic rehabilitation devices, actuation systems, and control paradigms.

The chapter begins with an in-depth examination of impairments affecting the upper limb, particularly at the scapular-glenohumeral complex level, as well as issues concerning trunk stability and control. This section not only describes the nature and extent of various impairments but also explores potential rehabilitative approaches to address these challenges. This foundation establishes the requirements and capabilities needed in effective robotic rehabilitation solutions.

The review then analyzes existing robotic solutions for shoulder and trunk rehabilitation. This section highlights current technologies and their clinical applications, demonstrating how these systems can improve patient outcomes through enhanced precision, repeatability, and engagement during therapy.

Next, the chapter evaluates various actuation systems for robotic devices and explores control strategies specific to upper limb rehabilitation. It examines the technical aspects of these systems, assessing their effectiveness and potential integration into comprehensive rehabilitation programs. These sections are essential for understanding how advanced robotics can be tailored to meet specific therapeutic needs.

Finally, building upon insights from this state-of-the-art review, the chapter outlines the rationale for the doctoral thesis, highlighting the specific needs it addresses and the solutions it proposes.

## 2.1 Upper limb biomechanics

The biomechanics of the upper limb are highly complex, involving the shoulder girdle (comprising the scapula and clavicle) and the arm. The upper limb's extensive range of movements is enabled by multiple joints: the shoulder joint, elbow joint, wrist, and hand joints. These joints provide several degrees of freedom, facilitating complex functional tasks across a wide range of motion. The glenohumeral joint, a key component of the shoulder girdle, is a ball-and-socket diarthrodial joint that allows for multiaxial movements. This joint involves a dynamic articulation between the glenoid of the scapula and the proximal humerus. It serves as the primary articulation of the shoulder girdle, permitting movement in multiple planes (Figure 2.1 [25]).

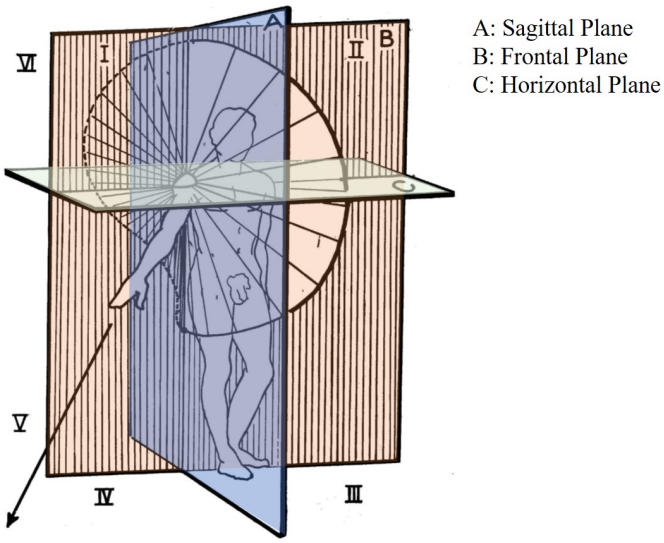



Fig. 2.1 Scheme of the physiological reference planes: specifically, (A) Sagittal plane: this plane runs in an anteroposterior direction, vertically dividing the body into two symmetrical halves, left and right, known as antimeres; (B) Frontal plane: this plane is perpendicular to the sagittal plane and divides the body into anterior and posterior portions; (C) Horizontal plane: this plane divides the body into an upper and a lower portion.

Characteristic movements of the Shoulder:

- Flexion: Moving the upper limb anteriorly in the sagittal plane. The primary muscles involved are the anterior deltoid, coracobrachialis, and pectoralis major, with the biceps brachii providing minor assistance (Figure 2.2 (Ib) [25], Figure 2.3 (red) [26]).
- Extension: Moving the upper limb posteriorly in the sagittal plane. The primary muscles responsible are the posterior deltoid, latissimus dorsi, and teres major (Figure 2.2 (I a), Figure 2.3 (green)).

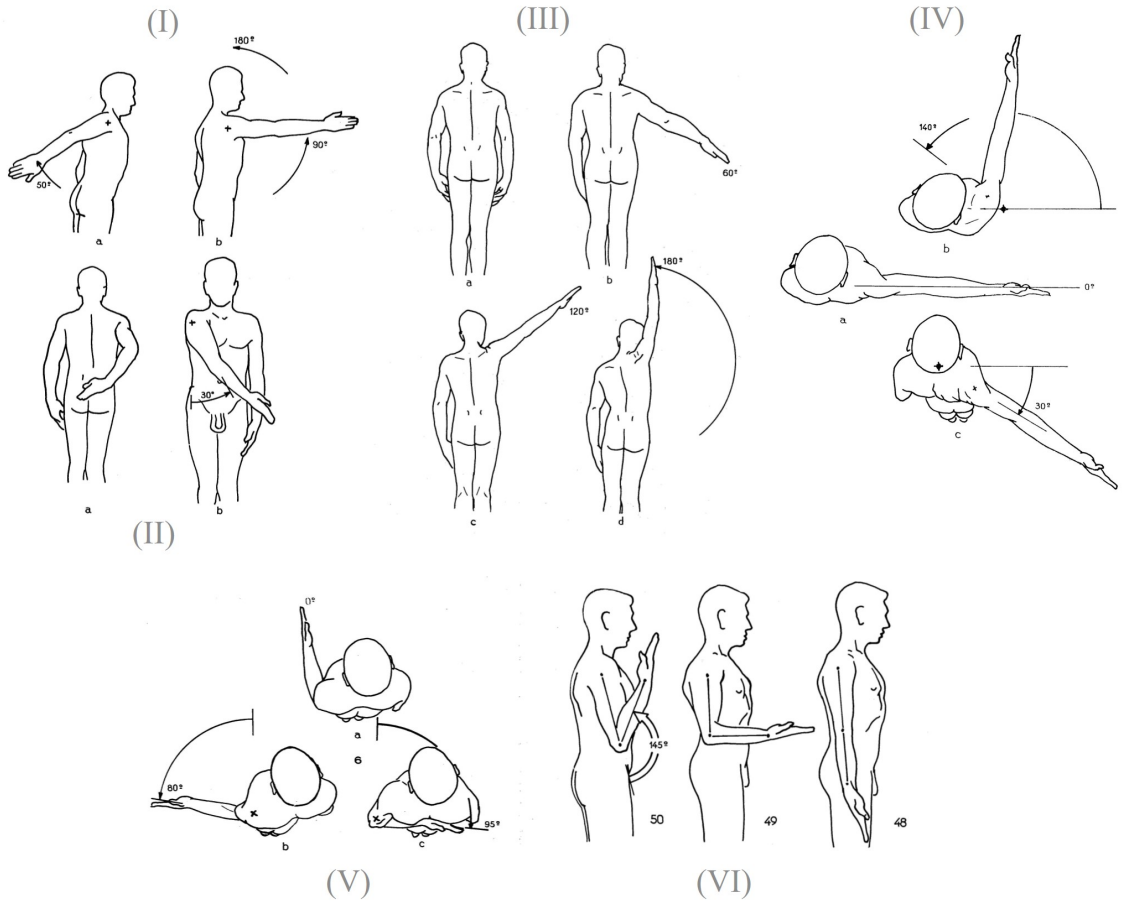



Fig. 2.2 Fundamental movements of the shoulder and elbow: For the shoulder, the following movements are represented: (I) Extension-Flexion, (II) Adduction, (III) Abduction, (IVb-c) Horizontal Adduction-Abduction, and (V) External Rotation. (VI) depicts Elbow Flexion-Extension.

- Internal Rotation: Rotating the upper limb towards the midline along a vertical axis. The subscapularis, pectoralis major, latissimus dorsi, teres major, and anterior deltoid are the primary muscles involved in this motion (Figure 2.3 (orange)).
- External Rotation: Rotating the upper limb away from the midline along a vertical axis. This movement is primarily facilitated by the infraspinatus and teres minor muscles (Figure 2.2 (V), Figure 2.3 (blue)).
- Adduction: Moving the upper limb towards the midline in the coronal plane. The primary muscles responsible are the pectoralis major, latissimus dorsi, and teres major (Figure 2.2 (II, IV b), Figure 2.3 (violet)).

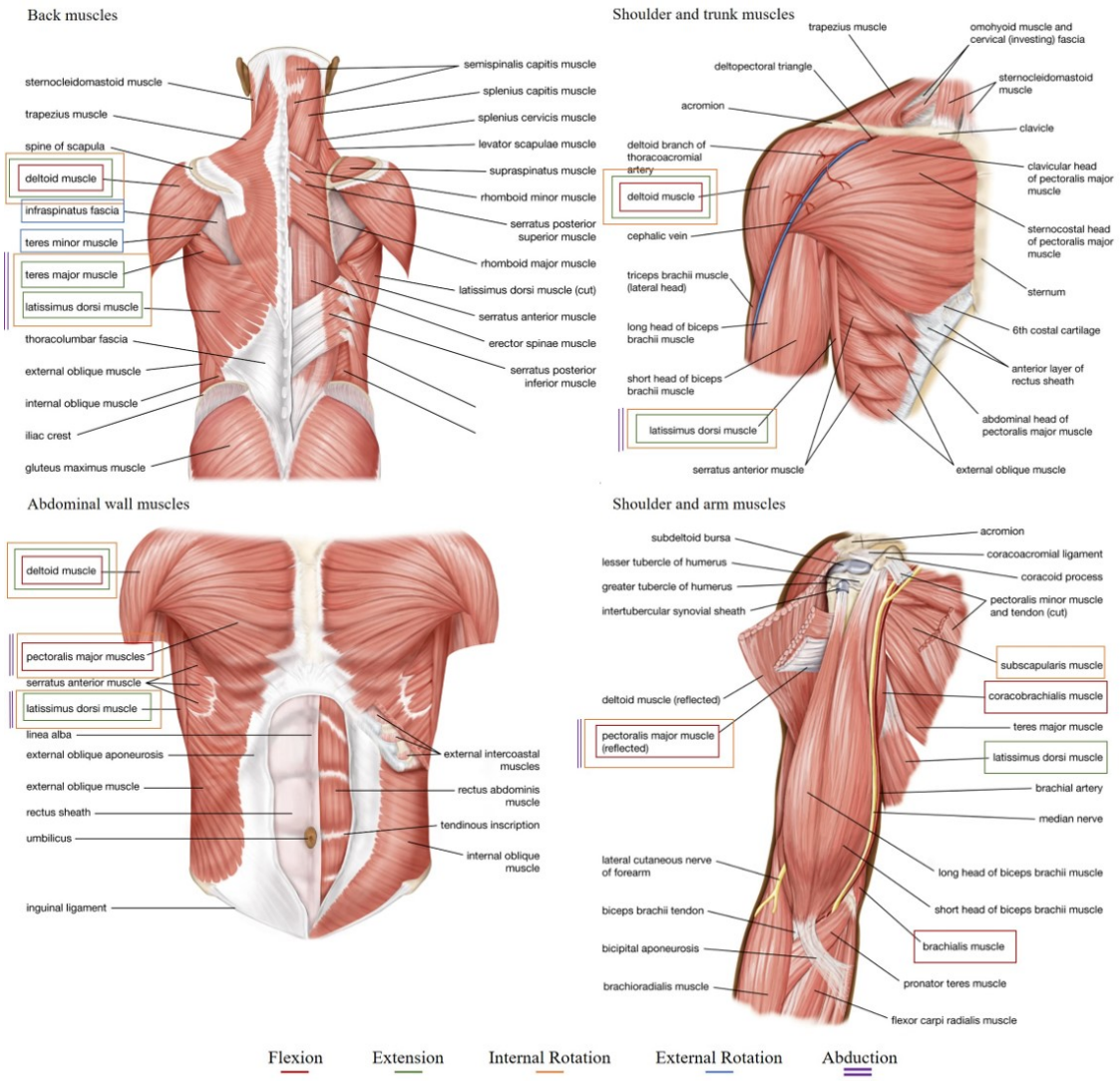



Fig. 2.3 The representation and labelling of upper body muscles highlight those involved in elementary motions, such as shoulder flexion, extension, internal and external rotation, and abduction. Images from.

- Abduction: Moving the upper limb away from the midline in the coronal plane. Understanding how different muscles contribute to this action is crucial, as the range of motion in the glenohumeral joint can help diagnose various pathologies (Figure 2.2 (III, IV c)).

Figure 2.2 (VI) also shows the elbow flexion-extension movement.

The physiological ROM for the aforementioned exercises is collected in Table 2.1.

Due to the complexity of human joint articulation, ensuring precise alignment between the body and the exoskeleton is crucial to prevent patient discomfort [27, 28] and to enable the robotic device to cover the full range of motion for the different movements. Also, since misalignment between

| Joint Motion | Range of Motion |
|---|---|
| Shoulder flexion/extension | 150°-180° / 40°-50° |
| Shoulder abduction/adduction | 180° / 30°-40° |
| Shoulder internal/external rotation | 70°-95° / 40°-70° |
| Elbow flexion/extension | 135°-140° / 0° |
| Forearm supination/pronation | 85°-90° / 70°-90° |
| Wrist flexion/extension | 73° / 70° |
| Wrist radial deviation/ulnar deviation | 27° / 27° |

Table 2.1 Physiological Joint Ranges of Motion

anatomical and robotic joints can lead to tissue compression, resulting in pain for the patient [29] [21], one fundamental requirement for exoskeletons design is a proper human-exoskeleton attachment interface system.

## 2.2 Upper body complex impairment

Studies indicate that approximately one-sixth of the global population lives with some form of disability, often affecting motor abilities [1] and limiting subjects' autonomy in movement. Reduced motor abilities, whether due to diseases or traumatic events, necessitate a rehabilitation process to maximize residual abilities in cases of permanent injuries and to expedite recovery for temporary injuries. In the context of upper limbs, orthopaedic and neurological injuries can result from trauma or pathological conditions, limiting the subject's ability to perform functional movements and carry out daily activities normally, significantly impacting independence and quality of life.

### 2.2.1 Orthopaedic

In orthopaedic contexts, such as in the treatment of patients with reverse shoulder prostheses or muscle transposition, the rehabilitation process typically follows a standardized protocol starting with early passive mobilization of the affected joints. This progresses to active-assisted mobilization and occupational therapy [13]. However, manual joint mobilization, though conducted by physiotherapists, has limitations in terms of duration, intensity, and variability due to the subjective judgment of the operator [30].

### 2.2.2 Neurological

In neurological treatment, deficits in strength resulting from injuries are accompanied by issues such as spasticity, synkinesis, and cognitive or sensory limitations, further complicating the rehabilitation

process [31]. The effectiveness of treatment heavily depends on the active involvement of the patient, thereby stimulating natural processes of neuronal reorganization and regeneration [7, 9, 31]. It is crucial to adjust the complexity of rehabilitation interventions according to the patient's residual capacities, especially during neurological recovery (shaping). Robotic therapy offers a significant advantage in this regard, allowing for more precise and adaptable modulation compared to manual therapy, which relies entirely on the sensitivity and experience of the operator.

### 2.2.3 Trunk control impairment

After a neurological event, the trunk often remains an impaired area, significantly impacting both balance and activities of daily living (ADLs). The trunk is essential for stabilizing the upper body, and when its function is compromised, it can lead to challenges in maintaining balance and performing routine tasks. In stroke patients, trunk muscle contractions, both isometric and isokinetic, are typically weaker compared to those in healthy individuals. Studies have demonstrated strong correlations between trunk impairment, functional performance, and muscle activity in stroke patients. Similarly, individuals with Spinal Cord Injury (SCI) who experience paralysis of the trunk muscles [10] often have diminished control over trunk movements and struggle to maintain a stable posture [11]. Another clinical condition that significantly disrupts trunk motor activity is Pusher Syndrome (or lateropulsion) [32], a specific variation of stroke characterized by a loss of proprioception related to one's posture. Individuals with this syndrome tend to apply a strong, constant push toward their hemiplegic side, regardless of their position [33]. This behavior actively resists any attempts to correct their posture passively, such as shifting their weight toward the body's midline or, through it, to the unaffected side. Pusher Syndrome presents various neuropsychological symptoms that affect motor function in distinct ways. Specifically, individuals often struggle in antigravity situations, showing an inability to recognize and process proprioceptive feedback. This leads to unbalanced postures that are misaligned with the body's midline [34].

Exercises performed during the early stages of rehabilitation can improve functional performance in the later stages. Patients often exhibit a poor antigravity response, which leads to compensatory movements involving greater engagement of the upper trunk and a reduced anterior tilt of the pelvis. Therapeutic interventions must be intensive, active, and challenging to promote optimal recovery. Position sense, a component of proprioception and essential for postural control, is often impaired in these patients, contributing to trunk instability. Patients with pusher syndrome and those in the post-acute phase are typically treated in a seated position to regain the ability to control imbalance-related falls. Standing exercises are usually performed to help the patient achieve an upright position by stabilizing the joints and using rigid legs for support. The aim is to maintain the patient in an upright position. The operational scope of such an approach could range from a complete lack of trunk control to its initial recovery, excluding the phase involving dynamic

function recovery such as walking. In the post-acute phase of recovery, the patient is lifted from bed, and seated, and efforts are made to manage the imbalance-related falls.

## 2.3 Upper-limb exoskeletons

Among the various rehabilitative interventions, robotic approaches are noteworthy. Mechatronic devices with multiple degrees of freedom can be programmed to deliver repetitive task training. Thus, the adoption of robotic devices in clinical settings can be leveraged to support motor learning and enhance motor control and strength [8].

Multi-degree-of-freedom robots allow for distributed interaction along the entire limb to be rehabilitated. They can perform movements along trajectories designed to resemble the motion paths typically facilitated by the therapist, allowing for adjustments in the number of repetitions based on the patient's needs [27]. This capability enables the therapy to be tailored in terms of duration and intensity based on individual patient requirements.

Exoskeletons, equipped with various sensors (for example position, velocity, torque, acceleration and orientation sensors), can also be utilized to monitor patient recovery by acquiring data relevant to the assessment of the reachable workspace and the exerted interaction forces.

The mechatronic design of exoskeletons involves extensive studies, ranging from kinematic analyses to actuation systems. These robotic devices can be categorized as either unilateral or bilateral, depending on whether they allow interaction and rehabilitation for one arm or both arms. Additionally, based on their portability [35], the devices can be classified as grounded, where the structure is fixed to the ground and cannot be moved, or ungrounded [36].

The kinematic chain, consisting of joints connected by links, is characterized by the number of degrees of freedom of the exoskeleton, which determines the possible range of movements.

### 2.3.1 Understanding exoskeleton capability to mimic physiological patterns

Rehabilitating the upper limb requires the development of technologies that can accurately replicate the spatiotemporal motion patterns observed in the human body [37]. The human shoulder's complexity poses a significant challenge in designing robotic rehabilitation devices that can effectively interface with it.

Although various kinematic models of the human body exist, many fail to capture the intricacies of human anatomy comprehensively [38]. Models based on dual-joint concepts, such as the inner and outer shoulder joints, have been proposed to simulate the human workspace. However, relying solely on goniometric descriptions often falls short of fully characterizing the glenohumeral shoulder

complex, particularly its functional limitations due to movement restrictions across multiple joints and planes [39].

Combining active and passive degrees of freedom (DoFs) can improve arm movements by adapting to the unique characteristics of human anatomy [40, 37]. As noted by Schiele et al. [41], two major challenges emerge: accurately identifying the location of human joints due to their complex interactions around various axes and geometries, and addressing misalignment caused by slipping between the device and the limb, which is not inherently rigid.

The kinematic design must minimize collision risks and undesired motions, replicate the anatomical workspace, and ensure high manipulability [27, 28]. Proper alignment between anatomical and robotic joints is crucial for effective human-machine interaction and to prevent patient discomfort [42][43].

To tackle these challenges, various models have been proposed [44–46]. These models approximate the upper limb's kinematic structure, including the location and number of degrees of freedom. Such models can guide the design process and help minimize misalignment between human and exoskeleton joints. Emulating human redundancy, where the same pose in Cartesian space can be achieved with different joint configurations, is also complex.

The kinematic design should not restrict natural arm motion. Therefore, a viable approach involves relaxing the alignment requirements in favour of a kinematic structure that works in parallel with the human body, considering the anthropometry of the interacting limb without limiting its intrinsic redundancy.

Thus, it is essential to develop a solution that closely resembles the physiological movements of the shoulder and scapular complexes and can effectively interact with the impaired limb.

### 2.3.2 Kinematic analysis for shoulder synergy monitoring

In upper limb rehabilitation, analyzing shoulder synergies, specifically the joint center and scapular movements, with a focus on elevation and protraction/retraction patterns, can provide clinicians with valuable insights into rehabilitation progress. This analysis also offers assessment data on compensatory synergies that may arise and disrupt the glenohumeral-scapular rhythm following a traumatic event, whether orthopaedic or neurological. Therefore, monitoring scapular synergies within the scapulohumeral rhythm is essential for evaluating the rehabilitation of both neurological [47] and orthopaedic patients [48]. By assessing the synergy between scapular movements, such as protraction and elevation, in conjunction with shoulder movements, like horizontal abduction or flexion in the sagittal plane, clinicians can gain valuable indices for patient evaluation.

The field of human kinematics monitoring and motion tracking is rapidly growing, with applications in both biomedical and non-biomedical domains. Human motion tracking is widely

utilized across various fields, including medicine, sports, and animation. Traditionally, movement analysis is conducted in specialized environments using motion capture systems [49], which rely on reflective markers or advanced software like OpenSim for the reconstruction and analysis of kinematics and dynamics. Other systems use inertial tracking technologies, such as iFeelSuit and Xsens, or wearable RFID tags [50], offering more cost-effective solutions for human pose reconstruction. In rehabilitative robotics, particularly in exoskeleton-mediated therapy, access to sensor-equipped rooms with motion capture systems is not always practical. Likewise, sensor suits can cause discomfort and interfere with the human-machine interfaces of the exoskeleton. Therefore, it becomes crucial to explore how data directly extracted from the exoskeleton itself can be leveraged to map human kinematics effectively [51]. A kinematic evaluation based on the mutual synergy between the human body and the rehabilitative device can provide valuable insights into scapular-glenohumeral rhythms. By leveraging the exoskeleton's joint sensor data and understanding the kinematic alignment between the robot and the body, it becomes possible to record both the subject's active and passive range of motion, as well as the coverable workspace. This analysis can be applied to assess the subject's mobility during simple tasks, such as flexion and abduction, as well as functional therapy activities related to Activities of Daily Living (ADLs). However, the coupling between the human body and the exoskeleton does not always result in a direct correspondence between robotic and anatomical joint movements.

### 2.3.3 Commercial exoskeleton

Several robotic devices have been introduced in the literature over the past decades for upper-limb rehabilitation, including Alex [52], ArmeoPower [53], Anyexo[43], Harmony [54] and Aramis [55]:

- Alex: This device administers robotic therapy through video games (serious games) and enables mirror replication of movements from the healthy limb to the hemiplegic limb [52].
- ArmeoPower: Designed for rehabilitating patients with severe to moderate upper-limb impairments, this robotic device focuses on improving function in affected limbs [53].
- Anyexo: A versatile 6-DOF upper-limb exoskeleton equipped with low-impedance, torque-controllable series elastic actuators [43].
- Harmony: A 7-DOF exoskeleton for each limb, designed to assist with upper body movements in subjects with severe disabilities. It supports task completion through a supportive control mode and utilizes a poly articulated quadrilateral to recreate scapular rhythm [54].
- Aramis: A 5-DOF robo-mechatronic device designed to recreate arm natural movements allowing compliant interaction using SEAs [55].

These exoskeletons are intended for use in neurological, orthopaedic, and musculoskeletal rehabilitation, employing various actuation and kinematic solutions to mobilize the human arm. Alex, Harmony, and Aramis are bilateral exoskeletons capable of simultaneously mobilizing both upper limbs, while the other devices are unilateral. All these devices require the presence of a clinician for operation and adjustments and are generally used in a seated position. They utilize different kinematic structures to mimic scapular synergies, glenohumeral rhythm, and elbow movements. Additionally, they explore various control strategies ranging from passive control (where the exoskeleton fully mobilizes the human arm) to assistive modes (where the user actively and increasingly participates in the motor exercise execution). As a general definition, and following a user-centred perspective, the term 'passive control' will refer to a mode in which the subject remains passive while the exoskeleton solely performs the motion. Meanwhile, 'active control' will refer to modes requiring the subject's participation to complete the task [56].

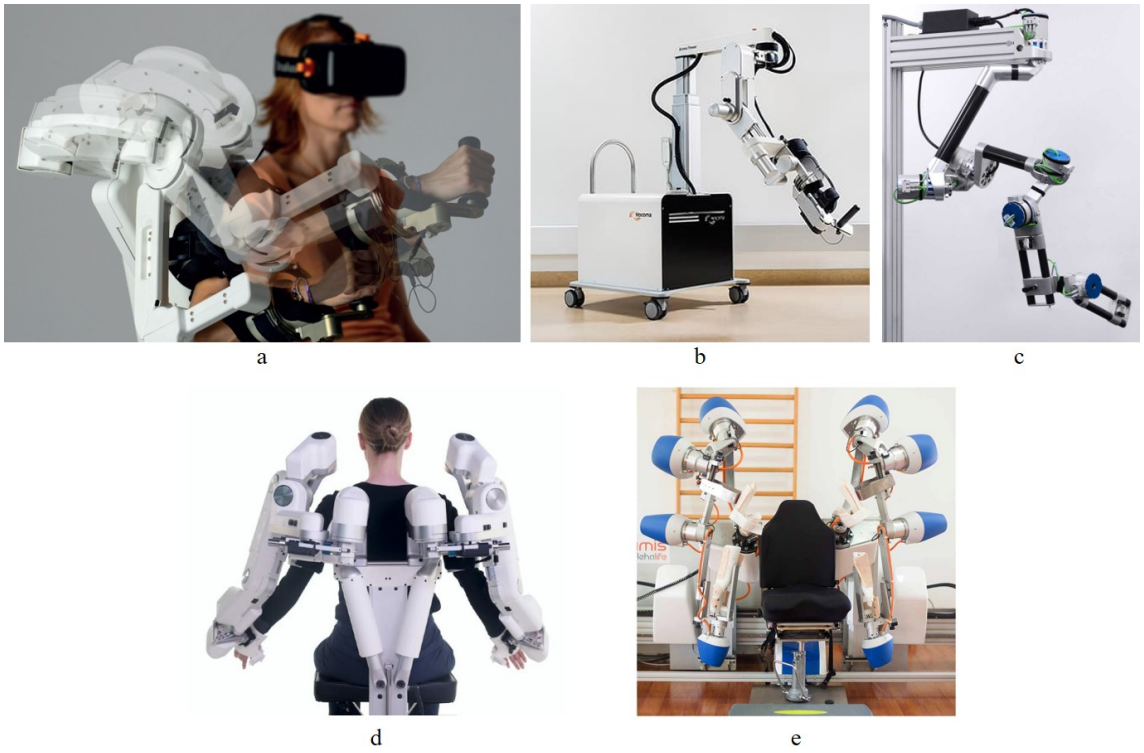



Fig. 2.4 Exoskeleton devices for upper limb rehabilitation: a) Alex, b) ArmeoPower, c) Anyexo, d) Harmony, and e) Aramis.



(a) (b)

Fig. 2.5 Float (a) and FloatEVO (b) exoskeletons for upper limb rehabilitation. The devices are equipped with a movable base on which the multi-jointed arm is mounted, allowing the subject to explore a wide range of motion while performing activities of daily living (ADL) movements. The Graphic User Interfaces (GUIs) used by clinicians to control the devices are also shown.

### 2.3.4 Float and FloatEVO

#### Float

Float [57] is an upper limb exoskeleton developed by the Rehab Technology IIT-INAIL Lab at Fondazione Istituto Italiano di Tecnologia. This device features five degrees of freedom (DoF) actuated by electrical motors utilizing harmonic drive gears. Its kinematics enable fundamental physiological movements to mobilize the shoulder, while the elbow is supported passively by an orthosis.

Primarily designed for orthopaedic patients, Float allows for repetitive exercises with customizable training intensity in terms of repetitions and exercise speed. The exoskeleton is equipped with a multi-articulated arm and a support system that offsets its weight, enabling its use in a standing position and facilitating exploration of the surrounding workspace to enhance functional task performance.

In addition to passive exercise modes, Float can operate in an assistive mode, where users experience minimal resistance from gravity and friction. It assists during the upward phase of flexion movements and supports during the descending phase.

#### FloatEVO

FloatEVO represents a new iteration of the Float exoskeleton, featuring advanced kinematics and a sensorized actuation system. These innovations enable closer mimicking of physiological

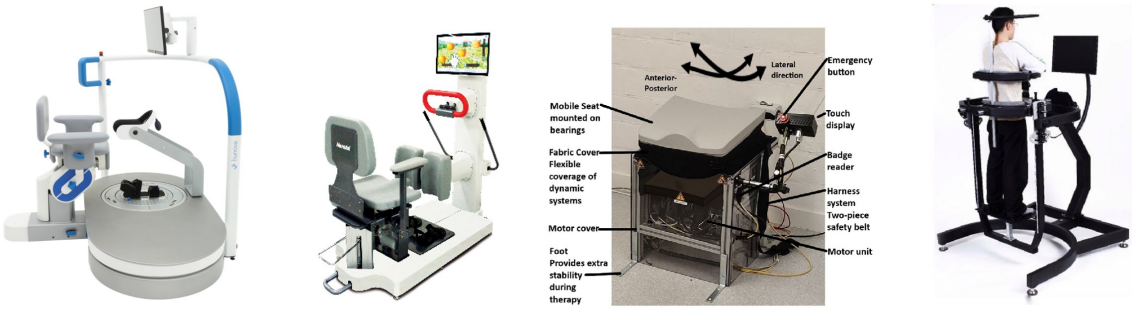
movements while also measuring interaction forces, which are leveraged to implement compliant control strategies.

FloatEVO is a 7-DoF fully actuated system: 3 joints are dedicated to scapular movement, facilitating scapular protraction/retraction and elevation, while a spherical wrist comprising 3 joints mimics the glenohumeral articulation with axes intersecting at the shoulder center. Additionally, the elbow is actuated, enabling full arm mobilization.

The new kinematic of FloatEVO offers a broader range of motion compared to the Float device, covering an expanded workspace that better aligns with the physiological one. Featuring Series Elastic Actuator (SEA) joints, FloatEVO supports various operating modes, including Assist-as-Needed, where patients actively engage in exercises. The torque sensors enable more precise gravity and friction compensation, resulting in a smoother interaction with the user during functional therapy.

## 2.4 Trunk commercial rehabilitation devices

Robotic trunk rehabilitation devices in the literature share a common approach: they leverage the principles of traditional therapy, which aims to enhance core strength, stability, and proprioceptive capabilities. By inducing specific movements through robotic platforms, these devices stimulate muscular activation, prompting patients to respond to the directed motion. Many devices adopted robotic seats to replicate traditional clinical tools like cushioning or physiotherapy balls to mobilize patients [58]. The adoption of robotics in this context not only accelerates adjustment processes but also enables therapists to conduct multiple exercises at high training intensity with a single device, while significantly reducing the physical demands traditionally required to support patient weight.




(a) (b) (c) (d)

Fig. 2.6 Commercial devices for trunk rehabilitation: (a) Hunova, (b) Trunk Control Robot 3DBT-33, (c) T-Chair and (d) SpaceBalance 3D

| Device Name | Target Patients | Range of motion | Max. supported patient's weight | Other available mechanical features | Usability |
|---|---|---|---|---|---|
| **Hunova** | Geriatric<br>Orthopaedic<br>Neurological | Bipodalic platform maximum inclination:<br>±18° in all directions<br><br>Monopodalic platform maximum inclination:<br>Ankle configuration (seating)<br>* Plantar flexion/extension: ±30°<br>* External flexion/extension: ±18°<br><br>Standing configuration:<br>* Plantar flexion/extension: ±18°<br>* External flexion/extension: ±18°<br><br>Robotic seat maximum inclination:<br>* Sagittal plane: ±13°;<br>* Frontal plane: ±13° | 150 kg | * Maximum angular speed: 180 °/s.<br>* Maximum transmissible torque, seat and platform: 200 Nm | Seat<br>Standing |
| **Trunk Control Robot 3DBT-33** | Stroke<br>Hemiplegic | The trunk movement is performed by the patient.<br>Tilting of the seat is provided to help to go from sitting to standing. | 140 kg | - | Sitting |
| **T-CHAIR** | Neurological | Motorised modes available movements:<br>* Flexion/Extension<br>* Lateral motion<br>* Circle<br>* Figure-of-8<br><br>Seat motion variability:<br>* up to ±50 mm for the mediolateral direction<br>* up to ±42 mm for the anteroposterior direction. | - | - | Sitting |
| **Space Balance 3D** | Neurological | Maximum range of motions:<br>* Front-back angle ±50°<br>* Left-right angle ±90°<br><br>Available motors: front-back, left-right and oblique<br>* Front-back motor: 10°, 20°, 30°, 40°, 50° controllable.<br>* Left-right motor: 10°, 20°, 30°, 40°, 50° controllable.<br>* Left-right and oblique motor: 10°, 20°, 30°, 40°, 50°controllable. | - | Angular resolution is measurable by front-back, left-right ±0.5° | Standing |

Table 2.2 Technical features comparison of devices used for trunk rehabilitation.

Table 2.2, with data sourced from [59–62], collects relevant features of some commercially available devices, among the commercial solutions it is possible to list:

- Hunova: a robotic platform designed for lower body rehabilitation, focusing on the trunk, spine, lower limbs, and ankles. This platform allows users to perform core stability and balance exercises in both sitting and standing positions, depending on individual needs. Its admittance control system actively involves users in rehabilitation tasks, making therapy both interactive and effective [63].
- Trunk Control Robot 3DBT-33: a robotic platform designed for stabilization training that integrates gamified scenarios to enhance engagement. Users shift their center of gravity by applying weight to sensors on either the chair or footrest, promoting muscle strength training while participating in interactive games. This approach encourages rehabilitation engagingly and effectively [64].
- T-Chair: a sensorized robotic chair that facilitates the mobilization of the pelvis and spine. It is designed for sitting balance therapy and trunk rehabilitation, aiming to restore upper body

functionality through technology-assisted sitting balance training. The focus is on improving core stability while promoting rehabilitation in a supportive, seated environment [65].

- SpaceBalance 3D: an active, standing-position device equipped with sensors that identify appropriate body positions to restore balance, posture, and overall body stability. Training programs can be customized to facilitate compensatory actions of the sensory-motor system by guiding the body into targeted positions that elicit specific muscle responses. This device is suitable for retraining basic movement control as well as supporting daily activities (ADLs) [66].

## 2.5 Actuation system for exoskeletons

Exoskeletons can employ different types of actuation, with the most common being electrical, pneumatic, and hydraulic [67]. Actuators used in rehabilitation exoskeletons must be lightweight, have a high operating bandwidth and deliver a large amount of torque. Additionally, actuators should ensure backdrivability and allow for rendering a wide range of mechanical impedances. For instance, they should present a minimal impedance to active mobilization by users (when the patient drives the exoskeleton motion). These aspects are fundamental, particularly during the later stages of rehabilitation, when users need the opportunity to get as close as possible to physiological control.

### 2.5.1 Electric, pneumatic and hydraulic actuations

Electrical actuation utilizes the capability of electric motors to produce high torques and achieve very precise movements [27]. Pneumatically actuated robots have a higher power-to-weight ratio compared to those actuated by electric motors, and their efficiency depends on factors such as pressure loss due to friction, air purity, and compressibility [68][69]. However, pneumatic actuation has the limitation of low bandwidth, which means the response rate to command signals is relatively slow.

Hydraulic actuation offers a high power-to-weight ratio but is less efficient when fluid leaks or pressure losses occur [56]. Additionally, hydraulic systems require noise reduction mechanisms to operate effectively. Variable power transmission is necessary for the robot's movement and must endure throughout the machine's operation. Specifically, for rehabilitative applications, it is crucial to provide high torque at low speeds on the load side shaft. Several solutions can achieve this: cable or wire drive systems offer low inertia, fast response times, and a long-range for power and force transmission, but they are prone to stretching and slipping, which can result in inaccurate movements [35]. Gear train transmissions, pulleys, or harmonic drives can also be employed.

Research groups often focus on harmonic drive designs because they prevent backlash, can be compact, are lightweight, and, due to their high gear ratios, can achieve the desired high torques.

### 2.5.2 Series Elastic Actuators

In robotic-assisted rehabilitation, ensuring compliance is crucial. For safe interaction between humans and robots in rehabilitation, robotic devices need to exhibit compliant behavior to assist with dynamic movements [70] and follow patient motions while minimizing interaction forces [71]. In recent decades, many exoskeletons have utilized sensed direct force contact, measured by force/torque sensors, as the primary signal for control implementation [72]. These devices employ sensorized actuation to estimate physical-human-robot interaction (pHRI). Notably, Harmony [54], AnyExo [73, 74], and Aramis [55] have adopted Series Elastic Actuators (SEAs) as an effective mechatronic solution [75]. Electric motors combined with geared systems ensure high torque at low speeds, typically generating less noise than hydraulic systems. Over the past two decades, interest in Series Elastic Actuators (SEAs) has grown [75]. Introduced by Pratt and Williamson in 1995, SEAs integrate three main components in series: a motor, a transmission system (often gear-based), and a spring. The stiffness of the compliant element can be tailored to meet various requirements such as shock resistance, safety, and bandwidth considerations [76]. Pratt and Williamson highlight several advantages of SEAs, noting that including an elastic element within the joint helps mitigate negative effects associated with gears. Gears contribute to system friction, torque fluctuations, noise, and backlash. Introducing elasticity acts as a low-pass filter, reducing peak forces on the gears [77]. SEAs show promise for achieving compliant human-machine interaction because they can measure interaction forces and torques through the deformation of the integrated elastic element. The reliability of SEAs makes them adaptable for different stages of rehabilitation [78]. While the presence of a compliant element reduces operational bandwidth, customizing spring stiffness to work in series with the actuator's stiffness lowers the overall system stiffness. Various robotic rehabilitative exoskeletons in the literature demonstrate SEA implementations: AnyExo uses AnyDrive sensorized joints [74], while Harmony [54] and Aramis [55] incorporate custom SEAs. A sensorized actuation system can facilitate the implementation of assistive controls during dynamic motions, reducing stiffness in human-robot interaction to minimize interaction forces [79]. Series Elastic Actuators (SEAs) enable closed-loop torque control strategies alongside basic position control. Choosing compliant element characteristics is critical. Examples include custom springs with varying stiffness. For instance, AnyDrive SEA joints feature low stiffness designs [74], while the FloatEVO exoskeleton uses custom SEAs with high spring stiffness tailored for upper limb biomechanics and torque sensing performance [80]. Opting for higher stiffness mitigates compliant element deformation under the exoskeleton's weight, improving joint output position accuracy and enabling precise position control. Incorporating SEAs in mechatronic designs aims for closed-loop torque-based control strategies. Torque control models human-machine interaction dynamics,

leveraging compliant control algorithms like impedance and admittance controls [81]. These algorithms include friction and gravity compensation and Assist-As-Needed (AAN) strategies, which adjust assistance levels based on pHRI to support patients in movements against or with gravity. Implemented in joint and task spaces, AAN strategies create a compliant system responsive to the subject's movements.

## 2.6 Control

The study of effective control strategies has garnered significant interest from researchers over the past decades. Implementing control algorithms to regulate and describe human-machine interactions is particularly crucial when working with patients undergoing rehabilitation. Depending on the joint mechanics, different control approaches can be adopted. Basic control methods, such as those utilizing position, velocity, and current loops (PID), can effectively follow desired targets. Specifically, using position control enables passive mobilization of a human limb. In the context of exoskeleton control, "passive control" refers to a mode in which the subject remains passive while the exoskeleton solely performs the motion. Conversely, "active control" requires the subject's participation to complete the task [56]. Active control strategies necessitate a compliant system that accounts for interaction torques exchanged during movement. The counterpart to position control is assistive control, which operates within a closed torque/current control loop. For such control, the joints must be equipped with torque sensors. In exoskeleton design, common solutions include Series Elastic Actuators (SEAs), which incorporate a spring inside the joint to function as a torque-sensing element; strain gauges, which detect linear deformations to reconstruct torsional torques; and surface multiaxial force-torque sensors, placed at interfaces to measure linear forces and torsional torques. Both passive and active control strategies are most effective when applied at specific stages of the rehabilitation process. For example, Proietti et al. demonstrated how different control modes can support the rehabilitation of post-stroke patients. A similar framework can also be applied to orthopaedic patients recovering from traumatic injuries or surgeries. In neurological rehabilitation, it is required modulation of the level of assistance considering the post-stroke recovery phase. During the acute phase, immediately following the neurological event, the impaired limb is typically unresponsive and requires full assistance. In this scenario, passive control (with the control loop closed on the position) is used. In the sub-acute phase, assistive and corrective controllers can be employed to gradually increase the patient's engagement and correct movement paths. Finally, during the chronic phase, when the limb regains responsiveness, resistive control modes can help rebuild strength and improve muscle control.

Several control strategies necessitate the implementation of both direct and inverse kinematics paradigms. In rehabilitative applications, these algorithms become even more critical due to the coupling of the robotic device with the human body, which is a highly redundant and dexterous

system [82]. This coupling introduces additional constraints on the direct and inverse kinematics problems, making these solutions more complex for physiological applications.

### 2.6.1 Inverse kinematics approaches for rehabilitative robotics

The mathematical and geometrical description of the correlation between the robot's joint configuration and the end-effector pose (position and orientation) is provided by the study of direct and inverse kinematics. Direct kinematics describes how the joints' rotations affect the end effector's pose, while inverse kinematics determines the required joint configurations to achieve a desired end effector pose. These mathematical problems are fundamental for describing robot behavior. The inverse kinematics problem in multi-degree-of-freedom robots has been tackled over the last three decades using various approaches, including analytical, geometrical, differential, and numerical methods. Each of these techniques has its advantages and drawbacks. The most common approach relies on differential kinematics, particularly through the inversion of the Jacobian matrix. However, this method also faces limitations when dealing with singularities and robot redundancies [83, 84]. In recent decades, several methods have been proposed to address these issues [85]. For instance, Tokarz *et al.* proposed a geometric approach to solving the inverse kinematics problem [86].

**Differential inverse kinematics** When using rehabilitative devices, commonly adopted control strategies are those that implement task space control (where Cartesian control of the end effector is targeted); these require computing the inverse kinematics solution. In solving this problem, it is often crucial to introduce additional constraints during the calculation of inverse kinematics solutions. Not all joint configurations are suitable, as some may lead the device into non-physiological positions, potentially compromising the patient's rehabilitation. To address this, various mathematical techniques can be considered beyond the traditional geometrical, analytical, and differential approaches.

One commonly used method is the differential approach, which leverages the Jacobian matrix to accurately compute the joint variables necessary to reach a specific position in Cartesian space. However, this method comes with several considerations: the Jacobian matrix is highly sensitive to the choice of the reference frame in which the end-effector's velocity is expressed [83]. Furthermore, this iterative numerical method has certain limitations: it provides only locally linearized solutions to the inverse kinematics problem [84], and calculating the inverse of the Jacobian can be computationally demanding. Another critical challenge is dealing with singularities, which can hinder the calculation process.

To address these challenges, optimized algorithms based on differential methods have been developed [87–90]. These algorithms, for example, allow the limitation of the solution space by imposing joint range constraints. The method discussed here extends the differential technique

by using the null space of the Jacobian to incorporate a secondary task, in this case, restricting joint configurations within a desired range [87]. The strength of this approach lies in its ability to achieve both objectives (accurate end-effector positioning and joint constraint enforcement) without interference between the two tasks [87].

The Jacobian matrix contains the first-order partial derivatives of the direct kinematic function [83]. The Jacobian is used to describe the relationship between the joint rates and the six-element vector formed by the angular and linear velocities of the end-effector, as expressed in Equation 2.1:

$$\dot{p} = \begin{bmatrix} v_x \; v_y \; v_z \; \omega_x \; \omega_y \; \omega_z \end{bmatrix}^T = J\dot{q} = J \begin{bmatrix} \dot{q_1} \; \dot{q_2} \; ... \; \dot{q_n} \end{bmatrix}^T \tag{2.1}$$

The Jacobian matrix can iteratively calculate the necessary joint angles to follow a specified task-space trajectory by discretizing and inverting it Equation 2.1:

$$\Delta q = J^{-1} \Delta p \tag{2.2}$$

As the complexity of a manipulator's joint structure increases, traditional methods like geometric, iterative, and algebraic techniques become insufficient to solve the inverse kinematics problem. Furthermore, as the robot becomes more sophisticated, calculating the inverse kinematics becomes increasingly challenging and computationally intensive. Unlike the direct kinematics problem, which has a unique solution, the inverse kinematics problem can yield no solution, a single solution, or multiple solutions, depending on the robot's redundancy, defined as the difference between the dimensions of the joint space and task space. Specifically, for redundant robots, the Jacobian matrix becomes rectangular, resulting in a non-unique inverse. In such cases, the set of joint-space solutions that correspond to a desired task-space pose is infinite, and the size of this solution space is tied to the degree of redundancy.

The most widely used method to solve the inversion of a rectangular matrix, and consequently to address the inverse kinematics of redundant robots, is the Moore-Penrose inverse, also known as the pseudoinverse. Equation 2.3 presents the differential inverse kinematics for redundant robots:

$$\Delta q = (JJ^T)^{-1} J^T \Delta p = J^\sharp \Delta p \tag{2.3}$$

Mathematically, the Moore-Penrose inverse provides the minimum norm solution to a system of linear equations with multiple solutions. Although it requires matrix inversion, this method is the most widely used and straightforward approach for solving inverse kinematics problems. However, it has limitations: specifically, it does not allow control over individual joint configurations, which can result in undesirable or unreachable joint positions.

**Gradient Projection Method** To ensure that the joint-space solution $(q_1, ..., q_n)$ of the inverse kinematics remains within specified joint limits, a possible approach is the gradient-projection method [90], [91], [92], which builds on the differential kinematics approach, introducing an additional term to the traditional approach. Equation 2.4 illustrates this method:

$$\Delta q = J^{\sharp}\Delta p - \alpha(I - J^{\sharp}J)\nabla H \tag{2.4}$$

The additional term centers around $\nabla H$, a gradient vector specifically designed to achieve a secondary task without interfering with the primary objective. This formulation, introduced by Wan et al. [87], is expressed as follows:

$$H(q) = \sum_{i=1}^{n} \frac{(q_{max_i} - q_{min_i})^2}{4(q_{max_i} - q_i)(q_i - q_{min_i})} \tag{2.5}$$

$$\nabla H(q) = \left[\frac{\partial H}{\partial q_1}, \frac{\partial H}{\partial q_2}, \ldots, \frac{\partial H}{\partial q_n}\right]^T \tag{2.6}$$

Where $q_{max_i}$ and $q_{min_i}$ represent the upper and lower limits of the range of motion (ROM) for each robot joint.

The introduction of this factor, which operates within the null space of the problem's solutions, helps avoid joint limits by redistributing the movement weights. This adjustment ensures that if a joint approaches its limit, the system will compensate by adjusting the movements of other joints.

**Neural networks for inverse kinematics** For non-redundant manipulators, constraining joint limits is often sufficient to achieve an acceptable end-effector orientation. However, redundant manipulators may require additional constraints on orientation. This is especially critical in exoskeleton applications, where the orientation of the end-effector is crucial. A given Cartesian position can typically be reached with various end-effector orientations, not all of which may be physiologically appropriate. To address these orientation constraints, neural network-based methods offer a promising approach to solving inverse kinematics.

Machine learning techniques, particularly those utilizing artificial neural networks (ANNs), offer significant advantages by bypassing the complexity and non-linearity of traditional inverse kinematics equations. Additionally, these methods are not hindered by singularities, which no longer pose a computational issue (though they remain a physical challenge) [84]. The effectiveness of ANN methods depends on training parameters that optimize the network structure. These methods address inverse kinematics problems by generating local regression models [84].

Artificial neural network (ANN)-based solutions can compute inverse kinematics by mapping the end-effector position to the joint domain. Among these methods, the focus here is on the adaptive neuro-fuzzy inference system (ANFIS). ANFIS networks offer several advantages over traditional approaches that rely on the Jacobian matrix inversion. Notably, ANFIS and neural networks, in general, are not impeded by the high non-linearity and complexity inherent in inverse kinematics equations.

ANFIS combines ANN and fuzzy inference system (FIS) techniques to leverage the strengths of both. It can be described as a multi-layer feed-forward network where each node performs a specific function on the input [93]. During the training phase (typically conducted offline), the training dataset and parameters related to membership functions (initial FIS) and weights (epoch numbers) are adjusted to meet minimum error criteria [94]. Direct kinematics is used to create the training dataset, which includes points scattered across the manipulator's workspace, considering joint constraints such as range of motion (ROMs) [95].

ANFIS can be applied to both redundant and non-redundant systems, depending on the training dataset provided. For each joint, a separate network is trained using a dataset that includes controlled Cartesian coordinates and their corresponding joint variables.

The aforementioned algorithms are particularly useful for implementing assistive and resistive controllers, whether based on joint or end-effector trajectory planning.

The current state of the art in exoskeleton-mediated rehabilitation involves three main control strategies: assistance, correction, and resistance. These strategies are analyzed below.

### 2.6.2 Assistive modes

Assistive controllers aim to gradually involve the patient in performing movements by progressively decreasing the level of assistance provided. This approach facilitates an active contribution from the patient as their recovery progresses.

**Passive Control Modes** Passive control strategies are particularly effective in stimulating neuroplasticity in the brain [96], especially during the early stages of recovery when the patient is not yet able to actively participate in task execution. Using a PID trajectory tracking control in a position-closed loop, it is possible to achieve complete mobilization of the human limb without considering human-machine interaction. The primary goal in this case is to precisely follow a predefined target trajectory, and the exoskeleton completes the task regardless of any effort made by the patient. This modality can also be employed in the so-called teach-and-replay method, where the exoskeleton records the movements while the patient's limb is mobilized by a therapist. These recorded movements, including position and timing, are then replicated by the exoskeleton joints.

Additionally, triggered passive controllers are commonly used in exoskeletons control. In this approach, motion is initiated after a specific trigger event [97], guiding the user's movement along the desired trajectory. Another passive control technique, widely applied in bilateral exoskeletons, is passive mirroring. In this mode, the healthy limb controls the movement of the impaired limb by imposing the same trajectory in a master-slave configuration. This method is particularly effective for restoring the ability to perform bimanual functional tasks, making it a valuable tool for rehabilitation.

**Partially Assistive Control Modes** Once the patient regains some autonomy in performing movements, assistive strategies can be introduced to encourage voluntary motion by providing appropriate support [68]. Assist-as-needed (AAN) control strategies can be tailored to the specific needs of patients and clinicians, aiding the patient in task completion. This group of controllers includes both time-dependent and time-independent approaches, as well as path/trajectory-dependent and trajectory-independent strategies, which encompass both corrective and assistive modes.

At the core of most AAN strategies lies transparent control, which involves compensating for gravity and friction to ensure seamless interaction between the user and the exoskeleton. Gravity compensation can be computed using the exoskeleton's dynamic model, such as a geometric model characterized by its mass and inertial properties. Additionally, clinicians may opt to include compensation for the weight of the patient's arm. This approach not only nullifies the perceptible weight of the exoskeleton for the user but also reduces or fully compensates for the load of the patient's limb, as required.

Building on transparent control, assistive strategies can be layered to guide and support the user in task completion. Exoskeletons often employ flexible control techniques like admittance and impedance control, which replicate human-like mechanical behavior by simulating virtual stiffness and damping characteristics. These methods use reduced corrective gains, contrasting with the high corrective gains (PID) used in passive control (position control). Specifically: admittance control is a position controller with force or torque feedback. Impedance control is a torque controller with position feedback. Both methods create a compliant and adaptive machine response to user interactions and are particularly effective when applied to back-drivable systems. These controllers are typically used for time-dependent trajectories.

The proposed controllers can operate at two levels:

- Joint level: Compliance is managed at the individual joint level by controlling joint trajectories and torques.
- End-effector level: Compliance is applied to the Cartesian path planning of the exoskeleton's end-effector.

A model-based assistive strategy example at the end-effector level is the attractive force-field or velocity-field approach. In this method, reference targets are defined in Cartesian space and virtual forces are computed accordingly. These forces are then mapped back to the individual joints using inverse dynamics. This allows the design of time-independent control strategies, where reliance on predefined trajectories is eliminated [98].

Time-independent vector Fields (TIVeF) can also be applied to control exoskeletons at the joint level, as demonstrated in [99, 100], although they are more commonly employed at the end-effector level to compute desired AAN target torques. Many TIVeF strategies are based on the virtual tunnel concept, which defines an area or volume around the target path where assistive control is applied [101–103].

In upper limb rehabilitation, restoring functional motion is paramount, which is why Cartesian space control is generally prioritized over joint-level control [104, 103]. Examples of virtual tunneling applied to upper-limb exoskeletons are provided in [101–103]. These studies demonstrate how tunneling effectively distinguishes robotic assistance in tangential and orthogonal directions relative to the end-effector's reference motion.

### 2.6.3 Corrective modes

In combination with the assistive component, an additional corrective force can be calculated using tunneling and virtual force fields. Specifically, a radial component can be added to the assistance direction to address deviations from the reference path. The primary goal of coordination corrective control is to prevent maladaptive compensatory strategies, which are common among post-stroke survivors and orthopaedic patients. Such controllers are designed to restore proper joint synergy by controlling the relative positions and velocities of the joints to achieve the desired coordination during movement.

Corrective components are valuable in rehabilitation for improving and restoring inter-joint coordination.

**Tunneling** Corrections can be applied both inside and outside the assistive tunnel: when correction is applied within the assistive tunnel, it combines with the assistive component to create a vectorial flux, guiding the user smoothly toward the desired trajectory [105]. If the correction is applied outside the assistive tunnel, it acts as an external force at the end-effector level (reflected at the joint level). This force pushes the end-effector back inside the tunnel when it is detected to have deviated from it.

**Virtual force fields** Another possible solution is the implementation of Cartesian-distributed repulsive force fields. This approach enables the creation of virtual walls and boundaries, which increase resistance as the end-effector approaches restricted zones. These boundaries discourage the user from deviating and guide them to stay within the correct path area.

To implement such controllers effectively, both direct and inverse kinematics and dynamics must be employed. These mathematical models are essential for mapping the position and forces exerted at the end-effector level to the corresponding positional and torque targets at the joint level. This ensures precise coordination and correction throughout the movement.

### 2.6.4 Resistive modes

Resistive control involves implementing a resistive interaction against the user's motion. This approach is designed to make tasks more challenging for the user, testing their ability to adapt to external perturbations and complete tasks under such conditions [81]. These controllers present significant challenges for the robot's mechanics, as the actuation system must provide high torques safely to ensure secure human-machine interaction. Resistive controllers can be implemented using the same algorithms as impedance or admittance controllers but with the direction of the contribution reversed. This allows for the implementation of viscous behaviors in the system and the characterization of vector fields that oppose voluntary motion, such as mimicking virtual walls.

## 2.7 Rapid Control Prototyping

In an ever-evolving technological landscape, the development of new technologies demands the availability of rapid and efficient testing procedures. These procedures play a crucial role in expediting the validation process, ensuring the timely introduction of developed technologies to the market. This is essential to prevent the risk of technological obsolescence, which may occur if the testing procedures linger unnecessarily. In the context of rehabilitative robotics, over the past decade, several exoskeletons for upper limb rehabilitation were proposed (Float [57], Alex [52], Armeo [53], CleverArm [106] AnyExo [73], Harmony [54], Aramis [55]).

Several of the aforementioned devices followed a Rapid Control Prototyping (RCP) approach in their early stages of development. Literature offers a variety of platforms for the control design: ARMin [107] runs on MATLAB/Simulink XPC target (now known as Simulink Real-Time), ANYexo runs on a control PC running a Linux operating system and interfaces with the hardware by EtherCAT communication; Harmony is operated by a real-time control system running Linux patched with RT-Preempt and communicates via EtherCAT. Furthermore, these exoskeletons share a similar system architecture, with a central control unit overseeing the coordinated actions of

various motor control boards distributed throughout the robotic structure. In terms of control strategies, a remarkable consistency can be observed. These systems offer a range of control modes, from precise position control for passive mobilizations to more sophisticated and adaptable approaches like impedance and admittance control, commonly used in rehabilitative robotics to guarantee a compliant human-machine interaction [81]. In the development process of rehabilitative devices, RCP and Hardware In the Loop (HIL) emerge as pivotal approaches, allowing the quick implementation and testing of complex control strategies.

RCP approach enables early testing on hardware, even in a prototype stage, allowing for a swift assessment of how the control algorithms perform in a real-world setting. Additionally, RCP facilitates code reusability across different testing platforms, leveraging flexibility in hardware integration. The real-time application allows quick modifications to the control architecture.

By combining HIL and RCP, the developed software can be deployed and tested in a realistic environment. This approach allows for an early validation of both hardware and software characteristics, encompassing the testing of potential faults. The synergy between HIL and RCP supports the parallel development of hardware and software, with continuous updates and testing. This concurrent approach increases the number of design and test iterations, expediting the definition of final device characteristics and, in turn, reducing time consumption and overall costs.

Several platforms are available for RCP and HIL applications. Among the commercial development environments there are: (i) dSPACE RCP by dSPACE [108], which exploits hardware and software tools to expedite the prototyping, testing, and iteration of control strategies in diverse domains; (ii) MathWorks, through MATLAB/Simulink Real-Time, enables real-time execution of Simulink models on dedicated hardware like Speedgoat's real-time target machines [109], making it ideal for comprehensive model-based control testing; (iii) National Instruments (NI) VeriStand [110] provides a software solution for configuring real-time testing applications. Additionally; (iv) Opal-RT (RT-LAB) [111], ETAS (LABCAR) [112], and Quanser [113] offer real-time simulation platforms tailored for both HIL and RCP applications, serving as crucial tools for testing embedded control systems.

## 2.8 Rationale behind the research project

The Float exoskeleton presents several strengths, including a simple kinematic design and a lightweight structure. This technology certainly has potential for rehabilitation purposes; however, it also has critical limitations. Among these are a limited workspace that significantly reduces the physiological range of motion (allowing approximately 100 degrees of abduction and 90 degrees of flexion), the lack of active actuation at the elbow, and the absence of suitable sensors to estimate interaction torque. The latter is essential for implementing control strategies that improve human-

robot interaction. A review of the literature also reveals that several devices have been developed for shoulder rehabilitation, but no standardized methodology exists to evaluate these designs. There is a clear gap in establishing a consistent evaluation method that can objectively assess the advantages and disadvantages of each solution in mimicking human kinematics. For these reasons, and to enable the comparison of different design solutions aimed at improving the Float exoskeleton, one of the key objectives of this thesis is to define and test precise metrics that can assess the effectiveness of a robotic device in shoulder rehabilitation by replicating physiological movement patterns. Additionally, the literature shows various examples of Series Elastic Actuators (SEA) used in collaborative robotics, quadruped robots, and rehabilitation. However, these works generally focus on delivering the final design outcome rather than explaining the evaluation methods that led to it. In the case of medical robotics, it is crucial not only to provide guidance on the overall actuator design but also to focus on the sensing component design, specifically the torsional spring. While several designs combining materials and geometries have been proposed, there remains a lack of literature explaining the methodology behind the design of such components and their subsequent characterization and use as torque sensors. Therefore, this thesis will specifically address the analysis of the sensing component, aiming to define a procedure for its testing and characterization when used as part of the actuation system in rehabilitation robots. Various control strategies have been studied and presented in the literature, but their implementation into a final device for use in certified systems is often costly and requires a multidisciplinary team with diverse skills. To support research and improve the testing, tuning, and definition of the best control strategies, this thesis proposes a Rapid Control Prototyping (RCP) model, designed in MATLAB-Simulink. This model is customizable, modular, and easy to modify for interfacing with various robotic devices and testing control strategies. Finally, an important aspect of upper-body rehabilitation is the possibility of rehabilitating trunk motor control. Currently, active devices used in rehabilitation involve indirect trunk mobilization. With the goal of expanding FloatEvo's functionality to include trunk rehabilitation, turning it into a complete upper-body rehabilitation device, this work proposes the design of a trunk mobilizer prototype. This prototype modifies and actuates the structure of the existing passive multi-articulated arm supporting the exoskeleton. The control system will be adapted from the model created for the exoskeleton prototype, leveraging its modularity and adaptability. To summarize, by building on the insights gained from analyzing the state of the art, this thesis addresses several aspects of upper-body robotic-mediated rehabilitation. First, it tackles the need for specific methodologies to evaluate rehabilitation exoskeleton designs and to enhance their functionality with alternative control strategies. Lastly, to address the gap in combined robotic rehabilitation for both the trunk and shoulder, a new concept for trunk robotic-mediated rehabilitation is proposed.

# Chapter 3

# Kinematic Analysis

This chapter presents the robotic analysis conducted to explore and evaluate various kinematic solutions for upper limb rehabilitative exoskeletons. It includes a mechatronic analysis of the kinematic chains of the Float, Spherical Float, and FloatEVO exoskeletons, followed by a methodology proposed in this thesis to evaluate the shoulder complex's capability to mimic physiological motion. The last two sections present additional studies: a preliminary assessment of scapular synergies using only kinematic relationships derived from the exoskeleton joints, and a comparative analysis of inverse kinematics methods for solving the inverse kinematics problem in systems that must account for coupling with the human body.

## 3.1 Kinematic analysis of upper limb exoskeleton design

During the design of upper limb exoskeletons, analyzing the impact of robotic kinematics on physiological movements is essential. Establishing evaluation metrics to assess how well a kinematic solution mimics the natural rhythm of the body can guide the design process, helping optimize the structure to better align with human motion needs. The more accurately the exoskeleton replicates and follows scapular synergy and rhythm patterns, the more effective the rehabilitation outcome will be, enabling injured individuals to properly retrain their musculoskeletal shoulder mechanics. The redesign of the Float exoskeleton focused on three key aspects: enhancing scapular complex mobilization, redesigning the spherical wrist to maximize workspace and minimize collisions with the human body, and introducing an active elbow joint for improved functionality.

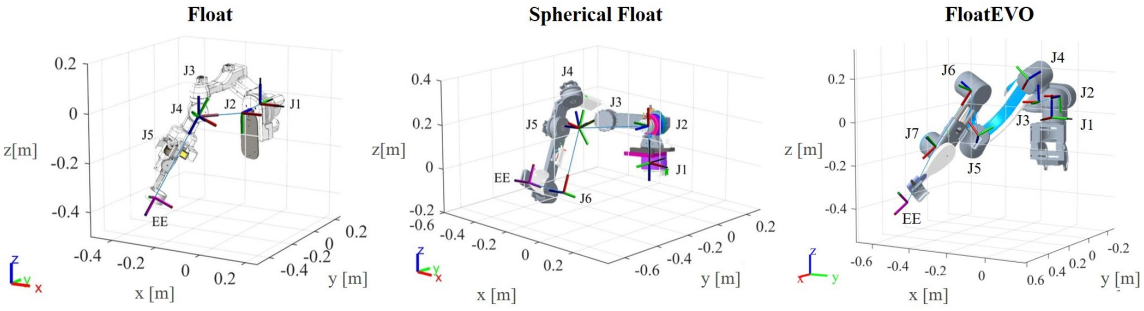



Fig. 3.1 Design of IIT-Rtech Laboratory upper limb exoskeletons. (a) Float: 5-Dof device, (b) Spherical Float: 6-Dof prototype, (c) FloatEVO: optimized 7-Dof design.

### 3.1.1 Float

In the Float exoskeleton design, for the shoulder model, an Eulerian wrist design was adopted. This solution, consisting of three rotational degrees of freedom, enables the rotation around three orthogonal axes that intersect each other in one common point (J3, J4, J5 axes concerning Figure 3.1 (a)). The Eulerian wrist, depicted in Figure 3.1 (a), is described using three angles (Euler angles) specifying consecutive rotations (e.g. z-x-z, x-y-x, y-z-y) about the coordinate axes. Despite achieving successful results [57], this design could not cover the entire physiological range (e.g., limited flexion and rotation movements) limiting the workspace in a 90 *deg* flexion - 90 deg abduction space. The kinematic chain can be described exploiting the modified Denavit Hartenberg (mDH) convention introduced in [114], the related mDH parameters and the ROM for each joint are reported in Table 3.1:

| $J_{id}$ | $a[m]$ | $\alpha[rad]$ | $d[m]$ | $\theta_i[rad]$ | $\theta_{min}[rad]$ | $\theta_{max}[rad]$ |
|---|---|---|---|---|---|---|
| J1 | 0 | 0 | 0 | $\theta_1$ | $-9 \cdot \frac{\pi}{180}$ | $26 \cdot \frac{\pi}{180}$ |
| J2 | 0.010 | $-\frac{\pi}{2}$ | -0.189 | $\theta_2$ | $-8 \cdot \frac{\pi}{180}$ | $37 \cdot \frac{\pi}{180}$ |
| J3 | -0.193 | $\frac{\pi}{2}$ | -0.032 | $\theta_3$ | $-1 \cdot \frac{\pi}{180}$ | $100 \cdot \frac{\pi}{180}$ |
| J4 | 0 | $\frac{\pi}{2}$ | -0.003 | $\theta_4$ | $-95 \cdot \frac{\pi}{180}$ | 0 |
| J5 | 0 | $\frac{\pi}{2}$ | 0 | $\theta_5$ | $-55 \cdot \frac{\pi}{180}$ | $55 \cdot \frac{\pi}{180}$ |

Table 3.1 Modified Denavit-Hartenberg parameters for the Float Exoskeleton

The end-effector location is obtained with a translation along the J5 z-axis according to the adjustable link length $t_{5EE} = [0\,0\,L_{arm}]$.

### 3.1.2 Spherical Float

To broaden the reachable workspace and enhance overall maneuverability, a different kinematic structure was explored: a 3-DoF RPY wrist, shown in Figure 3.1 (b). The design of the new prototype, Spherical Float, can be described, similarly to the Eulerian wrist, using three angles representing the orientation of the joint in a global coordinate system (Roll-Pitch-Yaw angles). The spherical wrist features the axes oriented with 59° and 60°. In this prototype is also added a DoF for the mobilization of the elbow.

| $J_{id}$ | $a[m]$ | $\alpha[rad]$ | $d[m]$ | $\theta_i[rad]$ | $\theta_{min}[rad]$ | $\theta_{max}[rad]$ |
|---|---|---|---|---|---|---|
| J1 | 0 | $\pi$ | 0 | $\theta_1$ | $-43 \cdot \frac{\pi}{180}$ | $43 \cdot \frac{\pi}{180}$ |
| J2 | 0 | $-\frac{\pi}{2}$ | 0.009 | $\theta_2$ | $-43 \cdot \frac{\pi}{180}$ | $18 \cdot \frac{\pi}{180}$ |
| J3 | -0.193 | $\frac{\pi}{2}$ | 0 | $\theta_3$ | $-58 \cdot \frac{\pi}{180}$ | $72 \cdot \frac{\pi}{180}$ |
| J4 | 0 | $59 \cdot \frac{\pi}{2}$ | -0.003 | $\theta_4$ | $-67 \cdot \frac{\pi}{180}$ | $92 \cdot \frac{\pi}{180}$ |
| J5 | 0 | $\frac{\pi}{3}$ | 0 | $\theta_5$ | $-60 \cdot \frac{\pi}{3}$ | $110 \cdot \frac{\pi}{180}$ |
| J6 | 0 | $\frac{\pi}{2}$ | 0 | $\theta_6$ | $-88 \cdot \frac{\pi}{180}$ | $43 \cdot \frac{\pi}{180}$ |

Table 3.2 Parameters of modified Denavit-Hartenberg for the Spherical Float Exoskeleton

The mDH parameters for the Spherical Float prototype are described in Table 3.2. To locate the rotation axes as shown in Figure 3.1, it is needed to pre-multiply the rotation matrices described by the mDH for the following translational vectors: $t_{12} = [0\ 0\ -0.173]$, $t_{23} = [0\ 0.198\ 0.236]$, $t_{56} = [0\ -0.295\ 0]$.

Then the end-effector is placed with the following translation concerning the J6 frame: $t_{6EE} = [0\ -0.150\ 0.083]$.

### 3.1.3 FloatEVO

Based on the positive results obtained from the intermediate Spherical Float prototype (detailed analysis is provided in the following sections), an enhanced RPY configuration was designed, tested, and analyzed. This improved design aimed to achieve two main goals: to extend the range of motion, specifically increasing the capacity for internal-external rotation, and to minimize the device's interference with the user's body.

The new design incorporates three joints to replicate the natural scapular synergy. As depicted in Figure 3.1 (c), joints J1 and J3 work together to enable protraction and retraction movements, while joint J2 facilitates scapular elevation.

Joints J4, J5, and J6 form the new RPY complex, which is configured as a spherical wrist with axes oriented at 75 $deg$ and 62 $deg$. A distinguishing feature of this design is that the triangular configuration formed by these three joints points downward, ensuring that the user's shoulder

remains unobstructed, addressing the limitations of the previous Float and Spherical Float designs, which were more cumbersome. Lastly, joint J7 is dedicated to the rehabilitation of the elbow.

To each joint is assigned a reference frame, with its z-axis aligned with the joint's rotational axis. The robot's kinematic chain is represented as a sequence of homogeneous matrices, which define the rotations and translations required to transition from one reference frame to the next. These transformations are then adopted to compute the end-effector pose with respect to the base reference frame.

Defined the rotation matrix, around a generic $z_i$ axis, as:

$$\text{Rotz}(q_i) = \begin{bmatrix} cos(qi) & -sin(qi) & 0 & 0 \\ sin(qi) & cos(qi) & 0 & 0 \\ 0 & 0 & 1.000 & 0 \\ 0 & 0 & 0 & 1.000 \end{bmatrix}$$

The direct kinematics of FloatEVO can be described by the following homogeneous transformations.

$$T_{12} = \text{Rotz}(q_1) \cdot \begin{bmatrix} 0 & 0 & 1.000 & -0.079 \\ -0.998 & 0.052 & 0 & 0 \\ -0.052 & -0.998 & 0 & 0.092 \\ 0 & 0 & 0 & 1.000 \end{bmatrix}$$

$$T_{23} = \text{Rotz}(q_2) \cdot \begin{bmatrix} 0.996 & -0.087 & 0 & 0.100 \\ 0 & 0 & -1.000 & 0.025 \\ 0.0872 & 0.9962 & 0 & 0.023 \\ 0 & 0 & 0 & 1.000 \end{bmatrix}$$

$$T_{34} = \text{Rotz}(q_3) \cdot \begin{bmatrix} 0.601 & 0.693 & -0.397 & -0.006 \\ -0.523 & -0.034 & -0.851 & 0.127 \\ -0.604 & 0.719 & 0.342 & 0.119 \\ 0 & 0 & 0 & 1.000 \end{bmatrix}$$

$$T_{45} = \text{Rotz}(q_4) \cdot \begin{bmatrix} -0.029 & -0.244 & 0.969 & 0.332 \\ 0.993 & -0.118 & 0 & 0 \\ 0.114 & 0.963 & 0.245 & -0.192 \\ 0 & 0 & 0 & 1.000 \end{bmatrix}$$

$$T_{56} = \text{Rotz}(q_5) \cdot \begin{bmatrix} -0.302 & 0.359 & 0.883 & 0.117 \\ -0.766 & -0.643 & 0 & 0 \\ 0.567 & -0.676 & 0.469 & -0.279 \\ 0 & 0 & 0 & 1.000 \end{bmatrix}$$

$$T_{67} = \text{Rotz}(q_6) \cdot \begin{bmatrix} 0.939 & -0.342 & 0 & 0.312 \\ 0.342 & 0.939 & 0 & 0 \\ 0 & 0 & 1.000 & 0 \\ 0 & 0 & 0 & 1.000 \end{bmatrix}$$

$$T_{7EE} = \text{Rotz}(q_7) \cdot \begin{bmatrix} 1.000 & 0 & 0 & 0.274 \\ 0 & 1.000 & 0 & 0 \\ 0 & 0 & 1.000 & -0.132 \\ 0 & 0 & 0 & 1.000 \end{bmatrix}$$

The complete relation, describing the end-effector coordinates, can thus be obtained as:

$$T_{1EE} = T_{12} \cdot T_{23} \cdot T_{34} \cdot T_{45} \cdot T_{56} \cdot T_{67} \cdot T_{7EE}$$

and the Cartesian coordinates describing the direct kinematic equation computed as:

$$x = T_{1EE}(1,4);\ y = T_{1EE}(2,4);\ z = T_{1EE}(3,4);$$

The ROM for each joint is collected in Table 3.3.

| | J1 | J2 | J3 | J4 | J5 | J6 | J7 |
|---|---|---|---|---|---|---|---|
| $\theta_{min}[rad]$ | $-23 \cdot \frac{\pi}{180}$ | $-95 \cdot \frac{\pi}{180}$ | $-18 \cdot \frac{\pi}{180}$ | $43 \cdot \frac{\pi}{180}$ | $-172 \cdot \frac{\pi}{180}$ | $-50 \cdot \frac{\pi}{180}$ | $-130 \cdot \frac{\pi}{180}$ |
| $\theta_{max}[rad]$ | $23 \cdot \frac{\pi}{180}$ | $-44 \cdot \frac{\pi}{180}$ | $28 \cdot \frac{\pi}{180}$ | $220 \cdot \frac{\pi}{180}$ | $-9 \cdot \frac{\pi}{180}$ | $155 \cdot \frac{\pi}{180}$ | $0 \cdot \frac{\pi}{180}$ |

Table 3.3 FloatEVO joints ranges of motion.

## 3.2 Assessment methodology for evaluating the capability of a mechatronic system to mimic physiological shoulder movements

The physiological shoulder rhythm can be approximated by the combined rotation of at least 3 degrees of freedom (DoF). From a kinematic perspective, these joints can be organized in various configurations around the anatomical joint to ensure that the center of articulation is positioned at the intersection of the three robotic axes of rotation. Given the numerous possible kinematic arrangements, it is proposed to assess the mechatronic solution by evaluating the following robotic performance metrics: the size of the reachable workspace, the range of motion (ROM) for internal-external shoulder rotation, and the system's manipulability.

### 3.2.1 Size of glenohumeral reachable workspace, from Eulerian to RPY Wrist kinematic design

The reachable workspace of a device can be assessed from two key perspectives: its extension and its location. The size of the workspace can be evaluated by comparing the volume of the reachable spherical region with that of the physiological one, considering factors such as the abduction/flexion relation and overall performance. Another important consideration is the occurrence of singularities, specifically where gimbal locks may arise. Ideally, these singularities should be positioned as far as possible from the regions relevant to Activities of Daily Living (ADLs).

The location of the rotational joints within a spherical wrist configuration significantly influences where singularities occur in the workspace. By redesigning the Spherical Float and FloatEVO prototypes with an RPY (Roll-Pitch-Yaw) wrist configuration, the gimbal lock could have been successfully relocated away from the typical working areas used by humans, enhancing the usability and functionality of these devices (Table 3.4).

To analyze the reachable workspace surface for different spherical joint designs, the flexion ($\theta$) and abduction ($\Phi$) angles can be computed in various configurations. The workspace surface can then be evaluated using a surface integral, where $\theta_{\min}$, $\theta_{\max} \in [0, 2\pi]$ and $\Phi_{\min}$, $\Phi_{\max} \in [0, \pi]$. Specifically, by approximating the shoulder joint as a spherical joint, the workspace surface can be computed through a spherical surface integral as a first approximation.

$$A = \int_{\theta_{\min}}^{\theta_{\max}} \int_{\Phi_{\min}}^{\Phi_{\max}} R^2 \sin(\Phi) d\Phi d\theta \tag{3.1}$$

with

$$\theta_{min} \leq \theta \leq \theta_{max} \tag{3.2}$$

$$\Phi_{min} \leq \Phi \leq \Phi_{max} \tag{3.3}$$

The integration limits can be determined by exploiting an abduction-flexion graph (see Figure 3.2). The identified region can be approximated by subdividing it into rectangles. Then a spherical surface integral over these sub-regions can provide an approximation of the working space. Considering $n$ sub-regions, the area can be computed as:

$$A_{\text{tot}} = \sum_{i=1}^{n} \int_{\theta_{\min_i}}^{\theta_{\max_i}} \int_{\Phi_{\min_i}}^{\Phi_{\max_i}} R^2 \sin(\Phi)\, d\Phi\, d\theta \tag{3.4}$$

The resulting areas computed using the proposed double integral are: $A_{Float} = 0.219\ m^2$, $A_{SphFloat} = 0.687\ m^2$, and $A_{FloatEVO} = 0.896\ m^2$, demonstrating how the new design increases the robotic workspace. It is worth noting that the flexion and abduction angles shown are relative only to the spherical complex. These angles, especially the abduction angle, can be further increased through the elevation contribution provided by the rotation of Joint 2 (J2). This additional motion enables coverage of a 0 deg–180 deg abduction range at 0 deg flexion.

| **Float** | **Spherical Float** | **FloatEVO** |
|---|---|---|
| • Resting Position (J3 above J5): human arm resting on the side of the trunk<br>• Extended Flexion Movement (over 90 deg): human arm pointing orthogonally from the frontal plane | • Maximum extra-rotation: human arm trying to reach behind the neck<br>• Maximum intra-rotation: human arm trying to reach the counter-lateral shoulder | • Maximum intra-rotation: human arm trying to reach the counter-lateral pants frontal pocket<br>• Human arm trying to reach behind the lower part of back with the palm |

Table 3.4 Gimbal locks configurations for the analyzed devices.

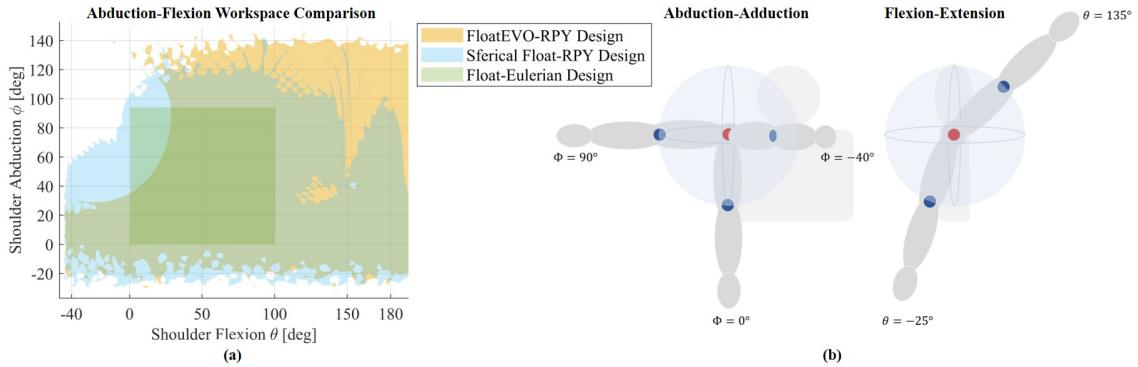



Fig. 3.2 The figure (a) depicts the relationship between the achieved angles of abduction and flexion in the Eulerian and RPY design (both for Spherical Float and FloatEVO). The plots illustrate which angle of abduction is attainable at a certain angle of flexion. Figure (b) shows some reference configurations identified by flexion-abduction angles: at 0 deg flexion - 0 deg abduction, the arm is considered relaxed along the body. Negative values of $\theta$ represent shoulder extension (meaning exploring the space behind the back), and negative abduction represents the arm closing towards the counter-side shoulder.

### 3.2.2 Manipulability evaluation

Manipulability serves as a metric indicator to enhance the kinematic performance of a device by optimizing its design. It is defined as the ability of a robotic device to alter the pose (position and orientation) of its end-effector for a given joint configuration.

Manipulability can be expressed in terms of the rotational Jacobian matrix and is calculated as the product of the singular values of the diagonal elements of the Sigma matrix $\Sigma$, derived from the singular value decomposition (SVD) of the Jacobian matrix ($U\Sigma V$).

$$\mu = \Pi_{i-1}^{m}(\sigma_i), i = 1...n_{Joints} \tag{3.5}$$

Manipulability ranges from zero to one, with higher values indicating greater ease in altering the end-effector pose within a given configuration. The analyzed workspace can be interpreted using an RPY (Roll-Pitch-Yaw) representation, which facilitates mapping relevant physiological movements into the robotic domain. In this context, roll corresponds to the internal-external rotation of the glenohumeral joint around the humerus axis, pitch refers to the elevation rotation of the glenohumeral joint, and yaw represents horizontal rotation in the azimuthal plane. To account for movements typical of basic Activities of Daily Living (ADLs), the yaw angle is constrained between -25 deg and 90 deg, while the roll angle falls between -90 deg and 45 deg.

The study of manipulability indicates that a more complex shoulder design can lead to reduced device usability in certain regions (Figure 3.3). For instance, when comparing the Float design (Eulerian wrist), where manipulability ranges from 0.53 to 1, to the Spherical Float design (RPY

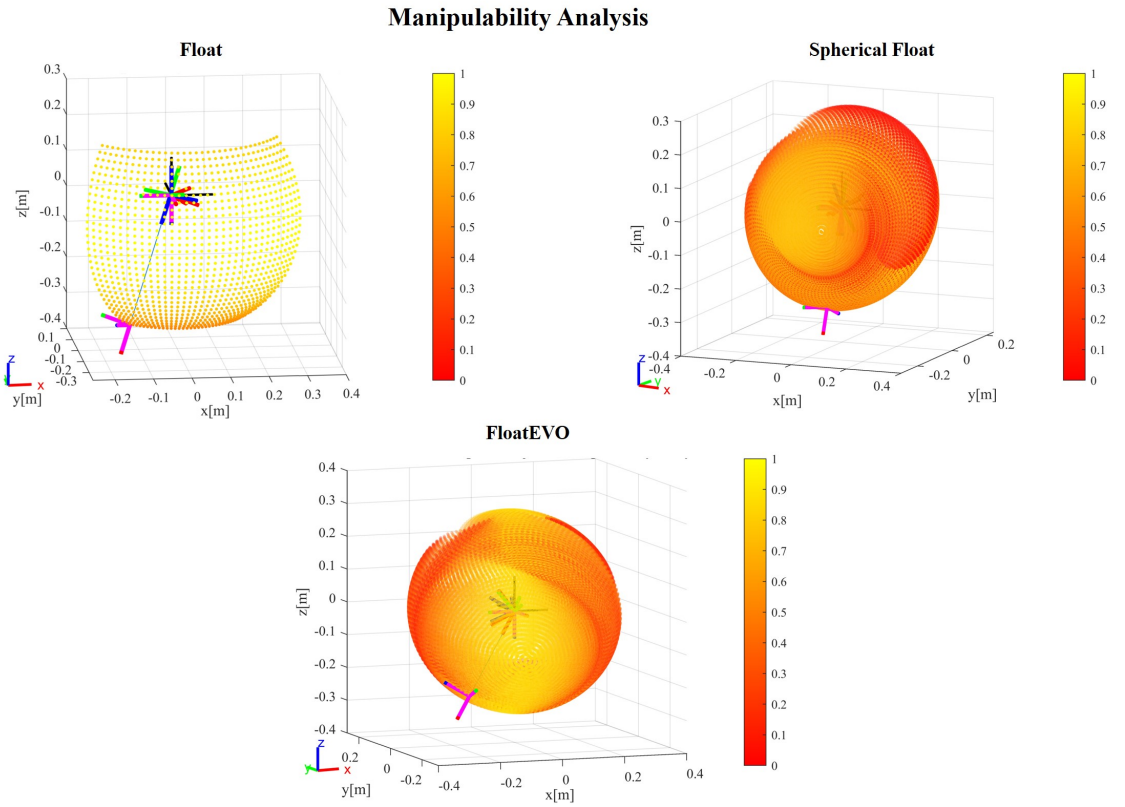



Fig. 3.3 Manipulability study and representation. Comparison between the three different kinematics: all the combinations of joint values inside the joint's working range (resulting in RPY-considered combinations) were used to compute the manipulability associated with that pose.

wrist), where manipulability varies between 0.014 and 0.74, a notable difference is observed. The FloatEVO design demonstrates an improvement, with manipulability ranging from 0.12 to 0.85. This highlights how the FloatEVO design achieves a favorable balance between usability and workspace expansion compared to the other designs.

### 3.2.3 Internal-external rotation performances

An RPY interpretation can once again be applied to analyze how the two different designs affect internal-external movements. The three successive rotations can describe the motion of a desired end-effector, such as the elbow: (I) Roll represents the internal-external rotation around the humerus axis, (II) Pitch corresponds to the elevation movement along the meridians of a spherical surface, and (III) Yaw describes the azimuthal movement along the parallels of the sphere.

By examining the roll angle, it becomes possible to assess the spherical wrist's ability to mimic the internal-external rotation of the shoulder complex.

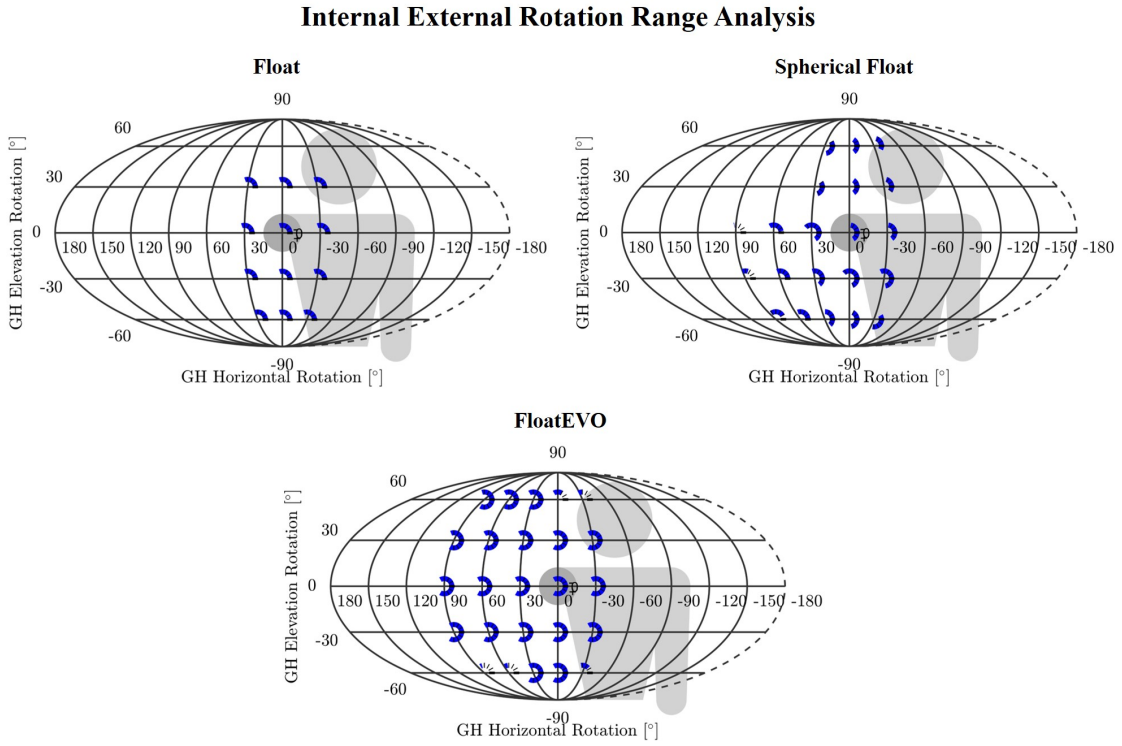



Fig. 3.4 Comparison between the internal-external rotation achievable with the 3-DOF Eulerian (Float) and RPY wrist solutions (Spherical Float and FloatEVO) within the analyzed range. The intra-extra rotation is quantified by the blue semi-circles, representing the range between maximum and minimum roll angles computed in that configuration, identified by yaw (GH Horizontal Rotation) and pitch (GH Elevation Rotation) coordinates on the planetary. This visualization method is recommended by A. H. Stienen and A. Q. Keemink.

The assessment of internal-external rotation, as shown in Figure 3.4, utilizes the representation introduced by A. H. Stienen and A. Q. Keemink [115]. This evaluation of the humerus rotation range is based on the Roll-Pitch-Yaw (RPY) framework. The range of internal and external rotation is illustrated by blue semi-circles, representing the span between the maximum and minimum roll angles. These angles are calculated within a specific configuration, determined by the yaw (glenohumeral horizontal rotation) and pitch (glenohumeral elevation rotation) coordinates on the spherical surface.

The internal-external rotation was analyzed, considering the neutral position (zero rotation) with the arm extended forward and the palm facing downward. The analysis highlights that this movement, facilitated by the RPY wrist design, can be performed across a significantly wider area of the workspace compared to the Float design. Specifically, the updated Spherical Float kinematics enable internal-external rotation within regions defined by yaw angles between $-30\ deg$ and $30\ deg$ and pitch angles between $30\ deg$ and $60\ deg$ as well as yaw angles between $60\ deg$ and $90\ deg$ and

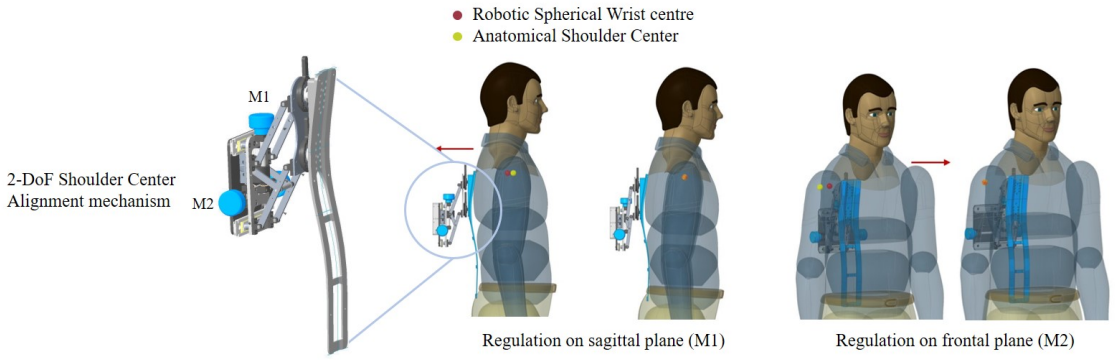



Fig. 3.5 2DoF mechanism for the alignment of the physiological shoulder joint center (yellow), with the robotic spherical wrist center (red), namely the intersection point between the three rotational axes of the joint dedicated to the shoulder complex of FloatEVO. The red arrow indicates the direction of the alignment movement on the sagittal and frontal planes.

pitch angles between $-60$ *deg* and 0 *deg* areas that were previously inaccessible with the Eulerian wrist design. FloatEvo further improved upon this, offering an extended range of rotation and enabling internal-external rotation within the critical region defined by yaw angles between 30 *deg* and 90 *deg* and pitch angles between 0 *deg* and 60 *deg*. This working area is essential for the recovery of functional movements, such as throwing objects, opening a cabinet door, or horizontally moving items on a high surface.

## 3.3 Preliminary analysis of scapular synergies

To study shoulder center movements, specifically focusing on scapular elevation and protraction/retraction angles, it is proposed to take advantage of the FloatEVO exoskeleton's centering mechanism for human-robot shoulder alignment. The FloatEVO exoskeleton features a 2-DoF system that allows for aligning the anatomical shoulder center with the robotic shoulder center (Figure 3.5). This alignment is achieved by acquiring anthropometric measurements from the subject, such as the sternum-to-acromion distance and the acromion-to-backrest plane distance. These measurements are used to ensure accurate alignment and to guarantee a smooth and comfortable usage of the device.

Assuming that, after the patient-exoskeleton alignment procedure, the physiological and robotic shoulder joint centers are aligned, it is possible to leverage the RPY wrist configuration of the exoskeleton. In this configuration, the robotic shoulder center is located at the intersection of the three joint axes, allowing for accurate identification of the shoulder center. Specifically, by utilizing the CAD model of the exoskeleton, the roto-translation transformation matrix between FloatEVO joint J6 and the spherical wrist center can be determined.

This matrix helps map joint positions to corresponding anatomical landmarks. By utilizing the direct kinematic relationships and multiplying the consecutive transformation matrices from joint 1 to joint 6, the computed position of the shoulder center becomes dependent on the rotations of all the precedent exoskeleton joints. This relationship can be further exploited during the device's operation in transparent mode, a control modality where both friction and gravity compensation are applied, allowing the user to move freely within the exoskeleton. This mode enables continuous monitoring of the user's movements, making it possible to evaluate the glenohumeral-scapular synergy both during basic tasks (e.g., shoulder flexion and abduction) and during activities of daily living (ADLs), such as reaching, grasping, or self-care tasks like brushing the hair or bringing a cup to the mouth.

The kinematic chain described above can be adjusted by positioning the end-effector of the rigid body tree at the shoulder center. Thus, the transformation from joint 6 (J6) to the shoulder center can be expressed through the equation 3.6.

$$T_{\text{J6_SH_CENTRE}} = T_{q6} \cdot \begin{bmatrix} 0.5802 & -0.7884 & -0.2039 & 0.0000 \\ 0.1918 & 0.3756 & -0.9066 & 0.0000 \\ 0.7914 & 0.4870 & 0.3692 & -0.1325 \\ 0 & 0 & 0 & 1 \end{bmatrix} \tag{3.6}$$

where $T_{q6}$ is the z-axes rotation matrix defined as

$$T_{q6} = \begin{bmatrix} \cos(\theta_6) & -\sin(\theta_6) & 0 & 0 \\ \sin(\theta_6) & \cos(\theta_6) & 0 & 0 \\ 0 & 0 & 1 & 0 \\ 0 & 0 & 0 & 1 \end{bmatrix} \tag{3.7}$$

The resulting body tree is depicted in Figure 3.6. Two movements were analyzed for this study: shoulder flexion and shoulder horizontal abduction. The rigid body tree in the starting position for the two analyzed movements is shown in Figure 3.6. The orange line indicates the trajectory of the shoulder center, which was computed using direct kinematics. The yellow area highlights the range of scapular activation during these movements, providing a visual representation of the scapular motion envelope during shoulder flexion and horizontal abduction. This helps to demonstrate how the shoulder center shifts in coordination with scapular dynamics throughout these key movements.

$$\text{SH_CENTRE_minActivation} : A(x_1, y_1) \text{ or } A(y_1, z_1) \tag{3.8}$$

$$\text{SH_CENTRE_maxActivation} : B(x_2, y_2) \text{ or } B(y_2, z_2) \tag{3.9}$$

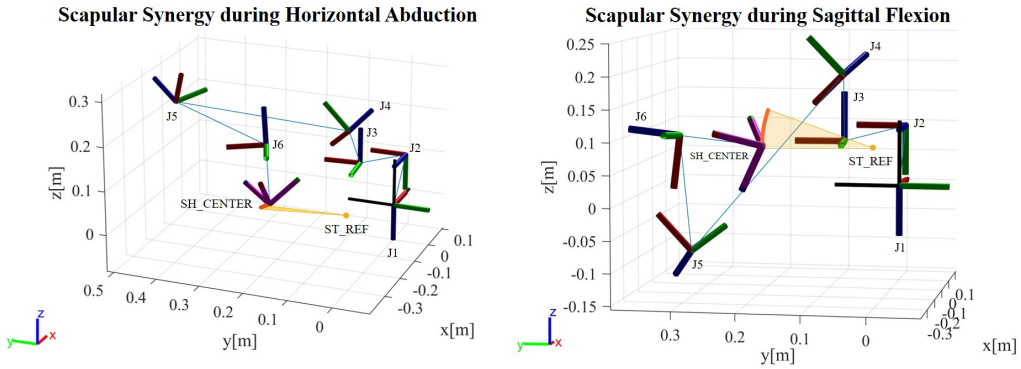



Fig. 3.6 Rigid body tree at the starting position for shoulder flexion and horizontal abduction. The orange line shows the computed shoulder center trajectory via direct kinematics, while the yellow area represents the scapular activation range during these movements.

$$\text{ST_REF} : C(x_3, y_3) \text{ or } C(y_3, z_3) \tag{3.10}$$

Calculate the vectors **AB and BC**:

$$\mathbf{AB} = B - A \tag{3.11}$$

$$\mathbf{BC} = C - B \tag{3.12}$$

Calculate the dot product between vectors **AB and BC**:

$$\text{dot_product} = \mathbf{AB} \cdot \mathbf{BC} \tag{3.13}$$

Calculate the norms (lengths) of vectors **AB and BC**:

$$\text{norm_AB} = \|\mathbf{AB}\| \tag{3.14}$$

$$\text{norm_BC} = \|\mathbf{BC}\| \tag{3.15}$$

Calculate the cosine of the angle between the two vectors:

$$\cos(\theta) = \frac{\text{dot_product}}{\text{norm_AB} \times \text{norm_BC}} \tag{3.16}$$

Calculate the angle in radians:

$$\text{scapularActivationAngle} = \arccos(\cos(\theta)) \tag{3.17}$$

The described method enabled the computation of scapular synergies for two analyzed movements: a 0 $deg$ to 130 $deg$ horizontal abduction and a 0 $deg$ to 180 $deg$ sagittal flexion. Initial validation was performed using an inclinometer and a measuring tape to assess scapular activation directly on the subject: to evaluate the elevation angle, an inclinometer was placed on the subject's clavicle, yielding a measured angle of $\phi_{el} = 19.4\ deg$. For horizontal abduction, the distance between the exoskeleton's back support and a reference point placed on the shoulder's acromion at the maximum angle was measured. The geometrically computed protraction angle was approximately $\phi_{pr} = 8.5\ deg$. However, these measurements were subject to uncertainty due to the difficulty of accurately positioning the instruments during movement. Motion capture analysis will be exploited in a future work to further investigate and validate this approach.

## 3.4 Comparative analysis of inverse kinematics methods for upper limb exoskeleton

Three methods for solving inverse kinematics are compared for the Spherical Float RPY prototype: traditional differential inverse kinematics, the gradient projection method, and the ANFIS-based solution. Tests were conducted using a Cartesian trajectory defined within the exoskeleton's workspace, ensuring it remains within the joints' range of motion (ROM). The algorithms were evaluated under the same conditions: a redundant system where fewer variables than the available degrees of freedom are controlled. Specifically, the exoskeleton's five active joints were used to control the three Cartesian positions $(x, y, z)$. The inverse kinematics (IK) algorithms computed the necessary joint motions based on the reference trajectories (Figure 3.7a). These motions were then used to regenerate the actual Cartesian trajectories. The effectiveness of the algorithms was assessed both qualitatively by visually comparing the reference and effective paths, and quantitatively by calculating the root-mean-square error (RMSE) between the reference and effective Cartesian trajectories. All tests were performed using numerical simulations in MATLAB. Regarding the ANFIS training, various networks were tested using MATLAB with a Sugeno fuzzy inference system. The initial FIS structure (`infis` option) was set to 3, while the number of epochs was varied across 10, 15, and 25 for different networks. The training dataset comprised all possible joint angle combinations within the range of motion (ROM) limits, with resolution steps of 5, 10, and 15, thereby influencing the size of the training dataset accordingly. Additionally, a comparison of the initial joint angles (used to generate the reference trajectory) with the effective joint angles (obtained from the IK solutions) was conducted. This comparison aimed to determine if any of the IK techniques resulted in joint angles exceeding the specified ROM (Figure 3.7b).

Based on the experiment results, the Jacobian-based differential method proved to be the most accurate when prioritizing the Cartesian position of the end-effector, as shown in Table 3.5. This

| | **Differential Inv.** | **Gradient projection** | **ANFIS** |
|---|---|---|---|
| $RMSE_x$ $[m]$ | 0.0036 | 0.0037 | 0.1309 |
| $RMSE_y$ $[m]$ | 0.0044 | 0.0034 | 0.0209 |
| $RMSE_z$ $[m]$ | 0.00055 | 0.0070 | 0.1261 |

Table 3.5 Spherical Float - RMSE on the 3 axes of motion between the reference and effective Cartesian trajectories computed with the three different IK methods: differential inverse kinematics, gradient projection method, and ANFIS networks.

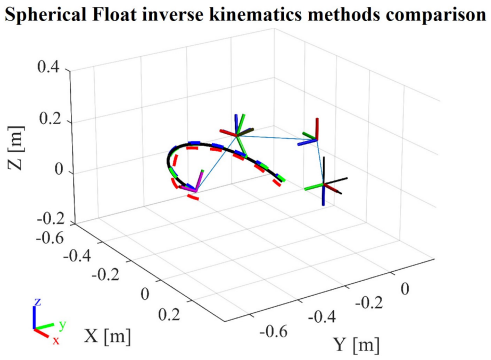
| | **Redundant** | **Non-Redundant** |
|---|---|---|
| $RMSE_x$ $[m]$ | 0.1309 | 0.0036 |
| $RMSE_y$ $[m]$ | 0.0209 | 0.0018 |
| $RMSE_z$ $[m]$ | 0.1261 | 0.0028 |

Table 3.6 Comparison of RMSE between reference and predicted Cartesian trajectories with two different ANFIS networks: one trained considering robot redundancy, one trained in a non-redundant task configuration.

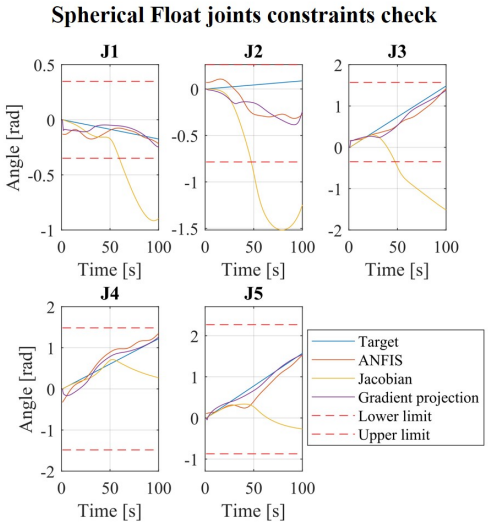
method achieved the lowest RMSE and successfully met the Cartesian position goal. However, the computed joint configurations were not restricted to the desired range of motion. Consequently, this method does not ensure control over joint boundaries, making it challenging to apply in rehabilitative settings. The gradient projection method successfully yielded joint configurations within the specified range of motion while incurring only a minor cost to the accuracy of the Cartesian position. This error arises from the additional term in the algorithm (Equation 2.4), which ensures the solution stays within the desired ROM. The optimization factor requires empirical determination, involving a trial-and-error approach to find an $\alpha$ coefficient that balances both Cartesian position accuracy and joint ROM constraints. Although this introduces a slight inaccuracy compared to the pure recursive method, the trade-off is acceptable given the benefit of managing joint motion weights to avoid approaching limit configurations.

ANFIS was successfully applied to the prototype inverse kinematics study. Despite the time-consuming nature of network training, which increases with system complexity, and with variations in training parameters (such as dataset size, membership functions, and number of epochs), the networks effectively predicted the required joint configurations based on target Cartesian coordinates. Although ANFIS showed slightly higher RMSE compared to other methods, it remains competitive, particularly due to its robustness against singularities. Like the gradient projection method, ANFIS can constrain joint solutions within the desired range, as demonstrated in Figure 3.7b, since training is conducted solely within the desired joint space.

The precision of ANFIS in computing joint variables and resulting trajectories can be enhanced by using a fully constrained (non-redundant) system. Table 3.6 illustrates that training ANFIS




(a) Comparison between the trajectories computed with different IK methods: target trajectory (black continuous line), differential approach (dashed green line), gradient projection methods (dashed blue line), and ANFIS prediction (dashed red line).




(b) Joint angles trends in Spherical Float while performing the task in Figure 3.7a. The blue solid line represents the original joint trend used to generate the reference trajectory, dashed red lines respectively show the upper and lower bounds of each robot joint, the solid orange line is the ANFIS prediction, the solid yellow line is the differential inverse kinematics prediction, solid purple line represents the prediction from the gradient projection method.

Fig. 3.7 Overall comparison of the trajectory and joint angles trends in Spherical Float.

networks on non-redundant tasks significantly reduces the RMSE between the desired and effective trajectories. It is important to note that stability is not guaranteed during the inference process. Therefore, implementing control strategies to prevent potential instability and ensure safe device operation is necessary for practical applications of this method.

In summary, the analysis suggests using gradient-projection methods (or other similar null-space projection techniques) for inverse kinematics problems involving redundant rehabilitative robots. For non-redundant inverse kinematics problems, it is instead recommendable to use neural network-based approaches, such as ANFIS.

# Chapter 4

# Actuation System: SEA for a compliant human-machine interaction

When designing upper limb exoskeletons, a crucial consideration is the selection of an appropriate actuation system. Various options are available, ranging from electrical, pneumatic, and hydraulic actuators to cable-driven systems. A commonly used solution in upper limb exoskeletons is Series Elastic Actuators (SEAs).

In this chapter, the design approach adopted for the exoskeleton SEA is presented, along with an analysis of different torsional springs to identify the most suitable option for meeting the requirements of the new IIT exoskeleton. Various combinations of materials and geometries for the SEA's spring design were studied and compared.

## 4.1 SEA design

Following the classification proposed by Lee and Kwak [116], the SEA design developed at the Rehab Technologies INAIL-IIT Lab of the Istituto Italiano di Tecnologia in Genoa belongs to the Rotary Force-sensing Series Elastic Actuator (FSEA) category. FSEAs are distinguished by the placement of the spring after the gear stage, which allows the output stage to be sensitive to the series elasticity. This configuration enhances force control by leveraging the compliance introduced by the spring. The joint system consists of three main components: (I) a brushless DC motor, (II) a harmonic drive reduction stage, and (III) a torsional spring (Figure 4.1). Two rotary absolute encoders are also positioned on either side of the spring to measure its deformation. While the motor and harmonic drive are commercially available components, the torsional spring is a custom-designed element.

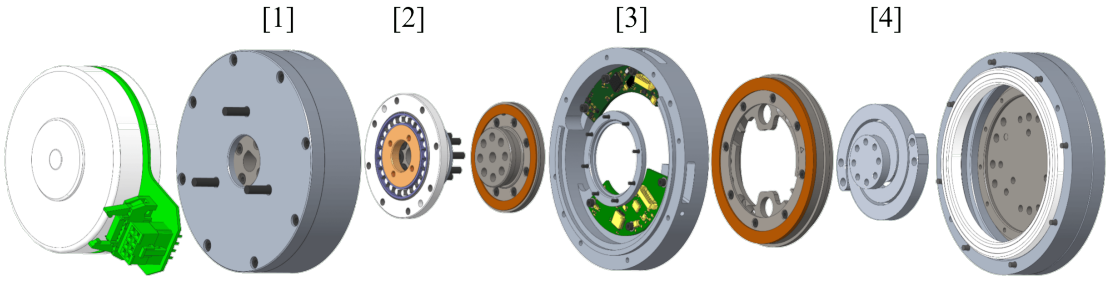



Fig. 4.1 Components view of a custom-made joint. The main components include: (1) the Maxon BLDC motor, (2) the harmonic drive, (3) encoders, and (4) the compliant element (torsional spring with spiral geometry).

### 4.1.1 SEA components

Various revisions of the Series Elastic Actuators (SEAs) have been analyzed and evaluated, with differences in motor selection, spring design, and component assembly. By exploring different solutions, the goal was to create a joint capable of accurately following human motion in terms of both frequency response and torque delivery, considering the structural and patient weights. The component description is provided:

#### Motor and reduction stage

For the initial joint design, Maxon brushless DC motors were selected, specifically the Maxon EC45 (Ø 43.5 mm, 80 W, $\tau_{stall} = 1.69$ Nm), EC60 (Ø 60 mm, 150 W, $\tau_{stall} = 4.3$ Nm), and EC90 (Ø 90 mm, 90 W, $\tau_{stall} = 4.94$ Nm). These motors were paired with reduction ratios of either 1:100 (for EC45 and EC60) or 1:120 (for EC60). The Harmonic Drive offers several advantages, including compact size and low weight, making it ideal for use in compact systems like exoskeleton joints. The number of teeth on the outer toothing of the flex spline is less than the number of teeth on the inner toothing of the circular spline. The reduction ratio is given by:

$$R_r = \frac{n_{fs} - n_{cs}}{n_{fs}} \tag{4.1}$$

where $n_{fs}$ and $n_{cs}$ represent the number of teeth on the flex spline and circular spline, respectively. This ratio allows for a compact implementation that produces high torque at slow speeds on the output shaft, which is ideal for exoskeleton design to support arm weight during rehabilitation tasks while also offering assistance when needed. The output shaft torque and speed, obtained by considering a unitary efficiency can be calculated as follows:

$$\tau_{out} = R_r \cdot \tau_{in} \quad \text{and} \quad \omega_{out} = \frac{\omega_{in}}{R_r} \tag{4.2}$$

where $\tau_{in}$ and $\omega_{in}$ represent the input torque and speed, respectively. It is important to specify that the harmonic drive operates with a non-constant efficiency, depending on the applied torque, temperature and rotational speed. A typical efficiency of 0.7 is assumed. Furthermore, since the efficiency is higher than the critical efficiency of 0.5, the system is considered to be reversible. Additionally, the Harmonic Drive operates without backlash, ensuring precise movement, and maintains high torsional rigidity across the entire torque range.

### Position encoders

The AksIM-2 off-axis rotary absolute encoders were selected due to their compact design, allowing integration into systems with limited space. These encoders consist of two main components: a magnetized ring and a read-head. They support data transmission through various communication protocols, including UART, SPI, PWM, and SSI.

The encoders offer a binary resolution ranging from 17 to 20 bits per revolution, meaning the absolute position can be mapped from 0 to $(2^{n_{bit}} - 1)$. By configuring the encoder's bit resolution, it is possible to achieve the desired precision in torque estimation. For the system described, the 19-bit resolution was chosen, allowing for the following torque resolution:

$$Res_{Nm} = \frac{1\,[ticks] \cdot 2 \cdot \pi\,[rad] \cdot k\,[Nm/rad]}{2^{19} - 1\,[ticks]} \tag{4.3}$$

### Compliant element

The core component of a Series Elastic Actuator (SEA) is the torque sensor, which is essentially a torsional spring sensitive to the load applied to the output shaft. Various geometries and materials can be used for these springs. In the following sections, an analysis of the different IIT-custom spring designs and material options is provided. In designing and evaluating the springs and the overall joint system, biomechanical requirements were a primary consideration. Literature provides extensive biomechanical analyses on the torques necessary for performing common Activities of Daily Living (ADL) movements, such as shoulder flexion, abduction, and internal/external rotation, both at the shoulder and scapulothoracic levels, as well as for elbow flexion. For shoulder and scapular mobilization, peak torques of approximately $\tau = 30$ Nm and $\tau = 20$ Nm are reported respectively [117, 118]. For elbow flexion, lower torques around $\tau = 15$ Nm are typically required [119].

Additionally, the torque characteristics of the actuation systems from two commercial upper limb exoskeletons were considered as a reference for this study. The Harmony exoskeleton [54] can generate up to 35 Nm at shoulder-specific joints and 13 Nm for elbow mobilization. Meanwhile,

the Clever Arm [106] produces torques ranging from 32 Nm to 54 Nm for the shoulder and scapular joints, and up to 21 Nm at the elbow joint.

The design of the actuation system must also consider the torque necessary to support the weight of the entire mechatronic system, accounting for the mass of the exoskeleton itself.

A higher spring deformation under the same torque load generally ensures better measurement quality; however, from a control standpoint, a less stiff structure can be more challenging to manage. Therefore, finding a balance between achieving high structural stiffness and maintaining good measurement sensitivity is crucial.

The key requirements for an effective compliant element, when considering torque and displacement measurements, include: (I) Linear Behavior: Ensures that the relationship between torque and displacement is consistent across the operating range. (II) Low Hysteresis: Hysteresis represents energy loss due to friction and sliding between components. A low hysteresis level indicates higher sensor accuracy, which is essential for precise control. (III) Absence of Dead Band: The compliant element should respond immediately to load changes without any delay or unresponsive range.

## 4.2 Compliant elements analysis

### 4.2.1 Design under evaluation

Frequency and torque analyses were conducted on various spring designs, combining different geometries and materials. Past research on spring geometries has shown that symmetrical structures help minimize deviations caused by radial forces acting in multiple directions. This leads to improved control accuracy by reducing vibrations associated with large radial or axial deformations [120, 121]. As a result, spiral geometries are commonly adopted for their effectiveness [122]. Four spring designs have been studied, which are illustrated in *Figure 4.2*:

- SPT2P: Spiral Titanium spring with two assembly pins.
- SPTF1P: Spiral Titanium flat spring with a single assembly pin.
- SPS1P: Spiral Steel spring with a single assembly pin.
- STS: Star-shaped Steel spring.

These designs incorporate various materials (Table 4.1) and geometries to achieve an optimal balance between stiffness, precision, and controllability.

To ensure appropriate behavior under elastic strain and resistance to high fatigue limits, materials with high resilience are primarily employed, such as titanium and steel alloys. Specifically, the

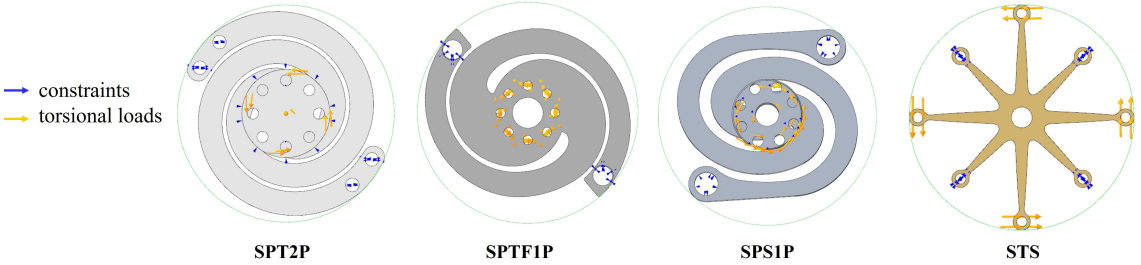



Fig. 4.2 Designed by the IIT-Rehab Technologies Laboratory, these compliant elements feature various geometries to optimize performance. The SPT2P and SPTF1P are titanium spiral springs, while the SPS1P is a steel spiral spring. The STS is a steel star spring, showcasing a diverse range of materials and designs tailored for specific applications.

following materials were used: Ti6Al4V for the SPT2P and SPTF1P designs, 39NiCrMo3 for the SPS1P design, and maraging steel hardened to 50-55 HRC for the STS design. Additionally, various manufacturing methods were explored, including Metal Laser Sintering for the SPT2P and STS springs, Water Jet Cutting for the SPTF1P, and CNC milling for the SPS1P.

To obtain proper behavior under elastic strain and assure resistance to high fatigue limits the most implemented materials are the ones with high resilience, such as titanium and steel alloys. Specifically: Ti6Al4V (SPT2P and SPTF1P), 39NiCrMo3 (SPS1P), and Maraging steel hardened 50 - 55 HRC (STS). Also, different manufacturing methods were explored: Metal Laser Sintering (SPT2P), Water cutting (SPTF1P), CNC milling (SPS1P), and Metal Laser Sintering (STS).

The geometric features of the custom springs are detailed in *Table 4.1*. The diameter ($\Phi$) refers to the circumference within which the spring can be inscribed, while the thickness ($h$) represents the portion primarily engaged in rotation (note that for the SPT2P and SPS1P designs, the support is excluded from the measurement). All proposed spiral designs are based on an Archimedean spiral geometry, which has been modified to achieve the desired stiffness and accommodate various joint assembly requirements.

### 4.2.2 FEM analysis

Finite Element Method Analysis (FEA) was conducted using CREO CAD modeling software to obtain both the static tension and deflection distribution models, which were subsequently used to establish the theoretical stiffness of the components. A torsional load was applied to each design to induce internal rotation (closure of the geometry). The constraints and load application points are illustrated in *Figure 4.2*. The maximum applied torques for the FEM were selected to ensure that tensions remained below the minimum tensile yield strength ($\sigma_s$). Specifically, the applied loads were: $\tau_{SPT2P} = 40\ Nm$, $\tau_{SPTF1P} = 30\ Nm$, $\tau_{SPS1P} = 57\ Nm$ and $\tau_{STS} = 40\ Nm$.

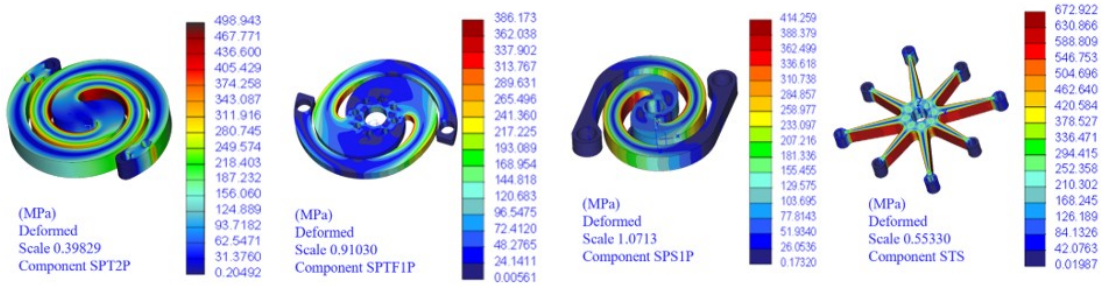



Fig. 4.3 Von Mises stresses under the maximum torsional load applicable by design, results from FEM analysis.

| | *Young's modulus [GPa]* | $\sigma_s$ *[MPa]* | $\Phi$ *[mm]* | *h [mm]* | *m [g]* | $k_{FEM}$ *[Nm/rad]* |
|---|---|---|---|---|---|---|
| SPT2P | 114 | 830 | 64 | 8.2 | 122.3 | 441.9 |
| SPTF1P | 114 | 830 | 80 | 5 | 78.5 | 1054.9 |
| SPS1P | 210 | 880 | 93 | 9 | 261.3 | 1622.3 |
| STS | 180 | 1875 | 65 | 5.8 | 27.2 | 948.2 |

Table 4.1 Materials properties and geometrical design characteristics of the proposed springs, including diameter, thickness, mass, and theoretical stiffness computed through FEM analysis.

A point on the geometry was selected, and its deflection was mapped within a circular domain. It was assumed that these points move along a circumference during deformation, allowing the stiffness to be computed as follows:

$$k_{FEM} = \frac{\tau_{load}}{\Delta\theta} \quad \text{where} \quad \Delta\theta = \frac{2 \cdot \pi \cdot \Delta d}{\pi \cdot \Phi} \tag{4.4}$$

In the formulation of $\Delta\theta$, the denominator represents the circumference of diameter $\Phi$ along which the movement of the point is considered, while $\Delta d$ is the FEM-computed static displacement. This procedure has been adopted for the computation of the stiffness of all the components. With results reported in *Table 4.1*.

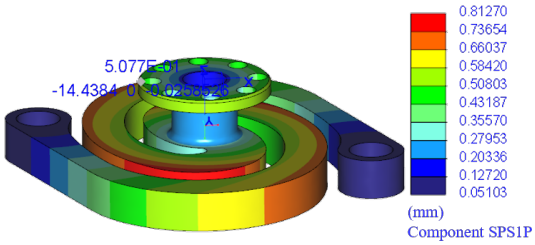



Fig. 4.4 Von Mises tensions under the maximum torsional load applicable by project, results from FEM analysis.

Following, it is reported a computation example: concerning *Figure 4.4*, $\Delta d = 0.507$ *mm*, $\Phi = 14.43 \cdot 2 = 54$ *mm*, and $\tau_{load} = 57$ *Nm* thus, according to (4.4), $\Delta\theta = 0.0284$ *rad* and finally $k_{FEM} = 1622.3$ $Nm/rad$.

The results from the FEM analysis indicate that the compliant elements were effectively designed to withstand loads that accommodate both the necessary biomechanical requirements for physiological movements (with torques of approximately $\tau = 30$ Nm [117] and $\tau = 20$ Nm [118] for shoulder and scapular mobilization) and the weight of the exoskeleton, which was approximately 20 kg for both Spherical Float and FloatEVO prototypes. The springs demonstrated the capability to operate under these and even greater torque loads without exceeding the minimum tensile yield strength.

In the proposed designs, springs with stiffness values between 380 $Nm/rad$ and 1500 $Nm/rad$ were adopted, therefore, with a 19-bit resolution, the theoretical minimum torque that could be detected, varied between *0.0046 Nm* and *0.0180 Nm*, considering the springs experimental stiffnesses and 19-bit resolution encoders the obtainable torque sensors sensibility are collected in Table 4.2.

| $ID_{spring}$ | $\tau_{max}$ $[Nm]$ | $k$ $[Nm/rad]$ | $n^\circ$ bit | *Sensibility* $[Nm]$ |
|---|---|---|---|---|
| SPT2P | 40 | 377.3 | 19 | 0.0045 |
| SPTF1P | 30 | 1059.2 | 19 | 0.0127 |
| SPS1P | 57 | 1451.5 | 19 | 0.0174 |
| STS | 40 | 955.55 | 19 | 0.0115 |

Table 4.2 The table presents data related to different spring geometries, including maximum tolerable torsional load, experimental spring stiffness, Aksim encoder bit resolution, and sensor sensitivity on the torque measurements. The sensor sensitivity depends on the Aksim bit resolution and the spring stiffness.

### 4.2.3 Joint test at the bench: experimental set-up

To test the spring behavior when a load is applied to the joint, an experimental set-up was mounted (see Figure 4.5) to be able to characterize the system in terms of: (I) spring stiffness, (II) hysteresis affecting the measurement and (III) frequency response.

The setup is shown in Figure 4.5 the joint is mounted on a support fixed to the bench, constraining the rotation at the output shaft. A bearing adapter is used to maintain alignment between the output shaft of the joint and the input shaft of the torsiometer (used to measure the torque exerted by the output shaft). The control model was developed using MATLAB-Simulink, and once compiled, it can be uploaded onto the Speedgoat Performance real-time target machine. This machine is also connected to EPOS servo motor controller boards to drive the Maxon motor. From the control PC, a custom graphical user interface allows different control modes to be set and the control signal

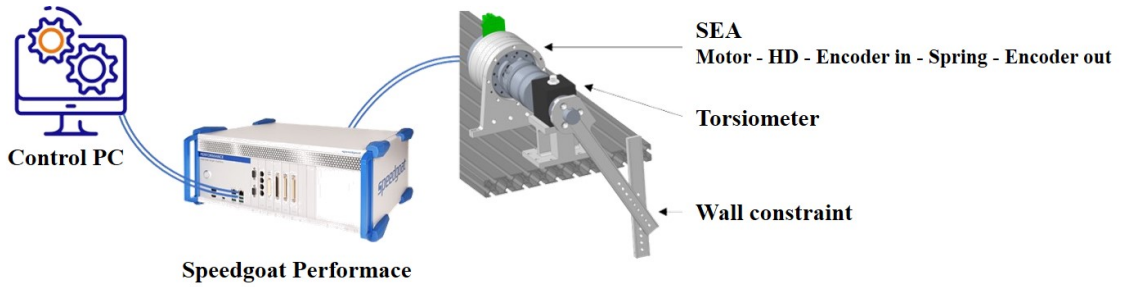
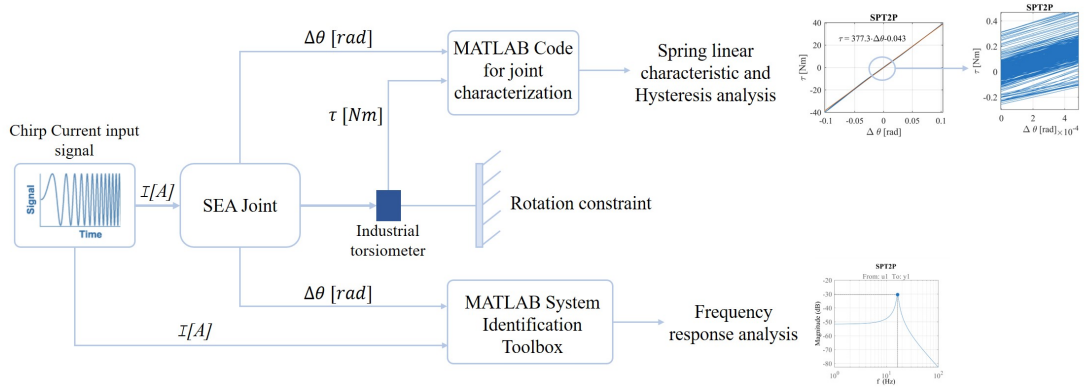



Fig. 4.5 Experimental hardware set-up adopted to test the joint under different load-frequency solicitations.




$I[A]$: *is the current control signal provided for the test. A chirp signal is adopted.*

$\Delta\theta$ $[rad]$: *is the spring deformation computed by the AKSIM encoders*

$\tau$ $[Nm]$: *is the industrial torsiometer torque measurement, torque applied by the fast shaft when the joint rotation is constrained*

Fig. 4.6 Schematic representation of the signal applied to and recorded from the SEA joint during the testing procedure, utilized for stiffness evaluation (linear characteristic analysis), hysteresis analysis, and frequency response assessment.

to be provided. The Speedgoat machine also receives signals from the AksIM encoders and the industrial torsiometer via a serial adapter.

### 4.2.4 Stiffness evaluation

The control signal used for all the analyses was a current chirp signal, which is a sinusoidal signal with constant amplitude and varying frequency (the block schema of the signals exploited for performed analysis is shown in Figure 4.6). To test the entire torque working range, the amplitude was set to $I = 1.5\ A$. The frequency of the chirp signal was selected based on bio-mechanical considerations: since typical human activities involving physiological shoulder movements occur at frequencies up to 12 $Hz$ [123], a frequency range from $f_{min} = 0.1\ Hz$ to $f_{max} = 20\ Hz$ was provided as input. Once the control signal is provided, data are collected from the absolute encoders, which measure the spring deformation, and from the torsiometer. By comparing the encoder readings

(specifically, the difference between the output-side encoder reading, $\theta_{out}$, and the reading from the encoder placed before the spring, $\theta_{in}$, the deformation of the component can be determined. Using these measurements alongside the torsiometer readings, a graph of torque $\tau$ versus deformation $\Delta\theta$ can be obtained (Figure 4.7). By applying linear regression, the relationship governing the SEA torque can be described using Hooke's Law:

$$\tau_{SEA} = ((\theta_{out} - \theta_{in}) - \Delta\theta_{offset}) \cdot k + \Delta\tau_{lm} \tag{4.5}$$

Here, $\Delta\theta_{offset}$ represents the encoder offset, which accounts for the assembly position difference between the two encoders when no load is applied to the joint. This offset is calculated as the average of the encoder sum readings when the torsiometer's sensed torque is close to zero (within the range of $-0.01\ Nm$ and $0.01\ Nm$). $\Delta\tau_{lm}$ is the intercept of the linear model, and $k$ is the stiffness of the spring. The experimentally obtained stiffness is reported in Table 4.3 along with their difference with the FEM expected value.

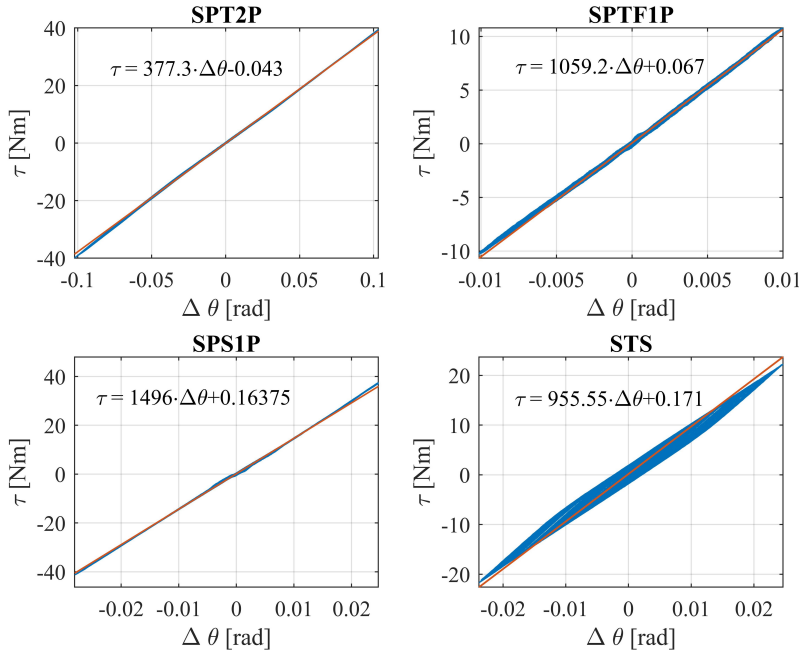



Fig. 4.7 These graphs illustrate the relationship between the torque measured by the torsiometer and the torsional spring deformation angle measured by the encoders. The slope of the linear model corresponds to the spring stiffness. The experimental spring characteristic is shown in blue, while the linear approximation is represented in red.

The observed torque-angle behavior was well represented by a linear regression model, as shown in Table 4.3, with regression coefficients around $R^2 = 0.99$. However, further analysis of the SPTF1P and SPS1P components indicated slight variations in the slope of the curves depending on the direction of deflection. Specifically, SPTF1P exhibited stiffness values of

| Joint ID | $k[Nm/rad]$ | $\Delta\tau_{lm}[Nm]$ | $R^2$ | $\varepsilon_{fem\%}$ |
|---|---|---|---|---|
| $J_{EC_{90}SPT2P}$ | 377.3 | -0.0426 | 1 | -14.6187 |
| $J_{EC_{45}SPTF1P}$ | 1059.2 | 0.0674 | 0.999 | 0.4019 |
| $J_{EC_{60}SPS1P}$ | 1451.5 | 0.1637 | 0.999 | -10.5283 |
| $J_{EC_{90}STS}$ | 955.55 | 0.1705 | 0.989 | 0.7805 |

Table 4.3 Experimental spring characteristic evaluation: considering the linear approximation, stiffness (angular coefficient), intercept, regression coefficient, and the relative error concerning the FEM theoretical stiffness are computed.

1015 $Nm/rad$ for positive deflection and 1075 $Nm/rad$ for negative deflections, while SPS1P showed 1478 $Nm/rad$ and 1496 $Nm/rad$ respectively. This more detailed torque estimation highlighted that the components exhibit directional differences under torsional load. However, these differences can be considered negligible for practical purposes. The RMSE of the computed SEA torques ranged from $RMSE_{SPTF1P} = 0.1027\ Nm$ and $RMSE_{SPS1P} = 0.2603\ Nm$, to $RMSE_{SPTF1P} = 0.08\ Nm$ and $RMSE_{SPS1P} = 0.1846\ Nm$ when using the more precise bi-linear model. Referring to Table 4.3, the difference between stiffness obtained from FEM analysis and experimental results was about 0.4% in the best case and 14% in the worst case. These discrepancies are acceptable, particularly given that the Young's modulus used in simulations may slightly differ from the real material's properties. Additionally, geometric manufacturing errors may lead to differences between the theoretical CAD models and the actual dimensions of the components, further explaining minor deviations between FEM predictions and experimental data. Furthermore, the stiffness of the Harmonic Drive ($8 - 13 \cdot 10^3\ Nm/rad$) slightly affects the overall actuator stiffness, resulting in a reduction of 5% and 15% depending on the compliant element used. This contributes to the underestimation of experimental stiffness compared to theoretical FEM estimates. Lastly, it is essential to note that during testing, the constraints on the springs are not perfectly rigid, unlike in the simulations, which can also lead to slight variations in the results.

### 4.2.5 Frequency analysis

Based on the data collected during the chirp tests performed on various SEA joints equipped with different spring designs, a system identification analysis can be conducted (see Figure 4.6). The assembled joint can be modelled as a second-order system characterized by an inertia term ($I$), damping coefficient ($\beta$), and stiffness ($k$). The parameters identified using MATLAB's System Identification Toolbox are summarized in Table 4.4.

A frequency analysis was then carried out to determine the system's resonance frequency ($f_n$), damping ratio ($\zeta$), and bandwidth ($B_w$). The Bode magnitude plots for the four tested springs are shown in *Figure 4.8*.

| *Joint ID* | $I[kg \cdot m^2]$ | $\beta[Nm \cdot s/rad]$ | $k[Nm/rad]$ | $f_n[Hz]$ | $\zeta$ | $Bw[Hz]$ | $\%_{fit}$ |
|---|---|---|---|---|---|---|---|
| $J_{EC_{90}SPT2P}$ | 0.0355 | 0.3206 | 380.673 | 16.47 | 0.0436 | 25.5 | 96.44 |
| $J_{EC_{45}SPTF1P}$ | 0.0043 | 0.1562 | 1068.2 | 79.56 | 0.0365 | 123 | 94.76 |
| $J_{EC_{60}SPS1P}$ | 0.010 | 0.3445 | 1479.6 | 61.28 | 0.0448 | 94.1 | 93.41 |
| $J_{EC_{90}STS}$ | 0.0116 | 3.6078 | 964.3 | 45.94 | 0.5399 | 56.1 | 90.81 |

Table 4.4 Dynamic and frequency characteristics obtained from system identification of the SEAs springs, it is reported the level of confidence of the fitting.

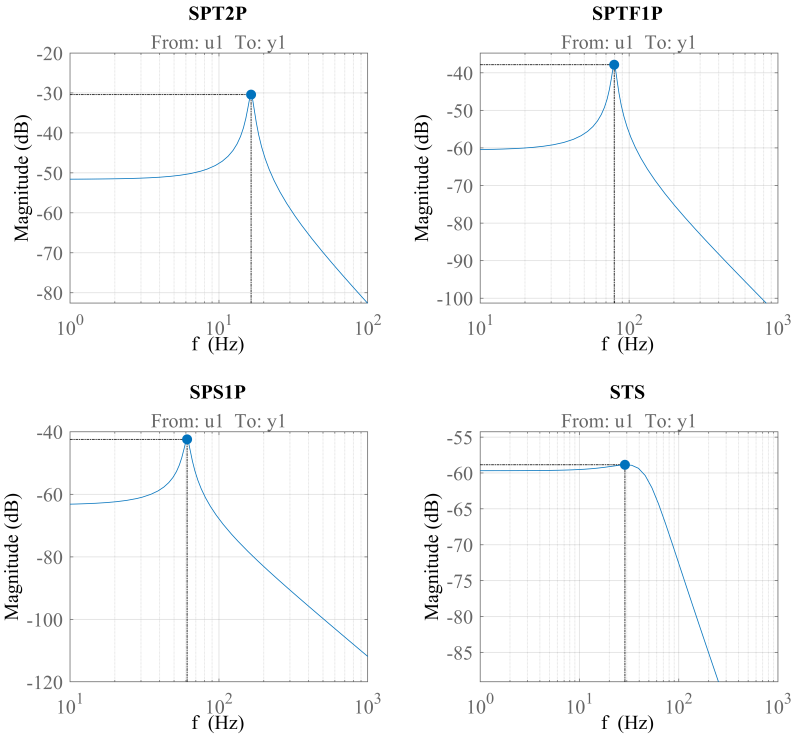



Fig. 4.8 Identified dynamics response of the different SEAs. The four plots report the magnitude Bode plots of the actuating units with the four different springs: SPT2P (top-left), SPTF1P (top-right), SPS1P (bottom-left), and STS (bottom-right). The frequency responses presented are the results of the analysis conducted using the MATLAB System Identification Toolbox, which is used for creating models of linear and nonlinear dynamic systems from input and output data. For this analysis, the input data was the motor's measured current, and the output data was the torque recorded by the SEA sensor when the joint was constrained in rotation.

Among the tested springs, the STS design demonstrated the highest damping coefficient, which was roughly an order of magnitude greater than that of the SPT2P spring, tested with the EC90 motor. The stiffness values obtained through system identification matched well with the results from FEM analysis and static stiffness characterization, assessing that the compliant element's stiffness is the dominant factor affecting system dynamics.

Given that the maximum frequency requirement for human activities during ADLs is around $f = 12$ Hz [123], all the designed SEA joints, including the different tested springs, are capable of functioning effectively within the human motion frequency range. To avoid resonance peaks and potential nonlinear behavior, the considered safe maximum operating frequencies are $f_{max} = 8$ Hz for SPT2P, $f_{max} = 30$ Hz for SPTF1P, $f_{max} = 20$ Hz for SPS1P, and $f_{max} = 10$ Hz for STS.

### 4.2.6 Hysteresis evaluation

Hysteresis serves as an indicator of the uncertainty affecting sensor measurements. The setup for this evaluation is shown in Figure 4.6. To ensure reliable torque sensing, the hysteresis band amplitude around a given measurement must be kept minimal, as high hysteresis can lead to multiple potential torque outputs for a specific displacement input, as illustrated in Figure 4.9.

Experimental analysis revealed that the level of hysteresis in the system is influenced both by the compliant element chosen (its geometry and material) and by the joint assembly procedure, an aspect that will be discussed in a subsequent section of this thesis. Hysteresis was evaluated concerning the no-load condition, specifically in the unloaded operational range where no torque is applied to the slow shaft. It is important to note that, even under these conditions, friction still impacts the system dynamics.

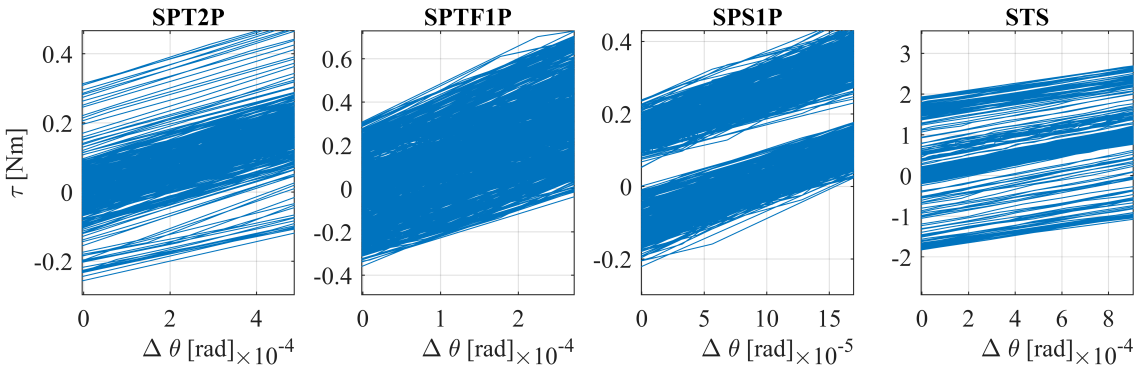



Fig. 4.9 Hysteresis behaviour around the origin of the torque-angle diagram, the picture is a zoom in of Figure 4.7. The x-axis represents the torsional spring deformation angle measured by the encoders, while the y-axis displays the torque measured by the industrial torsiometer at the joint output shaft under constrained rotation conditions.

Hysteresis is quantified as the maximum deviation between the loading and unloading phases of a non-ideal spring. The spiral geometries demonstrated an ability to maintain the uncertainty in SEA torque estimation within $\pm 0.5$ *Nm*. This level of error is acceptable, considering that typical human interactions involve significantly higher torques.

The STS spring, however, exhibited the highest hysteresis and thus proved to be the least favourable design, with an uncertainty of approximately $\pm 2$ *Nm*. This can be directly correlated

| Spring | Pros | Cons |
|---|---|---|
| **SPT2P** | • Capable of reaching higher deformations<br>• Low hysteresis | • Requires two connection pins for attachment to other components<br>• Lowest operational bandwidth<br>• Non-uniform tension distribution<br>• Susceptible to structural deflection due to exoskeleton weight (low stiffness) |
| **SPTF1P** | • Lowest damping coefficient<br>• Requires only one connection pin | • Non-uniform tension distribution |
| **SPS1P** | • Widest operational bandwidth<br>• Lower hysteresis<br>• Not affected by structural deflection<br>• Easy to integrate into the system | • High stiffness may amplify errors (e.g., friction effects)<br>• Non-uniform tension distribution |
| **STS** | • Better axial compactness<br>• Uniform tension distribution | • Highest damping coefficient<br>• Highest hysteresis<br>• Difficult to integrate (requires multiple attachment points) |

Table 4.5 Comparison of spring types, including their advantages and limitations.

with the higher damping coefficient of $\beta = 3.61\ Nm \cdot s/rad$, observed during the frequency characterization (refer to Table 4.4), which is roughly an order of magnitude greater than that of the worst-performing spiral geometry (SPTF1P). The considerably higher damping ratio explains the increased energy dissipation, as evidenced by the larger hysteresis cycle shown in Figure 4.7.

The energy losses observed could be attributed to the multiple pins required to assemble the STS spring within the joint. Each bearing fitted into the connection pins experiences both static and dynamic friction, which undermines the reliability of the system for sensing purposes.

Table 4.5 offers an overview of the pros and cons of the presented spring design. Based on the conducted analysis, the compliant element selected for the final version of the FloatEVO exoskeleton joints is the custom Archimedean spiral spring (SPS1P). This design, combined with a Kollmorgen BMS-1601 brushless DC motor and a Harmonic Drive with a reduction ratio of either 1:120 (FloatEVO J1, J2, J3) or 1:80 (FloatEVO J4, J5, J6) or 1:50 (FloatEVO J7), chosen according to the joint role in the kinematic chain, provides a compact and lightweight actuator that meets physiological requirements while offering precise and consistent torque sensing capabilities.

# Chapter 5

# Upper Limb Exoskeleton Control

This chapter focuses on the exoskeleton control design developed as part of this dissertation. The first section presents the characterization of the SEA torque sensor and the compensation methods for its dynamic linear and nonlinear uncertainties. Next, the preliminary control architecture, developed in the Simulink-MATLAB environment following an RCP approach, is discussed. This architecture was designed to control the Spherical Float device, with various control strategies implemented and proposed, including end-effector Cartesian-based control, joint-level control, and approaches utilizing external sensors. The third section introduces the control architecture of the embedded solution for the FloatEVO exoskeleton, emphasizing the contributions of this thesis, particularly the implementation of passive, transparent, and AAN (Assistance-As-Needed) control strategies.

## 5.1 SEA non-linearity compensation for improved torque sensing

This section proposes a testing procedure to characterize the SEA joints in terms of linear and non-linear behaviour. The adopted testing methodology involves the following steps: (I) Aksim encoder self-calibration procedure; (II) SEA testing at the bench under different loads: no load, minimum, maximum, and medium loads, while collecting encoder readings data; (III) Post-processing to characterize the linear behaviour of the spring using the data acquired under the maximum load condition; (IV) Characterization of the Fourier Series coefficients to describe the non-linear error in torque estimation under both no-load and loaded conditions; (V) Testing of the SEA joint mounted on the exoskeleton prototype, exploiting kinematic mode (position control); (VI) Comparison between the gravity torque (no interaction test) and the pHRI estimation obtained with and without the computed compensations.

### 5.1.1 Methodology

The SEA joint is securely fixed to the bench to perform the test. During the encoder self-calibration procedure, the joint spins freely without any applied load. The self-calibration function is designed to address errors induced by eccentricity, a significant factor affecting encoder accuracy due to the eccentric mounting of the ring.

Once the calibration process is completed, an adapter flange is mounted to the output side of the joint to facilitate the connection of known loads. These loads, which consist of weight plates, are attached using a steel bar.

#### No-load test acquisition

The joint is allowed to spin freely, with a fixed speed selected for all tests, and the motor is controlled using speed control. Data are collected for three successive rotations clockwise and three counter-clockwise. Encoder data are collected and stored for analysis.

#### Load test acquisition

For the two joints, weight plates are selected based on the reduction ratio and the intended purpose within the exoskeleton. In this study, $J_{rr80}$ is employed in the shoulder complex, while $J_{rr50}$ is dedicated to elbow mobilization. To test $J_{rr80}$, 5kg, 10kg, and 15kg weight plates are employed, whereas 2kg, 5kg, and 7kg weights are selected for testing $J_{rr50}$. The weights are connected through a steel bar to the adapter flange. The slow shaft is aligned to the vertical line to identify the zero position of both encoders Aksim1 and Aksim2, which will be used as reference zero position. The joint is then controlled in speed control and performs three clockwise and three counterclockwise rotations, recording the absolute encoder data.

#### Test on the exoskeleton prototype

The joints are assembled in their respective configurations on the exoskeleton prototype, which features 7 degrees of freedom: 3 joints dedicated to rehabilitating the scapular complex, 3 for the glenohumeral complex, and 1 for elbow mobilization (the complete exoskeleton design cannot be disclosed due to patent reasons). During testing, the exoskeleton executes movements of shoulder flexion-extension exploiting a position control. Tests were performed with and without HRI. Data collection includes information on the estimated SEA torque, both with the linear component alone and with the combination of the linear component and nonlinear corrections, as well as the theoretical gravity torque calculated using the robot's dynamic model.

### 5.1.2 Error compensation for improved torque and pHRI estimation

The collected data are post-processed using MATLAB2023b. Initially, the data from the maximum load tests are exploited to identify the spring characteristic model (Equation 4.5) via linear regression. Subsequently, the error in computed torque, under various joint working conditions, is computed as:

$$\varepsilon_{\tau} = \tau_{dyn_m} - \tau_{SEAl_m} \tag{5.1}$$

Here, $\tau_{SEAl_m}$ represents the sensed torque obtained from the linear approximation (Equation 4.5), while $\tau_{dyn_m}$ denotes the dynamic model of the system, geometrically computed as:

$$\tau_{dyn_m} = m \cdot g \cdot L \cdot sin(\theta_{bar}) \tag{5.2}$$

In this equation, $m$ is the mass of the tested weight, $g$ represents the gravitational constant, $L$ indicates the distance between the centre of the rotation and the load centre of mass (CoM), and $\theta_{bar}$ denotes the angle formed by the steel bar referenced to a zero vertical position.

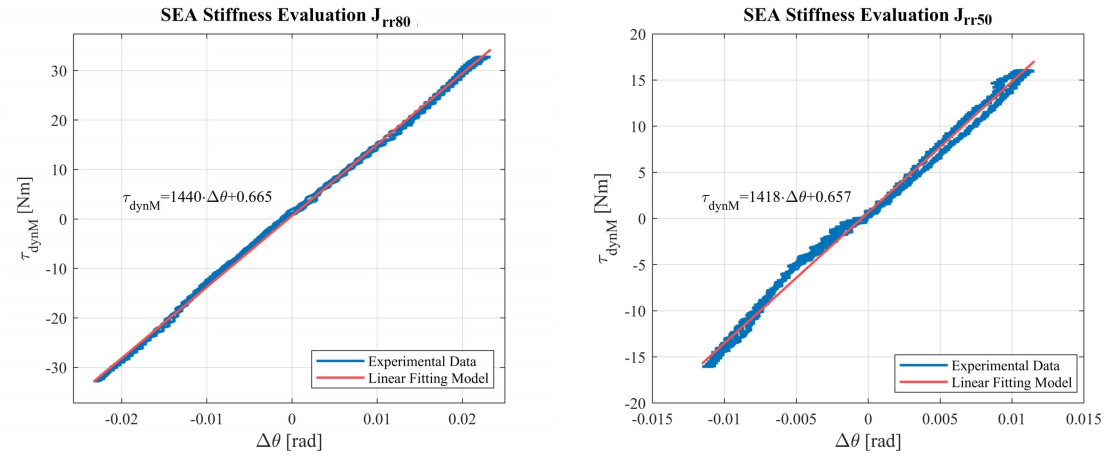
A preliminary test was conducted using an industrial torsiometer to determine the position of the centre of mass of the test load. By knowing the mass, gravitational constant (g), the angle formed by the bar to which the weight was attached, and the torsiometer sensed torque, it became possible to compute the position of the centre of mass relative to the centre of rotation of the output shaft of the SEA joint.

The no-load data are then used to establish the baseline position-dependent error ($\varepsilon_{FNL}$), expressed as a function of the motor-side absolute encoder Aksim2 (excluding consideration of spring deflection). This error is approximated by a first Fourier Series, with the highest coefficient grade chosen to prevent divergence of the series.

Next, the errors under load conditions are computed, and following the application of the initial correction $\varepsilon_{FNL}$, the resultant errors, at various loads, are expressed as a function of the Aksim2 encoder. These data are saved in a unified signal variable, allowing for the computation of a Fourier Series approximation ($\varepsilon_{FL}$) that considers all acquisitions and represents an average approximation of the collected data.

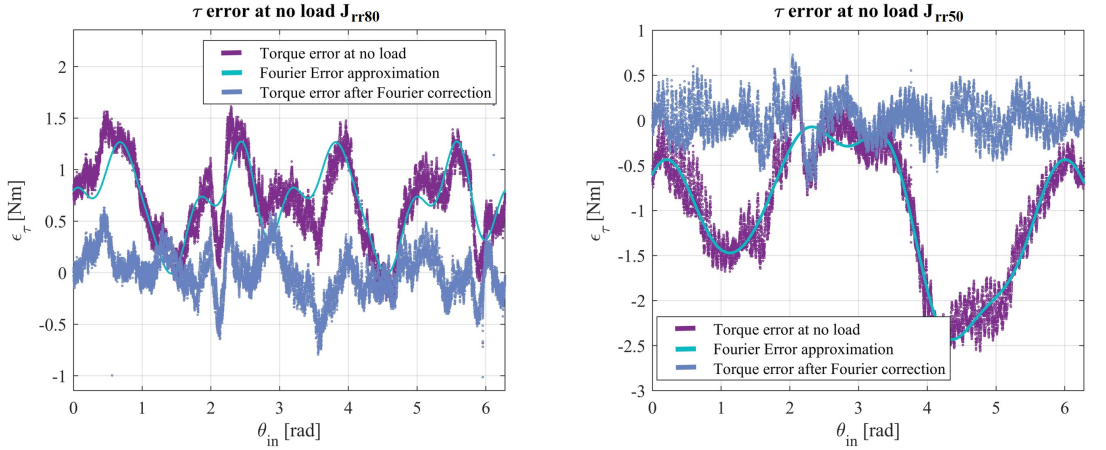
Once the error parameterization is computed, the SEA torque estimation (see Equation 4.5) can be improved by adding two compensation terms dependent on the Aksim2 encoder position ($\theta_{in}$):

$$\tau_{SEA} = (\Delta\theta - \Delta\theta_{offset}) \cdot k + \Delta\tau_{lm} + \varepsilon_{FNL}(\theta_{in}) + \varepsilon_{FL}(\theta_{in}) \tag{5.3}$$




(a) (b)

Fig. 5.1 SEAs springs experimental characterization: by expressing the relation between the dynamic model ($\tau_{dynM}$) computed torque and the spring deformation ($\Delta\theta$) it is possible to determine the linear behaviour of the compliant element, thus its stiffness and torque offset (residual torsional torque on the spring due to assembly procedure). The experimental data (blue line) are then interpolated by exploiting a linear fitting regression model (red line). The results are shown for two different SEAs with reduction ratios of 1:80 and 1:50 in (a) and (b) respectively.

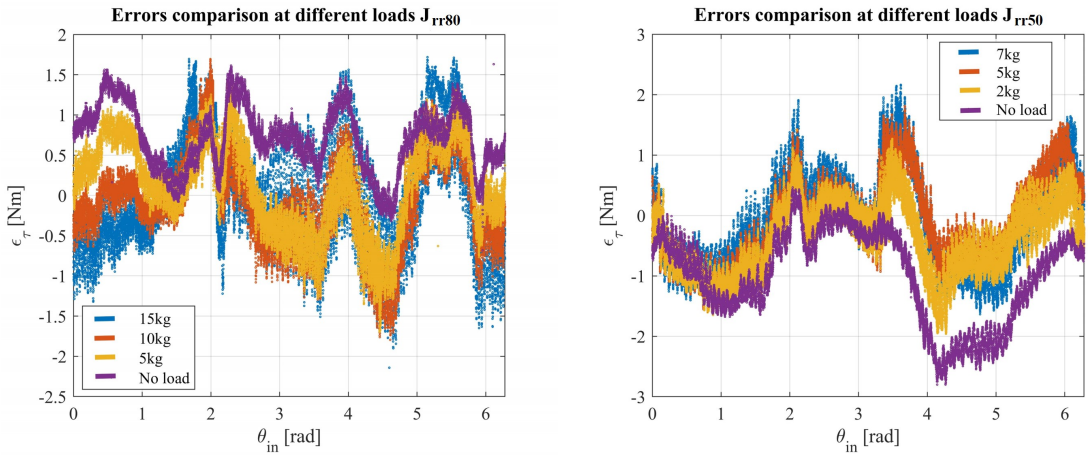



(a) (b)

Fig. 5.2 Analysis of the torque error affecting the SEA measurement at no load condition. The results are shown for the two analyzed SEAs with reduction ratios of 1:80 and 1:50 in (a) and (b) respectively. The torque error, computed as the difference between the dynamic model torque and the SEA one, is expressed in the function of the encoder at the motor side (Aksim2). This error is successfully approximated by a 5th-order Fourier Series. The recomputed errors, after the corrections, are shown. The corrected measure results centred around the origin, reduced in amplitude, and linearised in shape.

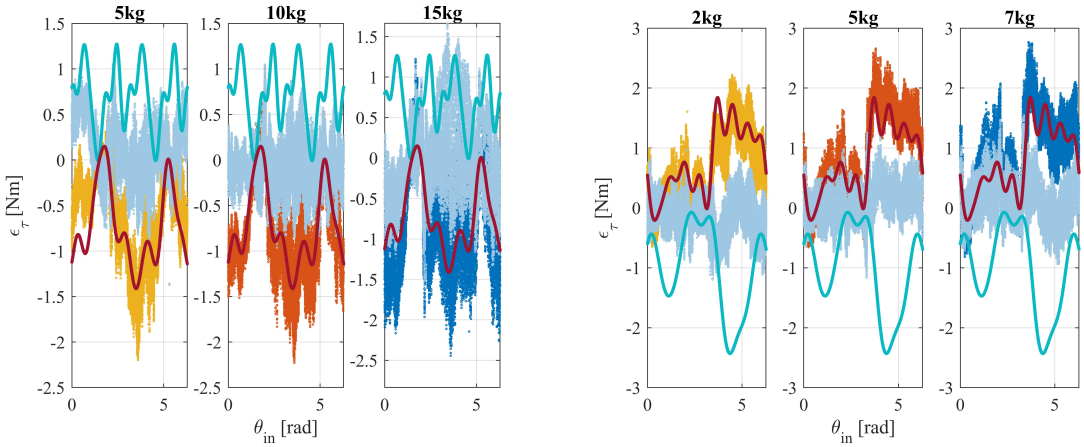
### Linear model for spring characteristic

The spring's linear characteristic is determined by linear regression of the relation between spring displacement (obtained by computing the encoder readings' difference) and the torque computed




(a) (b)

Fig. 5.3 In the figures are reported the torque errors, expressed in function of the motor side Aksim2 encoder, computed for SEAs with reduction ratio 1:80 and 1:50 in (a) and (b) respectively. The errors computed at the different load conditions are shown highlighting the load-dependent non-linear behavior of the SEA systems. This effect resulted in being amplified for a higher reduction ratio.




(a) (b)

Fig. 5.4 The load-condition errors shown in figure 5.3 are corrected with the no-load 5th order Fourier Series (green line), obtaining the signals here reported in yellow, orange, and blue lines. Then the second correction, 8th order Fourier Series (red line), is applied to the signals providing the final corrected SEAs torque measurements for the joints with reduction ratio 1:80 and 1:50 in (a) and (b) respectively.

with the dynamic model (see Equation 5.2) at maximum load conditions (15kg for $J_{rr80}$ and 7kg for $J_{rr50}$). The results for the linear slope (spring stiffness $k$) and the intercept (torque offset $\tau_{lm}$) are shown in Figure 5.1. The observed linear behaviour (Figure 5.1) suggests that hysteresis affects the two systems differently. In the system with a reduction ratio (RR) of 50, the hysteresis, defined as the lag between input and output torques, is higher than in the system with an RR of 80. These

analyses also unveiled uncertainties regarding torque measurements were more pronounced for the $J_{rr50}$ joint (up to $\approx 3\ Nm$ compared to $\approx 1\ Nm$ for $J_{rr80}$). This phenomenon can be explained by the concept of reflected inertia, which refers to the load inertia as seen by the motor. Reflected inertia is inversely proportional to the reduction ratio, meaning it is higher when the RR is lower. Higher reflected inertia can slow down the system's response, leading to increased imprecision in measurements. This is because the motor requires greater torque to move the load side, affecting the system's dynamic performance. Hysteresis can complicate system control, reinforcing the necessity for correction terms in the measurements to account for these discrepancies.

### No-Load error parametrization

The baseline error at the no-load condition, expressed as a function of the encoder position (motor side position $\theta_{in}$),is obtained by utilizing Equation 4.5 and Equation 5.1 for both joints, considering $\tau_{dym_m} = 0\ Nm$. The obtained errors are modeled using a 5th-order Fourier series resulting in a reduction of the peak-to-peak amplitude from 1.5 $Nm$ to $1Nm$ (33.33% error reduction) for $J_{rr80}$ and from 2.5 $Nm$ to 1 $Nm$ (60% error reduction) for $J_{rr50}$. The series also demonstrates beneficial effects in linearizing the waveform, minimizing its non-constant sinusoidal behaviour. The computed torque errors, before and after the corrections, along with the relative Fourier approximation ($\varepsilon_{FNL}$), are shown in Figure 5.2a and Figure 5.2b for $J_{rr80}$ and $J_{rr50}$, respectively. This error predominantly stems from friction within the connecting elements, leading to undesirable deflection of the compliant element. Notably, this phenomenon is then amplified given the chosen stiffness, which stands at approximately 1450 $Nm/rad$.

### Load error parametrization

The error at different load conditions is computed using Equation 4.5 and Equation 5.1 for both joints. The resulting errors, expressed as a function of the encoder position at the motor side ($\theta_{in}$) for each load condition, are shown in Figure 5.3a ($J_{rr80}$) and Figure 5.3b ($J_{rr50}$). These errors are then consolidated into a single variable and expressed as a function of ($\theta_{in}$) to compute the Fourier series (8th-order), resulting in an average approximation for all load conditions. Figure 5.4a and Figure 5.4b show, for the two joints, the errors at different load conditions, where SEA torque is computed with Equation 4.5 and the first baseline correction ($\varepsilon_{FNL}$) is applied, in yellow, orange, and blue. Additionally, the figures depict the Fourier approximation for the no-load condition ($\varepsilon_{FNL}$) in light green, the average correction for load conditions in red ($\varepsilon_{FL}$), and the recomputed error when all corrections are applied (light blue), and the SEA torque is computed with Equation 5.3. Table 5.1 collects the minimum and maximum torque errors over the SEA torque computation in the following cases: (I) no correction is applied, and the error is computed with Equation 4.5; (II) the first correction ($\varepsilon_{FNL}$) is applied to the torque estimation; (III) both corrections are applied,

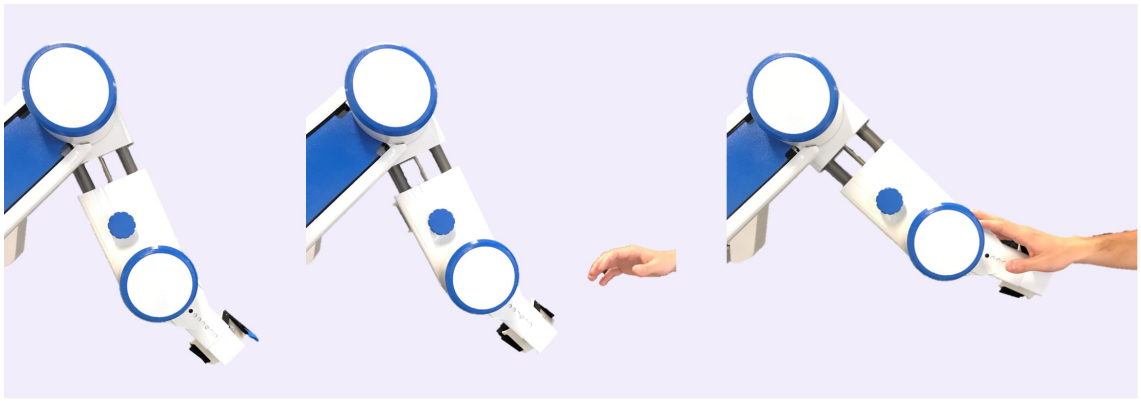
and the SEA torque is computed following Equation 5.3. Other interpolation methods were also tested and compared with the Fourier series results. Table 5.2 shows the maximum and minimum errors obtained after double compensation (NL and L conditions) using Gaussian and the sum of sines approximations as examples. As expected, the sum of sines produced results comparable to the Fourier series, though it was found to be less accurate in replicating signal behaviour, especially when the signal exhibited significant variability. On the other hand, the Gaussian approximation showed promise. However, to achieve convergence in the NL scenario, a minimum of six coefficients was required, which is higher than that for the Fourier method. Additionally, preprocessing was necessary to shift the signals into the positive domain for Gaussian application. Consequently, the signals had to be shifted back to their original domain after correction. The joints were tested under different load conditions, revealing an increase in error amplitude (evaluated at the same absolute position where torque measurement is performed) as the load increased. This phenomenon highlights the intricate nature of the nonlinear effects influencing the system. The calculated errors from the different tests are illustrated in Figure 5.3 and summarized in Table 5.1.

| | $J_{rr80}$ | | | $J_{rr50}$ | | |
|---|---|---|---|---|---|---|
| $\varepsilon[Nm]$ | 5kg | 10kg | 15kg | 2kg | 5kg | 7kg |
| $\varepsilon_{\tau m}$ | -1.694 | -1.795 | -2.142 | -1.958 | -1.635 | -1.635 |
| $\varepsilon_{\tau M}$ | 1.405 | 1.693 | 1.718 | 1.415 | 1.81 | 2.162 |
| $\varepsilon_{\tau mNL}$ | -2.197 | -2.228 | -2.444 | -0.7245 | -0.7791 | -0.8177 |
| $\varepsilon_{\tau MNL}$ | 0.582 | 1.018 | 1.223 | 2.219 | 2.658 | 2.766 |
| $\varepsilon_{\tau mNL-L}$ | -1.361 | -0.962 | -1.574 | -1.195 | -1.164 | -0.9347 |
| $\varepsilon_{\tau MNL-L}$ | 1.051 | 1.047 | 1.672 | 0.9641 | 1.257 | 1.541 |

Table 5.1 Fourier Series correction Error Analysis: the minimum (m) and maximum (M) absolute errors in Nm are reported for the different load condition tests. The errors are computed in three different cases: (I) no correction is applied, (II) the no-load (NL) Fourier Series correction is applied, (III) both the no-load (NL) and the load (L) Fourier compensations are applied to the measurements.

| | $J_{rr80}$ *Gaussian Approx.* | $J_{rr80}$ *Sum of Sines Approx.* |
|---|---|---|
| $\varepsilon[Nm]$ | 15kg | 15kg |
| $\varepsilon_{\tau mNL-L}$ | -1.551 | -1.670 |
| $\varepsilon_{\tau MNL-L}$ | 1.579 | 1.613 |

Table 5.2 Residual Error Analysis for Gaussian and Sum of Sines approximations: Minimum (m) and maximum (M) absolute errors (in Nm) are reported for a 15 kg load, with and without load (NL and L) compensations. Gaussian approximations use the 6th order for NL and the 8th order for L, while Sum of Sines uses the 5th order for NL and the 8th order for L, matching the Fourier series.



(a) (b) (c)

Fig. 5.5 Experimental test, on FloatEVO exoskeleton, for evaluating the pHRI, the following scenarios are depicted: (a) and (b) show a non-interaction scenario wherein the SEA joint, controlled in position control, adheres to the predefined trajectory. Subsequently, in (c), a user interacts with the exoskeleton by exerting resistance to the movement, which is subsequently recorded by the SEA sensor.

### 5.1.3 Test on the exoskeleton

The joint, with a 1:80 reduction ratio, underwent testing upon assembly onto the exoskeleton. Tests included flexion-extension trials without and with external disturbance mimicking user resistance. Position control ensured adherence to a predefined trajectory. The joint torque was estimated with and without Fourier correction, alongside gravity torque calculated via the dynamic model.

The interaction test is performed as shown in Figure 5.5: the exoskeleton movement is performed in position control and during the test a user interacts with the robotic arm opposing a resistive force to the movement. In Figure 5.6, on the left are reported the results of a test without HRI, it is possible to notice how the torque estimation, obtained through double correction, more closely aligns with the reference gravity torque provided by the dynamic model. Once it has been established that such measurements are more reliable, it becomes feasible to derive the interaction torque by comparing the estimated gravity torque with the theoretical one. The figure distinguishes zones where no HRI was detected from zones where the user applied resistance to the movement. The ability to accurately estimate this interaction holds implications, both for assessing the patient's condition during the rehabilitation session and for implementing more precise closed-loop torque control (AAN strategies implementation).

## 5.2 Preliminary control architecture implementation: RCP approach

In this paragraph, it is proposed an RCP-HIL methodology targeted at rehabilitative robotics applications. The testing of the control architecture performances for an upper-limb exoskeleton

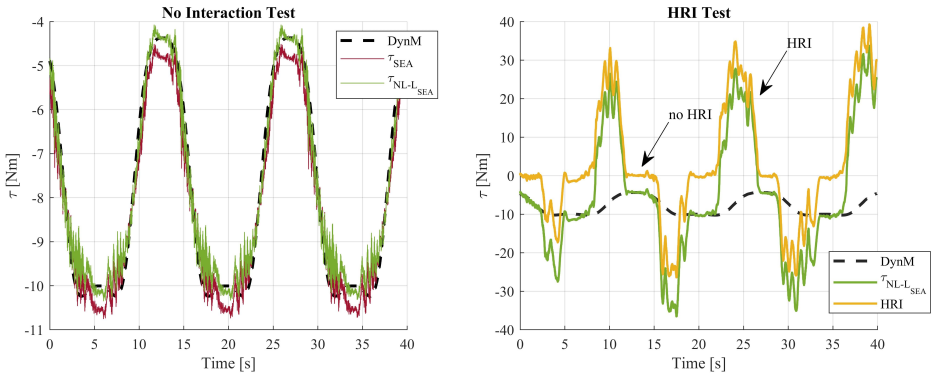



Fig. 5.6 The joint with a reduction ratio of 1:80 was tested once assembled on the exoskeleton. The following tests were performed: flexion-extension without HRI (flexion-extension with external disturbance given by the HRI (right) to mimic the possible resistance of a user in performing the movement. The joint was controlled in position to follow a predefined trajectory. The graph shows the estimated torque of the SEA joint calculated with and without Fourier correction and the gravity torque calculated using the dynamic model.

prototype is presented. The peculiarity of the proposed method lies in the early adoption of a unified development environment and a single programming language. For this development, MATLAB tools by MathWorks (Natick, MA, USA). However, the same methodology can be leveraged in any other RCP development environment.

### 5.2.1 Hardware platform for RCP-HIL test: Spherical Float setup

The Spherical Float prototype was adopted as a testing platform. The control boards, mounted directly on the joints, are then connected, as well as the SEA sensors, via CAN (Controller Area Network) to the central control unit (Speedgoat Baseline real-time target machine [124]). This is further connected to a panel PC where the control interface is displayed.

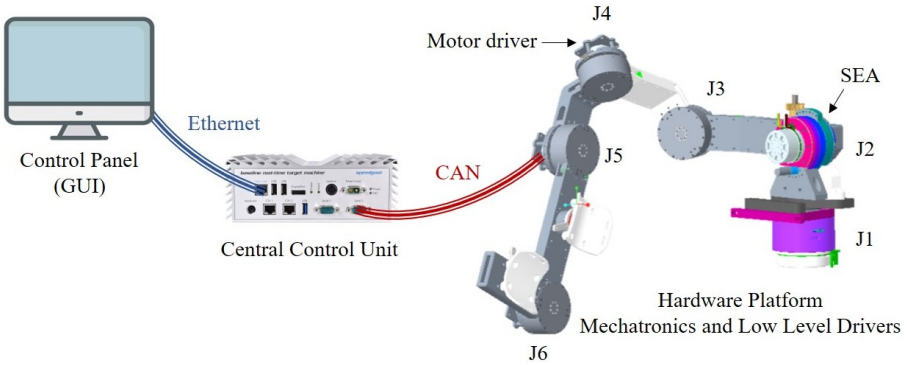



Fig. 5.7 Hardware setup: EPOS motor controller and SEA sensors are connected via CAN to Speedgoat Baseline real-time target machine. Speedgoat can communicate via ethernet with the host computer (Control Panel) receiving inputs from the GUI and providing feedback data about the running simulation.

### 5.2.2 Central control unit: Real-Time target machine for RCP development

To facilitate real-time simulations, a Real-Time Target machine has been employed, with Speedgoat serving as the platform for all conducted tests. Speedgoat offers high performances thanks to multi-CPU target computers. It can be adopted in different areas like RCP and HIL systems. It is specifically designed to integrate with Simulink and Simulink Real-Time tools from MathWorks. This machine enables the execution of real-time applications developed within the MATLAB Simulink environment. The incorporation of Speedgoat Simulink driver blocks within the model streamlines the process, allowing for the automatic generation of real-time applications. Subsequently, these applications are downloaded and executed on the machine with ease. The target machine has integrated communication ports that enable the device to interact with the outside world. Speedgoat can communicate with other devices through external ports, for our experiments, the CAN and Ethernet ports have been used, but many other communication protocols are available meeting the designer preferences (EtherCAT, PWM, SPI, I2C, SENT, and more [124]).

### 5.2.3 Control design methodology

The control strategy involves implementing all control levels (low, medium, and high levels) within the same environment (MATLAB R2021b). Thanks to the use of various tools, it is possible to obtain a unique control model that includes setting up control drivers, acquiring and processing data from the mechatronic structure, and designing control algorithms (implemented following state machine logic). The steps of the proposed methodology are described below.

#### Design of the Low-Level control

The setup of the EPOS boards' controllers is carried out with the following steps: (i) communication of the motor specifications (torque gain, resistance, etc), (ii) communication of the PID gains for the position, velocity, and current loops (that operates at $f = 1$ kHz), (iii) communication of the desired operational limits. The communication protocol used to work with EPOS4 is the CANopen protocol. Inside the CANopen network, the EPOS4 controllers are controlled as child nodes and coordinated by the Simulink model running on the Speedgoatreal-time target machine. CAN protocol has been set up by employing IO614 reading aset upiting modules on Speedgoat Baseline Real−Time Target Machine [124]. Concerning the top layer of the model (Figure 5.8), the CAN SETTINGS module is built to set up CAN connection exploiting CANopen protocol; the INPUT RECEIVED SIGNALS module manages the input signals from SEA sensors and EPOS boards (acquired at $f = 1$ kHz); CAN SETTINGS TO OUTPUT COMMANDS module sets up all the output control signals (computed and provided at $f = 1$ kHz) to communicate via CAN with the sensors and EPOS motor driver boards.

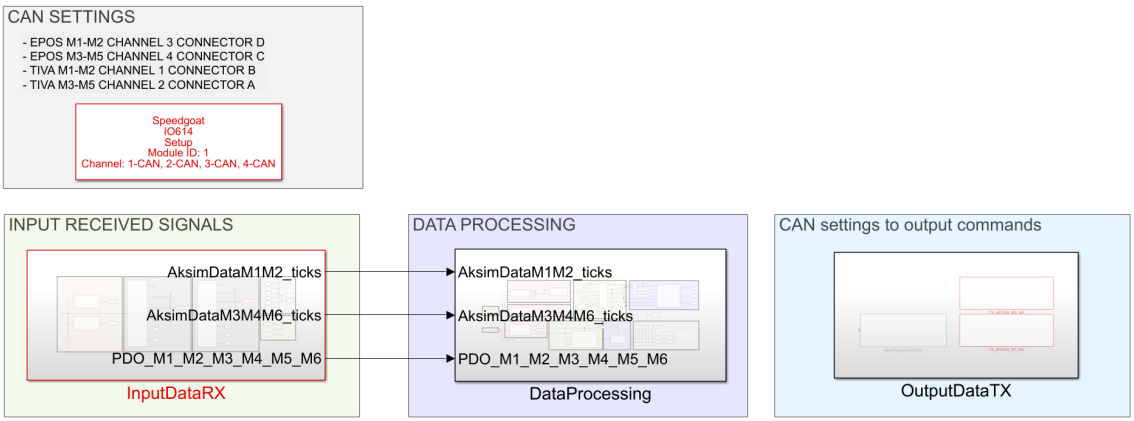



Fig. 5.8 Top Layer of the Simulink control model. The model is built and then deployed on Speedgoat's real-time target machine. In this layer it is possible to identify four main blocks: CAN communication setup, readings of sensor data, processing of all the received data (this unit establishes the exoskeleton behaviour), and the output block that sends over the CAN line the command signals.

### Design of the Middle-Level control

Exploiting Simulink and Stateflow enables the straightforward implementation of multiple state machines to characterize the operational modes of the exoskeleton and potential state transitions. Concerning Figure 5.8, the dedicated module is DATA PROCESSING, which is the core module where all the control is implemented using control algorithms and state machines. The processing unit describes all the possible state transitions between the different behaviours of the device. The tasks performed in the Data Processing subsystem are: (I) Estimation of the SEAs torques; (II) Setup and reaching of the homing position (resting position of the exoskeleton); (III) Managing of the different working modes (passive exercises, exercise with compliance achieved thanks to impedance control, transparency, learn and replay); (IV) Computation of the pose of the exoskeleton end-effector; (V) Computation of the scapular elevation coupling following the method suggested in [57]. The scapular elevation is a function of the shoulder flexion. Once the shoulder flexion overcomes 60 deg, refer to Figure 5.10a, J2 is coupled with J5 with a ratio 1:3); (VI) Trajectory generation; (VII) Computation of the gravity torques from the robot dynamic model; (VIII) Torque control target generation (friction compensation, impedance, transparency).

Three main control strategies were implemented: passive user mobilization, compliant and modular assistance, and transparency. Going from the first to the last modality, the goal is to increase user engagement and decrease exoskeleton assistance.

**Passive user mobilization** This working mode exploits the position control. The exoskeleton rigidly moves the human limb, without keeping into account the interaction forces. A target

trajectory is provided for each joint. The possible exercises are: shoulder flexion-extension, shoulder abduction-adduction, and elbow flexion-extension. Using the graphic user interface (Figure 5.9) it is possible to select the desired number of repetitions, timing (exercise duration), and maximum target angle. It is also possible to replicate, in position control, a recorded exercise. The model has a dedicated Stateflow state machine that can be used to perform the learn and replay. By exploiting the GUI buttons, it is possible to start the exercise recording (the exoskeleton goes into transparency mode and can be moved freely). The joint position data are recorded stored and used as the target trajectory for the replay.

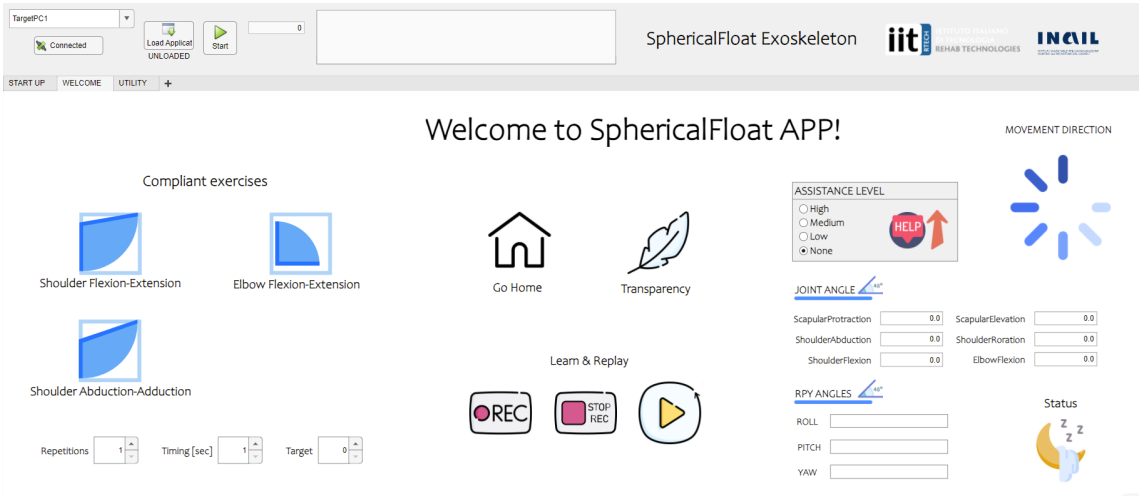



Fig. 5.9 Graphical User Interface Welcome Panel: within this tab of the GUI, crafted using the App Designer MATLAB Tool, users can establish the preferred working mode of the exoskeleton. This includes initiating straightforward exercises under passive or compliant control (with selectable levels of assistance) and configuring the number of repetitions, timing, and target positions for the exercises. Users can command the robot to return to the Home position or activate transparency mode. Additionally, functionalities such as learning and replaying are accessible. The GUI provides comprehensive information about the current phase of the exercise, the direction of the movement to be followed, the status of the machine (sleep, operative, fault), also, information about the joint's position and the end-effector orientation angles are available.

**Geometric model description** The robotic kinematic chain can be described using the Denavit-Hartenberg convention (DH) or the modified Denavit-Hartenberg (DH) convention [114]. For each frame (corresponding to a joint), it is possible to assign dynamic properties such as mass, the centre of mass, and the inertia tensor. To compute these properties, a CAD model should be utilized to facilitate the calculation of inertial properties concerning the different joint reference frames. Subsequently, a rigid body tree (RBT) model (a geometric model characterizing both the kinematics and inertial properties of the robot) can be designed. CREO PTC [125] was adopted as CAD software to obtain the dynamic characteristics and MATLAB Robotic Toolbox to build the exoskeleton rigid body tree model, as shown in Figure 5.10a. This RBT model is imported into the

Simulink model and utilized to compute the direct and inverse kinematics and the gravity torques to be compensated at each joint. The aforementioned procedure is described in Figure 5.11.

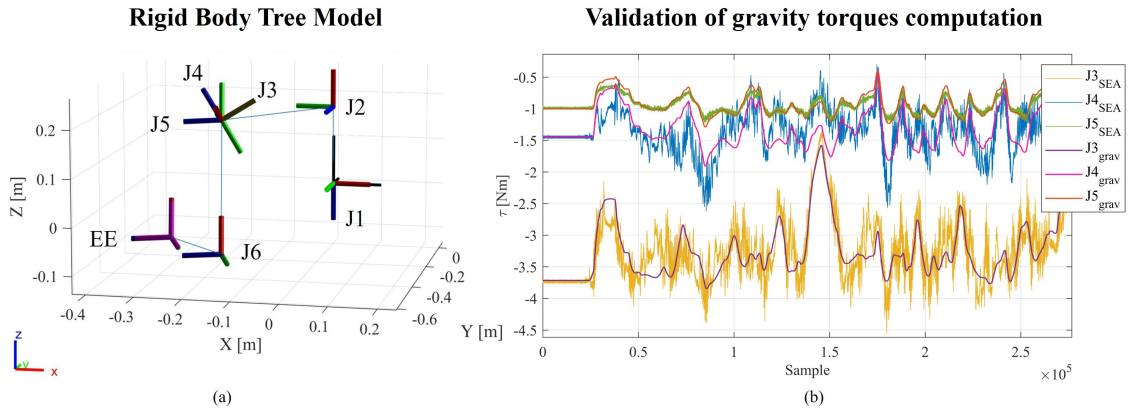



Fig. 5.10 (**a**) Rigid Body tree representing the kinematic chain of the 6−degree−of−freedom prototype. The Modified Denavit−Hartenberg (mDH) convention was followed for describing the kinematics. Each reference frame, representing a rotational degree of freedom, is associated with the dynamic properties of the body, including mass, the centre of mass coordinates, and the inertia tensor. (**b**) Graphical comparison between the torques estimated by the model and the ones measured by SEAs sensors. During the test, the exoskeleton was moved in position control without a user or a load. In the plot are reported, for each joint, the torques estimated by the SEAs and the ones real−time computed from the model through the robotic toolbox.

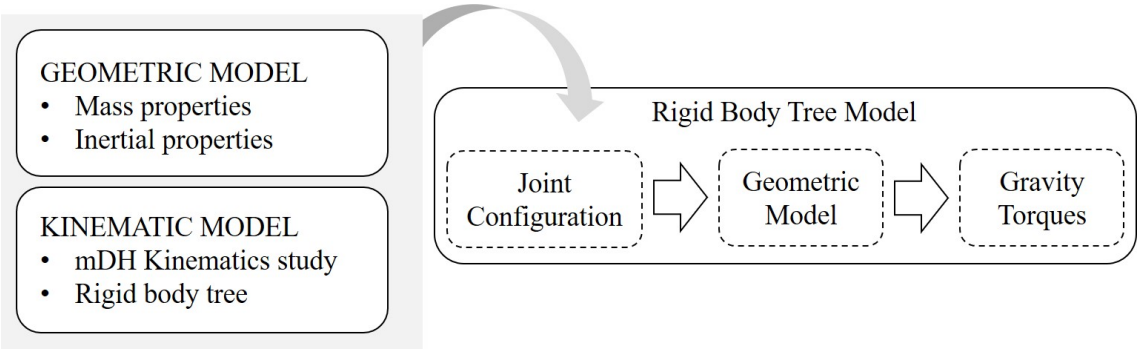



Fig. 5.11 Workflow to develop the gravity torque estimation model: the dynamic model characterization for real-time gravity torque computation involves the utilization of various tools. In the CAD model of the prototype, the set of reference frames is redefined following the modified Denavit-Hartenberg (mDH) convention. Properties such as mass, the centre of mass, and inertia tensor for the different components of the device are then computed concerning these reference frames. Using these dynamically derived properties, a rigid body tree model is constructed in MATLAB, adhering to the aforementioned mDH convention. This characterized model can be imported into the Gravity Torque function, which, in real-time, provides the joint torques necessary to maintain the robot at a specific configuration.

**Impedance Control to provide modular assistance during rehabilitative exercises** Impedance control can be exploited to support the patient in performing voluntary movements. Impedance

control manages the capacity to exchange force between the controlled system and the subject or the environment. Linear impedance parameters, like stiffness and viscosity, are described as second-rank twice covariant tensors [126]. This impedance embodies the correlation between force and motion dictated by the supervisor, encompassing both the static force/displacement relationship and any dynamic terms necessary for controlled dynamic behaviour [126]. Essentially, it dictates whether the robot exhibits rigidity or compliance upon interaction with external objects or surfaces. It belongs to the category of partially assistive controls [81], aiming to not only provide physical support but also to maintain the subject's motivation, training intensity, confidence in using the affected limb, and prevent negative reinforcement [127]. A tunable support level can be provided depending on the residual motor functionality of the user. The assistance level can be selected on the GUI, the target trajectories can be the ones of predefined exercises or a recorded complex trajectory stored during the learn-and-replay procedure. Impedance control can be used to ensure safety during human-machine interaction: it allows to dissipate torques and forces at the joint level and not to the external environment.

By tuning stiffness ($k_v$) and viscosity ($\beta_v$), it is possible to provide modular assistance increasing the user engagement while decreasing the provided support. The adopted impedance algorithm is developed in the joint space.

$$\Delta q = q_{target} - q_{actual} \tag{5.4}$$

$$\tau_{interaction} = \tau_{SEA} - \tau_{gravity} \tag{5.5}$$

$$\tau_{target} = \Delta q \cdot k_v + \dot{q} \cdot \beta_v + \tau_{interaction} \tag{5.6}$$

For each joint, the control scheme shown in Figure 5.12 is applied. Simulink allows us to fully explore the potential of real-time computation. Concerning Figure 5.12, the Joint target position is real-time computed for the standard exercises trajectory as a linear interpolation between the start and end position, set by the user into the GUI. This has to be performed in the desired amount of time and repeated for the selected number of repetitions. The trajectory can also be recorded during a learning process. The joint actual position and speed are provided by the EPOS board. For this implementation a reference velocity $\dot{q}_{tg} = 0$ has been considered at all times. The sensed actual torque is computed by the model starting from the SEA sensor encoders readings (a measure of the SEA spring deformation $\Delta\theta$), as explained in [80] :

$$\tau_{SEA} = ((\theta_{out} - \theta_{in}) - \Delta\theta_{offset}) \cdot k + \Delta\tau_{lm} \tag{5.7}$$

respectively $\theta_{out}, \theta_{in}$ and $\Delta\theta_{offset}$ are: the angular displacements after and before the spring, the mounting encoder offset, $\Delta\tau_{lm}$ is the linear model intercept and $k$ is the stiffness of the adopted compliant element. The gravity torque is obtained from a dedicated Simulink block of the robotic

toolbox as explained in Figure 5.11. All the aforementioned information is compared and elaborated to generate the control signals for the motor boards.

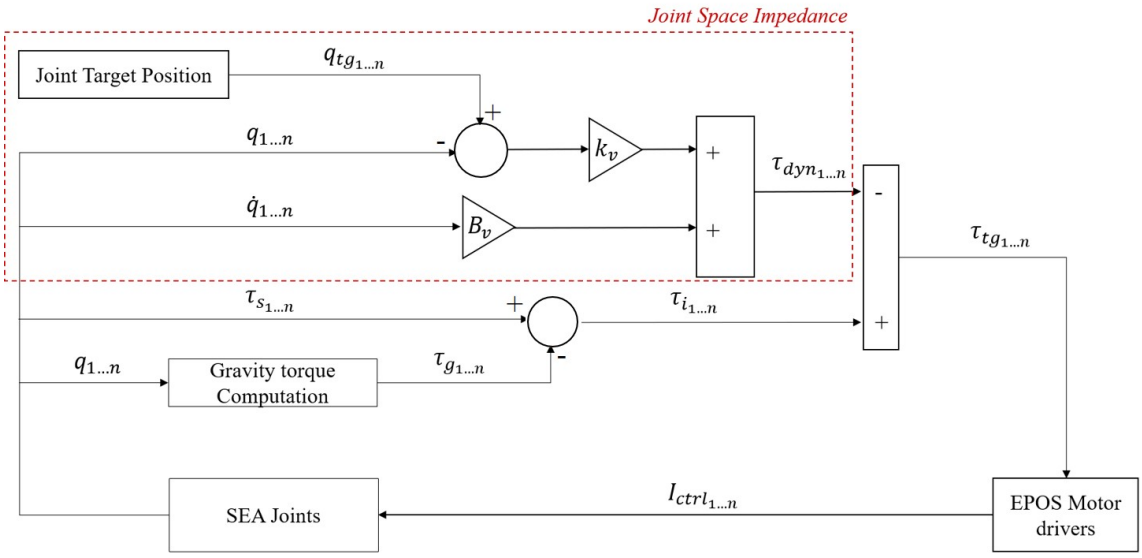



Fig. 5.12 The impedance control scheme employs the presented algorithm individually for each joint to compute the control signal. The reference target, representing the desired position, has to be reached by ensuring a certain compliance between the user and the device. The difference between the target and actual positions represents the delta displacement of a virtual spring, that multiplied by a virtual stiffness coefficient ($k_v$) provides the spring torsional torque. The actual joint speed introduces a viscous behavior, determined by the viscous coefficient ($\beta_v$). The interaction torque, calculated as the difference between the estimated SEA torque and the gravity torque, serves as the feed-forward term. This ensures that the user can displace the exoskeleton in a compliant manner.

Figure 5.13 illustrates a test conducted at three different assistance levels during a shoulder flexion exercise, specifically focusing on joint J5, which plays a significant role in this movement. The graph in Figure 5.13 displays both the target trajectory and the actual trajectories executed by the user, exploiting the dedicated joint, throughout the exercise in assistive mode.

| Compliance | $k_v$ [Nm/rad] | $\beta_v$ [Nm·s/rad] |
|---|---|---|
| High | 30 | 1.2 |
| Medium | 10 | 1.2 |
| Low | 5.5 | 0.6 |

Table 5.3 Pairs of stiffness and viscosity parameters ($k_v$ and $\beta_v$) utilized in the impedance dynamic model to implement three different levels of assistance: decreasing $k_v$ corresponds to lower support and higher compliance.

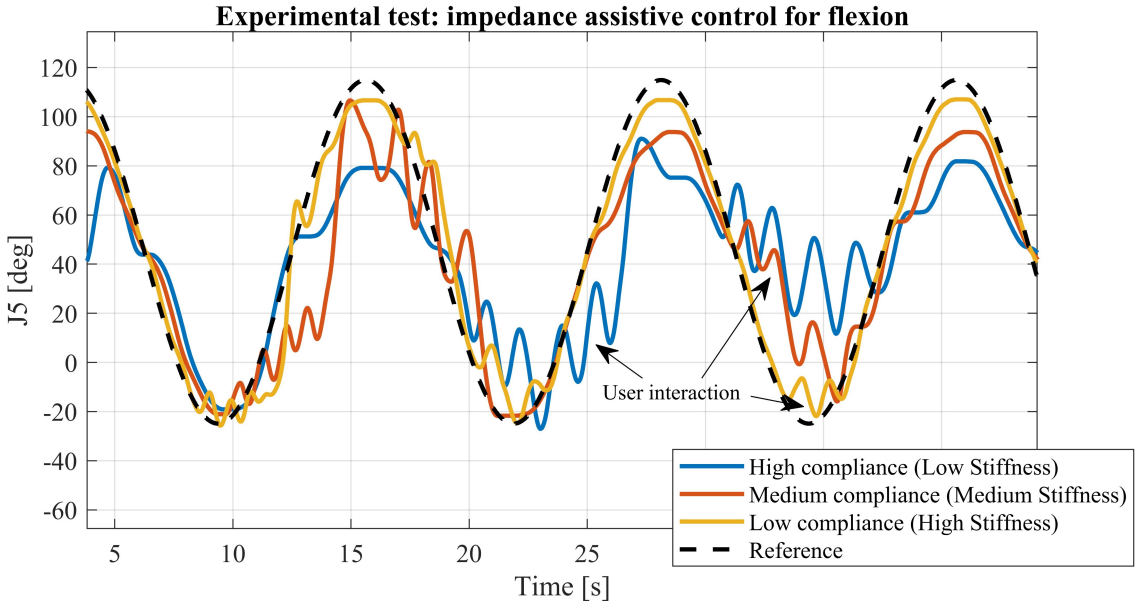



Fig. 5.13 Experimental results of impedance-based assistive control: three levels of assistance were tested by varying the stiffness−viscosity parameters of the impedance control (stiffness−viscosity couples are reported in Table 5.3). In the figure, the black line indicates the joint reference target, while the blue, orange, and yellow lines represent the results of three tests at different assistance levels. The displayed oscillations are the consequences of human interaction with the robot. It is noticeable that lower assistance (high compliance, low stiffness) allows for greater interaction with the robot, enabling the user to deviate significantly from the target trajectory. Higher assistance (low compliance, high stiffness) leads to better adherence to the target trajectory, albeit restricting interaction with the device to some extent.

**Transparency: Gravity and Friction Compensation** Transparency mode is implemented to let the user perform free movements, exploring the working space and minimizing the exoskeleton weight and friction effects that can interfere with the smoothness of the performed movement. The motor control is performed in torque (current), and the control signal is computed from the sum of different components: the gravity torque, the friction compensation torque, and the interaction torque (obtained from the SEA sensed torque). This control exploits two different layers:

- Gravity compensation: it is needed to compensate for the gravity effect to avoid the structure collapsing under its weight, thus a reliable gravity compensation model is needed. The obtained rigid body tree model (Figure 5.11) is exploited in Simulink by the Gravity Torque block of the Robotic Toolbox allowing real-time computing, given a certain joints' configuration, the gravity torques to be compensated.
- Friction compensation: frictions can result in a lack of smoothness during the movement, especially at low speeds when static frictions need to be won. A Stateflow state machine has been implemented to evaluate, based on the actual motor speed, a compensatory friction torque used to overcome friction dissipation.

The friction contribute is computed as $\tau_{fr} = -\beta_{fr} \cdot \dot{q}$, with $\beta_{fr}$ parameter evaluated by the state machine in a dynamic way following Algorithm 10. $\beta_{fr}$ is evaluated at each interaction. The highest compensation for overcoming frictions occurs at low speeds when static frictions need to be overcome. The coefficient $\beta_f$ remains constant within an accepted speed range for movement in transparency. If the motor speed exceeds a specified threshold, indicating that the joint is moving too fast, $\beta_f$ takes on a different value, increasing the viscous effect until reaching the maximum set velocity, thereby implying minimal support in overcoming frictions.

Real-time experiments have been conducted to validate the dynamic model obtained from the characterization of the Rfrom-Body-Tree shown in Figure 5.10a.

The test aims to verify the consistency between the torque estimated by the SEA sensors (obtained by evaluating the deflection of the elastic element) and the torque calculated using the dynamic model of the exoskeleton obtained with the methodology presented in Figure 5.11. To evaluate the performance of the exoskeleton, the robot was mobilized in transparency mode and recorded the executed movement (learn and replay mode). This recorded movement is then executed by the exoskeleton without the presence of a user, in position control (so that the SEA sensors detect only the gravity torque and not the interaction torque with the user). From the collected data of the experiment, it is possible to perform a comparison between the measurement of the gravity torque obtained from the SEA sensors and the one estimated using the MATLAB Gravity Torque Toolbox (based on the characterized dynamic model).

In Figure 5.10b are shown the Gravity Torques computed from the dynamic model and recorded by SEAs for the spherical joint complex (J3, J4, J5). The computed RMSEs and absolute errors, between the SEA measure and the gravity compensation model are reported in Table 5.4.

The algorithm implemented in the dedicated state machine for friction compensation involves monitoring the rotational speed of the joint. Depending on the speed value, the compensation effect is determined, mirroring the behaviour of a damper. Specifically:

- If the speed is below a minimum threshold, denoted as $\dot{q}_{\mathrm{s}}$, it indicates that the joint is initiating movement. To overcome initial static friction, the compensation effects against friction are amplified.
- Within a predefined ideal speed range for device activities, the compensation contribution remains constant.
- If the speed exceeds a high threshold, denoted as $\dot{q}_{\mathrm{f}}$, a gradual effect begins to compensate less against friction until minimal compensation is achieved at the predefined maximum speed, $\dot{q}_{\mathrm{max}}$.

| Joint ID | RMSE [Nm] | $\varepsilon_{\max}$ [Nm] |
|---|---|---|
| J3 | 0.2877 | 0.8338 |
| J4 | 0.3101 | 0.8703 |
| J5 | 0.0649 | 0.3449 |

Table 5.4 Root Mean Square Error (RMSE) and maximum error values for different joints. The maximum errors and RMSE ($\varepsilon_{\max}$) are computed by comparing the experimental measurements of SEA sensors with the output from the built-in gravity torque calculation function in the MATLAB Robotic Toolbox. The experiment was conducted with the exoskeleton covering various zones within the workspace while operating in position control to validate the consistency of the SEA sensor readings with the MATLAB model.

**Algorithm 1** Friction compensation algorithm

**if** $|\dot{q}| < \dot{q}_s$ **then**
  $\beta_{\text{fr}} \leftarrow \beta_s$
**else**
  **if** $\dot{q}_s \leq |\dot{q}| \leq \dot{q}_f$ **then**
    $\beta_{\text{fr}} \leftarrow \beta_f$
  **end if**
  **if** $|\dot{q}| > \dot{q}_f$ **then**
    $\beta_{\text{fr}} \leftarrow \beta_m \cdot \left(\frac{\dot{q}_{\max}}{|\dot{q}|}\right)$
  **end if**
**end if**

Exploiting the proposed RCP control model, additional control strategies have been implemented. Specifically, these include a Cartesian control utilizing a force-torque sensor placed at the interface between the arm and the exoskeleton, an admittance control, and a preliminary implementation of a velocity field.

**ATI Cartesian Control** An ATI force/Torque sensor was connected to the real-time target machine using a UDP protocol configuration. This bidirectional communication allows sending and receiving information packets to and from the sensor. Through dedicated Simulink blocks, the IP addresses for communication and the data packet sizes exchanged during communication were configured. A specific section of the GUI was developed to transmit four specific messages to the sensor: START, BIAS, UNBIAS, and STOP. These commands enable the initiation and termination of data streaming and allow an initial biasing of the sensor readings so that a null force/torque corresponds to a zero reading. The message structure is outlined in the table below.

By reading the forces exerted by the user on the structure, a simple mapping was implemented to relate the forces measured along the three Cartesian axes to the displacement of the end-effector in terms of coordinates $(x, y, z)$. The relationship between the sensor's reference system $(x, y, z)$ and the base reference system of the kinematic structure under analysis is as follows:

$$x_{\text{ati}} \rightarrow y_{\text{ee}}, \quad y_{\text{ati}} \rightarrow -z_{\text{ee}}, \quad z_{\text{ati}} \rightarrow x_{\text{ee}}$$

The control system receives the current motor positions as input, read from the EPOS boards. Using forward kinematics, the Jacobian matrix, and the forces exerted by the user, the following recursive formula is implemented:

$$q_{i+1} = q_i + J^{-1} \cdot v_{\text{ee}} \cdot \Delta t$$

Here, the term $v_{\text{ee}} \cdot \Delta t$ is experimentally derived from the change in Cartesian coordinates ($\Delta\text{Coordinates}_{\text{Cartesian}}$) between the current coordinates and those at $t+1$, estimated through the mapping $\text{Forces}_{\text{ATI}} \rightarrow \text{Positions}_{\text{End-Effector}}$. This recursive formula computes the next position references, which are then provided as position commands to the EPOS boards. These boards control motor movement in CSP (position control) mode.

**Single Joint Control: Viscoelastic Admittance with Gravity Compensation** The admittance filter is implemented for each joint and receives as input the torque estimated by the SEA (see Figure 5.14), subtracting the gravity component. The target position (homing position pos $= 0$) is compared with the position calculated by the filter, and the resulting signal is provided as input to the EPOS boards.

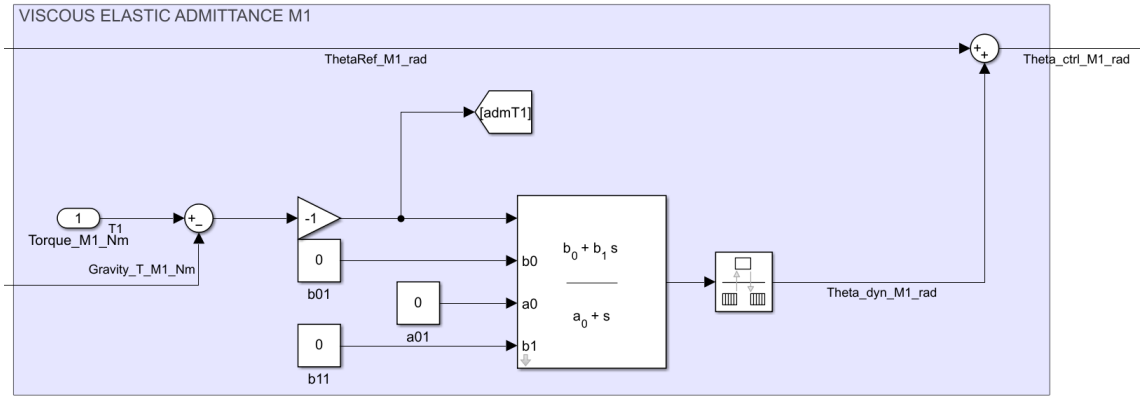



Fig. 5.14 Simulink blocks for the implementation of admittance filter, the same control is implemented to control each joint of the exoskeleton prototype.

The gravity component is estimated in real-time using a block from the real-time toolbox. This block computes the torque required to compensate for gravity in the analyzed configuration, given the current position and the robot's rigid body tree.

**Cartesian Control: Velocity Field** The implemented control equation is:

$$q_{i+1} = q_i + J^{-1} \cdot \begin{bmatrix} v_x(i) \\ v_y(i) \\ v_z(i) \end{bmatrix} \cdot \Delta t$$

Where $J^{-1}$ is the Jacobian pseudo-inverse. The system's input is the position read from the EPOS boards. Using blocks provided by the Robotics Toolbox in Simulink, the Jacobian matrix, inverse kinematics, and gravity compensation torques are calculated in real-time. The Simulink model for implementing the desired velocity field leverages the Robotics Toolbox to compute gravity torques, the end-effector transformation, and the Jacobian matrix in the robot's current configuration. The parameters of the velocity field can be selected, and the iterative formula is implemented to compute the new target positions.

The velocity field is described by the equations:

$$v_x = -\frac{2(x-x_0)}{a^2}, \quad v_y = -\frac{2(y-y_0)}{b^2}, \quad v_z = -\frac{2(z-z_0)}{c^2}$$

Here, $a$, $b$, and $c$ are variable parameters that determine the intensity of the field. Smaller values result in a stronger field. These parameters can be modified in real-time via the GUI.

The tests conducted confirm that the velocity field drives the end-effector to the target position $(x_0, y_0, z_0)$ set via the GUI. Once the field intensity is selected (e.g., $a = b = c = 50$), the prototype can be moved manually, and the field gradually restores the desired position. As $a$, $b$, and $c$ decrease, the field acts more quickly, but with increased intensity, manual movement of the end-effector becomes impossible. The farther the end-effector goes from the field centre, the higher the recall force is.

In a subsequent application, the joint variable vector is used as input to the admittance control block. The goal is to simultaneously use viscous admittance and the velocity field to better support the patient.

### Design of the High-Level control

The deployed control model is integrated with a Graphic User Interface created using the MATLAB App Designer Tool. The GUI will serve as an interface between the user, the control model, and the real-time target machine. Through this GUI, users can dynamically select and customize the exoskeleton's behaviour, issuing commands (Figure 5.9) and monitoring key data for the prototype performance evaluation.

## 5.3 FloatEVO embedded control

### 5.3.1 Control layer architecture

The control architecture of FloatEVO, shown in Figure 5.15, is divided into three main control units: (I) Graphical User Interface (GUI), (II) Software, and (III) Firmware.

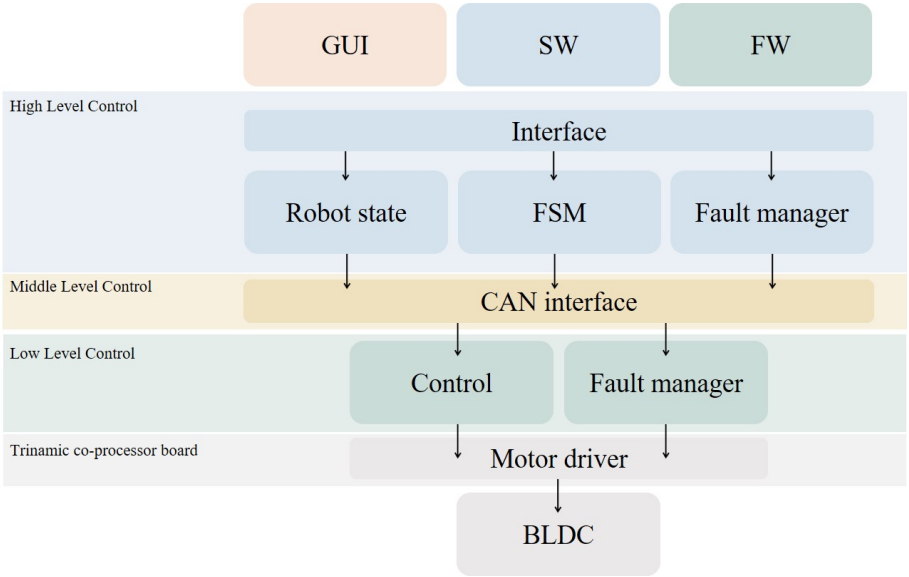



Fig. 5.15 Overview of the FloatEVO control layer architecture.

**GUI** The GUI serves as the interface between the exoskeleton and the user. It allows the selection of the exoskeleton's operating mode, the desired exercise with a configurable number of repetitions, and various target angles.

**Software** The software layer defines and determines the robot's behaviour. Specifically, the robot's state architecture is designed to collect information about the current status of the exoskeleton's joints, such as their positions. The Finite State Machines (FSM) within this layer generate the target control signals (position or torque).

Additionally, a fault manager is implemented to ensure the safe operation of the device by monitoring signals and handling risks according to the CEI EN 62304 standard for risk management.

**Firmware** The low-level control is implemented in the firmware, which is responsible for motor driver control. The drivers are custom-designed and utilize Trinamic controllers.

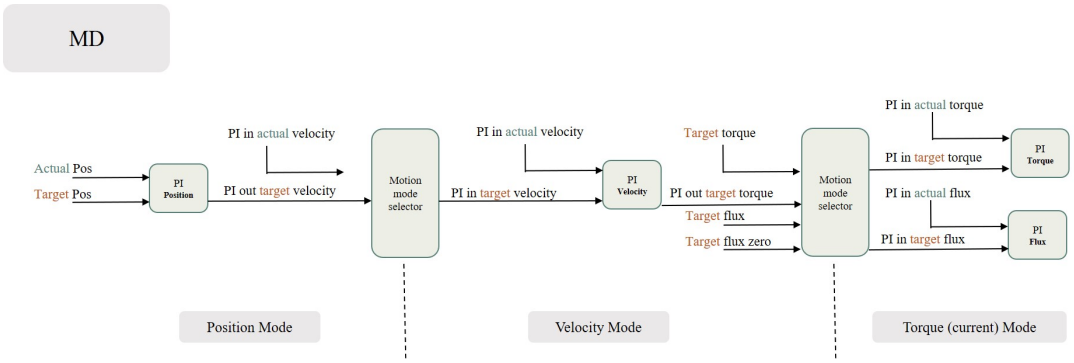



Fig. 5.16 The Trinamic control architecture integrates PI motor control for current, velocity, and position, providing precise and efficient motor regulation across all control levels.

Firmware tasks include configuring TMC motor parameters, executing the phasing procedure, and setting up control modes. The firmware also manages the CAN communication for signal handling (e.g., packaging signals for firmware-software communication). All computations related to SEA torque estimation, including torque computation, linearization, and friction estimation (using the observer proposed in [128]), are performed at the firmware level.

Furthermore, the firmware implements the low-level PI control loops for current, torque, speed, and position (Figure 5.16). It also manages fault handling and the EPROM of the joint boards.

### 5.3.2 Control modes

The custom actuation system, which exploits Series Elastic Actuators, allows for the development of control strategies that utilize measurements of the human-exoskeleton interaction through internal torque sensors embedded in the actuators. This enables the implementation of various control paradigms, including compliant, assistive, supportive, and resistive modes. Currently, FloatEVO can operate in the following modes, which have been developed in an embedded software solution in the context of this thesis:

#### Transparency (with or without assistance and/or support)

In this mode, the exoskeleton compensates for its gravity and friction, allowing free motion for the user to explore the workspace. Using the “learn” function, a desired motion path can also be recorded (Figure 5.18). If assistance or support is enabled, an additional torque is provided to help with elevation and dampen the descending phase. This contribution is proportional to the weight of the arm and forearm, computed using a double-pendulum model where the centres of masses are determined based on the subject’s anthropometry. For the low, medium, and high assistance, the compensated arm weight is respectively 20%, 30% 50%, and in the descending phase, the

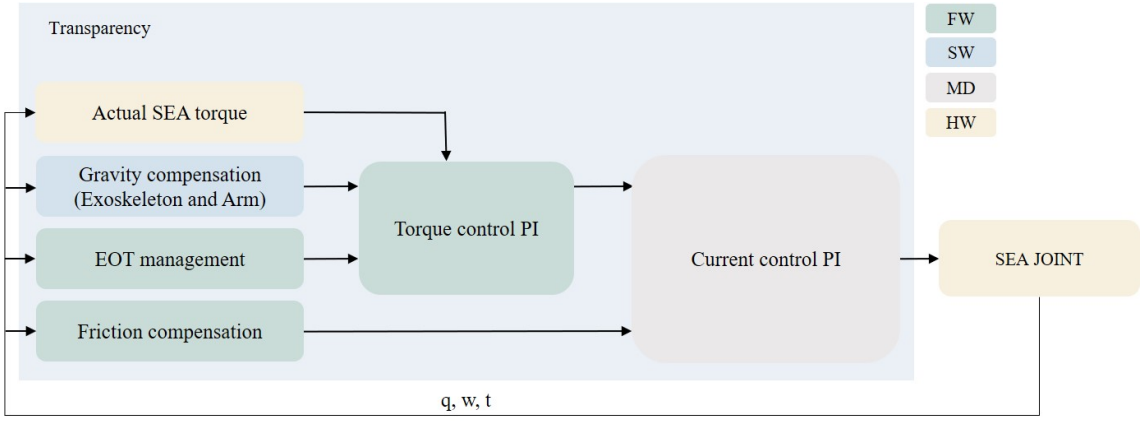



Fig. 5.17 The transparency control block schema includes a PI torque controller that compares the torque measurements from the SEAs with those provided by the dynamic model, while also managing the End of Travel (EOT) conditions. The resulting control signal is then processed by the inner current PI loop, which translates it into a motor current control signal. This process also incorporates a feedforward term for friction compensation, ensuring precise and responsive control. From the SEA are received the position (q), velocity (w) and torque (t) measurements.

supported arm weight is respectively 15%, 25% 45%. The assistive (and support) torque outputs are given by:

$$\tau_{arm_6} = \%\text{Comp} \cdot (g \cdot m_7 \cdot (l_{7\text{CM}} \cdot \sin(q_6 + q_7) + l_6 \cdot \sin(q_6)) + g \cdot l_{6\text{CM}} \cdot m_6 \cdot \sin(q_6))$$

$$\tau_{arm_7} = \%\text{Comp} \cdot (g \cdot l_{7\text{CM}} \cdot m_7 \cdot \sin(q_6 + q_7))$$

where:

$$\begin{aligned} m_6 &= \text{upperArmWeight}, \\ m_7 &= \text{forearmWeight}, \\ l_6 &= \text{upperArmLength}, \\ l_{6\text{CM}} &= \text{upperArmCoM}, \\ l_{7\text{CM}} &= \text{forearmCoM}, \\ q_6 &= \text{shoulderFlexionAngle}, \\ q_7 &= \text{elbowFlexionAngle}. \end{aligned}$$

Gravity compensation is calculated using the dynamic model of the exoskeleton. An algorithm has been developed to compute the gravity torque contribution at each joint independently. This modular approach ensures that any changes made to a link-joint complex can be easily accommo-

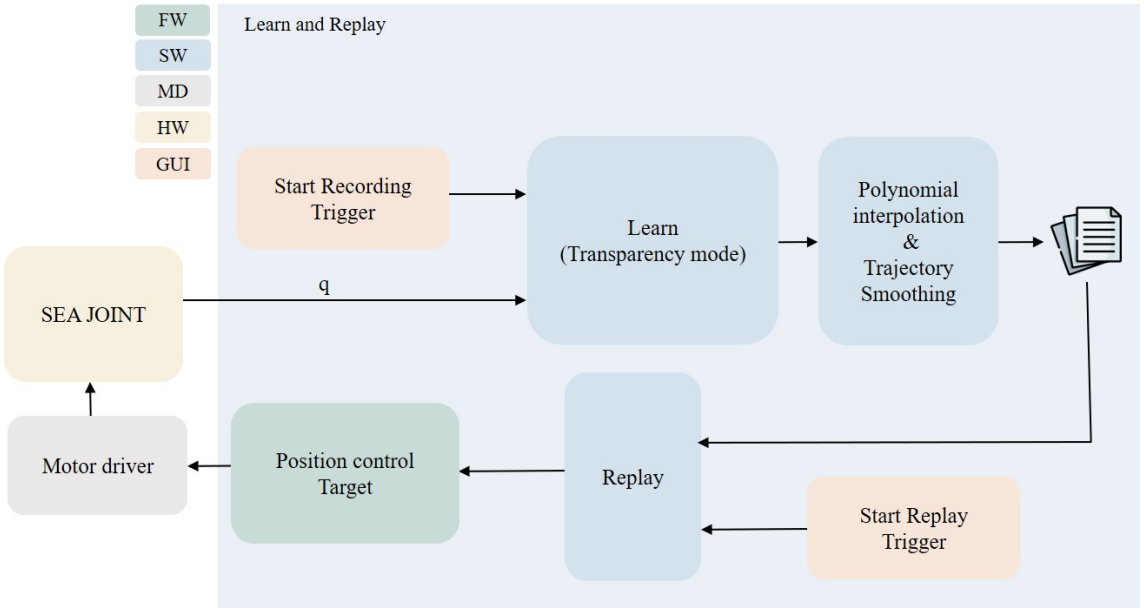



Fig. 5.18 The schema of the Learn and Replay mode operates as follows: the exoskeleton functions in transparency mode (torque control), allowing for natural user-driven movement. When the learn function is activated, joint signals are recorded, filtered, and saved to a file. Subsequently, the recorded movement can be reproduced in position control mode by reading and executing the saved data.

dated by recalculating the overall formulas using symbolic equations. Data related to mass, inertia, link dimensions, and the respective centres of mass were extracted from the CAD model. For each joint, the resulting torque can be determined as the sum of contributions from the various mass components (as shown in Figure 5.17). As an example, the complete computation for the first joint in the chain is provided.

The gravitational force for Joint 1 ($J_1$) is calculated as follows: the center of mass (COM) coordinates for each link, expressed in the corresponding joint reference frames, are given by:

$$\mathbf{coms} = \begin{bmatrix} \text{com1x} & \text{com1y} & \text{com1z} \\ \text{com2x} & \text{com2y} & \text{com2z} \\ \text{com3x} & \text{com3y} & \text{com3z} \\ \text{com4x} & \text{com4y} & \text{com4z} \\ \text{com5x} & \text{com5y} & \text{com5z} \\ \text{com6x} & \text{com6y} & \text{com6z} \\ \text{com7x} & \text{com7y} & \text{com7z} \end{bmatrix}$$

To convert the COM coordinates into homogeneous coordinates:

$$\mathbf{coms}_h = [\mathbf{coms}, \mathbf{1}]$$

The rotation axes for each joint, expressed in the base reference frame, are:

$$\mathbf{z_0} = \begin{bmatrix} 0 \\ 0 \\ 1 \end{bmatrix}, \quad \mathbf{z_1} = T_{01}(1:3,3), \quad \mathbf{z_2} = T_{02}(1:3,3), \quad \ldots, \quad \mathbf{z_7} = T_{07}(1:3,3)$$

The joint positions in the base reference frame are:

$$\mathbf{p_0} = \begin{bmatrix} 0 \\ 0 \\ 0 \end{bmatrix}, \quad \mathbf{p_1} = T_{01}(1:3,4), \quad \mathbf{p_2} = T_{02}(1:3,4), \quad \ldots, \quad \mathbf{p_7} = T_{07}(1:3,4)$$

The center of mass positions in the base frame are computed as:

$$\mathbf{com_1} = T_{01} \cdot \mathbf{coms}_h(1,:)', \quad \mathbf{com_2} = T_{02} \cdot \mathbf{coms}_h(2,:)', \quad \ldots, \quad \mathbf{com_7} = T_{07} \cdot \mathbf{coms}_h(7,:)'$$

Then, the positional part is extracted:

$$\mathbf{com_1} = \mathbf{com_1}(1:3), \quad \mathbf{com_2} = \mathbf{com_2}(1:3), \quad \ldots, \quad \mathbf{com_7} = \mathbf{com_7}(1:3)$$

The gravity vector, assuming that the y-axis points upwards, is:

$$\mathbf{g} = \begin{bmatrix} 0 \\ -9.81 \\ 0 \end{bmatrix}$$

The gravitational forces acting on each link are:

$$\mathbf{F_1} = m_1\mathbf{g}, \quad \mathbf{F_2} = m_2\mathbf{g}, \quad \ldots, \quad \mathbf{F_7} = m_7\mathbf{g}$$

The relative position vectors between the joint 1 and each link's center of mass are:

$$\mathbf{r_1} = \mathbf{com_1} - \mathbf{p_1}, \quad \mathbf{r_{12}} = \mathbf{com_2} - \mathbf{p_1}, \quad \ldots, \quad \mathbf{r_{17}} = \mathbf{com_7} - \mathbf{p_1}$$

The gravitational torque acting on joint 1, due to the forces on all links, is given by:

$$\tau_1 = \mathbf{r_1} \times \mathbf{F_1} + \mathbf{r_{12}} \times \mathbf{F_2} + \mathbf{r_{13}} \times \mathbf{F_3} + \mathbf{r_{14}} \times \mathbf{F_4} + \mathbf{r_{15}} \times \mathbf{F_5} + \mathbf{r_{16}} \times \mathbf{F_6} + \mathbf{r_{17}} \times \mathbf{F_7}$$

Finally, the torque is projected onto the rotation axis of joint 1 to obtain the gravitational torque:

$$\text{gravity_torque}(1) = \tau_1 \cdot \mathbf{z_1}$$

This approach involves treating the kinematic chain as subsets of components, each composed of the rotating part of the joint, the subsequent connecting link and the fixed part of the following joint to ensure that the dynamic model remains modular and easily adaptable in the event of modifications to any part of the exoskeleton. Each subset is independently characterized by its own mass properties, whose weight is sensed and reflected onto each preceding joint.

To estimate and compensate for frictions at the joint levels, the observer algorithm proposed by Le Tien et al. in [128] has been implemented. The joints are operated in closed-loop torque control.

### Passive mobilization

In this mode, the user remains completely passive during mobilization, which is rigidly performed by the machine to guide the upper limb through the motion. These strategies rely on position control, and the exercise trajectories can either be the default ones (traditional exercises) or user-specific, recorded via the "learn" mode. In the context of this work, and based on the clinician's request,

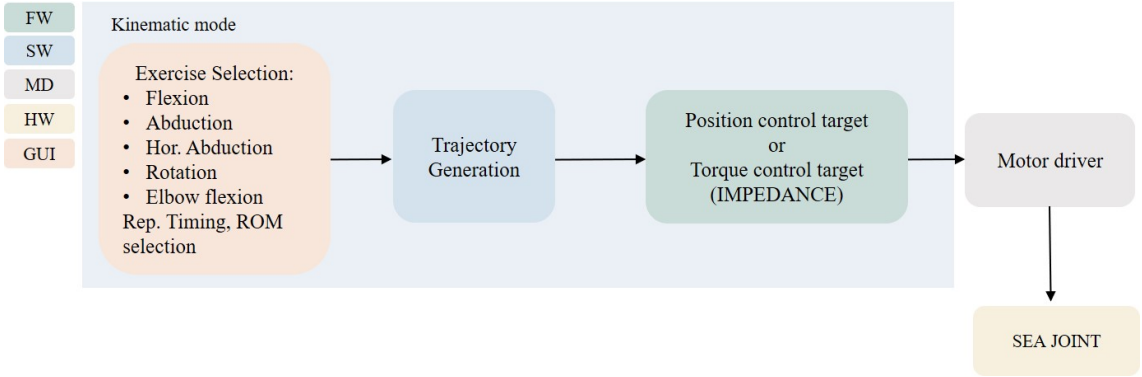



Fig. 5.19 The block representation of the exoskeleton kinematic mode operates as follows: From the GUI, the user can select the desired exercise, range of motion (ROM), number of repetitions, and timing. These inputs are used to compute the corresponding trajectory (for each joint). If the Assistance-As-Needed (AAN) mode is activated, the impedance filter is triggered, and the exercise is executed by the exoskeleton in torque control. Alternatively, if the passive mode is selected, the exoskeleton rigidly mobilizes the arm using position control.

several exercises have been implemented in the embedded C++ code of the exoskeleton. For each exercise (listed in Figure 5.19), a comfortable starting position has been defined. The kinematic mode dictates that the robot moves from the homing position to the start position of the exercise, and then continues through the execution of the exercise until the target is reached.

**Elbow Flexion** This exercise is performed with the arm abducted at 30 degrees. The movement is driven by Joint 7 (J7), which defines the range of motion. The trajectory is calculated using interpolation, ensuring that both the initial and final points of the repetition have zero velocity, thus making the trajectory smooth at the endpoints. The possible range of motion is from 0 deg to 120 deg.

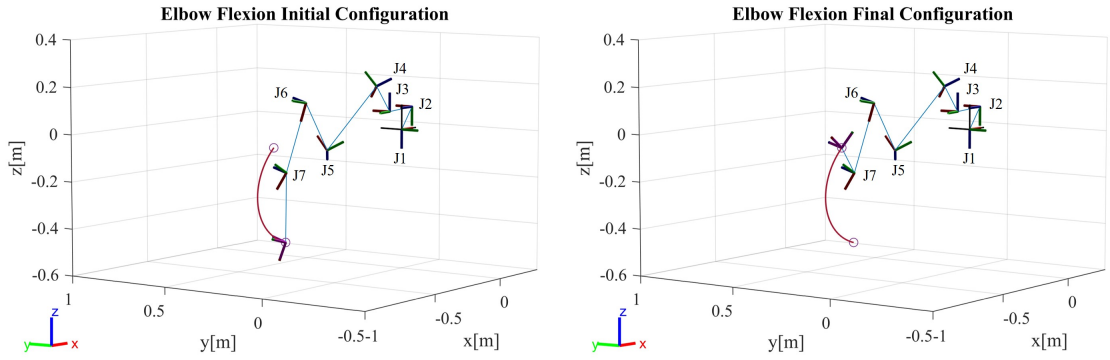



Fig. 5.20 Cartesian trajectory of the end-effector (positioned at wrist level) during elbow flexion performed at the maximum allowable range of motion (ROM). Joint J7 is the only active joint during this movement.

**Shoulder Abduction** The movement is performed in a plane 15 degrees off the frontal plane, with a starting abduction of 35 degrees. Although the pure movement on the frontal plane was also implemented, clinicians preferred the modified configuration to avoid creating too challenging a posture for impaired subjects. Once 90 *deg* of abduction is reached, a scapular elevation coupling (J2) is triggered. The possible range of motion is from 35 *deg* to 180 *deg*.

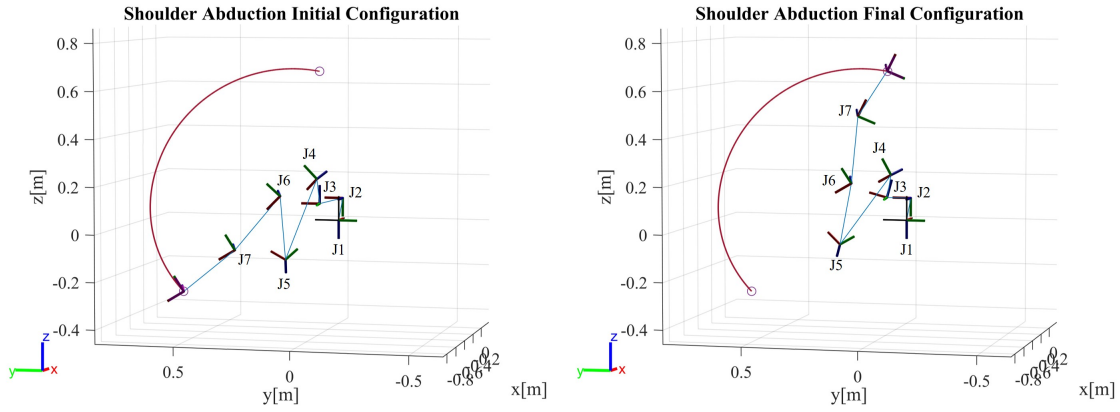



Fig. 5.21 Cartesian trajectory of the end-effector (positioned at wrist level) during shoulder abduction performed at the maximum range of motion (ROM). The movement is primarily guided by Joint J6, with Joint J2 contributing to scapular elevation as needed.

**Shoulder Horizontal Abduction** The motion is performed in the horizontal plane. Once 90 *deg* of horizontal abduction is reached, a scapular protraction coupling involving J1 and J3 is activated to ensure a physiological pattern. The possible range of motion is from 0 *deg* to 130 *deg*.

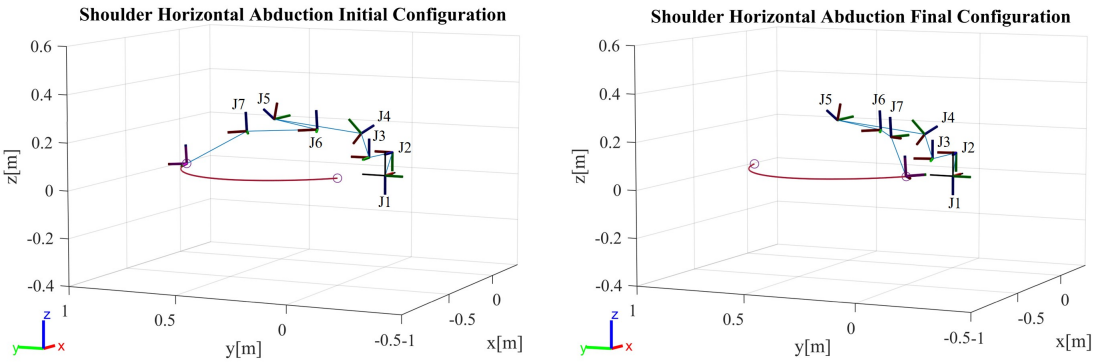



Fig. 5.22 Cartesian trajectory of the end-effector (positioned at wrist level) during shoulder horizontal abduction at the maximum range of motion (ROM). The movement occurs on the horizontal plane and is primarily guided by Joint J6, with J1 and J3 contributing to scapular protraction as needed.

**Internal-External Rotation** This movement requires the synergistic rotation of J4, J5, and J6. In this case, J5 is the leading joint, with J4 and J6 coupled through a polynomial relation. The exercise is designed so that the overall rotation of the arm is performed around the humeral axis. The possible range of motion spans from $-54$ *deg* of external rotation to 54 *deg* of internal rotation.

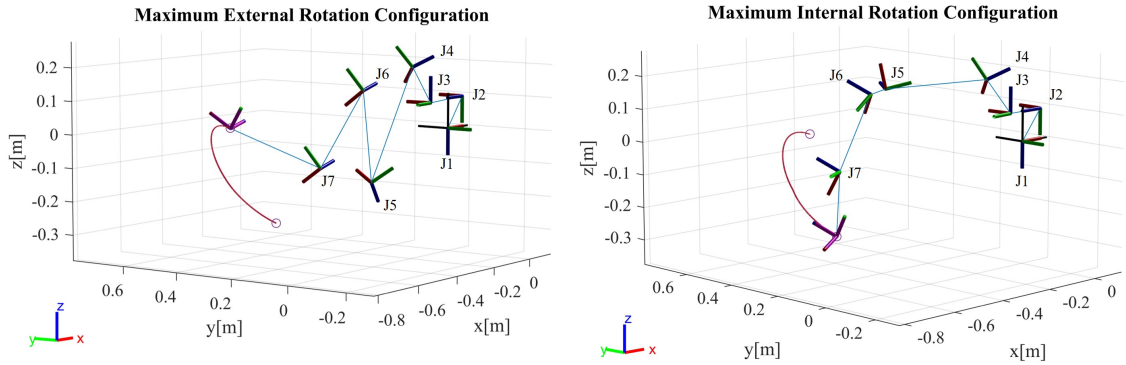



Fig. 5.23 Cartesian trajectory showing the position of the end-effector (positioned at wrist level) at the maximum internal and external rotation configurations. The movement is guided by Joint J5, with J4 and J6 coupled to it.

**Shoulder Flexion** The movement is commanded by Joint 6 (J6), but to remain within the selected flexion plane, a combined motion of the other joints is required, specifically J4 and J5. Their trajectories are coupled through a polynomial relation, computed using the Mechanism tool in CREO PTC. Once 90 *deg* of flexion is achieved, J2 initiates scapular elevation, following a coupling with the shoulder flexion angle (J6 angle). The possible range of motion is from $-20$ *deg* to 180 *deg*.

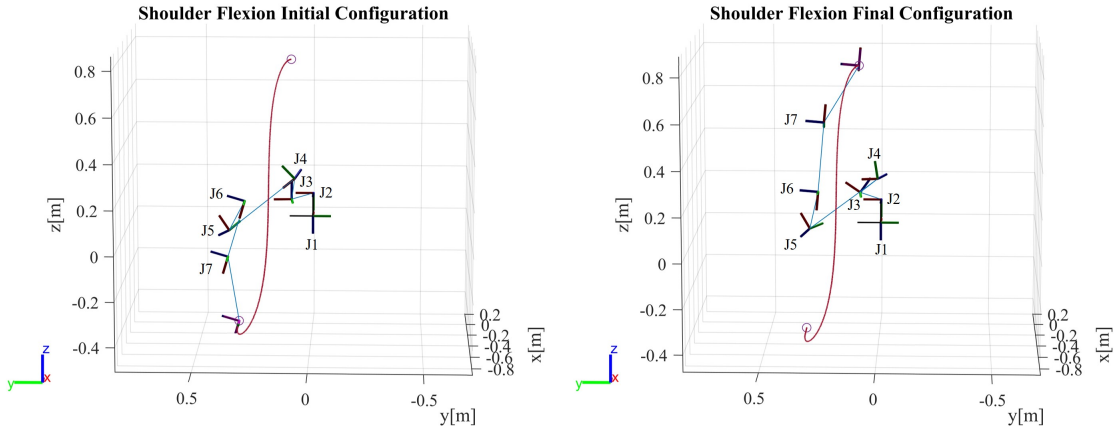



Fig. 5.24 Cartesian trajectory of the end-effector (positioned at wrist level) during the performance of a flexion-extension at the maximum range of motion (ROM). To ensure subject comfort in the starting position, the trajectory begins in an abducted configuration before transitioning to the sagittal plane for the exercise. The movement involves Joint J6, with J4 and J5 coupled to it, and Joint J2, which facilitates scapular elevation coupling.

### Assist As Needed

This mode exploits an impedance control (closed loop torque control with position feedback) with a spring-damper model, the user can deviate from the target trajectory but a recall force guides him/her along the correct path with variable levels of assistance. The impedance filter receives as target positions the ones of the kinematic exercises trajectories. Different assistance levels can be selected, those are characterized by the following virtual stiffness and damper parameters: low assistance ($k_v = 4\ Nm/rad$, $\beta_v = 0.4\ Nm \cdot s/rad$), medium assistance ($k_v = 5.5\ Nm/rad$, $\beta_v = 0.6\ Nm \cdot s/rad$) and high assistance ($k_v = 15.5\ Nm/rad$, $\beta_v = 1.2\ Nm \cdot s/rad$). Parameters have been empirically tuned.

### Time independent AAN

The design of this control strategy integrates Cartesian-space assistance, joint-level impedance (to optimize torque management), and gravity and friction compensation to ensure seamless

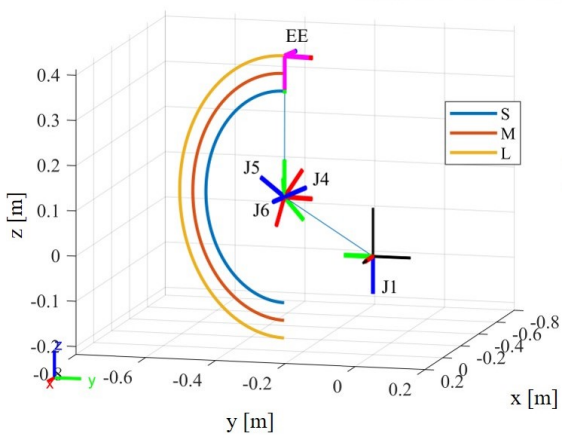



Fig. 5.25 Shoulder flexion paths are defined in the sagittal plane within Cartesian space, with varying link sizes (S, M, L) to accommodate different user anthropometries. Joint J1 aligns with the fixed base and focuses on scapular motion, while J4, J5, and J6 represent the glenohumeral joints, enabling diverse shoulder movements. The end-effector (EE) is positioned at elbow level to accurately replicate the desired motion.

exoskeleton movement, providing a transparent and intuitive user experience. The proposed control system aims to help patients understand and follow the correct path through feedback delivered at the end-effector.

This assistance is offered within a tunnel of variable diameter centred on the reference path, allowing for customizable user support based on the user's current position and adapting to their physiological needs. The proposed method involves the following steps:

The proposed method involves the following steps: (I) defining a reference path for the end-effector and approximating it with a parameterized curve; (II) identifying the tunnel where assistance is provided; (III) computing the actual position of the end-effector by leveraging direct kinematics; (IV) determining the minimum distance point on the reference path concerning the current end-effector position; (V) computing the assistive contribution at the end-effector; (VI) implementing joint-level impedance and computing torque contributions for gravity and friction compensations.

**Reference paths** The proposed reference trajectory for this preliminary study focuses on shoulder flexion, with scapular and rotational movements constrained to achieve pure shoulder flexion within a defined plane (30 degrees open relative to the sagittal plane). The trajectories were designed considering variable link lengths based on user anthropometry, representing the 1st (S), 50th (M), and 99th (L) male percentiles, as illustrated in Figure 5.25.

**Path parametrization and tunnel** A conic curve approximation was used to parametrize the reference path, and the resulting fit is represented by a degenerate ellipse, which in this case, simplifies to a circumference.

Considering the parametric equations of the ellipse in polar form, rotated by an angle $\Phi$:

$$\begin{aligned} x_r &= x_0 + a \cdot \cos(\varphi) \\ y_r &= y_0 + b \cdot \sin(\varphi) \end{aligned} \tag{5.8}$$

$$R = \begin{bmatrix} \cos(\Phi) & \sin(\Phi) \\ -\sin(\Phi) & \cos(\Phi) \end{bmatrix} \tag{5.9}$$

Where $(x_0, y_0)$ and $(x_r, y_r)$ represent the coordinates of the centre of the ellipse and points on the ellipse, respectively, $a$ is the semi-major axis, and $b$ is the semi-minor axis. The parameter $\varphi \in [0, 2\pi]$ is the angle used to parametrize the ellipse. After parametrization, the resulting set of equations (Equation 5.8) was multiplied by the rotation matrix $R$ (Equation 5.9) to obtain the correct orientation of the ellipse. The approximated curves are represented with the parameters provided in Table 5.5.

| $a[m]$ | $b[m]$ | $\Phi[rad]$ | $x_0[m]$ | $y_0[m]$ | $z_0[m]$ |
|---|---|---|---|---|---|
| 0.3096 | 0.3096 | 0.0 | - | -0.3059 | 0.0946 |

Table 5.5 Ellipse Parameters for FloatEVO flexion path.

The proposed control system focuses on developing an assistive field to guide users through simple tasks, such as shoulder flexion, which is essential for many ADLs. FloatEVO's selected joints (J1, J4, J5, J6) can navigate the Cartesian space across three coordinates. A control tunnel with a variable diameter was designed to reproduce shoulder flexion. Inside, movement assistance is provided, using a push in the direction of the tunnel's main axis. The design decision was to offer assistance within a wider tunnel at the trajectory extremes while narrowing it to around 90 degrees. This ensures that the feedback provided to the user (in the form of a push) encourages them to maintain movement on the predefined sagittal plane, particularly at 90 degrees where the load force is at its maximum. As shown in Figure 5.26a the tunnel diameter $d_t$ varies within a specified range, from 0.10 $m$ to 0.30 $m$, following the relationship: $d_t = (0.1 + 0.2 \cdot |sin(\varphi)|)[m]$.

**Mapping of actual position on the reference path** Once the actual end-effector pose is known, it is proposed to map its coordinates onto the reference path. The nearest point to the actual position on the reference path is assumed to correspond to the intersection between the reference path (ellipse) and the line passing through both the ellipse centre and the actual position, as illustrated in

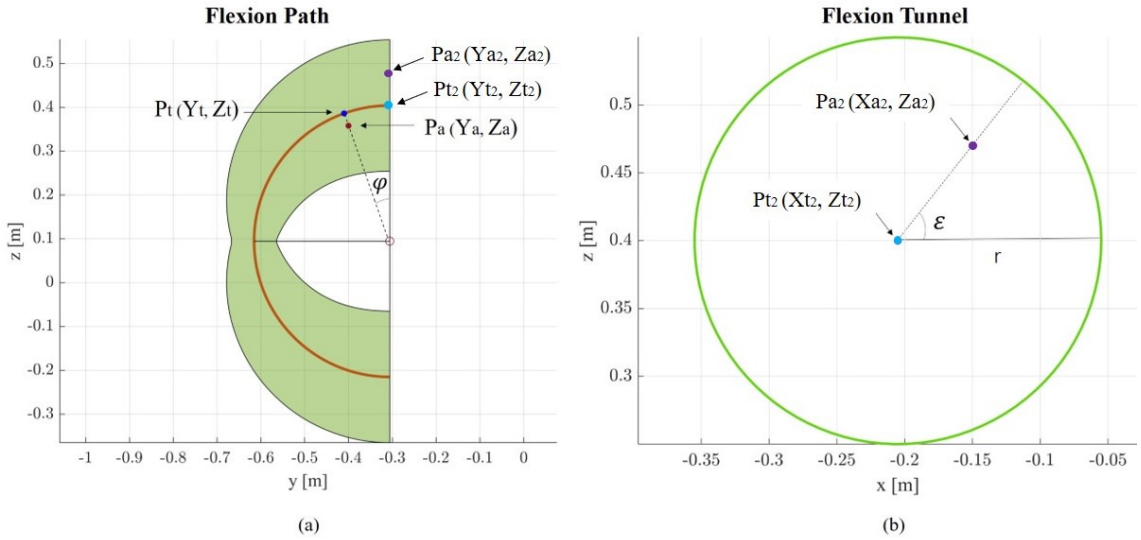



Fig. 5.26 Reference end-effector trajectories (obtained with ellipse parametrization) for FloatEVO, specifically: (a) FloatEVO tunnel section (green) on the YZ plane of the flexion path (red). (b) Tunnel section at maximum diameter for assistance (case of 180 *deg* of flexion), with the reference trajectory point (*t2*) in light blue. The violet marker denotes the current end-effector position (*a2*). Assistance is provided only inside the tunnel based on the Euclidean norm between the coordinates.

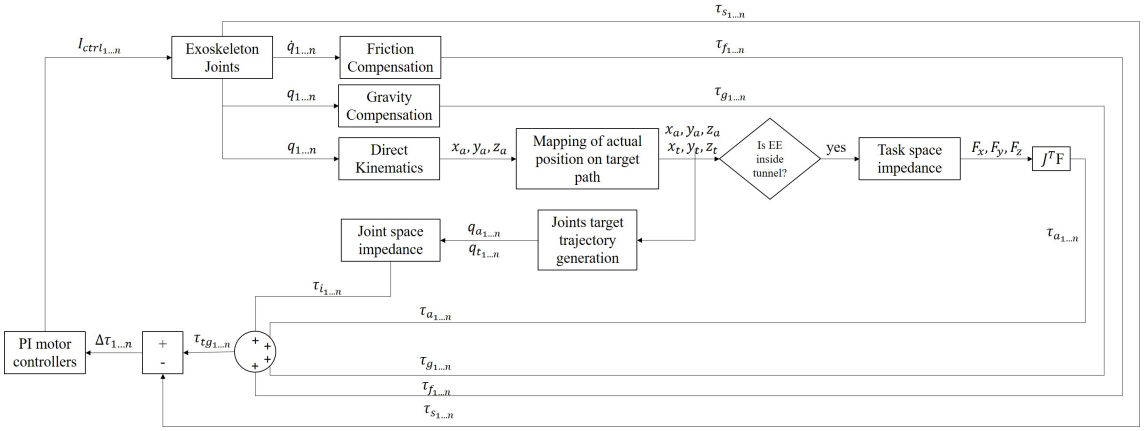



Fig. 5.27 Control algorithm for implementing time-independent assist-as-needed mode in the task space: parameters such as joint position, velocity, and estimated torque contribute to gravity, friction, and assistance compensations. Forward kinematics calculates the end-effector pose, which is mapped onto the reference trajectory to determine assistance (force in task space, translated to joint torque via the transposed Jacobian). Joint-level impedance can be implemented to provide additional guidance. The contributions are summed up following the superposition principle, yielding the reference control torque.

Figure 5.26a. The same level of assistance will be provided for all actual points lying on this line, following the direction of the reference path.

Once the corresponding point on the reference path $(X_t, Z_t)$ is defined, it is necessary to determine whether assistance should be provided. A Euclidean norm is computed to verify that the distance between the end-effector $(X_a, Z_a)$ and the centre of the tunnel $(X_t, Z_t)$ is smaller than the tunnel radius $r$, as shown in Figure 5.26b.

**Task space impedance** Task space impedance enables the design of interaction forces applied at the end-effector level by utilizing a spring-damper dynamic model. In this context, the end-effector is considered to be at the elbow level. The stiffness and damping matrices have been tuned to apply a force of $\pm 3\,\mathrm{N}$ at the exoskeleton end-effector when at the maximum distance (i.e., the tunnel radius). For the showcase implementation, the problem has been simplified by considering only the diagonal elements of the stiffness and damping matrices.

The task space forces can be computed as:

$$\begin{bmatrix} F_x \\ F_y \\ F_z \end{bmatrix} = K \cdot \begin{bmatrix} \Delta x \\ \Delta y \\ \Delta z \end{bmatrix} + B \cdot \begin{bmatrix} \dot{x} \\ \dot{y} \\ \dot{z} \end{bmatrix} \tag{5.10}$$

where,

$$K = \begin{bmatrix} k_{xx} & 0 & 0 \\ 0 & k_{yy} & 0 \\ 0 & 0 & k_{zz} \end{bmatrix} \textit{ and } B = \begin{bmatrix} \beta_{xx} & 0 & 0 \\ 0 & \beta_{yy} & 0 \\ 0 & 0 & \beta_{zz} \end{bmatrix} \tag{5.11}$$

are stiffness and damping matrices, $\Delta x, \Delta y, \Delta z$ are the difference between coordinates of the next target on the reference path and the actual ones, and $\dot{x}, \dot{y}, \dot{z}$ are the end-effector actual speed components. The forces computed in task space can be translated into joint torques by leveraging the Jacobian transpose. In a system with $n$ joints and $m$ degrees of freedom, this relationship can be expressed as follows:

$$\tau_{a_{(n,1)}} = J^T_{(n,m)} \cdot F_{(m,1)} \tag{5.12}$$

**Joint space impedance** Joint space impedance can be computed to introduce an additional corrective effect on the end-effector position relative to a desired reference. By using inverse kinematics, both the actual joint configuration $q_{a_{(1\ldots n)}}$ and the corresponding joint configuration based on the reference path point $q_{t_{(1\ldots n)}}$ can be determined.

To avoid the complexity of solving the inverse kinematics problem and computing the Jacobian inverse, the joint reference position can be set arbitrarily within a reasonable range around the current joint position. This approach allows for the implementation of a low stiffness impedance, which encourages the subject to maintain the exoskeleton joints close to these reference values.

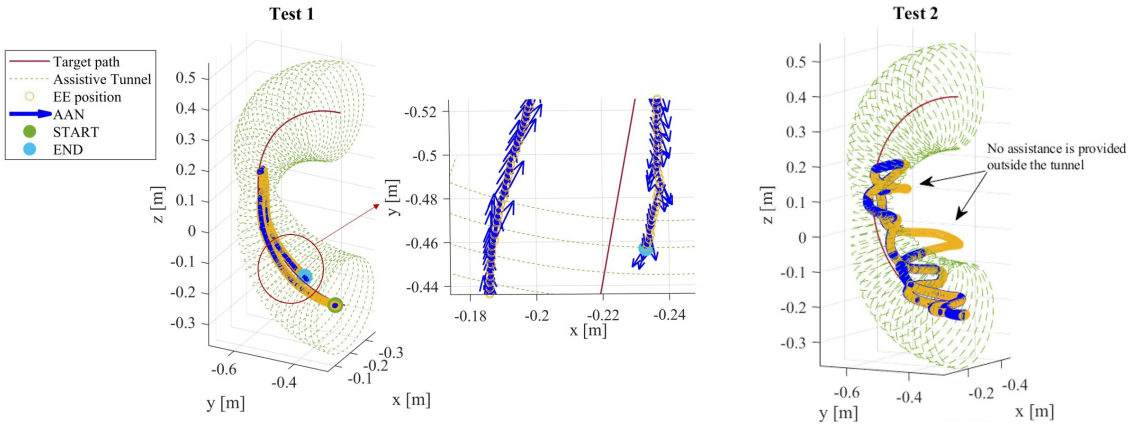



Fig. 5.28 Results from the experimental test on the upper limb exoskeleton are presented. Blue and yellow data are collected In Test1, a flexion was executed while staying inside the tunnel, depicting the reference (blue) and actual (yellow) paths. Assist-as-needed (AAN) forces are applied at the end effector, aiding in the movement performance in both directions (flexion-extension). Test 2 demonstrates that AAN is exclusively applied inside the tunnel.

By imposing stiffness $k_j$ and damping $\beta_j$ coefficients, joint-level impedance control can be implemented as:

$$\tau_{i_{(1\ldots n)}} = k_j \cdot \Delta q_{(1\ldots n)} + \beta_j \cdot \dot{q}_{(1\ldots n)} \tag{5.13}$$

**Superposition principle to compute reference torques** The low-level control strategy employs a closed-loop Proportional-Integral (PI) torque controller. Torque feedback is obtained from the torque sensors in the SEA joints. The reference torque control signal is composed of: task space-based assistance torque $\tau_a$, joint level impedance $\tau_i$, gravity torque $\tau_g$, and friction compensation $\tau_f$. The resulting reference torque required at each joint can be computed as:

$$\tau_{tg_{(1\ldots n)}} = \tau_{a_{(1\ldots n)}} + \tau_{i_{(1\ldots n)}} + \tau_{g_{(1\ldots n)}} + \tau_{f_{(1\ldots n)}} \tag{5.14}$$

**Experimental control validation** The exoskeleton was operated with the activated Assist-As-Need strategy. The results are presented for two experiments: Test 1, where flexion was performed within the tunnel, and Test 2, where the end effector was moved inside and outside the tunnel to assess AAN contributions. In Figure 5.28, the blue line represents the reference path, and the green area denotes the implemented assistive tunnel. The yellow trajectory illustrates the end-effector's path during the test, with (for Test 1) start and end points of flexion movements from -20 to 130 degrees. AAN support activates only if the end effector stays within the predefined tunnel. Figure 5.29 displays the computed end-effector force components and corresponding joint torques.

The results demonstrate how the proposed algorithm correctly identifies the position of the end effector relative to the virtual tunnel (Figure 5.28) and calculates the corresponding AAN contribution (Figure 5.29). For these preliminary results, the same combinations of k and $\beta$ were adopted for the three force components ($k_{xx} = k_{yy} = k_{zz} = 50\ N/m$, $\beta_{xx} = \beta_{yy} = \beta_{zz} = 3\ N \cdot s/m$). The assistance correctly provides support along the direction of movement. During Test 1 (Figure 5.28 Test 1), the main force component is Fz, indicating that the movement direction is indeed flexion. The resulting predominant torque is at joint J6, which, in the proposed kinematics, has the greatest influence on flexion. The contribution to other joints is justified because the movement does not perfectly follow the reference path plane, resulting in minor components along x and y, affecting J1, J4, and J5. During Test 2 (Figure 5.28 Test 2), the end effector was moved inside and outside the tunnel, especially using the scapular joint. In this case, the main force component is Fx, and the highest torque is on J1. From this behaviour, it is evident how the force components along x and y could also play a corrective role, counteracting the exit from the tunnel and preventing the user from deviating too far from the reference path. In subsequent work, the Fx and Fy components could be tuned to oppose movements aiming outside the tunnel. A potential improvement involves introducing the capability to personalize human-robot interaction (HRI) by implementing variable,

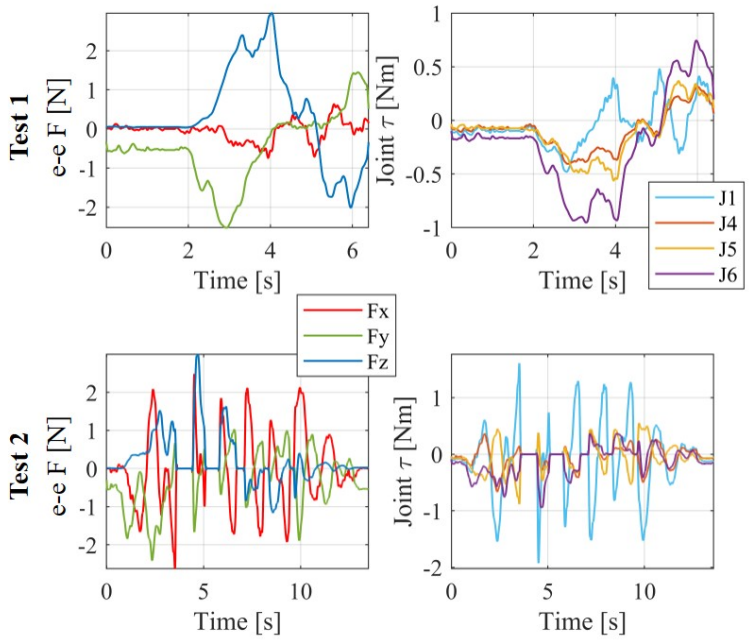



Fig. 5.29 The assistance was designed to provide a torque contribution of approximately ±2 Nm at the joint level. The figure shows at the left the x, y, and z components of the force that need to be applied at the end-effector to deliver the intended assistance. On the right, the computed joint torques necessary to achieve this force are displayed.

path-phase-dependent assistance through the modulation of impedance in Cartesian space. For instance, the control could provide more assistance during flexion i.e., when the arm is forwardly extended, to help overcome the gravitational load. Further developments include integrating the assistive effect within the tunnel with an external corrective force. This external correction aims to guide the end-effector back into the predefined tunnel in case of deviation from the desired path.

### Resistive Control

Resistive control was preliminarily explored as a method to support muscle strengthening, particularly beneficial in the final stages of rehabilitation. The controller was built upon the existing impedance control framework, which maintains a low level of impedance to ensure compliance with human interaction. This approach acts as a safety filter, mitigating the impact of sudden movements that could pose a risk to the user.

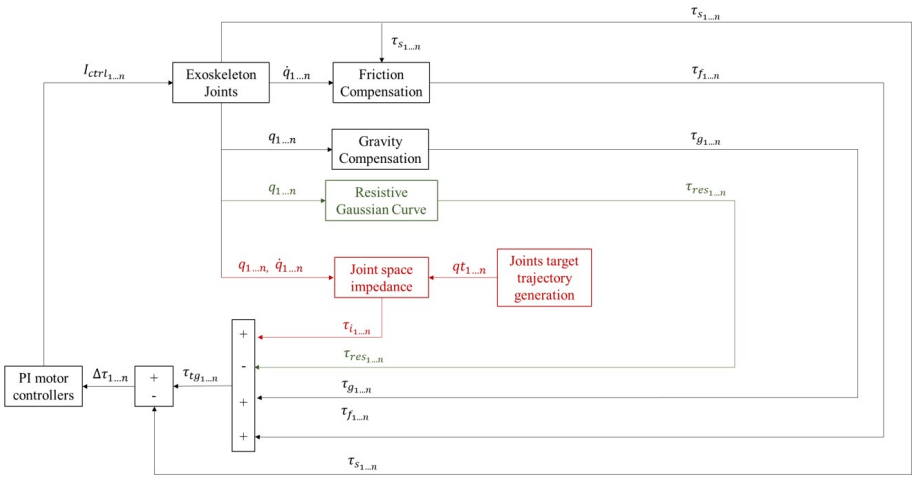



Fig. 5.30 The resistive control leverages the presence of a Series Elastic Actuator (SEA) and is implemented using a closed-loop torque control approach. Once the target trajectory for the desired exercise is computed, a low-impedance filter is applied to ensure compliance with the user's voluntary motion. The resistive contribution, which acts as a resistance to the motion, is calculated based on the actual position of the joint leading the movement. This contribution is derived using a Gaussian function to model the resistance profile. The resistive torque is subtracted from the control signal, effectively opposing voluntary motion while maintaining smooth interaction. Friction is compensated using a feedforward term, which is calculated with an observer proposed by Le Tien et al.

The control scheme, illustrated in Figure 5.30, incorporates a resistive contribution based on the position of the movement-leading joint. A Gaussian profile is employed to model the resistance, allowing for user-defined parameters such as the location of the peak resistance, its intensity, and the amplitude of the Gaussian curve. This design enables precise customization to meet specific training requirements.

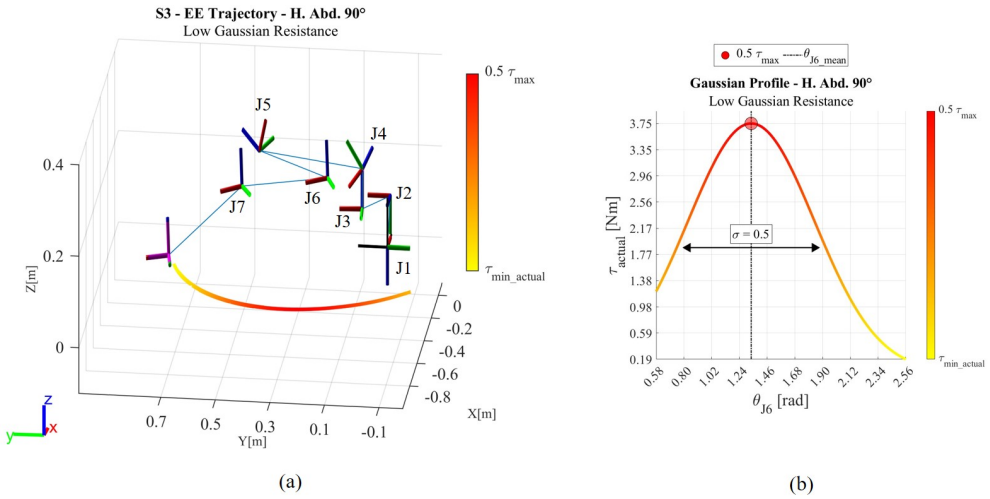



Fig. 5.31 (a) A Cartesian representation of the end-effector trajectory and the resistance applied is presented, as it is directly correlated to the motion of Joint 6 ($J_6$), which is responsible for horizontal abduction. All other joints remain stationary once the starting position is reached and are not involved in the motion. The colour map illustrates the variations in resistive contribution, varying from the initial state shown to the maximum range of motion achieved. The starting configuration shown in (a) corresponds to the joint angle $\theta_{J_6} = 2.56$ rad, as depicted in (b). The Gaussian profile was designed for a low resistance level, modulated with a factor of 0.5 relative to the maximum achievable torque of 7.5 Nm, which is reached at the highest selectable resistance level.

The resistive torque contribution applied at the joint level can be calculated as follows:

$$\tau_{resistive}(q) = \frac{1}{\sigma\sqrt{2\pi}} \exp\left(-\frac{(q-q_{mean})^2}{2\sigma^2}\right) \tag{5.15}$$

Where $q$ represents the joint position, $q_{\text{mean}}$ denotes the mean of the distribution (i.e., the joint angle corresponding to the peak of the Gaussian curve), and $\sigma$ is the standard deviation. For instance, a higher value of $\sigma$ results in a broader Gaussian bell shape.

The Gaussian profile offers an additional advantage: it gradually introduces resistance after the movement begins, preventing sudden forces from being applied to the user upon activation of the control.

As shown in Figure 5.31, during a horizontal abduction trajectory, the resistance levels were dynamically modulated based on the leading joint trajectory. In this case, resistance was directly correlated with the motion of Joint 6 (J6), which determined the resistive behaviour.

This preliminary implementation demonstrated the feasibility of deploying resistive controllers using the custom SEAs. It also enabled the exploration of various shapes and intensities of the applied resistive torque.

# Chapter 6

# Design of an Upper Body Robotic Mobilizer for Neurological Disorders

To broaden FloatEVO's capabilities by incorporating trunk rehabilitation and transforming it into a comprehensive upper-body rehabilitation system, this study presents the development of a prototype for trunk mobilization. The proposed prototype enhances the existing passive multi-articulated arm that supports the exoskeleton by introducing structural modifications and actuation.

In this chapter, the conceptualisation of a new paradigm for trunk rehabilitation is proposed, going outside the state-of-the-art concept that mainly proposes the adoption of motorised seats and platforms. The final developed prototype has been constructed, and different control strategies have been implemented and tested using a real-time rapid control prototyping approach.

This thesis proposes a robotic mobiliser designed to provide robust and stable rehabilitation of the core muscles through direct trunk mobilisation using a specially modified orthopaedic corset. Unlike other commercial solutions that indirectly induce trunk motion by using sensorized seats to generate pelvic movement, this alternative approach aims to improve trunk mobility and stability by directly mobilising the upper body.

In future developments, this prototype could be integrated with FloatEVO, turning it into a fully comprehensive device capable of assisting clinicians throughout every stage of upper-body rehabilitation, from trunk recovery to the shoulder complex.

## 6.1 Device design

The ideation of the proposed design stemmed from close collaboration between researchers, engineers, and clinicians, following a user-centered design approach. The mechanical and control

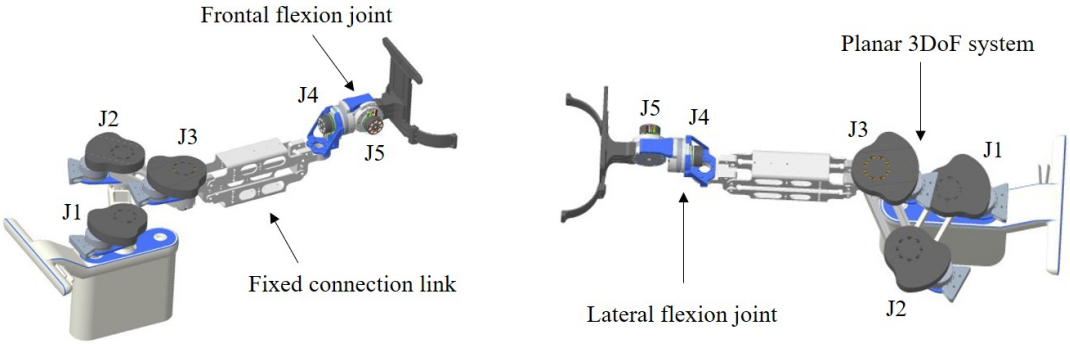



Fig. 6.1 The mechanical design of the trunk device features a planar system composed of J1, J2, and J3, which enables the exploration of a wide working area. When combined with the rotations of J4 and J5, the system facilitates rotational and flexion movements.

design requirements were gathered from feedback during interactions with clinicians. The primary goal was to enable patient rehabilitation using a robotic device from the early acute phases, when trunk proprioception and balance have yet to be restored, providing clinicians with a valuable tool to mobilise the trunk and stimulate the recovery of upper body control.

### 6.1.1 Kinematics

The device is inspired by the passive multi-jointed arm supporting the Float exoskeleton [57]. Compared to the Float multi-jointed arm, the new design incorporates actuation via Series Elastic Actuators (SEAs) for the planar kinematics. Additionally, two more SEA joints are added at the end of the kinematic chain to enable frontal and lateral trunk flexion and a corset to support and interface with the patient's trunk. Unlike in the Float system, where the central part of the arm was adjustable in height, it is now a fixed connection link. The proposed system is designed with five actuated degrees of freedom, as shown in Figure 6.1. Joints J1, J2, and J3 enable planar movement, which is particularly active during trunk rotation. These joints also work in synergy with J4, primarily involved in lateral flexion, and J5, responsible for trunk flexion in the frontal plane.

The kinematic of the system follows the Denavit-Hartenberg convention and can be described as reported in Table 6.1; the parameters have been identified as shown in Figure 6.2. The joints' ranges of motion are reported in Table 6.2; those are defined with respect to the zero-configuration shown in Figure 6.2.

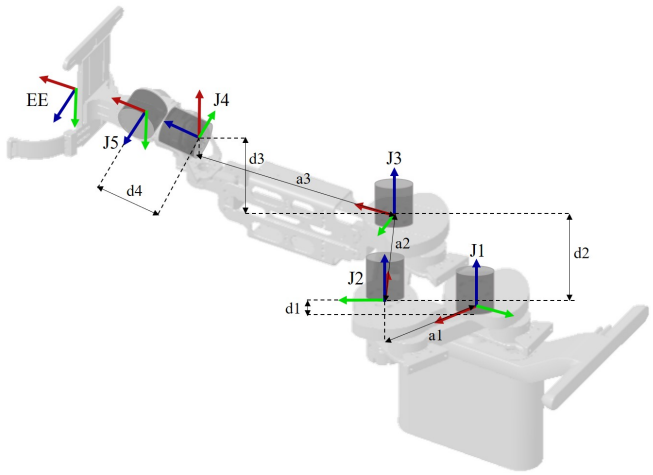



Fig. 6.2 Graphical representation of the Denavit-Hartenberg convention parameters, as defined in Table 6.1. The parameters $a$ and $d$ correspond to translations along the x- and z-axes of the current frame, respectively. The depicted configuration represents the zero-rotation reference for each joint. Consequently, the range of motion (ROM) values in Table 6.2 should be considered relative to this reference.

| $Link_{id}$ | $a\ [m]$ | $\alpha\ [rad]$ | $d\ [m]$ | $\theta_i$ |
|---|---|---|---|---|
| $l_1$ | 0.24 | 0 | 0.075 | $\theta_1$ |
| $l_2$ | 0.24 | 0 | 0.033 | $\theta_2$ |
| $l_3$ | 0.533 | $\pi/2$ | 0.082 | $\theta_3$ |
| $l_4$ | 0 | $\pi/2$ | 0.101 | $\theta_4$ |

Table 6.1 Trunk device Denavit-Hartenberg kinematic parameters.

| $Joint_{id}$ | $\theta_{min}\ [rad]$ | $\theta_{max}\ [rad]$ |
|---|---|---|
| $J1$ | $-67 \cdot \frac{\pi}{180}$ | $30 \cdot \frac{\pi}{180}$ |
| $J2$ | $-20 \cdot \frac{\pi}{180}$ | $65 \cdot \frac{\pi}{180}$ |
| $J3$ | $-82 \cdot \frac{\pi}{180}$ | $41 \cdot \frac{\pi}{180}$ |
| $J4$ | $-20 \cdot \frac{\pi}{180}$ | $20 \cdot \frac{\pi}{180}$ |
| $J5$ | $-10 \cdot \frac{\pi}{180}$ | $30 \cdot \frac{\pi}{180}$ |

Table 6.2 Ranges of motion for each joint limited by its mechanical end of travel.

Following clinicians' requests, the links connecting the different joints and the actuation system have been dimensioned to guarantee the frontal and lateral flexion ranges of motion reported in Table 6.2 (J4, J5). Specifically, the system allows for $\pm 20$ *deg* of lateral flexion in the frontal plane, 10 *deg* of extension and 30 *deg* of flexion in the sagittal plane.

### 6.1.2 Actuation

All the joints are equipped with torque sensors. Series Elastic Actuators (SEAs) have been adopted in the design to implement control strategies that account for human interaction in the loop.

The joints are actuated using EC45 Maxon brushless motor for J1-J2-J3 and EC60 for J4-J5. They are combined with a Harmonic drive with a reduction ratio of 1:100 and 1:120, respectively. Aksim-2 absolute encoders are adopted to measure the spring displacement and translate it into a torque measurement. Since 19-bit encoders are adopted, the sensor torque resolution ranges from 0.011 $Nm$ to 0.018 $Nm$, depending on the stiffness of the compliant element. The last element in the joints assembly is the custom spring; two different spring designs have been incorporated into the joints: a titanium spiral spring (SPTF1P) for J1-J2-J3 and a steel spiral (SPS1P) spring for J4-J5. They have been characterised and presented in Chapter 4. The torque estimation can be obtained by exploiting Hooke's law (Equation 6.6). The values of the spring stiffness $k$ and the linear model intercept $\Delta_{\tau_{lm}}$ obtained from bench characterisation of the joints are reported in Table 6.3.

| | J1 | J2 | J3 | J4 | J5 |
|---|---|---|---|---|---|
| $k\ [Nm/rad]$ | 878 | 1017 | 920 | 1528 | 1517 |
| $\Delta\tau_{lm}$ [Nm] | 0.056 | 0.451 | 0.047 | 0.306 | 2.594 |
| Spring type | SPTF1P | SPTF1P | SPTF1P | SPS1P | SPS1P |

Table 6.3 Value of the spring stiffness $k$, and linear intercept $\Delta_{\tau_{lm}}$ of the linear model of the spring inside the joints.

### 6.1.3 System sizing

Aligning with traditional therapeutic approaches, the device has been designed to mobilise a seated patient. The system has been dimensioned to accommodate a 95th-percentile male to guarantee upper body weight support.

The device configurations corresponding to the maximum joint loads were analysed using the Mechanism tool provided by CREO PTC CAD software. These configurations maximise leverage relative to the joints' rotational axes, specifically during full-frontal flexion (30 $deg$) and full lateral flexion (20 $deg$), as shown in Figure 6.3.

The load analysis was conducted using the following settings: the simulation was performed for a 95th percentile male (body weight: 96.78 kg, upper body weight: 48.39 kg). All joint rotations were restricted, and only the effects of gravitational force were considered. Table 6.4 summarises the resulting required joints maximum torques.

To achieve these maximum target torques, for the joints incorporating the EC45 motors, an additional reduction stage with a ratio of $1:2.88$ was implemented for the joints composing

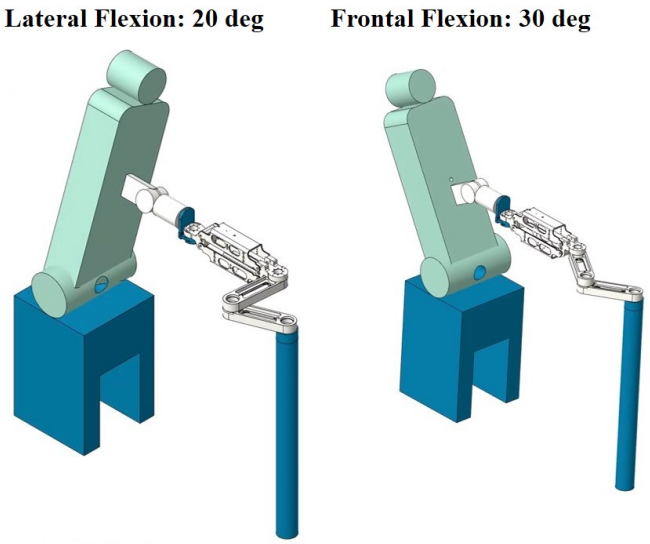



Fig. 6.3 Configurations adopted for the load static analysis.

| | $\tau_{J1}$ [Nm] | $\tau_{J2}$ [Nm] | $\tau_{J3}$ [Nm] | $\tau_{J4}$ [Nm] | $\tau_{J5}$ [Nm] |
|---|---|---|---|---|---|
| Lateral Flexion | -15.56 | 15.93 | **-18.25** | 0.00 | 0.00 |
| Frontal Flexion | -8.82 | **25.25** | 8.06 | -0.08 | 0.00 |

Table 6.4 Torque values, simulated in CREO PTC Mechanism analysis, for maximum lateral and frontal flexion across joints.

the planar complex. This design choice was guided by the following considerations: movement simulations were performed in CREO PTC in agreement with clinicians' suggestions, and the maximum desired speed for exercise performance was set to 6.66 rad/s (40 deg/s). The SEAs (Series Elastic Actuators) used in the joints embed a harmonic drive with a 1 : 100 reduction ratio, resulting in a fast shaft speed of:

$$\omega_{\text{fast}} = rr \cdot \omega_{\text{slow}} = 100 \cdot 6.66 = 666 \text{ rpm} \tag{6.1}$$

From the harmonic drive data sheet, the maximum average input speed is given as $\omega_{HD_{\text{avgMax}}} = 3500$ rpm. To meet this limitation, the maximum allowable second-stage reduction ratio can be computed as follows:

$$rr_{\text{secondStage}} = \frac{\omega_{HD_{\text{avgMax}}}}{\omega_{\text{fast}}} = \frac{3500}{666} = 5.25 \tag{6.2}$$

The maximum slow shaft torque deliverable by the SEA is the product of the motor's nominal torque and the harmonic drive reduction ratio:

$$\tau_{SEA_{\text{max}}} = \tau_{nomEC45} \cdot rr = 0.167 \cdot 100 = 16.7 \text{ Nm} \tag{6.3}$$

Respecting the datasheet limit of 27 Nm for the harmonic drive output torque. Finally, considering space constraints and assembly requirements, a new reduction stage was implemented using a geared mechanism with two gears (18 and 52 teeth, respectively), resulting in:

$$rr_{\text{secondStage}} = \frac{52}{18} = 2.88 \tag{6.4}$$

This design allows for the delivery of a maximum output torque of:

$$\tau_{\text{max}} = \tau_{SEA_{\text{max}}} \cdot rr_{\text{secondStage}} = 16.7 \cdot 2.88 = 48.09 \text{ Nm} \tag{6.5}$$

This is sufficient to support the computed maximum loads presented in Table 6.4, also ensuring a safety coefficient 1.9.

### 6.1.4 Electronic setup

The prototype has been connected to a Speedgoat baseline real-time target machine [1]. Five EPOS boards were programmed to control the motors and communicate with the target machine via CAN. Additionally, a custom logic board was used for each motor to read data from the Aksim-2 encoders on both sides of the SEA torsional spring. These components are connected to the Speedgoat via four CAN lines and are powered by a 36 V supply. A separate 12 V line provides power to the logic boards' CAN connections.

### 6.1.5 Human-Robotic Device interface

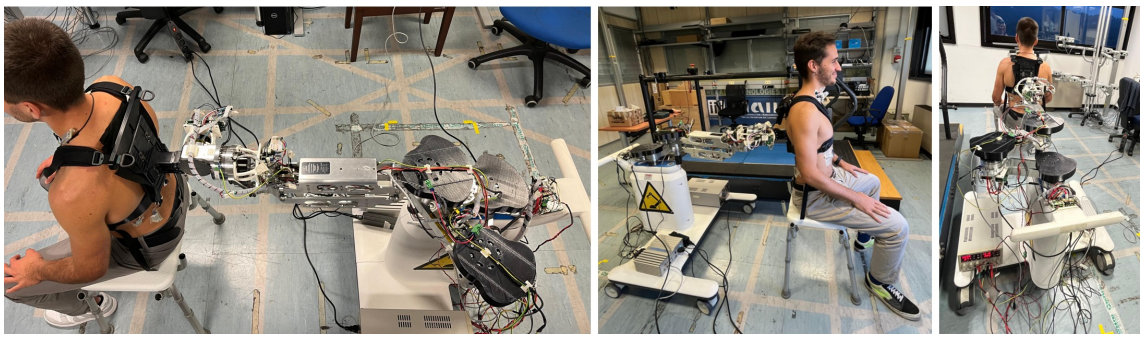


Fig. 6.4 The prototype is shown during a preliminary usability test with two subjects. It is possible to notice the corset used to interface the upper body with the device's end effector, which facilitates trunk mobilisation for performing the desired exercises.

An orthopaedic corset was incorporated to maintain the patient in the correct position and to support their weight. A custom interface was designed to secure the corset and attach it to the

[1] https://www.speedgoat.com/products-services/real-time-target-machines/baseline-real-time-target-machine

device's end effector (Figure 6.4). This interface is adjustable in width and height to accommodate different body sizes. It offers a height adjustment range from 20 mm to 100 mm, measured from the centre of the corset, and a side brace width adjustment range from 285 mm to 375 mm, ensuring compatibility with various body percentiles.

## 6.2 Control design

The control system follows the RCP structure proposed in the previous chapter of this dissertation. The model has been modified and adapted for the new device, developing target control strategies for the following use cases: (I) Pusher Syndrome Use Case: Fixed target impedance control to restore posture proprioception. (II) Spinal Cord Injury Use Case: Resistive control to train muscle strength. (III) Post-Stroke Use Case: Retraining of elementary movements.

The control model was developed in the MATLAB 2022b Simulink environment. The upper layer of the model consists of three units: input signal reception, signal processing, and control signal generation, as well as output signal interfacing. State machines manage the different control modes. The processing block performs the following tasks:

- SEA torque estimation.
- Gravity torque computation and compensation - using MATLAB robotic toolbox.
- Friction torque computation and compensation - following the Algorithm 10 tested in RCP approach and presented in Chapter 5.
- Trajectory generation, allowing for selecting different exercises with adjustable repetition numbers, amplitude, and duration.
- Computation of the target control torque signal, enabling the selection of different control models.

The Simulink model communicates with a custom graphical user interface (GUI) developed using the MATLAB App Designer tool. The GUI runs in real-time, along with the control model on the target machine, at a frequency of 500 Hz. From the GUI, users can select exercise characteristics and control modes. Specifically, the messages sent from the GUI to the control generation state machine include the selection of the exercise type and control mode, setting of the number of repetitions, movement amplitude target and exercise duration.

The GUI also receives signals from the hardware system, allowing for monitoring and debugging of the device's functionality. These signals include (I) motor status, (II) motor actual position, (III) Aksim-2 actual position, and (IV) SEA torque displayed for each joint.

Figure 6.5 shows the overall control scheme.

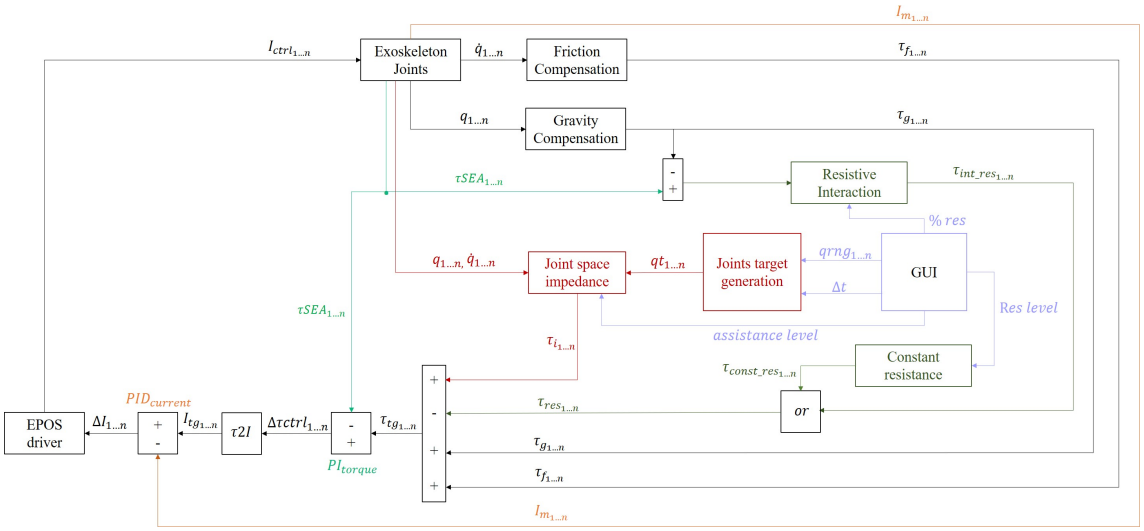



Fig. 6.5 The proposed torque control scheme operates as follows: the internal loop generates the target torque signal, which is compared with the SEA torque through a closed-loop sensor measurement (green). The control signal is converted to a current signal and managed by the PID controller (orange) of the EPOS driver boards. Gravity and friction compensation (in black) remain active in all modes. A state machine governs control modes and algorithms, with input from the GUI (in violet). The GUI facilitates trajectory generation for assistive mode, setting reference values for impedance and resistive reference values control. In constant resistance mode, a predefined joint-level resistance opposes motion. In "keep posture" mode, the impedance target aligns with the homing position, while in "against interaction" mode, each joint applies counterforces proportional to human-robot interaction forces.

### 6.2.1 SEA torque estimation

Thanks to incorporating SEAs, designing closed-loop control systems that account for human-robot interaction becomes feasible. Specifically, the torque sensed by the SEAs can be computed as:

$$\tau_{SEA} = ((\theta_{AKout} - \theta_{AKin}) - \Delta\theta_{AKoffset}) \cdot k + \Delta\tau_{lm} \tag{6.6}$$

Here, $\theta_{AKout}$, $\theta_{AKin}$, and $\Delta\theta_{AKoffset}$ represent, respectively, the angular displacement measured after the spring, the angular displacement measured before the spring, and the encoder offset of the assembly. Additionally, $\Delta\tau_{lm}$ denotes the intercept of the linear model, while $k$ corresponds to the stiffness of the spring.

### 6.2.2 Control modes

The following control modes have been implemented:

**Passive kinematic exercises** In position control mode, the device rigidly mobilises the user, guiding them through standard rehabilitative movements, such as frontal and lateral flexions. For this control mode, a trajectory generation algorithm has been implemented for the real-time generation of target positions. The exercise trajectories were initially generated by simulating the movements in CREO, from which joint angles at each time step were extracted. These trajectories were approximated using straight lines, except for the J2 trajectory during lateral flexion, which was approximated using a cosine function.

To allow customisation of the movement range ($q_{rng}$) and duration ($\Delta t$), the trajectories were integrated into the control framework using the following general formula:

$$q_{tg} = \frac{q_{rng}}{\Delta t} \cdot (t_{el}) + q_{start}$$

Where $t_{el}$ is the elapsed time from the beginning of the movement, and $q_{start}$ is the joint starting position (homing configuration). The computed trajectories for frontal and lateral trunk flexion are shown in Figure 6.6 and Figure 6.7. Figure 6.8 and Figure 6.9 showcase the device configurations at the maximum and minimum ROM for the desired trajectories.

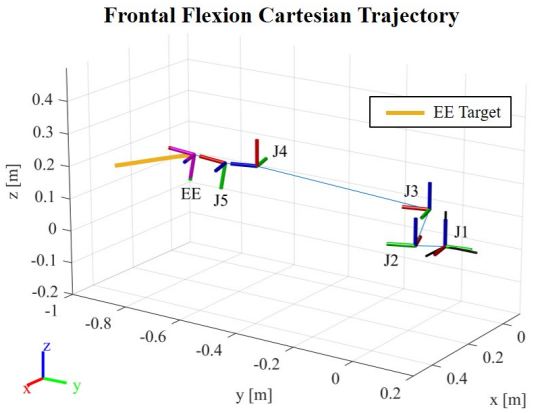



Fig. 6.6 Rigid body tree of the trunk device with the end effector trajectory (yellow) shown for the maximum range of movement in the sagittal plane (from $-10$ *deg* to 30 *deg* for extension-flexion).

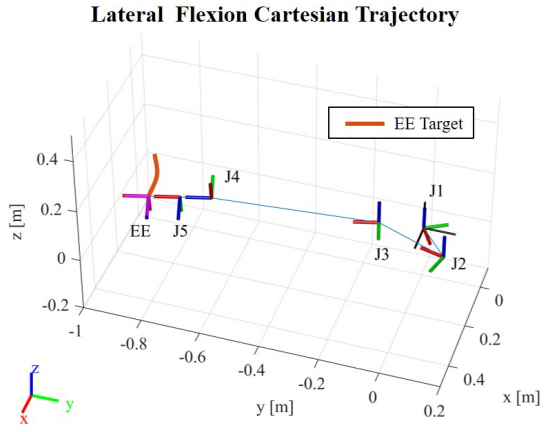



Fig. 6.7 A rigid body tree of the trunk device is shown, with the end effector trajectory (orange) for the maximum range of movement in the frontal plane (from $-20$ *deg* to 20 *deg* for lateral flexion).

**Assistive control and keep posture mode** In torque control mode, the same movements proposed in the passive kinematic mode can be performed gradually, actively involving the user in the movement. Three levels of assistance have been empirically tuned by modulating the impedance control's virtual stiffness and damping coefficients. Virtual impedance stiffness ($k_v$) and damper ($\beta_v$) parameters set for the different assistive levels are defined as follows: low assistance ($k_v =$

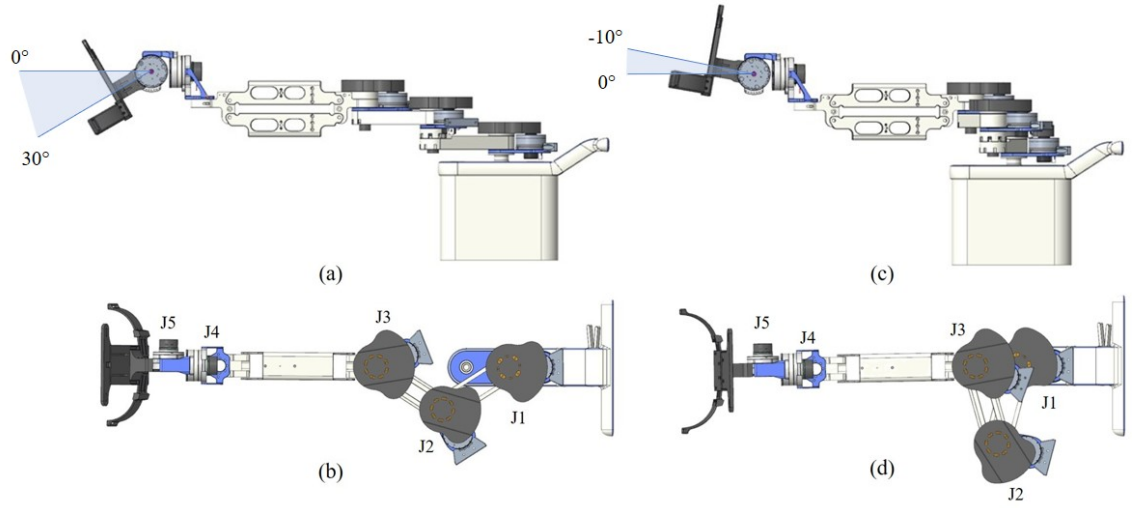



Fig. 6.8 Trunk device kinematic configurations at the frontal flexion maximum range of motion: (a, b) 30 deg flexion and (c, d) -10 deg extension

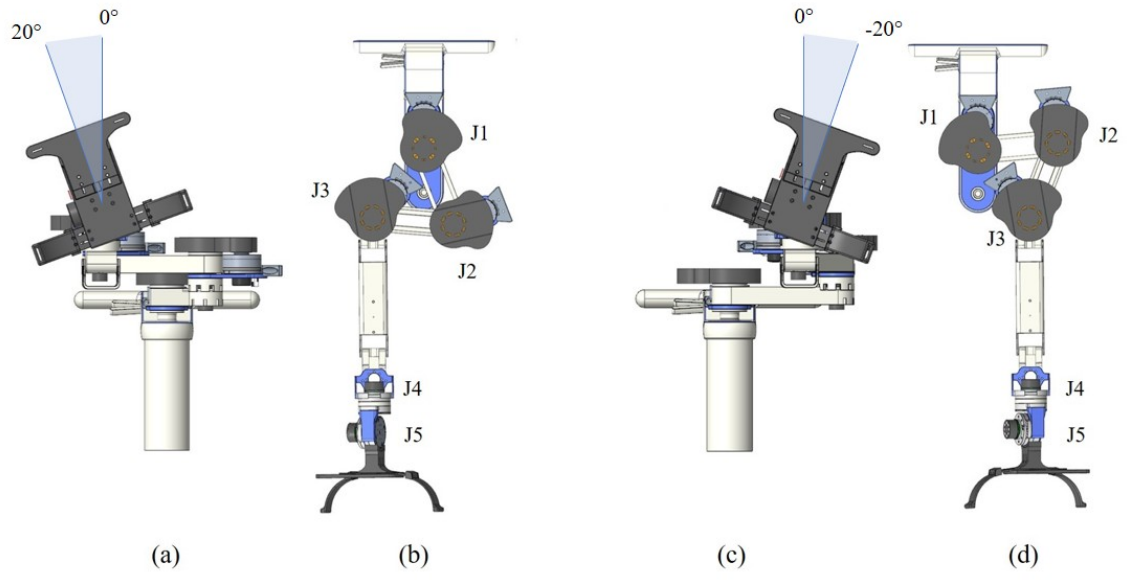



Fig. 6.9 Trunk device kinematic configurations at the lateral flexion maximum range of motion: (a, b) 20 deg lateral flexion and (c, d) -20 deg lateral flexion.

31 $Nm/rad$, $\beta_v = 15\ Nm \cdot s/rad$), medium assistance ($k_v = 125\ Nm/rad$, $\beta_v = 25\ Nm \cdot s/rad$) and high assistance ($k_v = 250\ Nm/rad$, $\beta_v = 35\ Nm \cdot s/rad$).

The lower the level of assistance, the greater the involvement required from the user. The impedance contribution can be computed as:

$$\tau_{i_i} = (q_{t_i} - q_i) \cdot k_v + \dot{q}_i \cdot \beta_v, \quad i = 1 \dots N \tag{6.7}$$

The resulting torque control signal for each joint can be written as:

$$\tau_{ctrl_i} = \tau_{g_i} + \tau_{f_i} + \tau_{i_i}, \quad i = 1 \dots N \tag{6.8}$$

Suppose the 'Keep Posture' mode is selected from the GUI. In that case, impedance control is applied with the springs' equilibrium points centred on the homing position (corresponding to the device configuration that keeps the subject in the correct seated position), thus $q_{t_i} = const$. This control strategy uses a virtual spring-damper effect to correct deviations from the correct posture, guiding the subject back to the proper position through the resulting virtual forces (Figure 6.10). Three levels of assistance are also available for this mode.

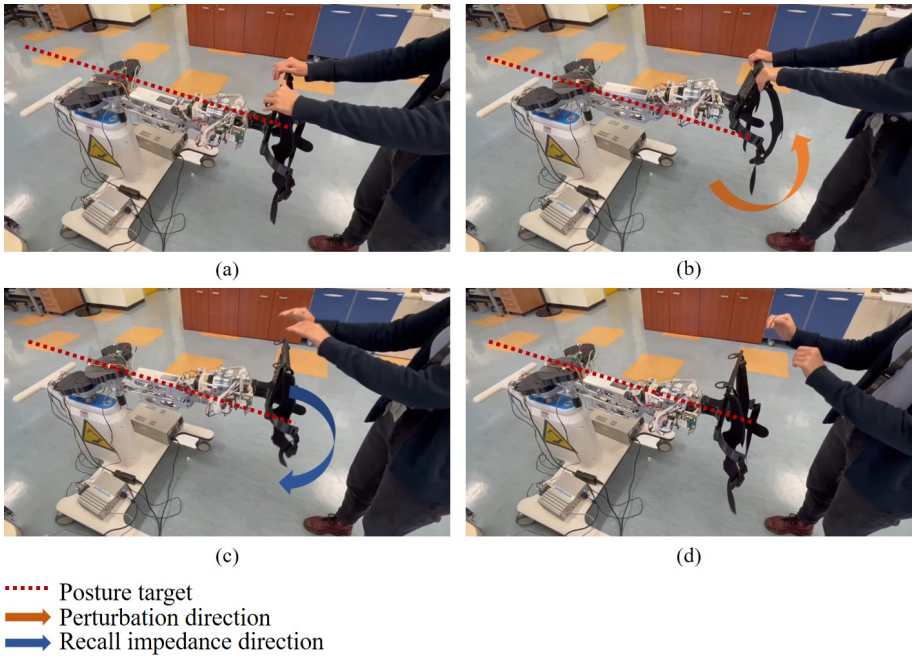



Fig. 6.10 Experimental Testing of the Keep Posture Mode: during experimental testing, the robotic device operates in torque control mode. (a) The target position is fixed at the homing configuration. (b) Perturbations are simulated by an operator manually moving the device from the outside, mimicking a patient's deviation from the correct posture. (c) In response, the device applies a recall force at all joints generated by the impedance parameters. (d) This recall force continues to act until the device returns to the target position.

**Resistive control mode** In this mode, a constant resistive contribution is provided along with an impedance contribution ($\tau_{i_i}$) exploited to guarantee a compliant and safe interaction with the machine. The resistance opposing the user's motion can be selected from the GUI for each SEA joint ranging from 1 Nm to 15 Nm ($\tau_{res} = const$), allowing to customise the training, targeting a specific movement and selecting the exercise intensity.

**Against interaction mode** Exploiting the SEA reading, it is possible to compute the interaction torque as:

$$\tau_{int_i} = \tau_{SEA_i} - \tau_{g_i}, \quad i = 1 \dots N \tag{6.9}$$

Interaction-based resistive contributions can be implemented as:

$$\tau_{res_i} = \%_{res} \cdot \tau_{int_i}, \quad i = 1 \dots N \tag{6.10}$$

The resistance is expressed as a percentage ($\%_{res}$) of the user's driving force. The gain factor can be selected for each joint, allowing customisation of the delivered resistive therapy. For example, if 50% resistance is selected, the system opposes half of the force transmitted via human-machine interaction. If 100% resistance is selected, the user should not be able to move the system at all. To avoid excessively rigid behaviour, also, in this case, an impedance term ($\tau_{i_i}$) is applied to the joints so that the device remains partially compliant with human interaction even when an opposing force is generated. The torque control signals for the aforementioned resistive control strategies can be computed as follows:

$$\tau_{ctrl_i} = \tau_{g_i} + \tau_{f_i} + \tau_{res_i}, \quad i = 1 \dots N \tag{6.11}$$

In this chapter, the mechanical design of a trunk mobilizer was presented, along with the final prototype, whose control was developed and tested within the RCP framework, enabling the exploration of assistive and resistive control modes.

# Chapter 7

# Discussion

This doctoral thesis addressed key scientific questions in rehabilitative robotics: How can metrics and methodologies be established to evaluate the effectiveness of exoskeletons in replicating human motion? What design guidelines and control strategies can be developed to create mechatronic systems that accurately mimic physiological movement and remain competitive with the state of the art? Additionally, this dissertation explored innovative control paradigms for trunk rehabilitation that extend beyond current robotic solutions.

In this doctoral thesis, various aspects of robotic rehabilitation were addressed, beginning with a comprehensive kinematic analysis. The dissertation then progressed to the characterization of the actuation system, followed by an in-depth exploration of the developed control strategies. The work concludes with a design study focused on the development of a robotic device specifically aimed at trunk rehabilitation.

## 7.1 Insights from kinematic analysis: key outcomes

The kinematic analysis and modelling of the devices' kinematic chains in a virtual environment were fundamental in enabling accurate analysis and simulations. These efforts aimed to evaluate the potential of each proposed design, with the models further enhanced by incorporating dynamic properties to facilitate more complex analyses that account for inertial effects. This dissertation introduced a novel methodology, to understand and assess the compatibility of robotic rehabilitation devices with the human body's physiological motion, that combines reachable workspace, internal-external rotation, and manipulability analysis. This approach also provided a benchmark against physiological motion, ensuring the device's design met rehabilitative needs.

The results demonstrated that for the shoulder complex design, replacing the Eulerian wrist with an RPY wrist significantly improved the range of motion and adaptability for shoulder rehabilitation,

although it marginally reduced overall manipulability. These findings underscore the importance of designing robotic rehabilitation devices that are both effective and intuitive for individuals with shoulder impairments. The FloatEVO RPY solution represents a significant advancement over the Float Eulerian joint and the RPY design featured in the Spherical Float. It enables broader movements, including adduction and extension, while notably enhancing external rotation capabilities. This ensures the possibility of performing numerous Activities of Daily Living (ADL) movements, whose training is crucial for achieving positive rehabilitative outcomes. These findings were instrumental in the design of control strategies. By leveraging knowledge of the available workspace and manipulability, it was possible to design feasible trajectories that meet both robotic and physiological requirements. Furthermore, understanding critical areas, particularly concerning internal-external rotation and manipulability performance, was essential for guiding exoskeleton users effectively. This guidance helps users navigate the exoskeleton's workspace while avoiding configurations that could hinder movement or training efficacy.

As a preliminary study for control implementation, different algorithms for solving inverse kinematics were investigated. This problem is particularly crucial when dealing with rehabilitative robotic devices that have a high number of degrees of freedom. Challenges arise not only due to potential singular configurations but also because a robotic configuration capable of reaching a certain end-effector pose may not always be compatible with the physiological configuration of the user. Three different methodologies for solving the inverse kinematics problem were presented, implemented, and tested in the context of performing redundant workspace tasks. Based on the results, the following guidelines and best practices are suggested for selecting the most suitable inverse kinematics approach for rehabilitative robots: the differential kinematics approach demonstrated the best performance in terms of accuracy, as evidenced by the lowest root mean square error (RMSE). However, its use in rehabilitative devices is not recommended, as it does not provide control over the joint boundaries. Neural network-based solutions, specifically ANFIS-based inverse kinematics, proved to be a powerful method, offering greater safety against singularities. However, it showed a reduction in accuracy when applied to redundant tasks. To fully exploit the capabilities of ANFIS, it is recommended to train the system on a fully defined (non-redundant) configuration, as this improves the method's accuracy.

## 7.2 Series Elastic Actuators: sensing challenges and design considerations

After gaining a thorough understanding of the exoskeleton's kinematics, the author proceeded to study the actuation system. Series Elastic Actuators (SEA) were selected as the mechanical solution, but an analysis of different possible torsional spring designs (serving as the compliant and sensing

element of the SEA) was necessary to complete the mechanical definition of the exoskeleton joints. Consequently, a mechanical analysis was conducted to evaluate various combinations of spring geometries and materials, ensuring that the system exhibited appropriate frequency and torque characteristics for effective coupling with the human body.

Both static and dynamic characterizations were performed to compare different compliant element designs and their corresponding driving systems. Considering the aforementioned required characteristics, along with the need for compactness, repeatability, and reduced manufacturing costs, the analysis indicated that using a custom Archimedean spiral spring geometry (SPS1P) in combination with a brushless DC motor (the Maxon EC60 was used for testing) and a 1:100 Harmonic Drive provided the most effective solution. This combination guarantees the design of a compact, lightweight, and physiologically relevant actuator with precise and repeatable torque sensing capabilities.

Although the existing literature on the characterization of Series Elastic Actuators (SEAs) for robotic rehabilitation is limited, a comparison of the proposed solutions with those adopted by other research groups was possible. The designed SEA provides torque values comparable to those of the Harmony [54] and Clever Arm [106] SEA joints. In terms of integration, it is more compact (M < 2 kg, h < 100 mm, d < 100 mm) than the Aramis exoskeleton joints [55], while its weight is similar to that of AnyDrive SEAs. The AnyDrive actuator guarantees a torque bandwidth around 60 Hz [73], with a spring stiffness of $k = 160$ Nm/rad [74]. The proposed design, which integrates the SPS1P spring, offers a promising solution to cover a physiological bandwidth while providing higher joint stiffness. This ensures that the joint output position is less affected by the deformation of the compliant element under the exoskeleton's weight, enabling more accurate position control for the exoskeleton joints.

Once the SEA design was selected, the characterization of the sensor was performed. Specifically, this thesis proposes a testing methodology for SEA joints, as the need for close interaction with the human body requires the implementation of closed-loop control strategies that rely on torque sensing during human-robot interaction. To effectively implement compliant assistive control strategies that utilize interaction forces, it is essential to ensure that transparency, particularly frictions and gravity compensation, is successfully achieved. This is done by exploiting available sensors (in this case, the SEA torsional spring) to close the control loop.

To accurately estimate interaction torque, it is crucial to refine the measurements by eliminating non-linear effects. The proposed compensation approach improves sensor measurements without the need for complex dynamic models of the mechatronic components. Instead, an experimental procedure is followed to characterize the SEA joint's behaviour by modelling both the linear and non-linear components of the measured torque, under both load and no-load conditions. In this phase of the work, positive outcomes were obtained to assess the human-robot interaction (HRI).

Further tests will focus on evaluating the effect of double correction on the performance and stability of the sensor when closing torque control loops.

## 7.3 Reflections on control architecture design and implementation

The development of an exoskeleton is a complex endeavour that requires a multidisciplinary engineering approach, encompassing activities ranging from mechanical design to electronics and control software development. This process can be highly time-consuming, often hindering the implementation of more sophisticated control strategies. Therefore, especially during the initial iterative phases, it became evident to the author that having a fast and effective method for developing a first control prototype was crucial. Consequently, a primary objective of this dissertation was the development of a Rapid Control Prototyping (RCP) platform in the MATLAB/Simulink environment. This platform was used to implement and test several control strategies on the Spherical Float prototype, allowing for the testing of most control systems during the RCP phase before transitioning to the final FloatEVO device.

The developed model was designed to accelerate control prototyping and hardware testing by consolidating the entire control architecture into a single interface. The results highlight how this goal was achieved through the integration of system modelling, low-level driver configuration, control strategy development, and user interface implementation, all within a unified development environment using the same programming language. The availability of a real-time machine (Speedgoat) was crucial in ensuring high standards and efficiency in the development of advanced technologies. This approach enabled rapid implementation and testing, an otherwise challenging task with conventional development tools while eliminating the need to switch between different programming languages. Additionally, the modular nature of this model made it possible to adapt it for controlling a different device, specifically a trunk robotic mobilizer, developed during the final phase of the PhD project. Kinematic exercises, transparency, and Assist-As-Needed control strategies were tested within the RCP environment, enabling the exploration of various paradigms, from impedance and admittance control to velocity fields and Cartesian-based controls. Following consultations with clinicians, the features selected for the FloatEvo exoskeleton were translated into an embedded solution. For the FloatEVO exoskeleton, exercise trajectories were designed, along with an Assist-As-Needed impedance-based assistive control and a transparency mode, where gravity and friction are compensated. Additionally, an assistive contribution was incorporated to compensate for a selectable percentage of the patient's arm weight.

Two additional control strategies were implemented and tested on the FloatEVO platform for research purposes: a force-field time-independent assistive control and a resistive control.

These control paradigms were explored to better understand their applicability in the rehabilitative context. The author believes that incorporating assistive forces shaped within assistive tunnels not only addresses clinical needs but also engages users, encouraging them to follow the correct movement path during exercises. Furthermore, the proposed algorithm, which combines task-space and joint-level impedance controls, offers adaptability to physiological requirements through customizable assistive tunnels and reference trajectories. This approach allows for a more personalized experience, steering robotic interventions toward being more patient-centric and adaptable.

Additionally, resistive control has shown the potential to improve user engagement by requiring users to apply an active force to counter the resistance of the exoskeleton during movements. This presents an opportunity to transition from the assistive phase to a more active rehabilitation stage. The author believes that resistive controllers are worth further investigation, particularly in combination with external feedback mechanisms (e.g., vibrotactile and visual cues), as they could add significant value to the rehabilitative process.

For these reasons, resistive controls were also implemented and explored in the control design of the trunk rehabilitation device proposed in the final section of this dissertation.

## 7.4 FloatEVO's next frontier: advancing trunk rehabilitation

This dissertation seeks to expand FloatEVO's functionality on multiple fronts, addressing not only kinematics and control but also extending its application to trunk rehabilitation. To this end, the thesis presents an innovative approach specifically designed for trunk core rehabilitation, detailing a trunk mobilizer prototype's mechanical and control design that enhances the existing passive multi-articulated arm through structural modifications and actuation.

The device was developed with input and suggestions from clinical partners, ensuring its suitability for addressing various neurological pathologies. The control strategies were implemented using a rapid control prototyping approach and validated through bench testing, confirming the functionality of different control modes. Future work will focus on obtaining hardware and software certification to enable testing on healthy subjects, followed by trials with patients. Additionally, the integration of EMG signals acquisition is planned to fine-tune the assistive and resistive controllers, enhancing the machine's support capabilities (assistive mode) and optimising muscle activation to promote strengthening and recovery (resistive mode).

## 7.5 Future perspectives

Future clinical trials will allow the author to evaluate the control paradigms developed for the FloatEVO exoskeleton, assessing their physiological impact on impaired subjects, including those with orthopedic and neurological conditions. Additionally, the developed methodologies may also serve as a foundation for further enhancements in both kinematic and actuation systems or be adapted for evaluating other rehabilitative devices. Planned investigations will explore resistive and assistive, time-independent, and trajectory-less control strategies. The exoskeleton will also be validated as a human motion monitoring system, enabling the detection and correction of compensatory movements to help restore proper musculoskeletal synergies.

Further work will also focus on achieving hardware and software certification for the trunk mobilizer, enabling its safe testing on healthy individuals, followed by clinical trials. These trials will determine whether the proposed solution can effectively support trunk control restoration. If the validation of the device yields positive feedback from clinicians, future steps will focus on integrating the system with FloatEVO with the aim of replacing the current passive multi-articulated arm for enhanced functionality and performance. This integration aims to create a fully comprehensive robotic solution capable of dynamically following the patient's movements and supporting the recovery of the entire upper body.

# Appendix A

# PhD Secondary Activities

During the PhD, research activities were also conducted as part of the RAISE Spoke 2 project, funded by the European Union - NextGenerationEU and the Ministry of University and Research (MUR) under the National Recovery and Resilience Plan (NRRP), Mission 4, Component 2, Investment 1.5. The project, titled “RAISE - Robotics and AI for Socio-economic Empowerment” (ECS00000035), focuses on utilizing sensorized environments to monitor frailty.

The proposed telemonitoring approach incorporates non-invasive sensors into specific environments, particularly for individuals with chronic conditions. Ambient Assisted Living (AAL) solutions and activity recognition technologies are employed to enhance caregiving, improving the quality of life and independence for individuals with frailty.

Since the concept of frailty extends beyond aging, encompassing degenerative diseases and pediatric conditions, the project aims to design and install sensor-equipped environments to cover the following use cases: (I) Monitor the impact of Multiple Sclerosis on cognitive and mobility performance. (II) Analyse mobility patterns and activity levels in elderly individuals. (III) Examine child-caregiver interactions, dependency, and correlations between pain levels and mobility.

The proposed solutions and adopted technologies include the utilization of sensorized glasses and insoles to gather insights into cognitive and mobility performance for the Multiple Sclerosis (MS) use case, the deployment of cameras, sensing floors, sensorized seats, mattresses, and insoles to measure activity levels and movement quality, the monitoring body balance and pressure to prevent falls from bed for the geriatric use case and the deployment of cameras, sensing floors, sensorized seats, mattresses, and insoles to interpret interactions between subjects and analyze activity patterns for the pediatric use case.

In the context of the presented PhD research, significant efforts were directed towards:

(I) Collaborating with hospitals in Genoa: partnerships with E.O. Ospedali Galliera, Istituto Giannina Gaslini, and the FISM centre to define system requirements and develop the technology accordingly.

(II) Implementation of processing algorithms: developing algorithms to interpret sensor data effectively.

(III) Designing clinician-friendly visual interfaces: creating intuitive visual tools to support clinical data consultation.

(IV) Defining and submitting clinical protocols: writing and submitting protocols to test the system with both healthy participants and impaired subjects.

This appendix also includes the two publications resulting from the research conducted. The first has already been presented at the *2024 24th International Conference on Control, Automation and Systems (ICCAS)*, while the second has been accepted for publication on *IEEE International Conference on Rehabilitation Robotics (ICORR)*, to be presented during RehabWeek 2025.

2024 24th International Conference on Control, Automation and Systems (ICCAS)
Jeju Shinhwa World, Jeju, Korea. Oct 29 - Nov 1, 2024

# Enabling Frail Subjects Telemonitoring: A Sensor Network System for Enhanced Health Assessment

Giulia Bodo[*,1,2], Giulio Sciortino[*,3], Alexey Petrushin[2], Emanuele Seminerio[4], Wanda Morganti[4], Gian Luca Bailo[3], Carlos Beltrán-González[3], Alberto Pilotto [4,5], Matteo Laffranchi[+,2] and Alessio Del Bue[+,3]

[*]Co-First authors, equal contribution, [+]Co-Last authors, equal contribution
[1]Politecnico di Torino, Torino, Corso Duca degli Abruzzi 24, 10129, Italy.
[2]Rehab Technologies Laboratory at Istituto Italiano di Tecnologia, Genova, Via Morego 30, 16163, Italy.
[3]Pattern Analysis and Computer Vision at Istituto Italiano di Tecnologia, Genova, Via Enrico Melen 83, 16152, Italy.
[4]Geriatrics Unit, Department of Geriatric Care, Neurology and Rehabilitation, Galliera Hospital, Genoa, Italy
[5]Department of Interdisciplinary Medicine, University of Bari "Aldo Moro", Bari, Italy

**Abstract:** Telemonitoring, telemedicine, and telerehabilitation are becoming essential technologies for improving healthcare. Particularly useful for assessing the physical and cognitive status of frail individuals, telemonitoring has applications in elder care and neurodegenerative disease management. This study presents a smart room prototype for medium to long-term telemonitoring of frail subjects. The system captures real-time video/data from various sources, processes it with advanced AI, and displays the results for real-time viewing and control. Its modular architecture includes components like pressure floors and sensorized mattresses, integrated via a web-based interface. The system effectively evaluates subject interactions in the sensorized environment, with real-time Mobility and Sleep Indexes to track activities.

**Keywords:** Sensors and Signal Processing; Artificial Intelligent Systems; Biomedical Instruments and Systems

## 1. INTRODUCTION

The evolution of assistive technologies increasingly focuses on a user-centered design approach [1], integrating usability from the early stages to align services with the needs of patients and clinicians [2]. Designers must prioritize user acceptance, ensuring devices are safe and secure. This is crucial in telemonitoring, where devices should be user-friendly, minimally invasive, and privacy-conscious. Telemonitoring integrates non-invasive sensors into specific environments, particularly for monitoring individuals with chronic diseases [3]. Ambient assisted living (AAL) solutions and activity recognition technologies help caregivers deliver better care, enhancing the quality of life and independence for older adults with disabilities [4].

Frailty is an age-related specific decline in functioning affecting several physiological systems and increasing the vulnerability to stressors, which nowadays is better defined as a multidimensional construct, involving clinical consequences, frailty manifestations, biological and physiopathological mechanisms [5]. Multidimensional frailty (MF) is a reversible and preventable condition thus its early identification is of extreme importance [6] and can be supported by technological devices. MF encompasses several domains, thus, a sensor network capable of integrating various types of data from multiple sources in real-time, could enhance older people health assessment. Given the heterogeneity of aging and the interplay of different domains in assessing an individual's status, a multidimensional approach can be adopted to integrate all the relevant components affecting the health-related domain. Each individual has, in fact, a distinct profile of comorbid diseases, social environment, physical and mental health statuses [7], requiring a complex assessment considering several variables. The literature shows that the gold standard for the evaluation of older people's needs is the Comprehensive Geriatric Assessment (CGA) [5]. Thus, the most reliable indexes and assessment tools should rely on this approach to give an extensive overview of the individual. Among the tools inspired by the CGA approach, the Multidimensional Prognostic Index (MPI) is the most accurate in predicting mortality and adverse health outcomes (e.g., institutionalization) compared to other indexes [8], reliable [9], and sensitive to changes of health and functional status [10]. Thus, the MPI effectively translates the clinical assessment of frailty into a clinimetric score ranging from 0 to 1, sensitive to changes and accurate in predicting mortality and other adverse outcomes, thereby serving as a prognostic tool for older adults. In this work, a prototype of a sensorized environment for the non-invasive telemonitoring of the elderly is proposed. Once the sensors integrated into the smart environment are linked to a central intelligent unit, artificial intelligence algorithms can be employed and tailored to extract metrics for assessing the patient's condition. The authors suggest a modular, customized sensor network architecture along with a graphical monitor designed to report the results of the monitoring in real-time. Specifically, this work proposes and measures several metrics for evaluating daily and nocturnal activity: gait speed or position variations can offer insights on behaviour patterns, continuous data on number of steps, speed of movement, and activity levels could provide noteworthy insights into functional status, rehabilitation progress and mobility interventions effectiveness, also, monitoring sleep patterns continuously may assist in the diagnosis of sleep disorders. The overall aim



Authorized licensed use limited to: IIT - Istituto Italiano di Tecnologia. Downloaded on December 16,2024 at 07:34:44 UTC from IEEE Xplore. Restrictions apply.

of this study is to propose a comprehensive representation of the patient's activity and status based on the aforementioned metrics.

## 2. MATERIALS AND METHODS

### 2.1 Sensor Network System Architecture

The proposed sensor network framework is implemented to offer a comprehensive solution for real-time sensor data acquisition and analysis. The architecture is modular, enabling seamless integration of various sensors and AI modules. Each module included in the architecture serves a specifc purpose, specifically:
*Sources*: namely input modules, acquire data. Cameras and sensors with various purposes can be integrated and connected to the network.
*Stream Normalizers*: these redirector modules receive input from sources and standardize or normalize the data stream, converting the video stream to MJPEG and adding a timestamp to ensure compatibility with subsequent modules.
*AI Modules (AIM)*: container modules that allocate various algorithms (e.g., YOLO for object detection). These intelligent modules process the data streams, providing the requested results or useful insights about the received data.
*Actuators*: these modules provide control signals and plan actions based on the results provided by the AIM. They can control external devices such as robots, relays, etc.
*Viewers*: modules accessible via the web allow users to view the processed video streams and results in real time.
*Recorders*: the system records the data streams and makes them available as web services for further analysis or review.

### 2.2 Graphic Language Interface

To facilitate user-network interaction, a graphical representation of the sensor network is proposed in Figure 1. Through this web-accessible interface, developers can easily integrate new modules (nodes) into the network and establish connections. A node is an atomic specialised component of the network aimed at performing a specific task (sensors, AI algorithms, actuators, etc.). Additionally, the interface provides a visual representation of activated and deactivated data flows. One of the primary advantages of a graphical language is the ability to abstract complex processes: by representing algorithms and data flows with visual elements, users can understand and manipulate them without delving into the underlying code.

### 2.3 Telemonitoring environment: concept

The conceptualization of the proposed sensorized environment began with the concept of user-centered design: the goal was to design a non-obtrusive, minimally invasive, ecological, and person-centered system. From a technological standpoint, the objective was to create

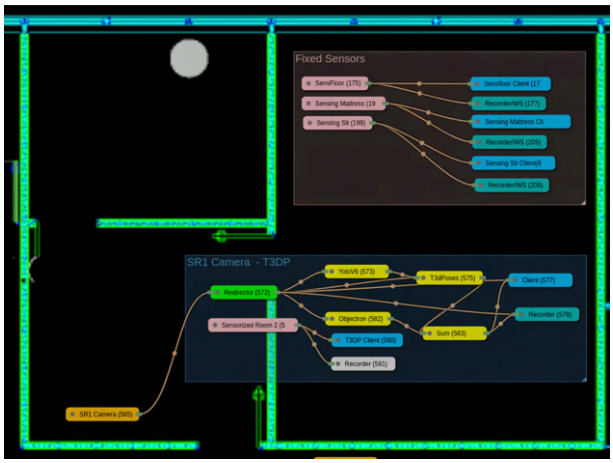



Fig. 1. Sensor Network Graphical Interface: This interface visually represents sensor connections with the acquisition system. Nodes are color-coded: orange (camera), pink (sensor), green (redirector), yellow (AI algorithm), blue (visualizer), dark green (recorder), and grey (disabled module). The upper right block shows connections for the sensing floor, seat, and mattress, while the lower block displays the camera connection for recording experiments. The sensorized environment's walls are highlighted in green.

a real-time system characterized by a strong emphasis on privacy awareness and capable of providing a continuous flow of data. We propose a sensorized room equipped with minimally invasive sensors (as pressure textiles shown in Figure 2) integrated into the aforementioned sensor network architecture. The acquired data are sent, stored, and accessed only via a closed local cloud platform that adopts cybersecurity protocols to protect and guarantee data privacy.

In order to provide easily accessible and readable data interpretation, we also propose a custom front-end (developed in Angular [1] environment) page where the metrics evaluating the monitoring session are displayed graphically, explaining the subjects' activity within the sensorized environment (see Figure 2 and Figure 5).

### 2.4 Sensorized Room Prototype

The sensor network represented thorough the schematic shown in Figure 1, acts as an abstract input module, receiving data from various sensors and channeling them into the sensor network system. This abstraction allows for the easy integration of a wide range of sensors. For the purpose of obtaining a mobility index to describe the user's activity, we propose to adopt three main sensors, with reference to Figure 2: a sensorized floor (1), two sensing textiles - one adapted to sensorize a seat (2) and the other to sensorize a bed mattress (3).

[1] https://angular.dev/



Authorized licensed use limited to: IIT - Istituto Italiano di Tecnologia. Downloaded on December 16,2024 at 07:34:44 UTC from IEEE Xplore. Restrictions apply.

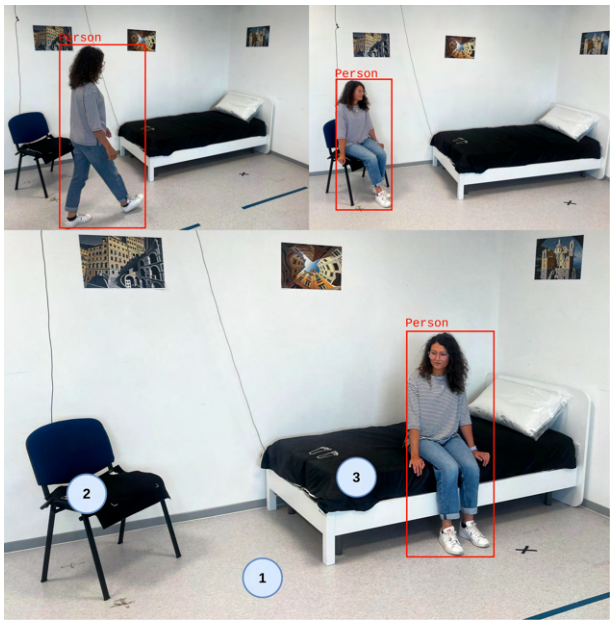



Fig. 2. In the Sensing Room prototype, the environment is characterized by minimally invasive sensors. The floor has been modified to detect walking using SensFloor sensors (1), while the chair (2) and bed (3) are also sensorized using sensing textiles.

#### 2.4.1 Sensing Floor

The prototype room was equipped with a sensing floor, utilizing commercial instrumentation provided by Future Shape [2]. The floor cells, functioning as proximity sensors, enable tracking of object motion, providing data regarding the distance walked and the number of steps, along with the coordinates of the path within the room.

#### 2.4.2 Sensing Textiles

For design choices, the authors propose adopting two sensing textiles to monitor activity on a seat and a bed. This choice allows for tracking various resting phases, from sitting on the chair to lying down and resting on the bed. The sensing textiles integrated into the sensor networks are provided by SensingTex [3]. This sensor-printed technology enables obtaining pressure map distributions on the activated area. We accessed and processed the raw data with computer vision to evaluate the pressure patterns and categorize the information as person seated (on the chair), person seated (on the bed), and person lying (on the bed). The method was implemented as described in Section 3.3

## 3. DESIGN

The proposed design aims to offer a comprehensive assessment of the subject's activity within the sensorized environment. Specifically, the analysis will concentrate on evaluating mobility and sleep patterns.

[2]FutureShape: `https://future-shape.com/en/`
[3]SensingTex: `https://sensingtex.com/product/mattress-mat-dev-kit-2-0/`

### 3.1 Graphic Interface

A user interface has been designed to provide real-time reporting of the monitored subject's activity state. The interface is built in the Angular development environment, with graphs that update directly based on data from the sensor network system. Specifically, with reference to Figure 5 the GUI includes six different boards:

- Board 1: Contains information about the subject and the acquisition, such as subject ID, age, and date of the test.
- Board 2: Updates with step counter data received from the sensing floor. It displays the performed steps and the covered walking distance on a circular graph, representing performance relative to a predefined target.
- Board 3: Monitors average speed, showing variations in speed over the capture time.
- Board 4: Serves as an activity monitor, reporting changes in activity state (walking, sitting - bed or chair), and the relationship between active and resting times.
- Board 5: Analyzes the resting phase, evaluating the position assumed during rest, the number of position changes, and the Sleep Regularity Index.
- Board 6: Displays a spider plot that provides an overall assessment of the patient based on metrics mapped between 0 and 1. A wider covered area indicates a more positive performance by the subject.

### 3.2 Metrics

In this work, authors propose various metrics to evaluate patient activity, specifically:

1. **Number of Steps**: A metric ranging from 0 to 1, proportional to the number of steps taken relative to a target (set by the therapist).
2. **Speed Monitor**: Evaluates the root-mean-square jerk (the related metric is $SpeedMonitor = 1 - RMS_{jerk}$) of the speed of movement to detect sudden changes during the deambulation (due to limp, unbalancing, etc.) [11].
3. **Mobility Index**: Evaluates activity periods relative to the overall session duration (sum of active and resting times).
4. **Sleep Duration**: The sum of the time spent in supine, left-side, and right-side positions, compared to the optimal resting time. Studies proposed by [12] and [13] reveal that for the geriatric population the recommended sleep duration is around 7 hours, thus we propose a Gaussian distribution to assign the score to the "Sleep Time" metric, considering that the maximum score is assigned to the optimal sleep time of 7 hours. The Gaussian function is defined as follows:

$$f(x) = e^{-\frac{(x-\mu)^2}{2\sigma^2}} \tag{1}$$

where: $x$ is the input value, $\mu$ is the mean or central valueand $\sigma$ is the standard deviation.
In this specific case: $\mu = 7$ (central value), $\sigma = 1$ (standard deviation).

5. **Sleep Quality Index (SQI)**: This score is derived from various contributions, each mapped between 0 and



Authorized licensed use limited to: IIT - Istituto Italiano di Tecnologia. Downloaded on December 16,2024 at 07:34:44 UTC from IEEE Xplore. Restrictions apply.

1. The considered indicators are: sleep time in supine ($\Delta t_{SP}$), right side ($\Delta t_{RS}$), and left side positions ($\Delta t_{LS}$), all normalized (*nrt*) on the total sleep duration, the number of relevant changes in position during the night (pCh) normalized with respect to a maximum of 1 pCh every minute (the pCh are considered relevant only if more than two changes in position are recorded in a predefined time interval (e.g. 1 min)), and sleep interruptions duration (slInt) normalized on the total rest time (sleep time + interruption time). It is considered a sleep interruptions any action that brings the subject out from the "lay" state, so if the subject is sitting or walking. Each of these contributions is multiplied for a selected score so to obtain a weighted sum.
The overall formula is:

$$SQI = \Delta nrt_{\text{SP+LS}} \cdot \alpha + \Delta nrt_{\text{RS}} \cdot \beta - pCh \cdot \gamma - slInt \cdot \delta \quad (2)$$

The scores have been chosen so that, in an undisturbed sleep scenario, the index assumes its highest values. Instead, penalties are assigned to adverse sleep events, giving more relevance to sleep interruptions that have a higher negative impact on the resting phase, influencing the subject's life expectancy in good health and in the absence of chronic diseases [14]. The study of side sleeping positions is particularly intriguing due to their physiological effects. Previous studies have shown that sleeping on the left side improves digestion, enhances blood flow, reduces pressure on major organs, and lessens strain on the back. Additionally, this position promotes better lymphatic circulation [15]. For these reasons, the left side scores higher in the index calculation compared to the right. Arbitrary preliminary values have been assigned to scores are reported in Table 1.

| Metrics | Coeff. | Score |
|---|---|---|
| Sleep t supine/left side | $\alpha$ | 1.0 |
| Sleep t in right side | $\beta$ | 0.85 |
| n° Changes in sleep position | $\gamma$ | 0.15 |
| n° Sleep interruptions | $\delta$ | 0.8 |

Table 1. Score coefficients for the weighted sum of the different contributions to the computation of the sleep quality index. Depending on the metrics, different weights can be assigned to provide more relevance to some of the examined events.

### 3.3 Sensing Textiles algorithms for activity detection

The floor pressure sensor directly provides data related to the number of steps, walking distance, and subject speed. The sensing textiles offer data in the form of a pressure cell activation matrix, which is used to evaluate the pressure distribution on the sensorized surface. Thus, these data need further elaboration to be meaningful for assessing the subject's activity. The solution adopted consists in a fine-tuned object detection model based on Yolo M v8.1.98 by Ultralytics [4]. We tested the finetuning with several versions of yolo, specifically nano, medium and xl of both versions 5 and 8. We didn't find significant variations in the performance (intended in terms of the confusion matrix and mean average precision), with both xl models performing slightly better. The choice fell on yolov8m model, which is the newest released version among the tested ones and offers a good balance between computational time and performace. The fine-tuning was done on a set of 200 images of the pressure sensors matrix, visualized as a heatmap (see Figure 4). The dataset was collected based on 5 different people, laying in three different poses, nominally supine, left-side and right-side, divided in training (80%) and valuation dataset (20%). The fine-tuning was performed over 200 epochs and an initial learning rate of 0.01. The annotations were done manually. As visible in the confusion matrix (Figure 3), the resulting model shows a robust performance in detecting left and right side, however, when detecting the supine position, it produces a non-negligible amount of false positives. We attribute this to the peculiarity of side positions shapes compared to the supine one, which has a less visually notable feature. Moreover, the side positions present a more centered weight distribution, resulting in a higher contrast against the background. To mitigate the false positives, a minimum threshold of 0.5 confidence is applied. To enhance the precision for the Supine class, we implemented a post-processing (PP) step involving a minimum confidence threshold. By setting this threshold to 50%, we effectively filtered out lower-confidence predictions, thus reducing the number of false positives. Furthermore, a filter was introduced when more than one classes were found, keeping the class with the highest confidence found. This adjustment led to a significant improvement in precision among all classes (see Table 2). Computing precision ($p$) and recall ($r$) for all the classes we obtain

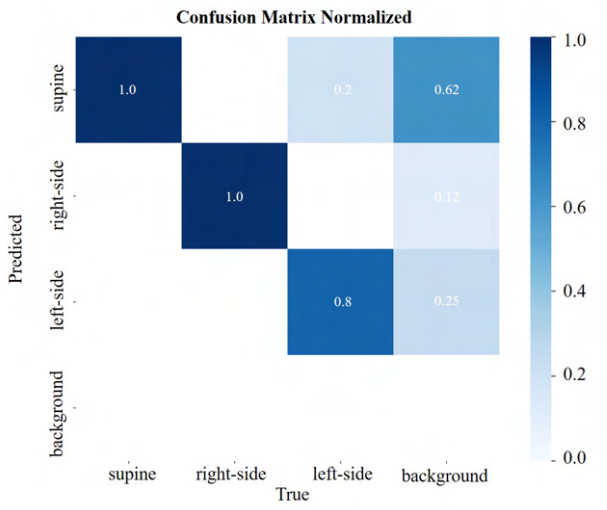



Fig. 3. The confusion matrix shows robust performance of the model across all three positions, with notable false positives for all classes, especially for the supine position. To mitigate false positives, a post-processing filter based on minimal confidence threshold has been applied.

[4]Ultralytics https://docs.ultralytics.com/



Authorized licensed use limited to: IIT - Istituto Italiano di Tecnologia. Downloaded on December 16,2024 at 07:34:44 UTC from IEEE Xplore. Restrictions apply.

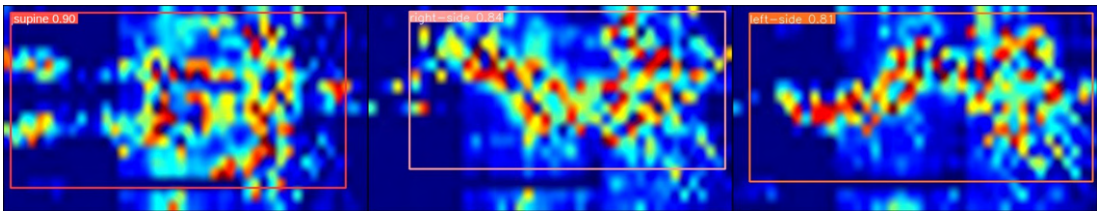



Fig. 4. The figure shows random samples from predicted validation batch. In all cases, the correct pose (supine, right side, left side) has been detected, with the relative confidence score.

the following results:

| Class | Before PP | | After PP | |
|---|---|---|---|---|
| | ***p*** | ***r*** | ***p*** | ***r*** |
| Supine | 55% | 100% | 96% | 98% |
| Left-side | 89% | 80% | 98% | 97% |
| Right-side | 76% | 100% | 100% | 100% |

Table 2. Precision and Recall results before and after predictions post-processing.

## 4. RESULTS

The proposed sensor network acquisition system and the graphical interfaces were tested as a proof of concept during a 1h 25min acquisition sessions testing two possible activity scenarios, instead the nocturnal activity was simulated with synthetic data. In the first case-study (CS1), a balanced daily-nocturnal activity was analyzed, instead in the second scenario (CS2), it was spent more time sitting rather than walking and simulated irregular sleep. The target for the steps n° was set to 5000 steps. The recorded parameters for the activity and the simulated data for sleep analysis are collected in Table 3.

| Test data | CS1 | CS2 |
|---|---|---|
| n°steps | 3700 | 1500 |
| $\Delta t_{\text{stand}}[min]$ | 43.2 | 21.25 |
| $\Delta t_{\text{sit-ch}}[min]$ | 5.2 | 23.15 |
| $\Delta t_{\text{sit-bed}}[min]$ | 5.4 | 17 |
| $\Delta t_{\text{lay}}[min]$ | 31.2 | 23 |
| $\Delta t_{\text{Sleep}}[min]$ | 390 | 270 |
| $\Delta t_{\text{SP}} + \Delta t_{\text{LS}}[min]$ | 380 | 250 |
| $\Delta t_{\text{RS}[min]}$ | 10 | 20 |
| $pCh$ | 3 | 24 |
| $\Delta t_{\text{SlInt}}[min]$ | 0 | 60 |

Table 3. Activity and Sleep data computed by the smart system during two case studies experiments.

The computed metrics for the two case-study are collected in Table 4. These simulations were relevant for testing the developed algorithms and evaluating the efficacy of the graphs in providing a clear and immediate comprehension of the monitored activity. The results (from Board 3 to Board 6) of the CS1 acquisition are shown in Figure 5. Specifically, it was of interest to understand if the Board 6 spider plot was suitable for providing a clear overview of the overall subject assessment.

| Metrics | CS1 | CS2 |
|---|---|---|
| n° Steps | 0.74 | 0.3 |
| Speed Monitor | 0.82 | 0.55 |
| Mobility IDX | 0.51 | 0.25 |
| Sleep Duration | 0.88 | 0.01 |
| Sleep t in supine/left side | 0.97 | 0.93 |
| Sleep t in right side | 0.026 | 0.074 |
| Changes in sleep position | 0.0077 | 0.0889 |
| Sleep interruptions | 0 | 0.18 |
| SQI | 0.98 | 0.83 |

Table 4. Score obtained for the different metrics during test of two different activity scenarios within the sensorized room.

## 5. DISCUSSION AND FUTURE WORK

Our proposed telemonitoring system shows strong potential for clinical integration, enabling continuous monitoring to detect sporadic or evolving health issues, reducing the need for frequent exams. Its modular design allows easy integration with existing healthcare IT systems without major changes. The use of minimally invasive sensors enhances patient comfort and acceptance. Preliminary tests highlight the system's potential in assessing mobility and sleep, but further refinement of the algorithm is needed to improve score accuracy and correlation with clinical assessments. Also it will be possible to introduce a smartwatch in the network to recognize the sleep phases (e.g. REM). This work also presents preliminary results in detecting lateral side positions, a feature we plan to leverage in future applications to recognize and prevent the risk of falls from a mattress, which often occur during rolling movements. This refinement process will be facilitated by future trials, including those planned to involve healthy subjects. These trials will not only evaluate the technology's efficiency but also generate valuable datasets for training our AI algorithms, ultimately enhancing the system's performance and utility in clinical practice.

## 6. ACKNOWLEDGMENT

Funded by the European Union - NextGenerationEU and by the Ministry of University and Research (MUR), National Recovery and Resilience Plan (NRRP), Mission 4, Component 2, Investment 1.5, project "RAISE - Robotics and AI for Socio-economic Empowerment" (ECS00000035).



Authorized licensed use limited to: IIT - Istituto Italiano di Tecnologia. Downloaded on December 16,2024 at 07:34:44 UTC from IEEE Xplore. Restrictions apply.




Fig. 5. Graphical results of experimental and simulated tests are displayed on the ACTIVITY MONITOR (diurnal) and SLEEP MONITOR (nocturnal) boards. The SLEEP MONITOR continues the Lay state from the ACTIVITY MONITOR. The OVERALL ASSESSMENT board shows superimposed spider plots for two tests, CS1 (blue) and CS2 (red), illustrating the subject's better and worse conditions, respectively, and demonstrating the graph's consistent representation of the monitored situation.

## REFERENCES


[1] S. D. Stowe and S. Harding, "Telecare, telehealth and telemedicine," *European Geriatric Medicine*, vol. 1, pp. 193–197, 2010.

[2] A. Petrushin, F. Marco, G. Barresi, M. Bustreo, M. Laffranchi, A. Del Bue, and L. De Michieli, *IoT-Powered Monitoring Systems for Geriatric Healthcare: Overview*, pp. 99–122. 02 2022.

[3] R. Lavanya, M. Nivetha, K. Revasree, and K. Sandhiya, "Smart chair-a telemedicine based health monitoring system," pp. 459–463, 03 2018.

[4] G. Cicirelli, R. Marani, A. Petitti, A. Milella, and T. D'Orazio, "Ambient assisted living: A review of technologies, methodologies and future perspectives for healthy aging of population," *Sensors*, vol. 21, no. 10, 2021.

[5] A. Pilotto, C. Custodero, S. Maggi, M. C. Polidori, N. Veronese, and L. Ferrucci, "A multidimensional approach to frailty in older people," *Ageing Research Reviews*, vol. 60, p. 101047, 2020.

[6] M. Wleklik, I. Uchmanowicz, and E. Jankowska, "Multidimensional approach to frailty," *Frontiers in Psychology*, vol. 11, 03 2020.

[7] E. H. Gordon and R. E. Hubbard, "Frailty: understanding the difference between age and ageing," *Age and Ageing*, vol. 51, p. afac185, 08 2022.

[8] A. Pilotto, F. Rengo, and N. Marchionni, "Comparing the prognostic accuracy for all-cause mortality of frailty instruments: A multicentre 1-year follow-up in hospitalized older patients," *PLOS ONE*, vol. 7, pp. 1–9, 01 2012.

[9] R. M. Warnier and E. van Rossum, "Validity, reliability and feasibility of tools to identify frail older patients in inpatient hospital care: A systematic review," *The journal of nutrition, health & aging*, vol. 20, no. 2, pp. 218–230, 2016.

[10] S. Volpato and A. Pilotto, "Change in the multidimensional prognostic index score during hospitalization in older patients," *Rejuvenation Research*, vol. 19, no. 3, pp. 244–251, 2016.

[11] R. P. Young and R. G. Marteniuk, "Acquisition of a multi-articular kicking task: Jerk analysis demonstrates movements do not become smoother with learning," *Human Movement Science*, vol. 16, no. 5, pp. 677–701, 1997.

[12] J.-P. Chaput and C. Dutil, "Sleeping hours: what is the ideal number and how does age impact this?," *Nature and Science of Sleep*, vol. 10, pp. 421–430, 2018.

[13] J.-P. Chaput and C. Dutil, "Sleep duration and health in adults: an overview of systematic reviews," *Applied Physiology, Nutrition, and Metabolism*, vol. 45, no. 10 (Suppl. 2), pp. S218–S231, 2020.

[14] S. Stenholm and J. Head, "Sleep duration and sleep disturbances as predictors of healthy and chronic disease-free life expectancy between ages 50 and 75: A pooled analysis of three cohorts," *The Journals of Gerontology: Series A*, vol. 74, 02 2018.

[15] D. M. e. A. Simadibrata, "Left lateral decubitus sleeping position is associated with improved gastroesophageal reflux disease symptoms: A systematic review and meta-analysis," *World Journal of Clinical Cases*, vol. 11, pp. 7329–7336, Oct 2023.




Authorized licensed use limited to: IIT - Istituto Italiano di Tecnologia. Downloaded on December 16,2024 at 07:34:44 UTC from IEEE Xplore. Restrictions apply.

# An AI-Driven Telemonitoring System Exploiting Sensorized Glasses and Insoles to Correlate Cognitive Load and Mobility During ADLs

Giulia Bodo*,[1,4], Giulio Sciortino*,[2], Ludovico Pedullà[3], Erica Grange[3], Sara Giordanino[1,4], Gian Luca Bailo[2], Andrea Tacchino[3], Jessica Podda[3], Giampaolo Brichetto[3], Alexey Petrushin[1], Carlos Beltrán-González[2], Alessio Del Bue+,[2] and Matteo Laffranchi+,[1]

***Abstract*— Smart environments can play a crucial role in providing personalized assessment protocols for individuals. This study proposes a wearable telemonitoring system for non-invasively collecting and tracking mobility and mental effort parameters. The system consists of sensorized glasses, insoles, and AI algorithms for evaluating key metrics. To extract data, the activity "preparing coffee for two people" was performed by healthy participants. Preliminary results indicate that, on average, participants completed the task in 8 minutes. Mental workload, assessed through pupil diameter, showed a mean pupil diameter of $\mu = 5.19\ mm$ with a standard deviation of $\sigma = 0.99\ mm$. On average, participants took 340 steps during the task. Questionnaire responses demonstrated good system usability. The findings provide insights into user perceptions of the monitoring approach and highlight the system's potential for clinical adoption.**

## I. Introduction

In clinical practice, independence in and performance of activities of daily living (ADLs) are usually assessed by occupational therapists using observation-based instruments that include actual performance analysis and take into account the complexity of daily activities [1], [2]. However, these methods have several limitations, including low sensitivity to mild impairments, difficulty detecting smaller and more specific changes over time, and potential influence from raters' sensitivity [3]. Limited attention has been dedicated to the quantitative assessment of ADLs through technological solutions, such as non-intrusive environmental or wearable sensors, home-testing biomarker-sensing devices, immersive virtual reality devices, and assistive robots that can operate in everyday life situations [4]. Recently, the use of technology and IoT device-based smart diagnosing assistance systems has been integrated into clinical research and practice to monitor and recognize specific ADLs performed by older adults in their home setting [5], [6]. However, no literature is currently available regarding the use of technological devices and wearables to assess the quality and independence of ADLs performance for people with neurological conditions. Moreover, despite the growing number of assessment and rehabilitation tools, greater efforts must be dedicated to personalizing these strategies, taking into account the complexity of each individual [7].

Telemonitoring is showing great promise as a non-invasive method for tracking health-related parameters [8], particularly through the use of wearable devices that do not interfere with ADLs [9], ensuring the ability to perform tasks while maintaining an ecological setting for the test environment [10]. Thus, smart environments equipped with advanced sensors and artificial intelligence algorithms offer the possibility to quantify motor and cognitive performances through continuous measurements [11]. Several studies highlight the use of sensorized insoles for monitoring and evaluating gait, enabling the recognition and identification of different walking phases [12]. Additionally, research demonstrates the potential of using gaze characteristics, such as pupil diameter variation, to study and understand the cognitive load associated with tasks requiring varying mental effort [13],[14], as well as to assess participant engagement [15].

This work presents the results of a collaboration between our research institute and clinical partners specialized in Multiple Sclerosis (MS), a chronic degenerative condition characterized by inflammation and damage to the central nervous system. MS leads to symptoms such as impaired mobility and cognitive decline [16]. The objective of this study is to design and evaluate a telemonitoring system for continuously assessing MS patients' performance. By leveraging collected data, the system aims to promptly detect changes in participants' abilities [17]. This paper describes the experimental setup of a smart monitoring system, which integrates wearable sensors, including sensor-equipped glasses (Tobii) and sensorized insoles, with AI-based algorithms. This combination enables the aggregation of data from multiple sources and the extraction of multidimensional metrics essential for assessing individuals' health status and activities. The study includes a pilot experiment involving six healthy participants performing a specific ADL, preparing coffee for two people, while wearing the wearable devices. This preliminary study is essential for evaluating the system's usability and functionality before introducing it to more vulnerable populations. It allows researchers to identify and address technical issues, design flaws, and user interface

*Co-First authors, equal contribution
+Co-Last authors, equal contribution
[1]Rehab Technologies Laboratory at Istituto Italiano di Tecnologia, Genova, Via Morego 30, 16163, Italy.
[2]Pattern Analysis and Computer Vision at Istituto Italiano di Tecnologia, Genova, Via Enrico Melen 83, 16152, Italy.
[3]Scientific Research Area, Italian Multiple Sclerosis Foundation, Genova, Via Operai 40, 16149, Italy.
[4]Politecnico di Torino, Torino, Corso Duca degli Abruzzi 24, 10129, Italy.

challenges without the added complexity of managing health-related risks. Additionally, it facilitates the collection of an initial dataset of normative values for motor and cognitive metrics. These baseline values will later be compared with data from individuals with MS in a follow-up study planned for the next phase of the project.

## II. Methods

### A. Experimental protocol

As a daily living task, Preparing a coffee with a coffee maker and serving it for two people was chosen, based on the Assessment of Motor and Process Skills (AMPS) assessment tool [18]. This task requires the participant to focus on both motor and cognitive skills, allowing for a comprehensive evaluation of the participants' performance. The participants were asked to prepare the coffee for two people and serve it on a table. Before starting the task execution, a familiarization with the set-up of the environment, including the location of all needed tools and materials is provided. Participants were also asked to restore and return unneeded items to their original storage place, place dirty utensils in or besides the sink, wipe up any crumbs or spills. There were no specific rules regarding the coffee preparation process. The participants should proceed as they would at home. Ideally, the participant should not interact with the examiner, as they have all the information needed to complete the task independently. However, questions may be asked if necessary. The examiner will take notes as the participant performs the task. Before to start the task, sensorised glasses and insoles were worn by the participant as shown in Figure 1.

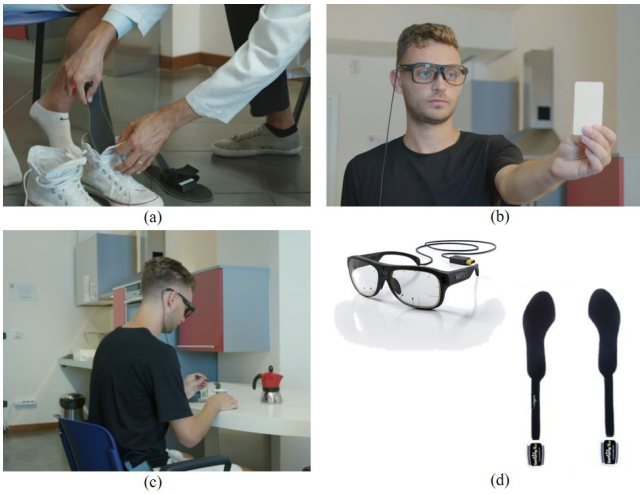



Fig. 1: Experimental Setup: (a) The wearable sensors are worn by the participant, with the insoles placed directly into their shoes. (b) Illustrates the glasses auto-calibration procedure, where the participant focuses on a fixed target to calibrate the gaze analysis. (c) Represents one participant wearing the devices during the test. (d) Shows the two devices adopted.

### B. Sensorized glasses

The Tobii glasses are wearable devices equipped with a front-facing camera that records the surrounding environment and internal cameras that track the participant's eyes to analyze gaze and pupil behavior. Thanks to this device, it is possible to gather data on the cognitive load of the participant. Extensive literature highlights how pupillometry, particularly the assessment of variations in pupil diameter, is closely correlated with mental effort, as explained in [19], [13].

### C. Sensorized insoles

The Sensing Tex sensorized insoles, fitted with 16 resistive pressure sensors, capture data on plantar pressure distribution through a $4 \times 3$ matrix of acquisition points located in the forefoot area and a $2 \times 2$ matrix in the rearfoot region. These flexible insoles are designed to fit comfortably inside regular shoes.

Both sensors communicate wireless with a central acquisition system, which manages the start and stop of data collection and gathers the recorded information at the end of each trial session.

## III. Algorithms Design

The proposed analysis aims to collect a comprehensive dataset from wearable sensors to describe user activity at both cognitive and mobility levels. The algorithms are specifically designed to track: the participant's time spent in specific zones of the testing environment, the interactions with objects used during task preparation and mobility-related data (e.g., number of steps and average step cadence). Through the adoption of an analysis pipeline and evaluation of the results, the authors propose a correlation between cognitive load (assessed via pupillometric analysis) and the zones or phases of the test performed.

### A. Object and QR code detection algorithm

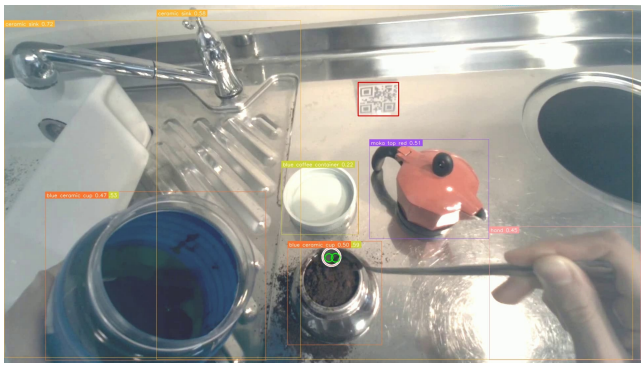


Fig. 2: Processing of a single frame from an experimental session. Bounding labeled boxes identify the recognized QR code zones and the detected objects.

The proposed system consists in a cascade of algorithms designed to perform object detection, QR code reading, and

hand-object interactions. For object detection, we employed YOLO World [20] a specialized version of YOLO v8 [21] fine-tuned on real-time open-vocabulary object detection, which demonstrated robust performance. YOLO World offers an easy way to detect a vast number of common-use objects without collecting and labeling an extensive dataset, resulting in a meaningful reduction of resources. Additionally, avoiding a manual fine-tuning process allowed us to quickly change setup during the first experimental phases and would not require any additional effort if the setting will change in the future. The ontology of the detected object is: coffee maker top red, coffee maker metallic bottom, hand, cup, coffee jar, spoon. As for the hand-object interaction, we selected frames in which the center of the bounding box of a detected object falls within that of a detected hand. When such situation occurs, it is interpreted as the hand holding the object.

The QR codes, stuck in the environment in their corresponding zone, were used to perform the detection of the zones involved in the scene during the execution of the task (an example of QR code and object detection is shown in Figure 2). The read QR codes correspond to shelf, stove area (coffee preparation area), living room and stock. The total time presence of these QR codes determines the presence of the user in the areas. The chosen python library was qreader.

### *B. Gait analysis pattern recognition: YOLO Model*

The extraction of the useful metrics from the gait data was performed by first predicting the foot state in each time frame, then using a Python script we computed the total number of steps, where a step is a succession of detected $foot \rightarrow forefoot \rightarrow foot$ classes. Then a time frame of 250 to 2000 milliseconds was empirically chosen to exclude unrealistic data from the sample, for example, when the sensor or the model missed a foot or a forefoot. Regarding cadence calculations, only effective steps were considered during actual walking periods. The analysis of kinematic parameters includes step duration, step count, and cadence. For each participant, the evaluated metrics comprised:

- Number of steps $(N_{steps})$.
- Step duration: determined by taking the difference between the current contact time of one foot and the previous foot contact time of the same foot, whenever the pattern $foot \rightarrow forefoot \rightarrow foot$ occurs.
- Step cadence: it is calculated as the number of steps taken divided by the acquisition duration (in seconds), starting from the first step. The result is then converted to steps per minute.

$$Step_{cadence} = \left( \frac{N_{steps}}{\Delta T_{acquisition}(s)} \right) \cdot 60 \qquad (1)$$

Due to the variability of participants' foot size and body weight, interpreting the step phase numerically via pressure data is unfeasible. Therefore, we adopted YOLOv8m for detecting the step phase based on the shape of the pressure distribution on the sole. We chose version 8 due to our experience with it and compatibility with our environment,

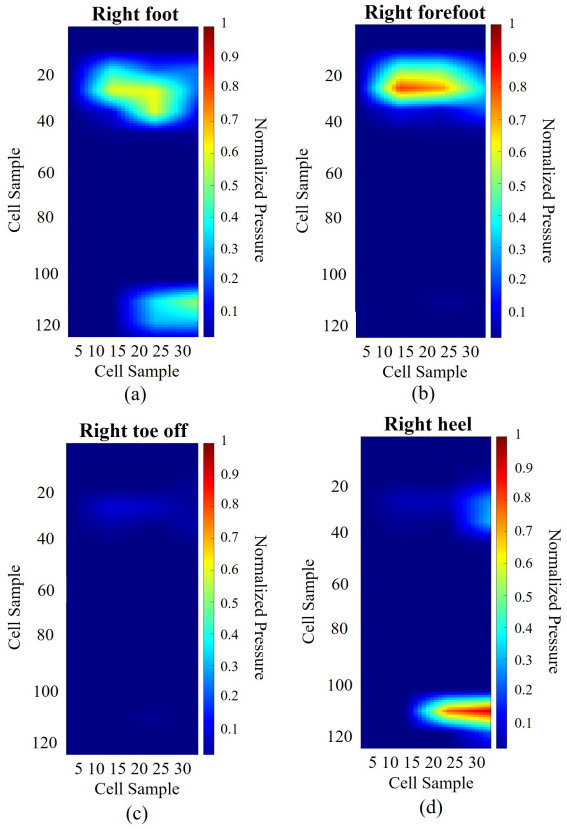



Fig. 3: Example of pressure maps captured from sensorized insoles for the right foot, illustrating different phases of gait: (a) stance, (b) push-off, (c) swing, and (d) heel strike.

specifically the medium model which offers a good balance between resources and precision. Object detection models offer an effective solution by assigning labels to pressure map configurations, and automatically recognize gait phases. This approach avoids manual analysis of individual sensor activations and uses labels to distinguish gait phases. Among the models considered for this purpose, YOLO was identified. The walking data over a distance of 6 meters were previously collected from 8 healthy participants and used to train the employed YOLO model. A MATLAB code was developed to convert the pressure maps, provided by the insoles, into jpeg images, by doing so we gathered a dataset of 2194 pressure map images for both feet (an example of the obtained pressure maps are shown in Figure 3). The dataset has been manually annotated. The following labels were used for the gait analysis:

- right_heel, left_heel: to identify heel strike
- right_foot, left_foot: to identify stance phase
- right_forefoot, left_forefoot: to identify the push-off
- right_toe_off, left_toe_off: to identify the swing phase

A total of 1123 samples were labeled for the left foot and 1071 for the right foot. The samples were then split into a training set and a validation set to train and validate the AI model. The split was randomized, assigning 20% of the

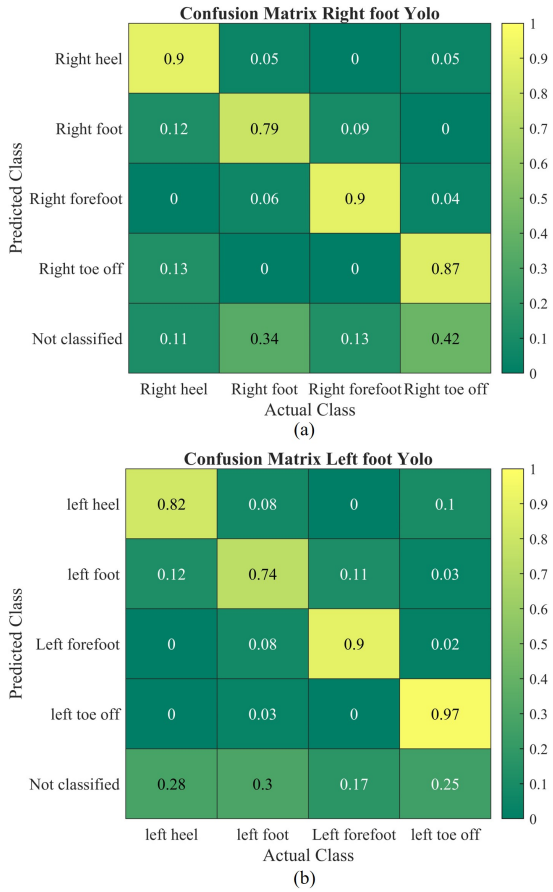



Fig. 4: Confusion matrices, related to the YOLO models for the right and left foot, evaluated on the validation set.

samples to the validation set: the training set contained 894 samples for the left foot and 854 for the right foot, while the validation set included 229 samples for the left foot and 217 for the right. Two distinct models were then trained, one for the right foot and one for the left foot. Each model was trained for 200 epochs and $lr0 = 0.1$, with results from the training process saved for further analysis. To evaluate the performance of the models, the confusion matrices for both left and right foot models are provided in Figure 4, and common metrics, as precision and recall are adopted to evaluate object detection models. Results as shown in Table I.

TABLE I: Precision and Recall for all classes in left and right foot YOLO model.

| **Class** | **Left foot** | | **Right foot** | |
|---|---|---|---|---|
| | ***p*** | ***r*** | ***p*** | ***r*** |
| Heel | 67% | 82% | 71% | 90% |
| Foot | 60% | 74% | 64% | 79% |
| Forefoot | 76% | 90% | 80% | 90% |
| Toe off | 71% | 97% | 63% | 87% |

## IV. Results

This section presents the results of monitoring the activities performed by the participants, reporting metrics related to both mobility and cognitive load. Due to hardware issues, the connection was lost with the sensors for two participants. As a result, sensor data are only available for four participants. The questionnaire responses were completed by all six participants.

### A. Mobility and Cognitive metrics

*1) Zone permanence timing:* The different room areas were tagged with QR codes to track the participants' movements within the environment, without relying on additional external sensors (such as floor sensors or cameras to capture the participant's movements). The objective was to analyze the time participants spent in each of the four identified areas. The results show that, on average, the percentage of the total task duration spent in each area is as follows: 4.75% in the shelf area (where the coffee maker and cups are stored), 66% in the coffee area (where the coffee maker is prepared), 2% in the stock area (where coffee and spoons are kept), and 27% in the living room (where the coffee is consumed). The proportion of time each participant spent in each area, relative to the overall task duration, is represented in the bar charts in Figure 5.

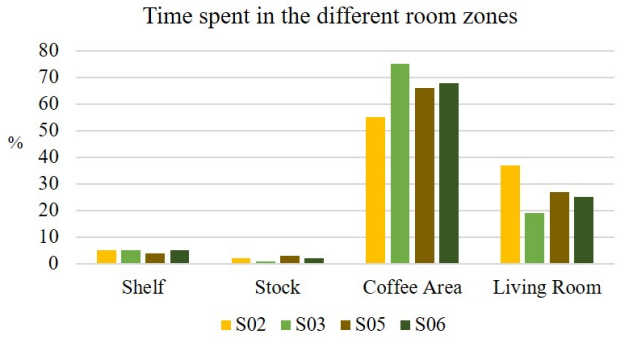



Fig. 5: The bar chart shows the proportion of total time each participant spent in four zones of the test area to complete the task. The zones are: the coffee preparation area (coffee area), the storage area for ingredients and spoons (stock), the coffee serving area (living room), and the shelf where the coffee maker and cups are stored (shelf). Results are provided for four participants.

*2) Gait analysis:* Insoles data were analyzed to compute the step numbers, cadence and mean duration as reported in Table II. Some anomalies were detected in participant S06's data, which can be attributed to manufacturing defects in the sensorized insole, whereas participants S03 and S02 exhibited a notably low cadence, attributed to frequent interruptions in their walking patterns.

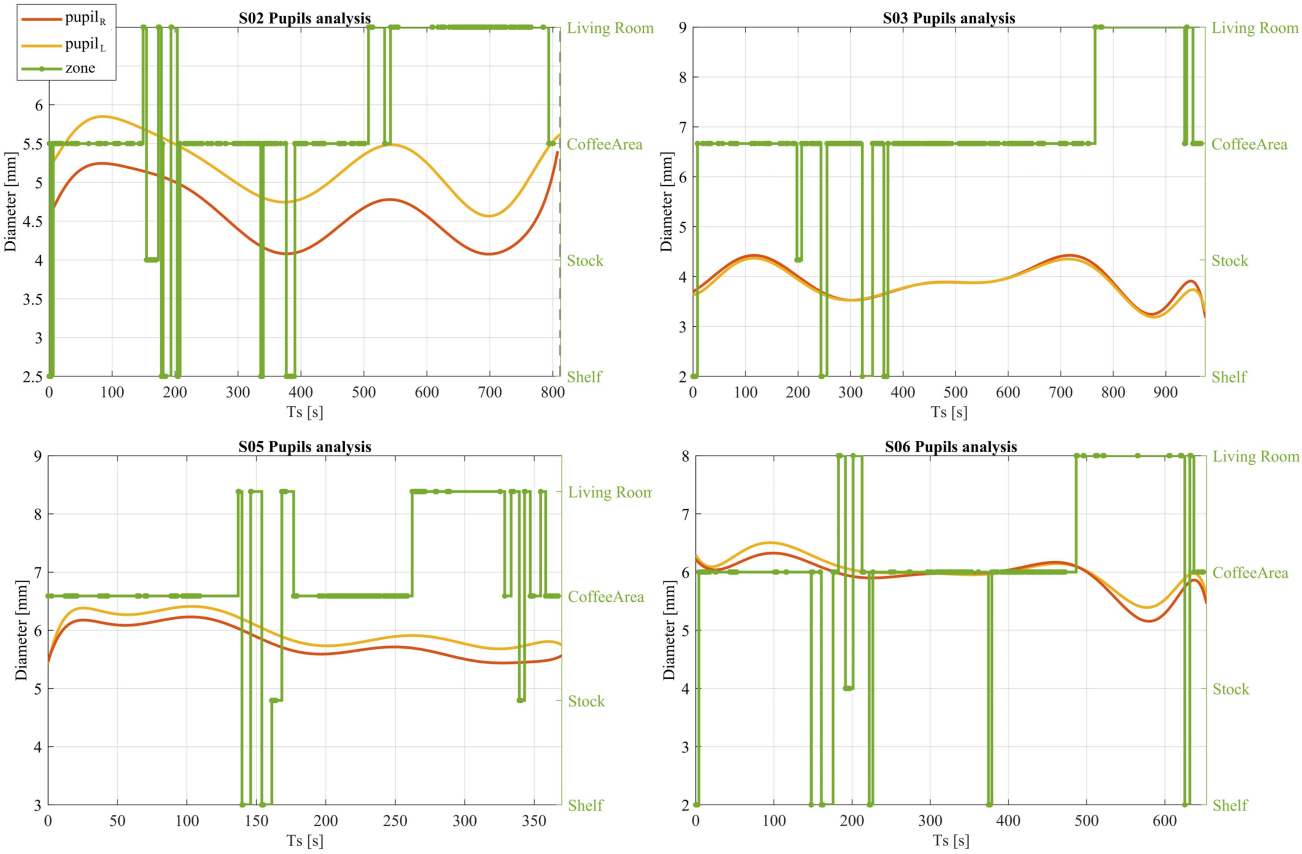



Fig. 6: The graphs show task duration, participant permanence in the different room zones (based on QR code data) and pupil diameter changes (left and right eyes). This allows for assessing mental effort during different task phases, with larger pupil dilation indicating greater mental effort.

TABLE II: Measured gait metrics.

| **id** | $N_{steps}$ | *Step Cadence* $[\frac{steps}{min}]$ | $\Delta t_{mean}$ $[ms]$ |
|---|---|---|---|
| S02 | 529 | 54.7 | 448.5 |
| S03 | 406 | 27.7 | 371.3 |
| S05 | 343 | 85.1 | 320.7 |
| S06 | 83 | 9.7 | 295.2 |

*3) Pupillometry analysis:* Table III lists, for each participant, the minimum and maximum pupil dilation values, along with the corresponding room zones where these measurements were taken and the pupil's coefficients of variation, computed as:

$$CV = \frac{\sigma}{\mu} \tag{2}$$

where $\mu$ is the signal mean and $\sigma$ is the standard deviation. Statistical considerations can be done on the recorded pupils analysis, by aggregating both right and left pupils signals recorded it is possible to compute the overall weighted mean $\mu_{\text{tot}}$ of the $n$ signals and the overall standard deviation $\sigma_{\text{tot}}$.

$$\mu_{\text{tot}} = \frac{1}{n}\sum_{i=1}^{n}\mu_i \tag{3}$$

$$\sigma^2_{\text{tot}} = \frac{\sum(\sigma_i^2 + \mu_i^2)}{n} - \mu^2_{\text{tot}}, \quad \sigma_{\text{tot}} = \sqrt{\sigma^2_{\text{tot}}} \tag{4}$$

Results indicate $\mu_{\text{tot}} = 5.187\ [mm]$ and $\sigma_{\text{tot}} = 0.992\ [mm]$. Figure 6 presents a correlation graph showing the relationship between cognitive load, as measured by pupil dilation, and the room zones where the participant was performing the task. With reference to Figure 6, in the case of S02, we can observe an increase in mental effort during the first part of the task, when the objects are retrieved and the coffee maker is prepared (from 0 to 200 seconds). Following this, as the participant waits for the coffee maker to be ready, pupil diameter decreases (from 200 to 450 seconds). The mental effort then increases again when the participant pours the coffee into the cups and brings them to the table (from 450 to 600 seconds). Finally, during the time spent in the living room, mental effort decreases once more. This analysis and interpretation are made easier by the availability of the video recorded with the Tobii system. Similar patterns can be observed in other participants, though the analysis is customizable for each participant.

*4) Object interaction timing:* The time participants spent interacting with key objects relevant to task completion was evaluated. The total interaction time with the coffee maker pot, cups, coffee jar, and spoon is summarized in Table IV. For all participants, the longest interaction time was with the coffee maker. This evaluation offers a useful

TABLE III: Pupillometry analysis includes maximum and minimum pupil dilation (right and left) associated with high and low cognitive effort zones, as well as the coefficients of variation for recorded pupil signals. The total task duration $\Delta t$ is also reported, measured from the end of the experiment explanation to the completion of table tidying.

| **id** | $\phi_{R_{min}}$ $[mm]$ | $\phi_{L_{min}}$ $[mm]$ | *Min. Eff. Zone* | $\phi_{R_{max}}$ $[mm]$ | $\phi_{L_{max}}$ $[mm]$ | *Max. Eff. Zone* | $\Delta t$ *[min]* | $CV_R$ | $CV_L$ |
|---|---|---|---|---|---|---|---|---|---|
| S02 | 2.98 | 3.18 | Coffee Area | 6.59 | 6.88 | Stock | 13.36 | 0.115 | 0.104 |
| S03 | 2.4 | 2.11 | Living Room | 6.43 | 6.08 | Coffee Area | 16.18 | 0.124 | 0.122 |
| S05 | 4.28 | 3.83 | Living Room | 7.51 | 7.34 | Coffee Area | 6.23 | 0.086 | 0.0762 |
| S06 | 3.42 | 3.38 | Living Room | 7.02 | 6.92 | Living Room | 10.96 | 0.063 | 0.062 |

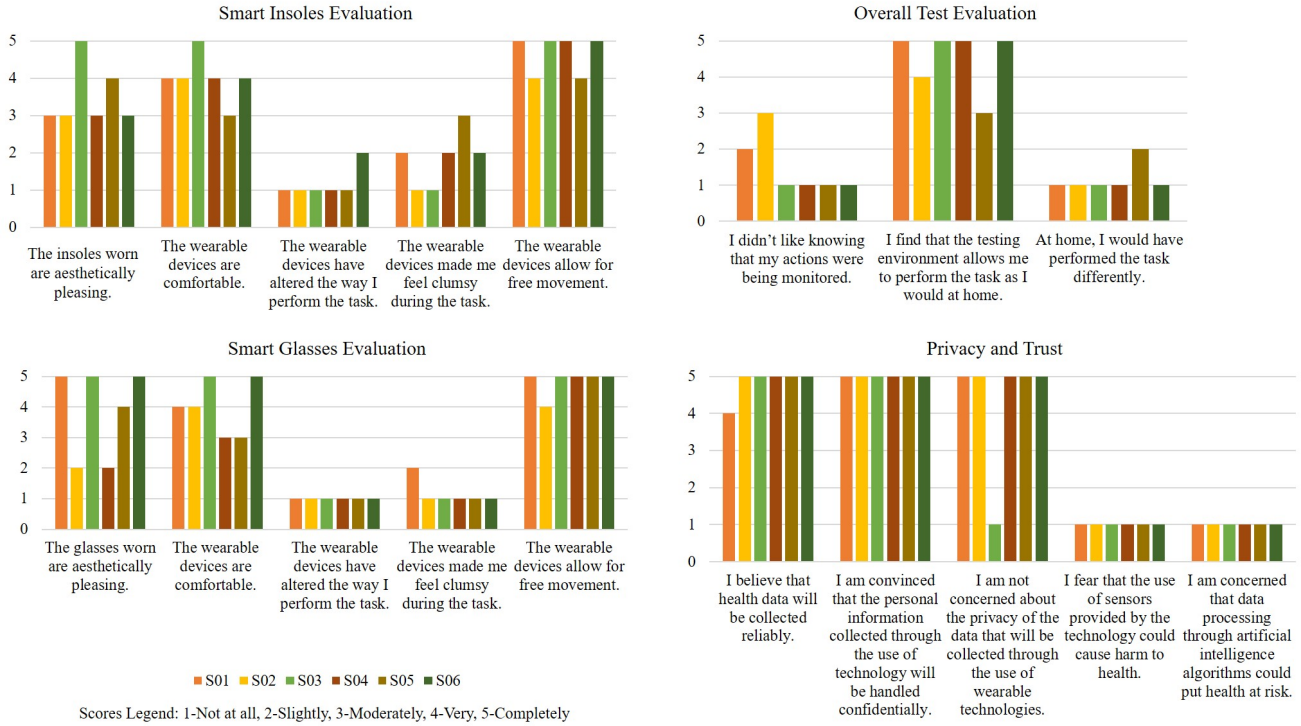



Fig. 7: The results of the questionnaires administered to participants at the end of the activities are presented. Participants were asked to evaluate various statements on a 1-5 scale (ranging from 'completely disagree' to 'strongly agree'). The investigation focused on both the usability and perception of the two wearables (insoles and glasses), as well as the overall impression of a telemonitoring AI-driven approach, including privacy-related concerns.

insight into the average coffee maker preparation time for a healthy participant that from this initial dataset, was found to be 7.93 minutes. Notably, participant S05 was particularly efficient, completing the task in a shorter time than the other participants (see Table III). The interaction time with the cups is also significant, especially in understanding the time required to "take the object and transport it" from the coffee preparation area to the living room and back. The average time for this action was about 48 seconds, consistent with the proximity of the two areas.

TABLE IV: Interaction time with various objects held by participants: the interaction duration is automatically computed using data derived from the YOLO processing algorithms for object detection. Four objects were considered for this analysis: a coffee maker pot, a cup, a coffee jar, and a spoon.

| **id** | *Coffee maker* $\Delta t$ $[min]$ | *Cup* $\Delta t$ $[min]$ | *Coffee Jar* $\Delta t$ $[min]$ | *Spoon* $\Delta t$ $[min]$ |
|---|---|---|---|---|
| S02 | 8.22 | 1.13 | 3.00 | 0.77 |
| S03 | 10.62 | 1.18 | 2.08 | 2.08 |
| S05 | 4.17 | 0.57 | 1.25 | 0.14 |
| S06 | 8.72 | 0.31 | 0.89 | 1.02 |

### *B. Questionnaires*

The questionnaires results, shown in Figure 7, indicate that the proposed solution is user-friendly and highly acceptable to healthy participants. Both the insoles and the glasses were rated as aesthetically pleasing and comfortable, with minimal impact on task performance. Participants were able to move freely during the experiment, and notably, they reported that they would have performed the task in the same way at home. This suggests that the assessment provides a reliable reflection of daily-life performance. Additionally, no concerns regarding privacy or data collection were raised, indicating trust in the process.

## V. Discussion and Conclusion

The results of this preliminary study offer valuable insights for future clinical applications. The extended interaction time with the coffee maker suggests that the chosen task is an effective proxy for assessing daily-life performance, reflecting challenges that may arise from cognitive or motor impairments (particularly manual dexterity), or a combination of both. Additionally, participants in this pilot study exhibited varying distributions of interaction times with objects and movement patterns across different areas of the room, indicating reliance on individualized strategies. This confirms that the task allows for personal planning, enabling participants to schedule activities freely while providing a quantitative and technologically robust assessment in a realistic, ecological environment. Pupil dilation data further highlight critical points in the task that may indicate increased effort, offering valuable insights into participants' specific challenges. Finally, gait analysis revealed that the participant who completed the task most quickly maintained the highest cadence, suggesting a correlation between lower-limb mobility, gait, balance and the achieved performance in completing the task. In future studies, it will be necessary to increase the sample size to 10–20 participants, as recommended for usability testing of eHealth devices [22]. Future acquisitions will be used to validate estimated interaction times and gait parameters, leveraging manual annotations of task phases and additional sensors such as a step counter. Additionally, correlations with individual characteristics, such as standard cognitive and motor assessments, will be examined. These analyses could help identify specific challenges faced by individuals with MS during this task and guide the development of personalized rehabilitative interventions. In conclusion, this study underscores the potential of task-based assessments in realistic settings to provide meaningful insights into the daily-life challenges. By integrating quantitative metrics, such as pupil dilation and gait parameters, with task performance analysis, authors believe that individual strategies and difficulties can be better understood. This approach lays the foundation for developing personalized, evidence-based interventions aimed at enhancing functional independence and quality of life for people with MS. The proposed solution holds also significant potential for extension to other conditions characterized by mobility impairments, fatigue, or cognitive challenges. By adapting the system's features to address condition-specific symptoms, it can be tailored to support elderly individuals or people with neurological disorders such as Parkinson's disease, stroke, or cerebral palsy, as well as other chronic conditions affecting functional independence.

## ACKNOWLEDGMENT

Funded by the European Union - NextGenerationEU and by the Ministry of University and Research (MUR), National Recovery and Resilience Plan (NRRP), Mission 4, Component 2, Investment 1.5, project "RAISE - Robotics and AI for Socio-economic Empowerment" (ECS00000035).

## References

[1] A Buzaid, MP Dodge, L Handmacher, and PJ Kiltz. Activities of daily living: evaluation and treatment in persons with multiple sclerosis. *Physical Medicine and Rehabilitation Clinics of North America*, 24(4):629–638, Nov 2013.

[2] J Jansa, S Ferdinand, M Milo, IG Løyning, T Huilla, L Kallmayer, S Ilsbroukx, N Filló, J Raats, J Jakobson, and D Kos. Performance of activities of daily living in people with multiple sclerosis. *Multiple Sclerosis and Related Disorders*, 57:103342, Jan 2022.

[3] N Mohammed Alotaibi, K Reed, and M Shaban Nadar. Assessments used in occupational therapy practice: an exploratory study. *Occupational Therapy in Health Care*, 23(4):302–318, Oct 2009.

[4] Tanuja Chitnis et al. Quantifying neurologic disease using biosensor measurements in-clinic and in free-living settings in multiple sclerosis. *NPJ Digital Medicine*, 2:123, Dec 11 2019.

[5] N Camp, M Lewis, K Hunter, J Johnston, M Zecca, A Di Nuovo, and D Magistro. Technology used to recognize activities of daily living in community-dwelling older adults. *International Journal of Environmental Research and Public Health*, 18(1):163, Dec 28 2020.

[6] YJ Park, SY Jung, TY Son, and SJ Kang. Self-organizing iot device-based smart diagnosing assistance system for activities of daily living. *Sensors (Basel)*, 21(3):785, Jan 25 2021.

[7] SD Stowe and S Harding. Telecare, telehealth and telemedicine. *European Geriatric Medicine*, 1:193–197, 2010.

[8] A Petrushin, M Freddolini, G Barresi, and et Al. Iot-powered monitoring systems for geriatric healthcare: overview. *Internet of Things for Human-Centered Design: Application to Elderly Healthcare*, pages 99–122, 2022.

[9] VJ Block, R Bove, C Zhao, and et Al. Association of continuous assessment of step count by remote monitoring with disability progression among adults with multiple sclerosis. *JAMA network open*, 2(3):e190570–e190570, 2019.

[10] C Reinier and GP Hancke. Development of a robust active infrared-based eye tracker. *IET Computer Vision*, 8(6):523–534, 2014.

[11] JO Taylor, JD Chulay, CF Landers, WB Hood Jr, and WH Abelmann. Monitoring high-risk cardiac patients during transportation in hospital. *The Lancet*, 296(7685):1205–1208, 1970.

[12] C Baoliang, M Xiaofan, X Feiyun, C Pin, and W Yong. Arch index measurement method based on plantar distributed force. *Journal of Biomechanics*, 144:111326, 2022.

[13] R Bauer, L Jost, B Günther, and P Jansen. Pupillometry as a measure of cognitive load in mental rotation tasks with abstract and embodied figures. *Psychological Research*, 86(5):1382–1396, 2022.

[14] S Mathôt. Pupillometry: Psychology, physiology, and function. *Journal of cognition*, 1(1), 2018.

[15] J Causer, SA McCormick, and PS Holmes. Congruency of gaze metrics in action, imagery and action observation. *Frontiers in human neuroscience*, 7:604, 2013.

[16] ND Chiaravalloti and J DeLuca. Cognitive impairment in multiple sclerosis. *The Lancet Neurology*, 7(12):1139–1151, 2008.

[17] SC Peirce, AR Hardisty, AD Preece, and G Elwyn. Designing and implementing telemonitoring for early detection of deterioration in chronic disease: defining the requirements. *Health Informatics J.*, 17(3):173–190, 2011.

[18] AG Fisher. *Assessment of Motor and Process Skills. Vol. 1: Development, Standardization, and Administration Manual*. Three Star, Fort Collins, CO, 6th edition, 2006.

[19] H Mitre-Hernandez, R Covarrubias Carrillo, and C Lara-Alvarez. Pupillary responses for cognitive load measurement to classify difficulty levels in an educational video game: Empirical study. *JMIR Serious Games*, 9(1):e21620, 2021.

[20] T Cheng, L Song, Y Ge, W Liu, X Wang, and Y Shan. Yolo-world: Real-time open-vocabulary object detection, 2024.

[21] G Jocher, A Chaurasia, and J Qiu. Ultralytics yolov8. `https://github.com/ultralytics/ultralytics`, 2023.

[22] SJ Coons, CJ Gwaltney, RD Hays, et al. Recommendations on evidence needed to support measurement equivalence between electronic and paper-based patient-reported outcome (pro) measures: Ispor epro good research practices task force report. *Value in Health*, 12:419–429, 2009.

# Appendix B

# Publications

This appendix presents the publications produced during the PhD. Some of the results discussed in this dissertation have also been partially published in the following articles.

These works were funded by the Istituto Nazionale per l'Assicurazione contro gli Infortuni sul Lavoro (INAIL) under grant agreements "PR19-RR-P2 - RoboGYM and "PR23-RR-P2 - ClinicEXO".

- 2022, *Comparative analysis of inverse kinematics methodologies to improve the controllability of rehabilitative robotic devices*, Bodo, Giulia; Di Bello, Pietro; Tessari, Federico; Buccelli, Stefano; Boccardo, Nicolo; De Michieli, Lorenzo; Laffranchi, Matteo, *RehabWeek - IEEE International Conference on Rehabilitation Robotics 2022*
- 2023, *Customized Series Elastic Actuator for a Safe and Compliant Human-Robot Interaction: Design and Characterization*, Bodo, Giulia; Tessari, Federico; Buccelli, Stefano; De Guglielmo, Luca; Capitta, Gianluca; Laffranchi, Matteo; De Michieli, Lorenzo, *RehabWeek - IEEE International Conference on Rehabilitation Robotics 2023*
- 2024, *A Preliminary Approach to Assessing Scapular Synergies with the FloatEvo Exoskeleton*, Bodo, Giulia; Boccardo, Nicolò; Capitta, Gianluca; De Guglielmo, Luca; Laffranchi, Matteo, *6th International Conference on NeuroRehabilitation (ICNR2024)*
- 2024, *Design Improvements to the Float Upper-Limb Exoskeleton Better Mimics the Glenohumeral Complex Kinematics*, Bodo, Giulia; Tessari, Federico; Capitta, Gianluca; De Guglielmo, Luca; Buccelli, Stefano; Laffranchi, Matteo, *2024 IEEE/RSJ International Conference on Intelligent Robots and Systems (IROS)*
- 2024, *A Modular, Time-Independent, Path-Based Controller for Assist- as- Needed Rehabilitative Exoskeletons*, Bodo, Giulia; Giannattasio, Raffaele; Ramadoss, Vishal; Tessari,

Federico; Laffranchi, Matteo, *2024 10th IEEE RAS/EMBS International Conference for Biomedical Robotics and Biomechatronics (BioRob)*

- 2024, *Human Exoskeleton Interfaces and Precision Robotic-Human Joint Alignment for Enhanced Upper Limb Rehabilitation*, Bodo, Giulia; De Angelis, Agnese; Taglione, Elisa; Capitta, Gianluca; De Guglielmo, Luca; Buccelli, Stefano; Laffranchi, Matteo, *2024 10th IEEE RAS/EMBS International Conference for Biomedical Robotics and Biomechatronics (BioRob)*

- 2024, *Improving SEA Joint Torque Sensing for Enhanced Torque Estimation in Human-Machine Interaction*, Bodo, Giulia; Vassallo, Christian; De Guglielmo, Luca; Laffranchi, Matteo, *2024 IEEE 20th International Conference on Automation Science and Engineering (CASE)*

- 2024, *A Rapid Control Prototyping and Hardware-in-the Loop Approach for Upper Limb Robotic Exoskeletons Control*, Bodo, Giulia; Tessari, Federico; Buccelli, Stefano; Laffranchi, Matteo, *Applied Sciences*

Accepted for publication:

- 2025, *A Novel Approach to Trunk Rehabilitation: Designing an Upper Body Robotic Mobilizer for Neurological Disorders*, Bodo, Giulia; Capitta, Gianluca; Modenese Mattia; De Guglielmo, Luca; Guanziroli, Eleonora; Laffranchi, Matteo, *RehabWeek - IEEE International Conference on Rehabilitation Robotics 2025*

These works were funded by the European Union - NextGenerationEU and by the Ministry of University and Research (MUR), National Recovery and Resilience Plan (NRRP), Mission 4, Component 2, Investment 1.5, project “RAISE - Robotics and AI for Socio-economic Empowerment” (ECS00000035).

- 2024, *Enabling Frail Subjects Telemonitoring: A Sensor Network System for Enhanced Health Assessment*, Bodo, Giulia; Sciortino, Giulio; Petrushin, Alexey; Seminerio, Emanuele; Morganti, Wanda; Bailo, Gian Luca; Beltrán-González, Carlos; Pilotto, Alberto; Laffranchi, Matteo; Del Bue, Alessio *2024 24th International Conference on Control, Automation and Systems (ICCAS)*

Accepted for publication:

- 2025, *An AI-Driven Telemonitoring System Exploiting Sensorized Glasses and Insoles to Correlate Cognitive Load and Mobility During ADLs*, Bodo, Giulia; Sciortino, Giulio;

Pedullà, Ludovico; Grange, Erica; Giordanino, Sara; Bailo, Gian Luca; Tacchino, Andrea; Podda, Jessica; Brichetto, Giampaolo; Petrushin, Alexey; Del Bue, Alessio; Laffranchi, Matteo, *RehabWeek - IEEE International Conference on Rehabilitation Robotics 2025*

# References


[1] T. Mikolajczyk et al. Advanced technology for gait rehabilitation: An overview. *Advances in Mechanical Engineering*, 10(7):1687814018783627, 2018.

[2] H. Nakayama, H. S. Jørgensen, H. O. Raaschou, and T. S. Olsen. Recovery of upper extremity function in stroke patients: the copenhagen stroke study. *Archives of Physical Medicine and Rehabilitation*, 75(4):394–398, 1994.

[3] B. Huisstede, S. Bierma-Zeinstra, B. W. Koes, and J. A. Verhaar. Incidence and prevalence of upper-extremity musculoskeletal disorders. a systematic appraisal of the literature. *BMC Musculoskeletal Disorders*, 7(1):1–7, 2006.

[4] Paul Issack and Kenneth Egol. Posttraumatic contracture of the elbow: Current management issues. *Bulletin (Hospital for Joint Diseases (New York, N.Y.))*, 63:129–36, 02 2006.

[5] J. Bosch, M.J. O'Donnell, S. Barreca, L. Thabane, and L. Wishart. Does task-oriented practice improve upper extremity motor recovery after stroke? a systematic review. *International Scholarly Research Notices*, 2014.

[6] Pirondini E. and al. Evaluation of a new exoskeleton for upper limb post-stroke neurorehabilitation: Preliminary results. *Jensen W., Andersen O., Akay M. (eds) Replace, Repair, Restore, Relieve – Bridging Clinical and Engineering Solutions in Neurorehabilitation. Biosystems and Biorobotics.*, 7:637–645, January 2014.

[7] E. Ambrosini, S. Dalla Gasperina, M. Gandolla, and A. Pedrocchi. Upper-limb exoskeletons for stroke rehabilitation. In *Mediterranean Conference on Medical and Biological Engineering and Computing*, pages 1722–1728. Springer, 2019.

[8] A. Pollock, S.E. Farmer, M.C. Brady, P. Langhorne, G.E. Mead, J. Mehrholz, and F. van Wijck. Interventions for improving upper limb function after stroke. *Cochrane Database of Systematic Reviews*, 11, 2014.

[9] A. M. Stewart, C. G. Pretty, M. Adams, and X. Chen. Review of upper limb hybrid exoskeletons. *IFAC-PapersOnLine*, 50(1):15169–15178, 2017.

[10] Xuefeng Bao, Aidan R. Friederich, Musa L. Audu, and Ronald J. Triolo. An integrated control system for optimal human trunk motion. In *2020 8th IEEE RAS/EMBS International Conference for Biomedical Robotics and Biomechatronics (BioRob)*, pages 1055–1060, 2020.

[11] NS Tharu, AYL Wong, and YP Zheng. Neuromodulation for recovery of trunk and sitting functions following spinal cord injury: a comprehensive review of the literature. *Bioelectronic Medicine*, 9(1):11, May 29 2023. Erratum in: Bioelectron Med. 2023 Jun 29;9(1):14. doi: 10.1186/s42234-023-00116-3.

[12] World health organization website. https://www.who.int.

[13] S. B. Brotzman and R. C. Manske. *Clinical Orthopaedic Rehabilitation E-Book: An Evidence-Based Approach-Expert Consult*. Elsevier Health Sciences, 2011.

[14] Q Qian, C Nam, Z Guo, and et al. Distal versus proximal - an investigation on different supportive strategies by robots for upper limb rehabilitation after stroke: a randomized controlled trial. *Journal of NeuroEngineering and Rehabilitation*, 16:64, 2019.

[15] Q Qian, X Hu, Lai Q, S.C Ng, Y. Zheng, and W Poon. Early stroke rehabilitation of the upper limb assisted with an electromyography-driven neuromuscular electrical stimulation-robotic arm. *Frontiers in Neurology*, 8:447, 2017.

[16] D. J. Reinkensmeyer and V. Dietz. *Neurorehabilitation Technology*. Springer, 2016.

[17] G. Morone et al. Robot-assisted gait training for stroke patients: current state of the art and perspectives of robotics. *Neuropsychiatric Disease and Treatment*, 13:1303, 2017.

[18] K. J. Nolan et al. Robotic exoskeleton gait training during acute stroke inpatient rehabilitation. *Frontiers in Neurorobotics*, page 86, 2020.

[19] O. Jansen et al. Hybrid assistive limb exoskeleton hal in the rehabilitation of chronic spinal cord injury: proof of concept; the results in 21 patients. *World Neurosurgery*, 110:e73–e78, 2018.

[20] A. Rojek, A. Mika, Ł. Oleksy, A. Stolarczyk, and R. Kielnar. Effects of exoskeleton gait training on balance, load distribution, and functional status in stroke: a randomized controlled trial. *Frontiers in Neurology*, 10:1344, 2020.

[21] N. Rehmat, J. Zuo, W. Meng, Q. Liu, S. Xie, and H. Liang. Upper limb rehabilitation using robotic exoskeleton systems: a systematic review. *International Journal of Intelligent Robotics and Applications*, 2(3):283–295, sep 2018.

[22] E. Hong et al. Mobility skills with exoskeletal-assisted walking in persons with sci: results from a three center randomized clinical trial. *Frontiers in Robotics and AI*, 7:93, 2020.

[23] G. A. Albanese et al. Efficacy of wrist robot-aided orthopedic rehabilitation: a randomized controlled trial. *Journal of NeuroEngineering and Rehabilitation*, 18(1):1–15, 2021.

[24] W. Verrusio, V. Gianturco, M. Cacciafesta, V. Marigliano, G. Troisi, and M. Ripani. Fall prevention in the young old using an exoskeleton human body posturizer: a randomized controlled trial. *Aging Clinical and Experimental Research*, 29(2):207–214, 2017.

[25] A.I. Kapandji and P.A. Pagani. *Fisiologia articolare. Schemi commentati di biomeccanica umana*. Monduzzi, 2009.

[26] Britannica encyclopedia. https://www.britannica.com/science/human-muscle-system.

[27] A.S. Niyetkaliyev, S. Hussain, M.H. Ghayesh, and Gursel Alici. Review on design and control aspects of robotic shoulder rehabilitation orthoses. *IEEE TRANSACTIONS ON HUMAN-MACHINE SYSTEMS*, 47(6):1134–1145, dec 2017.

[28] R. Gopura and K. Kiguchi. Mechanical designs of active upper-limb exoskeleton robots: State-of-the-art and design difficulties. *IEEE 11th International Conference on Rehabilitation Robotics Kyoto International Conference Center*, pages 178–187, jul 2009.

[29] A. Otten, C. Voort, A. Stienen, R. Aarts, E. van Asseldonk, and H. van der Kooij. Limpact:a hydraulically powered self-aligning upper limb exoskeleton. *IEEE/ASME transactions on mechatronics*, 20(5):2285–2298, 2015.

[30] Q. Qian et al. Distal versus proximal: An investigation on different supportive strategies by robots for upper limb rehabilitation after stroke: A randomized controlled trial. *Journal of NeuroEngineering and Rehabilitation*, 16(1):1–16, 2019.

[31] E. Pirondini et al. Evaluation of a new exoskeleton for upper limb post-stroke neurorehabilitation: Preliminary results. In *Replace, Repair, Restore, Relieve–Bridging Clinical and Engineering Solutions in Neurorehabilitation*, pages 637–645. Springer, 2014.

[32] Hans-Otto Karnath and Doris Broetz. Understanding and treating "pusher syndrome". *Physical therapy*, 83 12:1119–25, 2003.

[33] J Nolan, A Jacques, E Godecke, et al. Clinical practice recommendations for management of lateropulsion after stroke determined by a delphi expert panel. *Clinical Rehabilitation*, 37(11):1559–1574, 2023.

[34] Dott. in Ft. SERGIO GIGLI Dott. in Ft. GIULIANA LEANZA. La riabilitazione nella pusher syndrome: una particolare manifestazione clinica dello stroke, January 2009. Accessed: 2024-10-01.

[35] Islam Md R., Spiewak C., Rahman M., and Fareh R. A brief review on robotic exoskeletons for upper extremity rehabilitation to find the gap between research prototype and commercial type. *Advances in Robotics and Automation*, 6, January 2017.

[36] Piggott L. and Ziat M. Haptic neurorehabilitation and virtual reality for upper limb paralysis: A review. *Critical Reviews in Biomedical Engineering*, 44(1-2):1–32, January 2016.

[37] Nathanael Jarrasse and Guillaume Morel. Connecting a human limb to an exoskeleton. *IEEE Transactions on Robotics*, 28:697–710, 01 2011.

[38] Nives Klopčar and Jadran Lenarčič. Kinematic model for determination of human arm reachable workspace. *Meccanica*, 40(2):203–219, 2005.

[39] J IJspeert, R Lustenhouwer, RM Janssen, and et al. Reachable workspace analysis is a potential measurement for impairment of the upper extremity in neuralgic amyotrophy. *Muscle & Nerve*, 66(3):282–288, 2022.

[40] Stephen J. Housman, Le Vu, Talat Rahman, Rafael J. Sanchez, and David J. Reinkensmeyer. Arm-training with t-wrex after chronic stroke: Preliminary results of a randomized controlled trial. In *Rehabilitation Robotics, 2007. ICORR 2007. IEEE 10th International Conference on*, pages 562–568. IEEE, June 2007.

[41] André Schiele and Frans van der Helm. Kinematic design to improve ergonomics in human machine interaction. *IEEE transactions on neural systems and rehabilitation engineering : a publication of the IEEE Engineering in Medicine and Biology Society*, 14:456–69, 01 2007.

[42] Randa Mallat, Mohamad Khalil, Gentiane Venture, Vincent Bonnet, and Samer Mohammed. Human-exoskeleton joint misalignment: A systematic review. pages 1–4, 10 2019.

[43] Yves Zimmermann, Jaeyong Song, Cédric Deguelle, Julia Läderach, Lingfei Zhou, Marco Hutter, Robert Riener, and Peter Wolf. Human–robot attachment system for exoskeletons: Design and performance analysis. *IEEE Transactions on Robotics*, 39(4):3087–3105, 2023.

[44] Ajay Seth, Ricardo Matias, António P Veloso, and Scott L Delp. A biomechanical model of the scapulothoracic joint to accurately capture scapular kinematics during shoulder movements. *PLOS ONE*, 11(1):e0141028, 2016.

[45] Ahmet E. Engin and S. T. Tümer. Three-dimensional kinematic modelling of the human shoulder complex—part i: Physical model and determination of joint sinus cones. *Journal of Biomechanical Engineering*, 111(2):107–112, May 1989.

[46] Oliver Rettig, Laetitia Fradet, Philip Kasten, Patric Raiss, and Sebastian I. Wolf. A new kinematic model of the upper extremity based on functional joint parameter determination for shoulder and elbow. *Gait & Posture*, 30(4):469–476, 2009.

[47] A. Dabholkar. Assessment of scapular behaviour in stroke patients. *International Journal of Health and Rehabilitation Sciences*, 4(2):95–102, 2015.

[48] J. S. Scibek. Assessment of scapulohumeral rhythm for scapular plane shoulder elevation using a modified digital inclinometer. *World Journal of Orthopedics*, 3(6):87–94, 2012.

[49] H. Zhou. Human motion tracking for rehabilitation—a survey. *Biomedical Signal Processing and Control*, 3:1–18, 2008.

[50] C. Yang. Rfid-based 3d human pose tracking: A subject generalization approach. *Digital Communications and Networks*, 8:278–288, 2022.

[51] A. Ruiz. Exoskeleton-based robotic platform applied in biomechanical modelling of the human upper limb. *Applied Bionics and Biomechanics*, 6:205–216, 2009.

[52] Kinetec, alex exoskeleton. http://www.wearable-robotics.com/kinetek/products/alex/.

[53] Hocoma website. https://www.hocoma.com/solutions/armeo-power/.

[54] Kim B. and Deshpande A. D. An upper-body rehabilitation exoskeleton harmony with an anatomical shoulder mechanism: Design, modeling, control, and performance evaluation. *The International Journal of Robotics Research*, 36:414 – 435, 2017.

[55] Pignolo L., Dolce G., Basta G., Lucca L. F., Serra S., and Sannita W. G. Upper limb rehabilitation after stroke: Aramis a "robo-mechatronic" year=2012, volume=, number=, pages=1410-1414, doi=10.1109/BioRob.2012.6290868. In *2012 4th IEEE RAS and EMBS International Conference on Biomedical Robotics and Biomechatronics (BioRob)*.

[56] P. Maciejasz, J. Eschweiler, K. Gerlach-Hahn, A. Jansen-Troy, and S. Leonhardt. A survey on robotic devices for upper limb rehabilitation. *Journal of NeuroEngineering and Rehabilitation*, 11(3), 2014.

[57] S. Buccelli, F. Tessari, F. Fausto, L. De Guglielmo, and G. Capitta et Al. A gravity-compensated upper-limb exoskeleton for functional rehabilitation of the shoulder complex. *Applied Sciences*, 12(7), 2022.

[58] Se-Young Kim, Mi-Young Lee, and Byoung-Hee Lee. Effects of rehabilitation robot training on physical function, functional recovery, and daily living activities in patients with sub-acute stroke. *Medicina*, 60(5), 2024.

[59] Movendo website. https://www.movendo.technology/our-products/hunova/?lang=en#.

[60] Trunk stability rehabilitation robot trainer 3dbt-33 website. https://www.komachine.com/en/companies/man-tel/products/44955-trunk-stability-rehabilitation-robot-trainer-3dbt-33.

[61] C.M. Bauer, I. Nast, M. Scheermesser, R.P. Kuster, D. Textor, M. Wenger, J. Kool, and D. Baumgartner. A novel assistive therapy chair to improve trunk control during neurorehabilitation: Perceptions of physical therapists and patients. *Applied Ergonomics*, 94:103390, 2021.

[62] Space balance 3d website. http://cybermedic.koreasme.com/product/product_02.html.

[63] JA Saglia, A Luca, V Squeri, L Ciaccia, C Sanfilippo, S Ungaro, and L Michieli. Design and development of a novel core, balance and lower limb rehabilitation robot: hunova®. In *2019 IEEE International Conference on Rehabilitation Robotics (ICORR)*, pages 417–422, June 2019.

[64] Chae-gil Lim. Effects of trunk control robot training on balance and gait abilities in persons with chronic stroke. *Physical Therapy Rehabilitation Science*, 9:105–112, 06 2020.

[65] Liselot Thijs, Eline Voets, Evelyne Wiskerke, Thomas Nauwelaerts, Yves Arys, Harold Haspeslagh, Jan Kool, Patrick Bischof, Christoph Bauer, Robin Lemmens, Daniel Baumgartner, and Geert Verheyden. Technology-supported sitting balance therapy versus usual care in the chronic stage after stroke: a pilot randomized controlled trial. *Journal of NeuroEngineering and Rehabilitation*, 18, 07 2021.

[66] Y Ko, H Ha, YH Bae, and W Lee. Effect of space balance 3d training using visual feedback on balance and mobility in acute stroke patients. *Journal of Physical Therapy Science*, 27(5):1593–1596, 2015.

[67] Gopura R.A.R.C. and Bandara D.S.V. A brief review on upper extremity robotic exoskeleton systems. *6th International Conference on Industrial and Information Systems*, August 2011.

[68] Varghese R.J. and et al. Wearable robotics for upper-limb rehabilitation and assistance: A review of the state-of-the-art, challenges, and future research. *Wearable Technology in Medicine and Health Care.*, pages 23–69, January 2018.

[69] Shen Y., Ferguson W. P., and Rosen J. Upper limb exoskeleton systems—overview. *Wearable Robotics*, 2020.

[70] Frisoli A. Exoskeletons for upper limb rehabilitation. *Rehabilitation Robotics*, pages 75–87, January 2018.

[71] Yu H., Huang S., Chen G., Pan Y., and Guo Z. Human–robot interaction control of rehabilitation robots with series elastic actuators. *IEEE Transactions on Robotics*, 31(5):1089–1100, 2015.

[72] Wen Yu, Jacob Rosen, and Xiaoou Li. Pid admittance control for an upper limb exoskeleton. In *Proceedings of the 2011 American Control Conference*, pages 1124–1129, 2011.

[73] Zimmermann Y., Sommerhalder M., Wolf P., Riener R., and Hutter M. Anyexo 2.0: A fully-actuated upper-limb exoskeleton for manipulation and joint-oriented training in all stages of rehabilitation. *IEEE Transactions on Robotics*, 2023.

[74] Hutter M., Bodie K., Lauber A., and et al. Ep16181251 - joint unit, joint system, robot for manipulation and/or transportation, robotic exoskeleton system and method for manipulation and/or transportation. 2016.

[75] Calanca A. and Fiorini P. Human-adaptive control of series elastic actuators. *Robotica*, December 2014.

[76] Cempini M. et al. Relevance of series-elastic actuation in rehabilitation and assistance robotic: Two cases of study. *2015 IEEE 1st International Forum on Research and Technologies for Society and Industry Leveraging a better tomorrow (RTSI)*, pages 76–81, 2015.

[77] Pratt G.A. and Williamson M.M. Series elastic actuators. *Proceedings 1995 IEEE/RSJ International Conference on Intelligent Robots and Systems. Human Robot Interaction and Cooperative Robots*, 1:399–406 vol.1, 1995.

[78] Zhao W., Wang J., Qian W., Xiao X., and Guo Z. Design of a compliant upper-limb rehabilitation exoskeleton based on novel series elastic actuators. *2021 IEEE/ASME International Conference on Advanced Intelligent Mechatronics (AIM)*, pages 566–571, 2021.

[79] V Crocher, A Sahbani, J Robertson, A Roby-Brami, and G Morel. Constraining upper limb synergies of hemiparetic patients using a robotic exoskeleton in the perspective of neuro-rehabilitation. *IEEE Trans Neural Syst Rehabil Eng*, 20(3):247–257, 2012.

[80] Bodo G., Tessari F., Buccelli S., De Guglielmo L., Capitta G., Laffranchi M., and De Michieli L. Customized series elastic actuator for a safe and compliant human-robot interaction: Design and characterization. *IEEE Int Conf Rehabil Robot. 2023.*, sep 2023.

[81] Proietti T., Crocher V., Roby-Brami A., and Jarrasse N. Upper-limb robotic exoskeletons for neurorehabilitation: A review on control strategies. *IEEE Rev Biomed Eng.*, 9:4–14, April 2016.

[82] H. Kim, L. M. Miller, N. Byl, G. M. Abrams, and J. Rosen. Redundancy resolution of the human arm and an upper limb exoskeleton. *IEEE Transactions on Biomedical Engineering*, 59(6):1770–1779, 2012.

[83] B. Siciliano, L. Sciavicco, L. Villani, and G. Oriolo. *Robotics modelling planning and control*. Springer London Ltd, 2010.

[84] Sariyildiz E., Ucak K., Ohnishi K., Oke G., and Temeltas H. Intelligent systems based solutions for the kinematics problem of the industrial robot arms. *2013 9th Asian Control Conference (ASCC)*, pages 1–6, June 2013.

[85] Andreas Aristidou and Joan Lasenby. Inverse kinematics: a review of existing techniques and introduction of a new fast iterative solver. 2009.

[86] K. Tokarz and S. Kieltyka. Geometric approach to inverse kinematics for arm manipulator. *Proceedings of the 2003 International Conference on Machine Learning and Cybernetics*, 1, July 2010.

[87] J. Wan, H. Wu, and R. Ma et al. A study on avoiding joint limits for inverse kinematics of redundant manipulators using improved clamping weighted least-norm method. *Journal of Mechanical Science and Technology*, 32:1367–1378, June 2018.

[88] C.A. Klein, C. Chu-Jenq, and S. Ahmed. A new formulation of the extended jacobian method and its use in mapping algorithmic singularities for kinematically redundant manipulators. *IEEE Transactions on Robotics and Automation*, 11(1):50–55, 1995.

[89] Y.M. Nakamura, H. Hanafusa, and T. Yoshikawa. Task-priority based redundancy control of robot manipulators. *The International Journal of Robotics Research*, 6:15–3, 1987.

[90] A. Liegeois. Automatic supervisory control of the configuration and behavior of multibody mechanisms. *IEEE Trans. Systems, Man, and Cybernetics*, 7(12):842–868, 1977.

[91] B. Siciliano. Kinematic control of redundant robot manipulators: A tutorial. *Journal of Intelligent and Roboric System*, 3:201–212, 1990.

[92] H. Hanafusa, T. Yoshikawa, and Y. Nakamura. Analysis and control of articulated robot arms with redundancy. *IFAC Proceedings Volumes*, 14(2):1927–1932, 1981. 8th IFAC World Congress on Control Science and Technology for the Progress of Society, Kyoto, Japan, 24-28 August 1981.

[93] Jang J.-S. R. Anfis: adaptive-network-based fuzzy inference system. *IEEE Transactions on Systems, Man, and Cybernetics*, 23(3):665–685, 1993.

[94] Howard D.W. and Zilouchian A. Application of fuzzy logic for the solution of inverse kinematics and hierarchical controls of robotic manipulators. *Journal of Intelligent and Robotic Systems*, 23:217–247, October 1998.

[95] Ankarali A. and Cilli M. Anfis inverse kinematics and hybrid control of a human leg gait model. *Academic Platform Journal of Engineering and Science*, 1:34–49, January 2013.

[96] Molteni F., Gasperini G., Cannaviello G., and Guanziroli E. Exoskeleton and end-effector robots for upper and lower limbs rehabilitation: Narrative review. *PMandR*, 10:S174–S188, 2018.

[97] Gull M. A., Bai S., and Bak T. A review on design of upper limb exoskeletons. *Robotics*, 9(1), 2020.

[98] Kim H., Miller L.M., Fedulow I., Simkins M., Abrams G.M., Byl N., and Rosen J. Kinematic data analysis for post-stroke patients following bilateral versus unilateral rehabilitation with an upper limb wearable robotic system. *IEEE Trans Neural Syst Rehabil Eng.*, 21(2):153–164, March 2013.

[99] Andres Martinez, Brian Lawson, and Michael Goldfarb. A controller for guiding leg movement during overground walking with a lower limb exoskeleton. *IEEE Transactions on Robotics*, 34(1):183–193, 2017.

[100] Alexander Duschau-Wicke, Joachim Von Zitzewitz, Andrea Caprez, Lars Lunenburger, and Robert Riener. Path control: a method for patient-cooperative robot-aided gait rehabilitation. *IEEE transactions on neural systems and rehabilitation engineering*, 18(1):38–48, 2009.

[101] Hermano Igo Krebs, Jerome Joseph Palazzolo, Laura Dipietro, Mark Ferraro, Jennifer Krol, Keren Rannekleiv, Bruce T Volpe, and Neville Hogan. Rehabilitation robotics: Performance-based progressive robot-assisted therapy. *Autonomous robots*, 15:7–20, 2003.

[102] Tommaso Proietti, Vincent Crocher, Agnes Roby-Brami, and Nathanael Jarrasse. Upper-limb robotic exoskeletons for neurorehabilitation: a review on control strategies. *IEEE reviews in biomedical engineering*, 9:4–14, 2016.

[103] Stefano Dalla Gasperina, Loris Roveda, Alessandra Pedrocchi, Francesco Braghin, and Marta Gandolla. Review on patient-cooperative control strategies for upper-limb rehabilitation exoskeletons. *Frontiers in Robotics and AI*, 8:745018, 2021.

[104] Tobias Nef, Matjaz Mihelj, Gabriela Kiefer, Christina Perndl, Roland Muller, and Robert Riener. Armin-exoskeleton for arm therapy in stroke patients. In *2007 IEEE 10th international conference on rehabilitation robotics*, pages 68–74. IEEE, 2007.

[105] Guidali M., Duschau-Wicke A., Broggi S., Klamroth-Marganska V., Nef T., and Riener R. A robotic system to train activities of daily living in a virtual environment. *Medical and biological engineering and computing*, 49(10):1213–1223, July 2011.

[106] Zeiaee A., Soltani-Zarrin R., Langari R., and Tafreshi R. Design and kinematic analysis of a novel upper limb exoskeleton for rehabilitation of stroke patients. In *2017 International Conference on Rehabilitation Robotics (ICORR)*, pages 759–764, 2017.

[107] Tobias Nef, Matjaz Mihelj, Gabriela Kiefer, Christina Perndl, Roland Muller, and Robert Riener. Armin - exoskeleton for arm therapy in stroke patients. In *2007 IEEE 10th International Conference on Rehabilitation Robotics*, pages 68–74, 2007.

[108] dspace website. https://www.dspace.com/en/pub/home/applicationfields/portfolio/bussimulation/bussimulation_usecases/rapid_control_prototyping.cfm.

[109] Speedgoat rcp website. https://www.speedgoat.com/solutions/simulink-real-time-workflow.

[110] National instrument website. https://www.ni.com/docs/en-US/bundle/labview-control-design-and-simulation-module/page/lvsimconcepts/sim_c_config.html.

[111] Opal-rt website. https://www.opal-rt.com/rapid-control-prototyping/.

[112] Etas website. https://www.etas.com/en/company/realtimes-2021-next-generation-large-scale-prototyping.php.

[113] Quanser website. https://www.quanser.com/products/quanser-rapid-control-prototyping-toolkit-labview/.

[114] Chennakesava Reddy A. Difference between denavit - hartenberg (d-h) classical and modified conventions for forward kinematics of robots with case study. *International Conference on Advanced Materials and manufacturing Technologies (AMMT)*, pages 267–286, dec 2014.

[115] Arno H. A. Stienen and Arvid Q. L. Keemink. Visualization of shoulder range of motion for clinical diagnostics and device development. *2015 IEEE International Conference on Rehabilitation Robotics (ICORR)*, pages 816–821, 2015.

[116] Lee C., Kwak S., Kwak J., and Oh S. Generalization of series elastic actuator configurations and dynamic behavior comparison. *Actuators*, 6(3), 2017.

[117] Walmsley R. P. and Szybbo C. A comparative study of the torque generated by the shoulder internal and external rotator muscles in different positions and at varying speeds. *Journal of Orthopaedic & Sports Physical Therapy*, 9(6):217–222, 1987.

[118] Seth A., Matias R., Veloso A. P., and Delp S. L. A biomechanical model of the scapulothoracic joint to accurately capture scapular kinematics during shoulder movements. *PLOS ONE*, 11:1–18, 01 2016.

[119] O'Sullivan L. W. and Gallwey T. J. Forearm torque strength and endurance for elbow and forearm angles. *Proceedings of the Human Factors and Ergonomics Society Annual Meeting*, 45(14):1128–1132, 2001.

[120] Wang Y., Chen Y., Chen K., Wu Y., and Huang Y. A flat torsional spring with corrugated flexible units for series elastic actuators. In *2017 2nd International Conference on Advanced Robotics and Mechatronics (ICARM)*, pages 138–143, 2017.

[121] Wang S., Meijneke C., and van der Kooij H. Modeling, design, and optimization of mindwalker series elastic joint. In *2013 IEEE 13th International Conference on Rehabilitation Robotics (ICORR)*, pages 1–8, 2013.

[122] Lagoda C., Schouten A., Stienen A., Hekman E.E.G., and Kooij H. Design of an electric series elastic actuated joint for robotic gait rehabilitation training. pages 21 – 26, 10 2010.

[123] Qiao D., Pang G., Kit M., and Lam D. A new pcb-based low-cost accelerometer for human motion sensing. pages 56 – 60, 10 2008.

[124] Speedgoat website. https://www.speedgoat.com/products-services/real-time-target-machines/baseline-real-time-target-machine.

[125] ptc®.

[126] Neville Hogan. Impedance control: An approach to manipulation. *ASME Journal of Dynamic Systems, Measurement, and Control*, 107(1):1–24, 1985.

[127] Carolee J. Winstein and David Kay. Chapter 16 - translating the science into practice: Shaping rehabilitation practice to enhance recovery after brain damage. In *Sensorimotor Rehabilitation At the Crossroads of Basic and Clinical Sciences*, volume 218 of *Progress in Brain Research*, pages 331–360. Elsevier, 2015.

[128] Luc Le Tien, Alin Albu-Schaffer, Alessandro De Luca, and Gerd Hirzinger. Friction observer and compensation for control of robots with joint torque measurement. In *2008 IEEE/RSJ International Conference on Intelligent Robots and Systems*, pages 3789–3795, 2008.